



Université  
de Toulouse

# THÈSE

En vue de l'obtention du

## DOCTORAT DE L'UNIVERSITÉ DE TOULOUSE

**Délivré par :**

Institut National Polytechnique de Toulouse (Toulouse INP)

**Discipline ou spécialité :**

Energétique et Transferts

---

**Présentée et soutenue par :**

M. QUENTIN LAMIEL

le mercredi 23 octobre 2019

**Titre :**

Analysis of spray-wall impingement, fuel film spreading and vaporisation  
for reciprocating engine applications

---

**Ecole doctorale :**

Mécanique, Energétique, Génie civil, Procédés (MEGeP)

**Unité de recherche :**

Institut de Mécanique des Fluides de Toulouse ( IMFT)

**Directeur(s) de Thèse :**

M. DOMINIQUE LEGENDRE

**Rapporteurs :**

M. FABRICE LEMOINE, UNIVERSITÉ LORRAINE

M. GILLES BRUNEAUX, IFPEN

**Membre(s) du jury :**

Mme CHRISTINE ROUSSELLE, UNIVERSITE D'ORLEANS, Président

M. DOMINIQUE LEGENDRE, TOULOUSE INP, Membre

M. JÉRÔME HELIE, SOCIETE CONTINENTAL AUTOMOTIVE FRANCE SA, Invité

M. NICOLAS LAMARQUE, SOCIETE CONTINENTAL AUTOMOTIVE FRANCE SA, Membre

M. RAUL PAYRI, UNIVERSITAT POLITECNICA DE VALENCE, Membre



---

## ABSTRACT

The road transport is responsible of a considerable amount of pollutants emissions at the worldwide scale. To tackle this issue, many laws are trying to give a framework to reduce the emissions at the global scale. The law are always more restrictive, and they oriented the car manufacturers to the reduction of their gasoline engine size. This phenomenon, called downsizing, lead to the use of direct injection in order to improve the power/volume ratio of the engine. However, with direct injection the problem of particle emissions arose. Indeed, the liquid film generated during the injection process are responsible of inhomogeneities in the combustion chamber which lead to particles formation. In this context, the study of the fuel films in the combustion chamber is a major concern. To perform this study several experimental apparatus are designed in this thesis. A high-pressure 3-hole solenoid injector is used in order to generate liquid films. The generation and the spreading of the liquid films is observed and modelled. Then the thermal aspects of the spray impingement is studied, to characterise the local heat transfer. These thermal loss are delaying the evaporation of the liquid film, which will lead to inhomogeneities in the combustion chamber and particle generation. A modelling of the heat transfer is also proposed, finally the evaporation rate of alkanes films is proposed. Mono and multi-components films are studied, these measures were used to calibrate a numerical model for the evaporation of thin liquid films on hot walls. Together with the previous experimental investigations and models a test campaign on a real engine has been held. The objective is to confirm that, the results produced out of the engine are transposable to the engine (with careful attention). Conclusions on the different aspects are then presented.

## RÉSUMÉ

Le transport routier est responsable d'une partie des émissions de polluants sur la planète. Conscient de ce problème, des lois sur les émissions des véhicules sont régulièrement votées afin de réduire l'impact environnemental du transport automobile. Ces lois de plus en plus restrictives ont poussé les fabricants automobiles à réduire la taille des moteurs essence et à utiliser des procédés d'injection directe afin d'augmenter le ratio puissance/volume des moteurs et réduire la consommation. Cependant avec l'utilisation de l'injection directe, de nouveaux problèmes apparaissent, notamment la production de particules fines, elles-mêmes réglementées. Cette thèse s'inscrit dans ce cadre. En

---

effet, les films liquides engendrés par l'injection de carburant sont identifiés comme principaux responsables de la production de particules. Dans ce contexte, les films liquides sont étudiés expérimentalement à l'aide d'un injecteur haute pression disposant de 3 trous. Les aspects dynamiques de création et d'étalement du film liquides sont étudiés et modélisés. S'en suit une étude thermique de l'interaction entre le spray et la paroi. Afin de caractériser les pertes de chaleur observées lors de l'impact, ces pertes thermiques étant responsables d'un délai dans la vaporisation du carburant et donc d'inhomogénéités du mélange au moment de la combustion, une modélisation de ces pertes et du transfert thermique associé est aussi proposée. Enfin une étude des taux d'évaporation de plusieurs alcanes purs puis de mélanges est proposée. Ces mesures ont servi à la calibration d'un modèle numérique d'évaporation de films fins de carburants sur des parois chaudes. Autour de ces différentes études, une campagne d'essais moteurs a été effectuée. L'objectif est de confirmer que les études expérimentales faites en laboratoires sont bien transposables (moyennant la prise de certaines précautions) aux moteurs automobiles. Les conclusions des différentes études sont finalement proposées.



*A mon grand-père.*

## Acknowledgements

Après trois belles et longues années passées entre Continental et l'Institut de Mécanique des Fluides de Toulouse voici maintenant venu le moment des remerciements. C'est, pour ceux qui me connaissent, la partie qui est probablement la moins facile à écrire. Mais c'est un exercice comme un autre auquel il faut se soumettre.

Je vais commencer par remercier tous ceux que j'ai croisés de près ou de loin au cours de ma thèse et que je pourrais oublier de mentionner.

Merci aux membres du jury de m'avoir fait l'honneur d'accepter mon invitation, merci pour vos retours et appréciations, c'est le moment durant lequel j'ai pu me rendre compte de la portée potentielle de mes travaux de recherche, ce qui est assez agréable.

Je tenais à remercier mon directeur de thèse Dominique Legendre que j'ai eu comme professeur à l'ENSEEIHRT et avec qui j'ai grandement apprécié travailler durant ces 3 années. Merci pour la confiance qu'il m'a faite et pour ses conseils toujours avisés.

Merci aussi à Nicolas Lamarque le meilleur des encadrants, qui m'a dédié énormément de son temps et de son savoir au cours des 3 ans, j'ai tellement appris à son contact et je suis persuadé que la thèse ne se serait pas aussi bien déroulée sans son implication au quotidien.

Merci aussi aux personnes qui ont pu rendre le travail plus simple, je pense notamment aux membres du Test Center de Continental ainsi que les secrétaires de l'IMFT et de Continental, et les personnes avec qui j'ai pu être amené à échanger sur divers sujets professionnels.

Il y a aussi tous mes amis que j'aimerais remercier, pour tout le temps qu'on passe ensemble j'ai énormément de chance de les avoir.

Enfin je terminerai par remercier ma famille qui m'a toujours soutenu et accompagné durant ces trois années et toutes celles qui ont précédé. Merci du fond du coeur de m'avoir laissé la liberté de faire et finir ces longues études, j'en suis extrêmement reconnaissant.

Merci encore à tous, en espérant que la suite de l'aventure sera tout aussi belle que ces dernières années.

---

# Contents

<b>List of Figures</b>	<b>xi</b>
<b>List of Tables</b>	<b>xxv</b>
<b>Nomenclature</b>	<b>xxvii</b>
<b>1 Introduction</b>	<b>1</b>
1.1 General Context . . . . .	1
1.2 About injection process and engine working . . . . .	7
1.3 Dynamic of droplets and spray impingement . . . . .	10
<b>2 Engine Measurements</b>	<b>23</b>
2.1 Context . . . . .	23
2.2 Experimental Set-up . . . . .	26
2.3 Results . . . . .	31
2.4 Acknowledgment . . . . .	49
<b>3 Experimental Methods</b>	<b>51</b>
3.1 Fuel preparation system . . . . .	51
3.2 Shadowgraphy . . . . .	52
3.3 RIM . . . . .	55
3.4 Fast Thermocouple Measurement Plate . . . . .	68
3.5 X and Y translation . . . . .	71
3.6 Interferometric Measurement Device . . . . .	72
3.7 Atomic Force Microscopy . . . . .	75
3.8 Injector Position . . . . .	76
3.9 Goniometry . . . . .	78

## CONTENTS

---

<b>4</b>	<b>Liquid Film Spreading</b>	<b>81</b>
4.1	Orthogonal impingement film spreading . . . . .	82
4.2	Non-orthogonal film spreading . . . . .	105
4.3	on the thickness of spreading liquid films . . . . .	114
4.4	Conclusion . . . . .	117
<b>5</b>	<b>Heat Transfer Modelling</b>	<b>121</b>
5.1	Context/Introduction . . . . .	121
5.2	Spray wall heat transfer description . . . . .	122
5.3	Parameter Variations . . . . .	130
5.4	Flux Calculation . . . . .	136
5.5	Heat exchange modelling . . . . .	140
5.6	Conclusion . . . . .	144
<b>6</b>	<b>Vaporisation in the vicinity of hot walls</b>	<b>145</b>
6.1	Evaporation of isolated droplets . . . . .	146
6.2	Evaporation of mono/multicomponent liquid film (When $T_{wall} \leq T_{sat}$ ) . . . . .	151
6.3	Hot walls (When $T_{wall} \geq T_{sat}$ ) . . . . .	160
6.4	Conclusion . . . . .	166
<b>7</b>	<b>Conclusion</b>	<b>167</b>
<b>8</b>	<b>Appendix</b>	<b>171</b>
8.1	Roughness measurement on coked piston . . . . .	171
8.2	Additional material on the non-orthogonal spreading of liquid film . . . . .	172
8.3	Evaporation of thin liquid film of single and multi-component hydrocarbon fuel from a hot plate . . . . .	175
8.4	Spreading model for wall films generated by high-pressure sprays . . . . .	187
	<b>Bibliography</b>	<b>197</b>

# List of Figures

1.1	Endoscopic visualisation of direct injection and combustion inhomogeneities (probably soot luminescence or pool fires) [44]. . . . .	3
1.2	Visualisation of the tip wetting, during the injector purge (i.e. after the needle closure) [28]. Black lines highlight the area of liquid deposition. . .	3
1.3	Injector fooling due to tip wetting, carbon deposit slightly changes the hole geometry [30]. . . . .	4
1.4	Particle Number (PN) as a function of SOI and injection geometry [40].	5
1.5	Common position for the injector. Left: Central Mounted. Right: Side Mounted. Highlights the variability of impingement angle encountered in a Direct Injection (DI) engine. . . . .	6
1.6	High pressure injector, ECU and high pressure pump produced by Continental. (Courtesy of Continental website <a href="http://www.continental-automotive.com">www.continental-automotive.com</a> )	7
1.7	Schematisation of the four strokes of a gasoline engine. Intake, Compression, Power and Exhaust. The spark usually takes place at the very end of compression however for sake of clarity it is represented during the power stroke. Every stroke takes 180°CA (Crank angle). . . . .	9
1.8	Spray penetration for 50, 100 and 200 <i>bar</i> for ASTRIDE injector, based on shadowgraphy pictures in atmospheric conditions. Errorbar displaying the standard deviation of measurements based on 5 independent repeats. . . . .	11
1.9	Top: Spray penetration, as a function of time at various ambient pressures (injection pressure 1350 <i>bar</i> ) [77]. Bottom: Penetration curve and calculation of the penetration parameter [72]. . . . .	13

## LIST OF FIGURES

---

1.10	Evolution of mass flow rate and discharge coefficient for different injection pressure [53]. . . . .	14
1.11	Description of injectorwise and spraywise directions. . . . .	14
1.12	PDA measurement of the spray, and velocity distribution at 100 <i>bar</i> and 40 <i>mm</i> . . . . .	15
1.13	Reynolds and Weber distribution at 100 <i>bar</i> , 40 <i>mm</i> away from the injector (See Table 1.3 for definition). . . . .	15
1.14	Post impingement scenario of single drop impact on cold, rigid and dry wall [5]. . . . .	16
1.15	Schematic visualisation of spray-wall impingement and the interrogations raised by this phenomenon. Ombroscopy visualisation performed with a high pressure injector, injection pressure is 100 <i>bar</i> , injector to wall distance 13.5 <i>mm</i> at ambient temperature, light source is a nanolite with an exposure time of 25 <i>ns</i> . Courtesy of Continental. . . . .	20
2.1	Pictures of the instrumented engine in the test bench. Left: Global vue of the engine. Right: Vue of amplification devices for pressure sensor distributed in the air system of the engine. Green Type-K thermocouple wires distributed in the air system also visibles. . . . .	25
2.2	Coolant system, it replaces the one in the car, allowing to test the engine in different conditions. . . . .	26
2.3	Top visualisation of the instrumented engine. The piston in the middle is covered with gold in order to ensure the hot junction of the surface thermocouples (see Figure 3.21). . . . .	27
2.4	$p - v$ and $T - s$ diagrams of the air-standard Otto cycle [58]. . . . .	28
2.5	Position of the four thermocouples in regard of the spray targeting. Left: Injection targeting looking at the cylinder head. Right: Position of the thermocouples looking at the piston. . . . .	29
2.6	Working principle of the radio transmission of data from the cylinder body to the acquisition line. Source: MANNER Operating manual [55].	30
2.7	Bottom view of the piston, parts of the instrumentation are visible. . . .	31



**LIST OF FIGURES**

---

2.8	Cylinder head instrumentation, green area represents the intake, red area the exhaust. The black circle are thermocouples positions together with their names. . . . .	32
2.9	Evolution of piston surface temperature during a combustion cycle at 2000 <i>rpm</i> and a BMEP of 10 <i>bar</i> . . . . .	32
2.10	Filtered value of the evolution of piston surface temperature during a combustion cycle at 2000 <i>rpm</i> and a BMEP of 10 <i>bar</i> . . . . .	33
2.11	Averaged value and standard deviation over 1000 combustion cycles of the evolution of piston surface temperature during a combustion cycle at 2000 <i>rpm</i> and a BMEP of 10 <i>bar</i> . . . . .	34
2.12	Evolution of piston temperature for the four thermocouples. Strokes timing, SOI and ignition presented. Operating point 2000 <i>rpm</i> and a BMEP of 10 <i>bar</i> . . . . .	34
2.13	Temperature evolution during a combustion cycle [42]. They developed a cleaning process using fuel enriched in ethanol to clean the soot deposit. The deposit includes a delay and reduces the sensitivity of the thermocouple. Such study hasn't be done in the case presented here. . .	36
2.14	Map temperature for the piston. White circles: measured points. . . . .	37
2.15	Map temperature for the cylinder head. White circles: measured points. . . . .	38
2.16	Evolution of saturation temperature for n-heptane for different pressures realistic of engine operating points. NIST database. . . . .	39
2.17	Timescale and experimental protocol visualisation for the influence of piston impingement. . . . .	41
2.18	Simulation realised with IMPACT [29] (without aerodynamics) of the effect of SOI on piston impingement. Top: °CA of spray-piston impact. Bottom: Constant 90°C. Set point 2000 <i>rpm</i> 10 <i>bar</i> BMEP. . . . .	41
2.19	Spray deflection simulation in an engine, cylinder wetting. . . . .	42
2.20	Evolution of piston surface temperature for the standard SOI. Set point at 2000 <i>rpm</i> and a BMEP of 10 <i>bar</i> . . . . .	42
2.21	Temperature evolution at engine start and cylinder pressure evolution. Engine speed $\approx$ 400 <i>rpm</i> . Top: full temporal evolution. Bottom left: first combustion cycle. Bottom right: Temperature differences established. . . . .	44

## LIST OF FIGURES

---

2.22	Effect of oil pressure on piston temperature. Switch from 2 to 4 <i>bar</i> is performed at $t=60$ <i>s</i> . . . . .	45
2.23	Evolution of piston temperature for two early injection timing. Left: SOI -330°CA. Right: SOI -360°CA. Set point at 2000 <i>rpm</i> and a BMEP of 10 <i>bar</i> . The arrows highlight the impingement process. . . . .	46
2.24	PN generation for different SOI. Left: SOI steps and time evolution of particle generation. Right: PN level as a function of the SOI. . . . .	48
3.1	Working principle of Shadowgraphy, the object observed is placed between a light source and the camera. . . . .	53
3.2	Two different histogramms showing how to achieve a 0.02 <i>ms</i> exposure time. Top: Continuous light used with a "fast" shutter. Bottom: Pulsed light used with a "slow" shutter. . . . .	54
3.3	Close up shadowgraphy visualisation of 100 bar injection with two different light sources. Left: Continuous LED panel. Right: Pulsed Laser. Courtesy of Continental . . . . .	55
3.4	GDI spray impinging upon a smooth plate. Fuel pressure is 100bar. . .	56
3.5	Sketch of the Refractive Index Matching experimental setup; a) High-pressure pump b) GDI injector c) Plate holder d) Impinging plate e) Light source f) Heating collar g) Mirror h) High-Speed Video camera i) Computer. . . . .	56
3.6	Principle of RIM measurement. Left: Grazing Light illuminating a transparent plate; Right: Modification of light path caused by wetting . . . .	57
3.7	Early injection process of n-heptane at 200bar, injection duration 5ms, wall temperature 25°C . Left: Before spray impingement. Centre: Spray tip reaching the plate. Right: Secondary spray developing and starts of wetting. . . . .	58
3.8	Background subtracted images of secondary spray propagation during injection process of n-heptane at 200bar, injection duration 5ms, wall temperature 25°C . White arrows highlights the secondary spray corona. . . . .	58

**LIST OF FIGURES**

---

3.9	Steady state during injection process of n-heptane at 200bar, injection duration 5ms, wall temperature 25°C . Left: Mie scattering of the spray. Centre: Spreading phase. Right: Droplets reatomisation. Black arrows highlight the liquid film edge, yellow circle shows some droplets reatomisation. . . . .	59
3.10	Late injection process of n-heptane at 200bar, injection duration 5ms, wall temperature 25°. Left: Late droplets reaching the plate (white area in the middle of the liquid film). Right: After injection process. . . . .	60
3.11	Calibration process of RIM method. . . . .	60
3.12	Calibration process for RIM measurement. Injection of 4μL of 20% dodecane fuel. Top: Liquid film evolution. Left: Area evolution with respect to time. Right: Evolution of liquid film grey level. . . . .	62
3.13	Calibration curves for two different impingement angle . . . . .	63
3.14	Left: Boiling bubbles developing in the liquid film. Middle: Entrapped bubbles during injection process. Right: Direct visualisation of liquid film surface soon after the end of injection. Arrows indicate bubbles. . .	65
3.15	RIM Alu set-up. Left: a) High-pressure pump b) GDI injector c) High-pressure spray d) Aluminium plate e) Mirror f) Plate holder g) Light source h) High-Speed Video camera i) Camera. Right: Picture of the experimental set-up. . . . .	67
3.16	Visualisation of liquid film with RIM Alu method. Left: Raw image of liquid film. Right: Background subtracted image of the liquid film. . . .	67
3.17	Top visualisation of impingement plates used to perform RIM methods. . . . .	68
3.18	Left: Top view of the instrumented plate with gold coating. Right: Side view of the instrumented plate with apparent thermocouples. . . . .	68
3.19	Side cut of the thermo-instrumented plate. . . . .	69
3.20	Top view of the instrumented plate. . . . .	70
3.21	Left: Working principle of thermocouple. Right: Working principle of zero degree compensation in the case of iron-constantan couple [19]. . .	70
3.22	Top Left: Overview of the amplification system, in green the backpanel, in blue the amplification modules. Top Right: Break-out box. Bottom Left: Exit panel with BNC connections. Bottom Right: 5 V Power unit. . . . .	72
3.23	ETAS-ES 1000 used as acquisition surface for thermocouple signals. . .	73

## LIST OF FIGURES

---

3.24	Translation plate used to displace the thermocouple plate. Manual linear stage NEWPORT M-UMR 8.51. . . . .	73
3.25	Left: Positioning of optical pen for film thickness measurement. Right: Measurement principle of confocal interferometric device. Here the device measures the distance between a plate and a sample not the thickness of a liquid film (STIL-DUO user manual). . . . .	74
3.26	Two different visualisations of profiles sampled with AFM. Top: Zoom on sapphire trough and crest. Bottom: Same horizontal and vertical scales. The thickness presented here, is a height variation in relatively to the position of the probe. . . . .	76
3.27	Translation and rotation plate allowing the correct positioning of the injector. NEWPORT M-UMR12.63 and M-UTR120 material . . . . .	77
3.28	Left: Side vision of the impingement angle definition. Right: Top vision of the impingement angle definition. . . . .	77
3.29	Goniometer set-up for the advancing and receding angles of n-decane on a sapphire plate. . . . .	78
4.1	Images of a film spreading as visualized from bottom on the RIM setup. $P_i = 100$ bar $T_i = 6$ ms and $z = 50$ mm. Images are displayed every 1.25 ms. . . . .	83
4.2	Time evolution of the liquid film area. Experimental conditions: $T_i = 6$ ms, $P_i = 100$ bar, $z = 50$ mm. The vertical dashed line indicates the end of injection. . . . .	83
4.3	Evolution of digitation wavelength with respect to fuel pressure for $T_i = 6$ ms and $z = 50$ mm. The dashed line represent the power law $P_i^{-1/3}$ . . . . .	85
4.4	Detail of surface waves for different injection conditions for $T_i = 10$ ms and $z = 50$ mm. Left to Right: 50, 100, 200 bar. . . . .	85
4.5	Evolution of film surface waves speed with respect to their radial position $r$ . Experimental conditions $P_i = 100$ bar, $T_i = 10$ ms and $z = 50$ mm. The curves represent a $r^{-1/2}$ evolution expected for a planar radial wave. . . . .	86
4.6	Liquid film area for different injection times. Experimental conditions $P_i = 100$ bar and $z = 50$ mm. Continuous Line: Eq. 4.6, Dashed line: solution of Eq. 4.10. . . . .	87

4.7	Liquid film area for different injection pressures. Experimental conditions $T_i = 6$ ms, $z = 50$ mm. (top) film at the end of the injection from left to right for $P_i=50, 100$ and $200$ bar. (bottom) Time evolution of the film area. Continuous Line: Eq. 4.6. Dashed line: solution of Eq. 4.10. . . . .	88
4.8	Liquid film area for different injector-wall distances. Experimental conditions $T_i = 6$ ms, $P_i = 100$ bar. Continuous Line: Eq. 4.6, Dashed line: solution of Eq. 4.10. . . . .	89
4.9	Sketch of the modeled problem. The film thickness is supposed to be homogeneous. . . . .	89
4.10	Evolution of the film surface as a function of $P_i^{1/3} Q^{2/3} \eta^{-1/3} t$ for all the experiments presented above. Line: Equation 4.6 (see the text for the value of $K_P$ and $K_m$ ) . . . . .	91
4.11	Evolution of the dimensionless area $A^* = (A - A_o)/(A_i - A_o)$ versus the dimensionless time $t/T_i$ for different injection durations and pressures. . . . .	93
4.12	Impingement process of different fuel on sapphire plate. $T_i = 6$ ms, $P_i = 100$ bar $z = 50$ mm $T_w = 20^\circ\text{C}$ . Top: n-heptane spreading. Bottom: n-decane spreading. . . . .	95
4.13	Area evolution of n-heptane and n-decane. Injection conditions $T_i = 6$ ms, $P_i = 100$ bar $z = 50$ mm $T_w = 20^\circ\text{C}$ . . . . .	96
4.14	Impingement process on different roughnesses plate. $T_i = 6$ ms, $P_i = 100$ bar $z = 50$ mm $T_w = 20^\circ\text{C}$ . Top: Smooth sapphire plate. Bottom: $R_a = 20\mu\text{m}$ quartz plate . . . . .	97
4.15	Area evolution of n-decane on two different plate, a smooth sapphire plate and a rough $R_a = 20\mu\text{m}$ quartz plate. Injection conditions $T_i = 6$ ms, $P_i = 100$ bar $z = 50$ mm $T_w = 70^\circ\text{C}$ . . . . .	98
4.16	Liquid film visualisation 5 ms after the end of injection. From left to right, $22^\circ\text{C}$ , $70^\circ\text{C}$ , $90^\circ\text{C}$ , $120^\circ\text{C}$ . Injection conditions, $T_i = 6$ ms, $P_i = 100$ bar. . . . .	101
4.17	Area evolution for different temperature (injector and wall temperature set at the same level). Injection conditions, $T_i = 6$ ms, $P_i = 100$ bar. For some temperature less measurement point are performed, when the measurement were done the focus was on the spreading phase and not on the relaxation phase. . . . .	101

## LIST OF FIGURES

---

4.18	Effect of viscosity on spreading rate. Comparison between experimental data and power law $\eta^{-1/3}$ as presented by the spreading model. . . . .	102
4.19	Working principle of the algorithm used to optimise $K_m$ . Where $\Delta A^* = A^*(n+1) - A^*(n)$ . . . . .	103
4.20	Dimensionless area of n-decane liquid film for different injection duration (2, 4, 6, 8, 10 and 12 ms), different injection pressure (50, 100, 200 bar) and different temperatures (22°C, 70°C, 90°C, 120°C). Left: Before optimisation on the coefficient of mass deposition $K_m$ . Right: After optimisation on the coefficient of mass deposition $K_m$ . Black line represents $y = x$ equation. . . . .	104
4.21	Effect of the algorithm on $K_m$ and the fuel temperature at impact. Left: Evolution of the mass deposition coefficient $K_m$ with respect to injection temperature. Right: Evolution of the temperature of the spray at impact versus its temperature at the nozzle exit. Black lines present some iterations of the model. Black dots present the converged values. . . . .	104
4.22	Image of film spreading of n-decane on a quartz plate, with an impingement angle of 60°. $P_i = 100$ bar, $T_i = 6$ ms and $z = 50$ mm. . . . .	106
4.23	Evolution of liquid film shape with respect to impingement angle at 6.5 ms after start of injection. $P_i = 100$ bar, $T_i = 6$ ms and $z = 50$ mm. . . . .	107
4.24	Time evolution of the liquid film area for several impingement angle. Experimental conditions: $T_i = 6$ ms, $P_i = 100$ bar, $z = 50$ mm. . . . .	108
4.25	Evolution of ellipse focus position on time averaged image, the white area in the centre is the impingement area. Red squares present the position of the focus through time. White line displays the edge of the liquid film at the end of injection. Impingement angle is 60°. . . . .	108
4.26	Visualisation of liquid film edges together with ellipse contour and axes at a given time (5 ms after start of injection). Injection pressure $P_i = 100$ bar, injection duration $T_i = 6.0$ ms. . . . .	109
4.27	Description of the parameters of an ellipse. . . . .	109
4.28	Temporal evolution of ellipse descriptors ( $a + c$ ) and ( $a - c$ ) parameters for several angles. $P_i = 100$ bar, $T_i = 6$ ms. . . . .	111
4.29	Temporal evolution of ellipse descriptor $p$ for several angles. $P_i = 100$ bar, $T_i = 6$ ms. . . . .	111

**LIST OF FIGURES**

---

4.30 Temporal evolution of the liquid film eccentricity for different impingement angle. Injection pressure  $P_i = 100 \text{ bar}$ , injection duration  $T_i = 6 \text{ ms}$ . . . . . 112

4.31 Eccentricity evolution for different impingement angle, together with the fit proposed Equation 4.18. . . . . 113

4.32 Evolution of the spreading rate for the head  $(a + c)^2$  and back  $(a - c)^2$  of the liquid film, together with the fit proposed in Equation 4.19. . . . . 113

4.33 Evolution of the spreading rate for the side  $p^2$  of the liquid film, together with the fit proposed Equation 4.19. . . . . 114

4.34 Liquid film visualisation on quartz plate at several time after start of injection.  $P_i = 100 \text{ bar}$ ,  $T_i = 6 \text{ ms}$ . . . . . 115

4.35 Average thickness evolution for three different impingement angles ( $90^\circ$ ,  $60^\circ$  and  $45^\circ$ ) and pressures ( $50 \text{ bar}$ ,  $100 \text{ bar}$ ,  $200 \text{ bar}$ ). The mass injected is kept constant in all the injection scenario. . . . . 116

4.36 Area evolution for three different impingement angles ( $90^\circ$ ,  $60^\circ$  and  $45^\circ$ ) and pressures ( $50 \text{ bar}$ ,  $100 \text{ bar}$ ,  $200 \text{ bar}$ ). The mass injected is kept constant in all the injection scenario. During the first  $ms$  the area is highly overestimated due to image detection algorithm that has difficulties to differentiate the liquid film and the sparse droplets. . . . . 116

4.37 Mass evolution for three different impingement angles ( $90^\circ$ ,  $60^\circ$  and  $45^\circ$ ) and pressures ( $50 \text{ bar}$ ,  $100 \text{ bar}$ ,  $200 \text{ bar}$ ). The mass injected is kept constant in all the injection scenario. . . . . 117

5.1 Fast surface thermocouple measurement for n-heptane impingement. Injection duration  $6 \text{ ms}$ , injection pressure  $100 \text{ bar}$ , wall temperature  $100^\circ\text{C}$ , fuel temperature  $30^\circ\text{C}$  and injector to wall distance  $50 \text{ mm}$ . Left: Raw data with sample rate of  $0.2 \text{ ms}$ . Centre: Filtered data with  $2 \text{ ms}$  moving average. Right: Averaged measure over 10 repeats for the same injection conditions. . . . . 123

## LIST OF FIGURES

---

5.2	Fast surface thermocouple measurement for n-heptane impingement. Injection duration 6 <i>ms</i> , injection pressure 100 <i>bar</i> , wall temperature 100°C, fuel temperature 30 °C and injector to wall distance 50 <i>mm</i> . Left: Physical description during the impact. Right: Temperature evolution focussed on the heating phase. . . . .	124
5.3	Simultaneous temperature variation of the four thermocouples, for an impingement angle of 60°. Wall temperature is 100 °C , fuel temperature is 30°C , injector-wall distance is 50 <i>mm</i> and injection pressure and duration are 100 <i>bar</i> and 2.12 <i>ms</i> . . . . .	126
5.4	Temperature map for orthogonal impingement. Wall temperature is 100°C, fuel temperature is 50°C, injector-wall distance is 50 <i>mm</i> and injection pressure and duration are 100 <i>bar</i> and 6 <i>ms</i> . . . . .	127
5.5	Temperature profile generated by orthogonal impingement. Continuous and dashed line are the same data mirrored to asses symmetry of the profile. Same conditions as Figure 5.4. . . . .	127
5.6	2D Temperature map for 60° impingement angle, injection duration 6 <i>ms</i> , fuel temperature 30°C, injection pressure 100 <i>bar</i> Left: Wall temperature 100°C. Right: Wall temperature 150°C. . . . .	128
5.7	2D Temperature map for 45° impingement angle, injection duration 6 <i>ms</i> , fuel temperature 30°C , injection pressure 100 <i>bar</i> and wall temperature 100. . . . .	129
5.8	Effect of injection duration on wall cooling. Injection pressure 100 <i>bar</i> , wall temperature 100°C, fuel temperature 30°C, injector to wall distance 50 <i>mm</i> . . . . .	131
5.9	Effect of injection pressure. Wall temperature 100°C, fuel temperature 30°C, injection duration variable (i.e. constant mass), injector to wall distance 30 <i>mm</i> . . . . .	133
5.10	Effect of wall temperature, fuel temperature 30°C. Left: injection pressure $P_i = 50$ <i>bar</i> , injection duration $T_i = 3.0$ <i>ms</i> . Right: injection pressure $P_i = 200$ <i>bar</i> , injection duration $T_i = 1.5$ <i>ms</i> . . . . .	133
5.11	Nucleate boiling on the thermocouple for injection temperature of 150°C. Left: nucleation site attached. Right: thermocouple visible without nucleation. Arrow and circle highlight the thermocouple position. . . . .	134



**LIST OF FIGURES**

---

5.12	Effect of fuel temperature. Wall temperature $100^{\circ}C$ , injection pressure $P_i = 100 \text{ bar}$ , injection duration $T_i = 6.0 \text{ ms}$ . . . . .	135
5.13	Effect of spray travelling distance, wall temperature $150^{\circ}C$ , fuel temperature $30^{\circ}C$ and injection pressure $P_i = 100 \text{ bar}$ , injection duration $T_i = 2.12 \text{ ms}$ . . . . .	136
5.14	Heat flux and temperature temporal variation. . . . .	139
5.15	Heat transfer coefficient variation [89] . . . . .	139
5.16	Heat flux calculation of Arcoumanis [2] and Meingast [56]. . . . .	140
5.17	Heat flux and temperature temporal variation experiment vs model. Dashed line presents the model and plain lines presents the experimental data. Injection condition $P_i = 100 \text{ bar}$ , $T_w = 100^{\circ}C$ and fuel temperature is $30^{\circ}C$ . . . . .	142
5.18	Proposed shape for the heat transfer coefficient. . . . .	143
5.19	Evolution of heat flux and wall temperature for variable injection duration. Dashed line present the model, plain line the experimental data. For sake of clarity experimental data are not shown on the flux curve. Injection condition $P_i = 100 \text{ bar}$ , $T_w = 100^{\circ}C$ and fuel temperature is $30^{\circ}C$ . . . . .	143
5.20	Evolution of the heat transfer coefficient $h$ for different injection duration. Injection condition $P_i = 100 \text{ bar}$ , $T_w = 100^{\circ}C$ and fuel temperature is $30^{\circ}C$ . . . . .	144
6.1	Summary of state of the art in terms of cooling regimes [7]. . . . .	146
6.2	Simulation of streamlines inside a bubble flowing through gas by Chiang et al.[13]. . . . .	148
6.3	Heat flux evolution and droplet lifetime curve with respect to wall temperature. Case of gently deposited droplets, $T_{CHF} = T_{nuk}$ [59]. . . . .	149
6.4	Overview of droplet global representations of the impact regimes and transition conditions for a dry heated wall. (a) Bai and Gosman [4]; (b) Rein [76]; (c) Lee and Ryu [48]. As presented in [59]. . . . .	150
6.5	Images of Injector coking: Right [36] Cleaned, fouled and cleaned up injector. Left [30] SEM image of a coked injector hole . . . . .	152

## LIST OF FIGURES

---

6.6	Distillation curve for 91AI fuel, 91AI fuel + 10% methanol, 91AI fuel + 15% methanol [9] . . . . .	153
6.7	Composition of AI91 gasoline from [9] . . . . .	154
6.8	Fuel film thickness evolution. Left: hexane liquid film with $T_w = 23^\circ\text{C}$ . Right: heptane liquid film with $T_w = 30^\circ\text{C}$ . Dashed line illustrate the identified linear behaviour of the film thickness evaporation. . . . .	156
6.9	Fuel film thickness evolution. Left: iso-octane liquid film with $T_w = 23^\circ\text{C}$ . Right: decane liquid film with $T_w = 50^\circ\text{C}$ . Dashed line illustrate the identified linear behaviour of the film thickness evaporation. . . . .	156
6.10	Schematic vision of STIL measurements. The arrows present possible positions for the measurement in case of nucleate boiling. Position <b>a</b> : no problem encountered. Position <b>b</b> : thickness might be underestimated because of the bubble presence. Position <b>c</b> : too many interfaces to perform a correct measurement. Position <b>d</b> : the surface curvature makes the measurement impossible. . . . .	157
6.11	Fuel film thickness evolution. hexane/iso-octane liquid film with $T_w = 23^\circ\text{C}$ . Dashed line presents the vaporisation rate of single components superimposed in order to compare mono- and multi-components vaporisation behaviours. . . . .	158
6.12	Area evolution for Surrogate 2 fuel film injected on Aluminium plate. Left: Wall temperature $T_w=80^\circ\text{C}$ . Right: Injection pressure $P_i = 100\text{ bar}$ . 159	
6.13	Thickness evolution for surrogate 2 and 3 for a wall temperature $T_w = 80^\circ\text{C}$ . Left: injection pressure $P_i= 30\text{ bar}$ . Right: injection pressure $P_i= 100\text{ bar}$ . . . . .	160
6.14	Liquid film evolution for orthogonal impingement. Wall temperature $T_w = 150^\circ\text{C}$ , injection temperature $T_{FU} = 150^\circ\text{C}$ , injection duration $T_i = 6.00\text{ ms}$ and injection pressure $P_i = 100\text{ bar}$ . . . . .	161
6.15	Liquid film evolution for orthogonal impingement. Wall temperature $T_w = 180^\circ\text{C}$ , injection temperature $T_{FU} = 180^\circ\text{C}$ , injection duration $T_i = 6.00\text{ ms}$ and injection pressure $P_i = 100\text{ bar}$ . . . . .	162
6.16	Liquid film evolution for orthogonal impingement. Wall temperature $T_w = 210^\circ\text{C}$ , injection temperature $T_{FU} = 180^\circ\text{C}$ , injection duration $T_i = 6.00\text{ ms}$ and injection pressure $P_i = 100\text{ bar}$ . . . . .	163

## LIST OF FIGURES

---

6.17	Zoomed visualisation of a n-decane film 15 <i>ms</i> after the start of injection for different plate temperature. Injection duration $T_i = 6.00$ <i>ms</i> and injection pressure $P_i = 100$ <i>bar</i> . . . . .	163
6.18	Aluminium plate mimicking a bowl shape. Length 3.5 <i>cm</i> , width 3 <i>cm</i> , height 1 <i>cm</i> (between bottom and top of the bowl). . . . .	164
6.19	Shadowgraphy of spray impinging on a hot wall, bowl shape geometry. Wall temperature $T_w = 130^\circ C$ , injection duration $T_i = 2.12$ <i>ms</i> and injection pressure $P_i = 100$ <i>bar</i> . . . . .	164
6.20	Shadowgraphy of spray impinging on a hot wall, bowl shape geometry. Wall temperature $T_w = 200^\circ C$ , injection duration $T_i = 2.12$ <i>ms</i> and injection pressure $P_i = 100$ <i>bar</i> . . . . .	165
8.1	Coked piston visualisation together with the roughness measurements performed on a coked zone. Top: piston visualisation. Centre: roughness measurement in the non coked zone. Bottom: roughness measurement in the coked zone . . . . .	172

## LIST OF FIGURES

---

# List of Tables

1.1	Evolution of emission regulations in Europe. <b>CO</b> : Carbon monoxide, <b>NO<sub>x</sub></b> : Nitrogen oxides, <b>PM</b> : Particulate Matter, <b>PN</b> : Particle Number. . . . .	2
1.2	Characteristics of the injectors used in this study. . . . .	8
1.3	Notable dimensionless numbers for the study of impacting droplets. $A$ , $a$ and $b$ are constant that differs between the model and experimental facilities which helped defining the splashing criterion. . . . .	17
1.4	Splashing ratio in number and mass computed from the PDA analysis performed on ASTRIDE injector. Adhered mass regroups sticking, spreading and half of splashing droplets. Whereas, away mass correspond to rebounding and half of splashing droplets. . . . .	18
2.1	Characteristic temperature for selected alkanes for gently deposited droplet as depicted in [24] at atmospheric pressure. . . . .	38
2.2	Oil pressure test results. $\Delta T$ is the difference of temperature recorded when switching the oil pressure from 2 to 4 <i>bar</i> . . . . .	45
2.3	Temperature loss on thermocouple 2 due to spray impingement on the piston, extracted from Figure 2.23. . . . .	46
3.1	Amplitude parameter of plate roughness used in the different experimental methods. The arithmetical mean deviation $R_a$ , the profile root mean square $R_q$ , the maximum peak height $R_p$ , the maximum valley depth $R_v$ and the maximum height of the profile $R_t$ are common description parameters used to characterise surface roughness. . . . .	63
3.2	Optical pen measurement characteristics. STIL S.A. . . . .	74

## LIST OF TABLES

---

3.3	Roughness parameters obtained with an AFM microscope on the sapphire plate . . . . .	75
4.1	Value of the parameter $C$ for different pressures of injection and injection durations. . . . .	94
4.2	Spreading differences between n-heptane and n-decane in the same experimental conditions. . . . .	96
4.3	Spreading differences between smooth and rough plate in the same experimental conditions. . . . .	99
4.4	Selected n-Decane properties at variable temperature. . . . .	100
4.5	Overview of the experimental campaigns performed on film spreading topics. . . . .	119
5.1	Effect of injection duration on wall cooling. . . . .	132
6.1	Properties of Surrogate $n^{\circ}1$ at $20^{\circ}C$ . . . . .	153
6.2	Properties of Surrogate $n^{\circ}2$ at $20^{\circ}C$ . . . . .	154
6.3	Properties of Surrogate $n^{\circ}3$ at $20^{\circ}C$ . . . . .	155
6.4	Summary of vaporisation rate for Alcanes [ $\mu m/s$ ] . . . . .	157

# Nomenclature

$\alpha$	Thermal diffusivity
$\ddot{R}$	Temporal derivative of $\dot{R}$
$\Delta P$	Pressure driving the liquid film
$\Delta T$	Temperature variation from the set-point
$\dot{m}$	Mass flow rate
$\dot{R}$	Temporal derivative of $R$
$\epsilon$	Ellipse eccentricity
$\eta$	Efficiency of the cycle
$\eta$	Liquid dynamic viscosity
$\eta_l$	Liquid dynamic viscosity
$\eta_w$	Wall correction for viscosity
$\gamma$	Heat capacity ratio
$\Gamma_{impact}$	Jet cross section at the impact
$\Gamma_{injecteur}$	Jet cross section at the injector exit
$\lambda$	Digitation wavelenght
$\lambda$	Thermal conductivity of the materia
$\nu$	Liquid kinematic viscosity

## NOMENCLATURE

---

$\Omega$	Liquid film volume
$\Omega_i$	Liquid film volume at the end of injection
$\rho_a$	The discharge gas density
$\rho_f$	Fluid density
$\tau$	Dimensionless time
$\theta$	Impingement angle
$\theta$	Temperature deficit of the surface
$\theta_a$	Advancing angle
$\theta_r$	Receding angle
$\varphi_0$	Intensity of the constant heat flux
$\xi$	Dimensionless distance
$^{\circ}\mathbf{CA}$	Degree crank angle
$A$	Area of the liquid film
$a$	Major semi axis of the ellipse
$A^*$	Dimensionless area
$A_i$	Liquid film area at the end of injection
$A_o$	Area of impact
$A_o$	Area of the hole
$B$	Background grey level
$b$	Minor semi axis of the ellipse
$C$	Relaxation parameter
$c$	Distance between focus and center of the ellipse



## NOMENCLATURE

---

$C_a$	Area coefficient
$C_D$	Discharge coefficient
$C_v$	Velocity coefficient
$d$	Droplet diameter
$D_o$	Outlet diameter of the nozzle
$e$	Thickness of the liquid film
$F$	Focus of the ellipse
$h$	Heat transfer coefficient
$I$	Raw image grey level
$K$	Splashing parameter
$K_\eta$	Coefficient of wall correction for viscosity
$K_m$	Coefficient of mass
$K_P$	Pressure transfer function
$M_{dep}$	Mass deposited on the wall
$M_{imp}$	Mass impacted
$M_{inj}$	Mass injected
$M_{secS}$	Mass participating to the secondary spray
$p$	Semi-latus rectum of the ellipse
$P_i$	Injection pressure
$Q$	Injection discharge of the injector
$q''_w$	Heat flux density
$R$	Radius of the liquid film

## NOMENCLATURE

---

$r$	Compression rate
$r$	Radial distance from the center of the liquid film
$R_a$	Arithmetical mean roughness
$R_e$	Reynolds Number
$R_i$	Liquid film radius at the end of injection
$R_o$	Radius of impingement area
$R_p$	Maximum peak height
$R_q$	Profile root mean square
$R_t$	Maximum height of the profile
$R_v$	Maximum valley height
$S$	Spray penetration
$T$	Temperature
$T_f$	Fuel temperature
$T_i$	Injection duration
$T_w$	Wall temperature
$T_{FU}$	Injector temperature
$T_{init}$	Wall temperature at the set-point
$T_{Lei}$	Leidenfrost temperature
$T_{Nuk}$	Nukiyama temperature
$T_{sat}$	Saturation temperature
$V$	Liquid film velocity
$v$	Dimensionless grey level

## NOMENCLATURE

---

$v_b$	Liquid film velocity towards the backward direction
$v_f$	Liquid film velocity towards the forward direction
$v_s$	Liquid film velocity towards the side direction
$W_e$	Webber Number
$z$	Injector to wall distance
<b>AFM</b>	Atomic Force Microscope
<b>AI50</b>	Integrated area with 50% of heat release
<b>APC</b>	AVL Particle Counter
<b>BMEP</b>	Break Mean Efficiency Pressure
<b>CFD</b>	Computational Fluid Dynamics
<b>CMOS</b>	Complementary Metal Oxide semi-Conductor
<b>CO</b>	Carbon Monoxide
<b>ECU</b>	Electronic Control Unit
<b>GDI</b>	Gasoline Direct Injection
<b>LIF</b>	Laser Induced Fluorescence
<b>NEDC</b>	New European Driving Cycle
<b>NO<sub>x</sub></b>	Nitrogen Oxides
<b>OEM</b>	Gasoline Direct Injection
<b>PAH</b>	Polycyclic Aromatics Hydrocarbons
<b>PID</b>	Proportional integral derivative
<b>PM</b>	Particulate Matter
<b>PN</b>	Particle Number

## **NOMENCLATURE**

---

<b>RIM</b>	Refractive Index Matching
<b>SAWLI</b>	Spectroscopic Analysis of White Light Interferogram
<b>SCR</b>	Selective Catalyst Reduction
<b>SOI</b>	Start Of Injection
<b>TDC</b>	Top Dead Center
<b>WLTP</b>	Worldwide harmonised Light vehicles Test Procedure

# 1

## Introduction

### 1.1 General Context

The year 1958 held the first World Forum for Harmonisation of Vehicle Regulations. The purpose was to define some rules that would apply in all the signatory countries for the road vehicles. It gave some regulations on a lot of subjects such as safety, durability, environmental protection, energy efficiency, etc... In 1970, a first driving cycle has been defined, it is supposedly representative of the use of personal cars in Europe in an urban cycle. In 1990, they extended the driving cycle to extra urban cycles and in 1993, the Euro 1 standard for emission was created. Nowadays, the Euro 6d-TEMP is in use. In the mean time, different standards were created all over the world in order to meet the requirements of customers behaviours.

Table 1.1 shows the evolution of regulations for medium passenger cars in Europe. It appears that Carbon monoxide (CO) and Nitrogen oxides (NO<sub>x</sub>) emissions regulations have been reduced by almost three in 22 years. Regulations on NO<sub>x</sub> were introduced in 2001 and in 2011, the regulations on particle emissions were started. These standards need to be fulfilled during homologation cycles, which aim at being relevant of the normal use of a passenger car. The cycle itself is at least as important as the emission regulation. In Europe, from 1973 to 2018, the New European Driving Cycle (NEDC) was used (updated in 1996). It has been replaced in 2017 and 2018 by the Worldwide harmonised Light vehicles Test Procedures (WLTP) which is supposed to be more representative of real driving experience.

## 1. INTRODUCTION

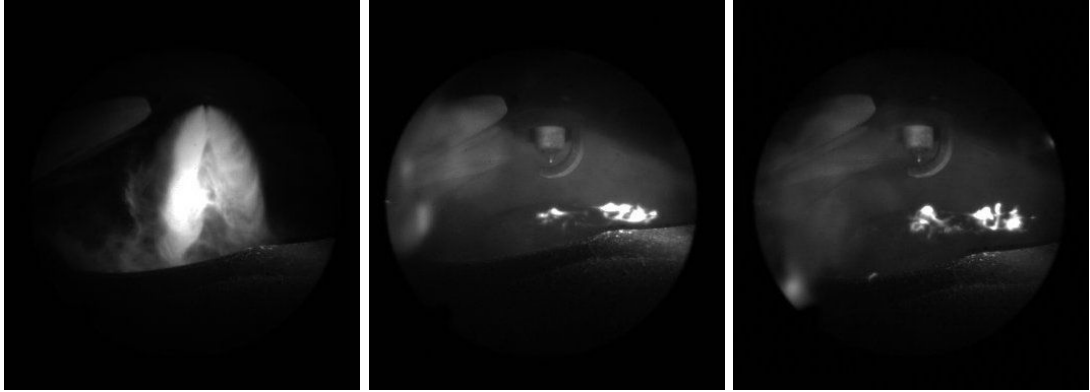
---

Name	Year	CO [ $g/km$ ]	NO <sub>x</sub> [ $g/km$ ]	PM [ $g/km$ ]	PN [ $\#/km$ ]
Euro 1	1993	2.72	-	-	-
Euro 2	1997	2.2	-	-	-
Euro 3	2001	2.3	0.15	-	-
Euro 4	2006	1	0.08	-	-
Euro 5	2011	1	0.06	0.005	$6.0 \cdot 10^{11}$
Euro 6	2015	1	0.06	0.0045	$6.0 \cdot 10^{11}$

**Table 1.1: Evolution of emission regulations in Europe. CO: Carbon monoxide, NO<sub>x</sub>: Nitrogen oxides, PM: Particulate Matter, PN: Particle Number.**

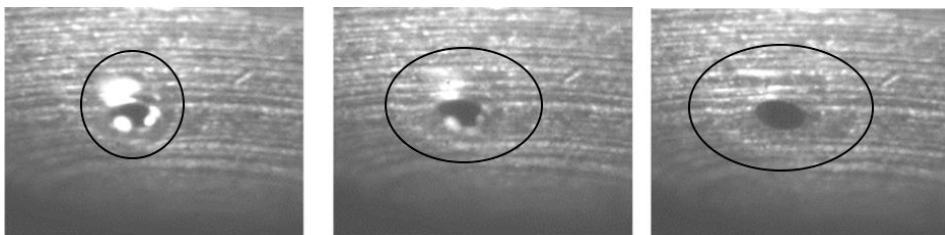
In the late 2000's and the early 2010's, together with these type approval legislations, the necessity to decrease the fleet average  $CO_2$  emissions lead the manufacturers to decrease the fuel consumption, and hence to reduce the engines size. The objective was to increase the power/volume ratio of the engine in order to maintain car power while reducing the consumption and emissions. To achieve these requirements, turbo-compressor and direct injection of gasoline were mainly used. Both elements help increasing the quantity of air admitted in the same volume, allowing to inject more fuel and hence increase the power produced during combustion. The turbocharger, by forcing more gases to enter in the combustion chamber, and the direct injection by cooling the admitted air thanks to fuel droplet vaporisation (the density of cold gases is higher than hot gases) .

However, the use of direct injection for gasoline engines also raised a new issue. Though gasoline engines were already producing particles, the use of direct injection increased significantly the particle level either PM or PN (mainly because of the apparition of liquid films and a worse mixture than in port-fuel injection engines, hence combustion inhomogeneities [42], Figure 1.2). Liquid films, in this context, are thin liquid deposit created by the injection process. It can either be because of the impact of fuel spray on the walls of the combustion chamber, or liquid deposited on the tip of the injector while the injector's needle is closing. Since these liquid film, were quickly identified as a source of pollutants, a great care has been taken to improve the injection process. Several axes of amelioration can be tackled. In [47], the discussion is addressed.



**Figure 1.1:** Endoscopic visualisation of direct injection and combustion inhomogeneities (probably soot luminescence or pool fires) [44].

Increasing the injection pressure allows to reduce the emission of particle number (PN). In [81], the reduction of particles is explained by a better air entrainment and a greater atomisation due to higher injection pressure. Therefore, it both implies a faster vaporisation and a better air/fuel mixing. It also allows to reduce tip wetting as mentioned in [16, 73]. Minimising tip wetting with the injector design is another way of improving the injection process, during the injection and specially at the end of injection. The purge of the injector promotes the apparition of liquid film on the injector tip [28]. It has been proven [70] that modifying the geometry of injector tip and/or holes can reduce significantly the tip wetting and consequently the particle generation due to this source.



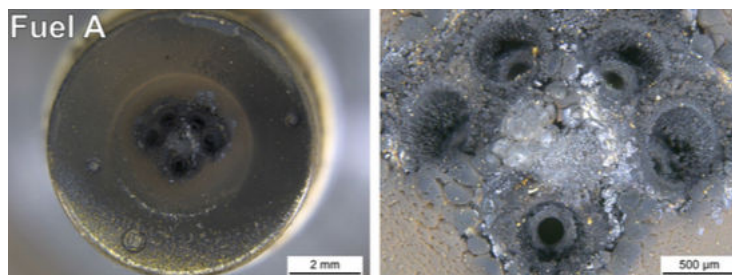
**Figure 1.2:** Visualisation of the tip wetting, during the injector purge (i.e. after the needle closure) [28]. Black lines highlight the area of liquid deposition.

Tip wetting is also responsible for injector fouling (carbon deposit on the injector surface Figure 1.3 presented in [30]). The carbon deposit is responsible of higher spray penetration (by slightly changing the geometry of the holes), increasing the wall im-

## 1. INTRODUCTION

---

pingement likelihood. It is also creating a porous media on the tip, where fuel gets entrapped and must lead to diffusion flame attached on the injector, the fouling of the injector can multiply the PN emissions by 100 [30].



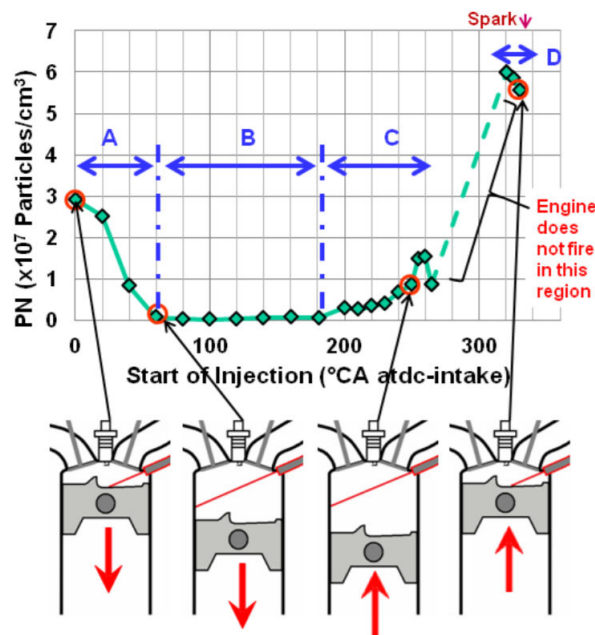
**Figure 1.3: Injector fouling due to tip wetting, carbon deposit slightly changes the hole geometry [30].**

Finally, the injector coking can be cleaned using fuels with additives [57]. This leads to the last point addressed in [47] which is the fuel itself. Indeed the combustion of Polycyclic Aromatics Hydrocarbons (PAH) is responsible of soot formation [20, 23]. Hence, the fuel composition can be responsible for a higher or hopefully a lower particle generation. In [17] they tested the influence of the addition of butanol to gasoline on the engine emissions and specific consumption.

An aspect not addressed in [47] is the injection timing. Indeed the injection timing is crucial in direct injection engines. Most of particles are created during the combustion process: the air/fuel mixture is especially primordial. Particles are generated if inhomogeneities in the mixture are experienced: the rich zones (fuel/air ratio  $> 1$  [74]) are of great concern [68] and they essentially occur next to liquid films, or if the turbulent flow does not have the time to correctly mix the gases. In [40], the timing of injection is studied in a 4 cylinder direct injection engine. Figure 1.4 shows how the particles number varies with the Start Of Injection (SOI). When the injection is too early (zone A), the spray impacts on the piston, creating a liquid film on the piston and, sometimes the cylinder head (due to splashing). The fuel vaporisation is too slow, and homogeneous mixture is not reached, leading to particle generation. When the start of injection is later (zone B), the fuel has a clear path, exchanges with the fresh gases are maximum, hence a good mixture is achieved and particle generation is really small. In zone C the conditions are relatively similar to zone B, however the time available for vaporisation is shorter, and the turbulence has decayed. A poorer mixture is achieved



and particle level starts to raise. Between zones C and D where the engine cannot lit, the mixture which is too inhomogeneous for the ignition to generate a viable flame. Finally, in zone D, thanks to the piston geometry, a combustible mixture is present next to the spark plug and a stratified combustion occurs. Though ignition is performed, the combustion quality is poor and a lot of particles are produced.



**Figure 1.4: Particle Number (PN) as a function of SOI and injection geometry [40].**

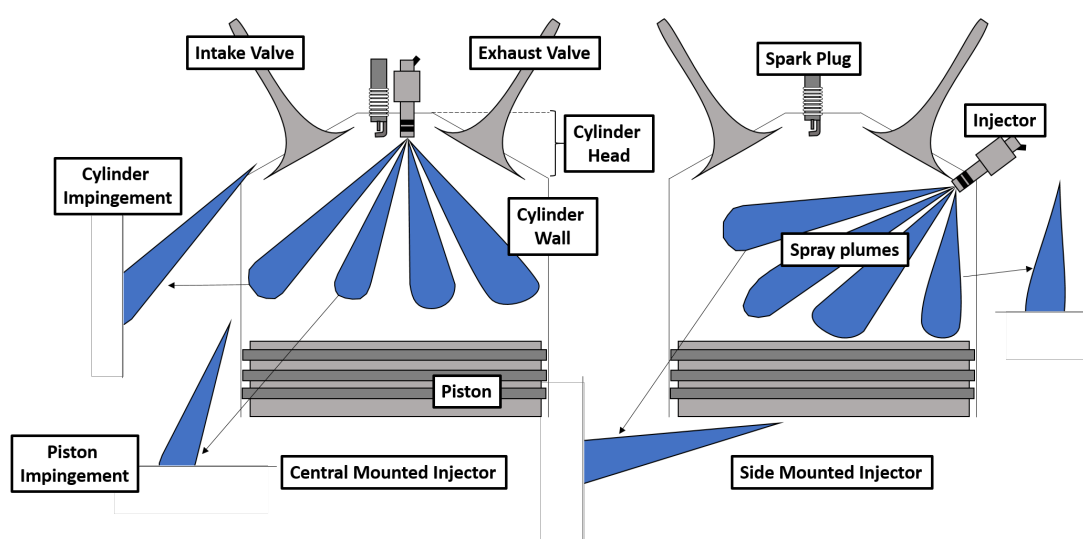
It now appears clearly that, in direct injection engines, taking care of the injection process is fundamental for the reduction of emissions. Hence, a closer look to the injection and the impingement process is necessary. Downsized engines which are (as mentioned before) very popular for gasoline cars, have a typical volume of 1 to 1.2 litres with 2, 3 or 4 cylinders. A one litre engine with three cylinders, gives three combustion chambers with a swept volume of 0.33 litre (which is quite small, as big as a soda can). Typical dimensions for the bore (cylinder diameter) is around 70 *mm* and the stroke (height travelled by the piston during one stroke) is around 80 *mm*. Injection is performed in this small volume by high-pressure injectors at pressures up to 350 *bar* or even more (500 *bar* applications are coming). Droplet ejection velocity is  $\simeq 100 - 300 \text{ m.s}^{-1}$ , spray penetration curves will later be presented. However, it is already possible

## 1. INTRODUCTION

---

to affirm that spray-wall impingement will occur at some point in the engine map.

Many different impingement configurations might be encountered, they depend mainly of the injector position and of the combustion chamber geometry. Figure 1.5 shows the two common configurations for the position of the injector (central and side), it also highlights the variability of impingement angles (between the spray plumes and the wall impacted wall). Last but not least, the impingement of sprays on walls is not



**Figure 1.5: Common position for the injector. Left: Central Mounted. Right: Side Mounted. Highlights the variability of impingement angle encountered in a Direct Injection (DI) engine.**

only encountered in direct injection engines. It is important to keep this in mind, as the worldwide trend is to reduce the development of high power fuel engines and replace it with electrical or hybrid engines. Though, fuel impingement also happens in port fuel engines (fuel is injected in the intake pipes and mixed air/fuel is admitted in the combustion chamber). In Selective Catalyst Reduction (SCR), urea is injected with modified port-fuel injectors in the catalyst system in order to reduce NO<sub>x</sub> emissions at the exhaust. SCR systems are also facing liquid films issues, which sometimes lead to solid by-product deposits and strongly deteriorate the system. Finally, non automotive applications can be found, specially for cooling systems as the heat removal of sprays is really important. The heat transfer of sprays will be addressed in Chapters 5 and 6.

### 1.2 About injection process and engine working

In the context of emission reduction, which is a worldwide concern, the injection process and specially the liquid film formation have been identified as major concerns. The objective of this PhD book is to improve the knowledge about fuel film generation, spreading and vaporisation. To do so, a closer look at the injection process is done.

To perform a correct injection, three main components are necessary: an injector, a fuel pump and an Electronic Control Unit (ECU). These three components are built by automotive suppliers. Continental is producing the three components in order to provide to car manufacturers an injection solution (Figure 1.6).



**Figure 1.6: High pressure injector, ECU and high pressure pump produced by Continental. (Courtesy of Continental website [www.continental-automotive.com](http://www.continental-automotive.com))**

The principal requirement (before looking at the emissions), is to inject the correct quantity of fuel to produce the power required by the driver at the required time. The ECU is in charge of triggering and powering the injector, it is previously calibrated to make sure the fuel request is in accordance with the power required by the car. Another requirement for Continental is to produce injectors with high reliability, as the injection process is performed thousands of times each minute. Finally, the targeting (spatial position of injectors plumes) of the injection needs to be elaborated, to satisfy the specificity of the engine in which the injector is placed.

The injector used in the following study has the following characteristics (Table 1.2). It is an experimental three-holes injector, developed on the body of the classical five or six-hole injectors of its generation (commercialised by Continental). It has been developed for the ANR-ASTRIDE [1]. The reason to use a three-hole injector is because it is much simpler to study. Indeed, while looking at a single plume the two others are

## 1. INTRODUCTION

---

not likely to disturb the visualisation. A five-hole injector described in Table 1.2 is the one used in the engines measurements presented in Chapter 2. It is only used in this chapter, for all the other measurements the ASTRIDE injector is used.

<b>Injector</b>	<b>Holes</b>	<b>Mass Flow Rate</b> [g/s] @100 bar	<b>Sauter Mean</b> <b>Diameter</b> [ $\mu m$ ] @100 bar	<b>Hole Diameter</b> [mm]
ASTRIDE	3	6.5	15.1 @ 75 mm	0.2
Serial	5	7.35	9.7 @ 50 mm	0.18

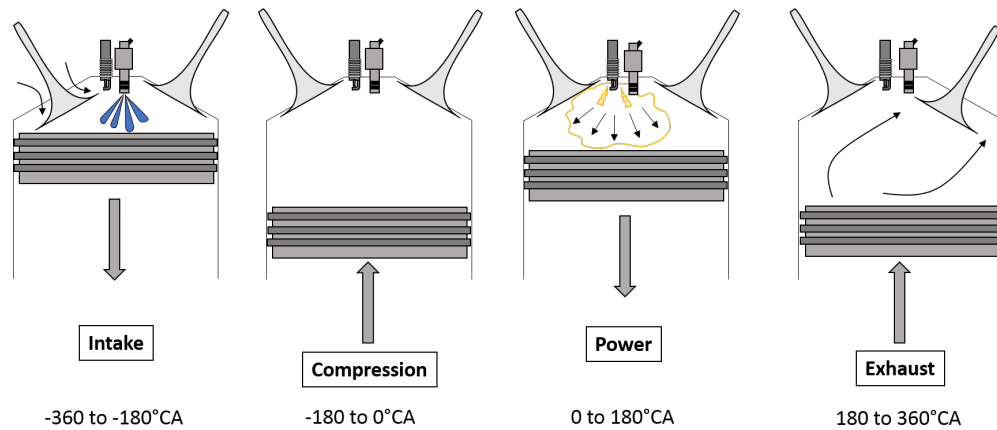
**Table 1.2: Characteristics of the injectors used in this study.**

As mentioned before, the injection of the correct quantity of fuel amount is necessary in order to perform a good stoichiometric combustion. However, it is also necessary to have a homogeneous mixture between air and vaporised fuel. It is therefore mandatory to give enough time to the fuel to vaporise. Consequently, a temporal window for injection can be defined to indicate when injection should happen and when it should not. The working principle of a gasoline engine is to chain combustion cycles in order to rotate a crankshaft which transmits power to the wheels (very simplified vision). During each combustion cycle, fuel is burned and pushes a piston, the combustion cycle is composed of four strokes depicted Figure 1.7 (the four strokes give its name to the four stroke engine, broadly used in automotive engines). To complete the four strokes, two complete rotations of the crankshaft are necessary, an engine running at 2000 rpm will then complete 1000 combustion cycles by minute and by cylinder. The four strokes are [31]:

- The Intake: during this phase, the intake valves are opened and the piston is going downward. It creates an aspiration of the fresh gases, introducing the necessary amount of oxygen in the combustion chamber. Generally the injection of fuel starts during the intake.
- The Compression: during compression, the intake valves are closed and the piston is going upward. The pressure of the chamber increases, and the fuel is vaporising and mixed thanks to the air motion generated by the combustion chamber geometry.

## 1.2 About injection process and engine working

- The Power: at the very end of the compression, the spark plug fires so the combustion of the air/fuel mixture starts at the beginning of the power stroke. The expansion of gases during the combustion generates a force that pushes the piston downward, and will give power to the wheels.
- The Exhaust: here, the piston is going upwards, and the exhaust valves are open. It sweeps most of the burned gases out of the combustion chamber. A new combustion cycle can start.



**Figure 1.7: Schematisation of the four strokes of a gasoline engine. Intake, Compression, Power and Exhaust. The spark usually takes place at the very end of compression however for sake of clarity it is represented during the power stroke. Every stroke takes  $180^\circ\text{CA}$  (Crank angle).**

Though the combustion takes place during the third stroke, it is the two first strokes that are primordial to achieve a good and clean combustion. As the injection, fuel vaporisation and air fuel mixing needs to be performed during these two strokes. In order to fix the figures for the reader, let us take an engine running at  $2000\text{ rpm}$  (typical engine speed for a gasoline engine). The intake and compression takes one rotation of the engine, that is to say  $30\text{ ms}$ . A typical injection duration is  $1\text{ to }8\text{ ms}$  depending on the load of the engine, the injector mass flow rate, and the injection pressure. As the impingement of the piston should be avoided, the injection generally starts after  $50 - 70^\circ$  of crank rotation, which is  $5\text{ ms}$ , hence it only leaves  $25\text{ ms}$  to complete injection, vaporisation and mixture. That is to say  $20\text{ ms}$  for vaporisation and mixture, this is most of the time enough and particle generation are kept low.

## 1. INTRODUCTION

---

However, and this is why the study of injection process and liquid film is important, in some cases, the time available is not long enough. At the engine start, after decelerating or while strongly accelerating (power is no longer needed so the engine cools down), the engine is relatively cold and vaporisation is deteriorated. Also, between two operating points, the inputs of the engine are changing really fast (injection duration, engine speed etc...) however it takes some time for the boundary conditions (piston and cylinder temperature) to follow the set point. Hence, it creates transient points which are likely to generate particles.

The injection problem is a very complex task, and calibration of injectors on engine map is a huge amount of work. For every engine, several people are working full time to develop injection strategies. The strategies should optimise the injection in terms of fuel consumption while minimising pollutant generation (in some extreme cases, it should make sure the cylinder will just fire correctly). Now that the injection process has been addressed as a frame for the study, a zoom at the injector scale and specially on the impingement process is proposed.

### 1.3 Dynamic of droplets and spray impingement

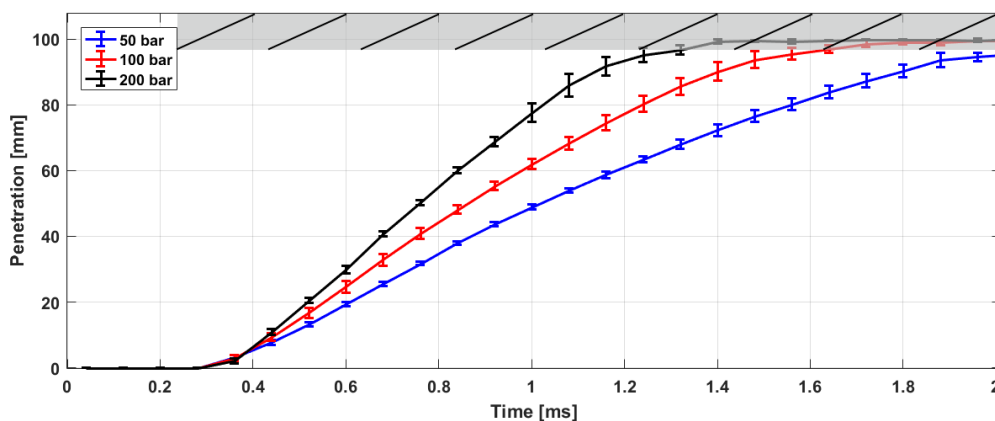
#### 1.3.1 Injector and spray description

Table 1.2 shows an insight of the injector characteristics. However, a full description of the spray produced by the injector is presented here as it is the cornerstone of all the studies presented later. As mentioned before, the injector is a three-hole solenoid injector, it has been specially developed for experimental studies. Performing direct visualisation of sprays or liquid films with 5 or 6 plumes is quite complicated. Two concrete examples are: i) when a plume is disturbing the background for shadowgraphy visualisation, ii) when the liquid films generated by two plumes are overlapping. Hence, having only three plumes was better for experimental research.

Figure 1.8 shows the penetration curves of the injector at 50, 100 and 200 *bar*. The observation window is limited to penetration smaller than 90 *mm*. It explains why the curve for 200 *bar* is completely flattened 1 *ms* after the start of injection. The penetration curves were made using backlit illumination (or shadowgraphy), the method is presented in Section 3.2. A delay is also visible at the beginning of the curves. The delay corresponds to the time between and the release of pressurised flow

### 1.3 Dynamic of droplets and spray impingement

in the air. During this period the ECU generates the signal for the injector opening and the opening of the needle are performed.



**Figure 1.8: Spray penetration for 50, 100 and 200 bar for ASTRIDE injector, based on shadowgraphy pictures in atmospheric conditions. Errorbar displaying the standard deviation of measurements based on 5 independent repeats.**

The penetration curve of high pressure injectors have been broadly studied, for diesel and gasoline applications. In [65], Naber and Siebers studied the spray penetration and derived a model. They show that spray penetration can be split in two parts: at the beginning the penetration is linear in time. Later on the penetration is proportional to  $\sqrt{t}$ . The reasons for this change of spray behaviour have been stressed and modelled in many research papers. Among them, is the evolution of droplet velocity with respect to the surrounding gas, which is then put in motion through momentum transfer (from the liquid to the gas). At the beginning, the penetration is linear and the droplets are much, still undergoing atomisation, faster than the gas. Afterwards, droplets and gas are moving at the same velocity and the penetration becomes proportional to  $\sqrt{t}$ . Some mathematical models for high pressure spray penetration are proposed in [72, 83]. The model presented by Payri in [72] defines the penetration of the spray  $S$  when  $t < t_r$  as:

$$S(t) = C_v \sqrt{\frac{2\Delta P}{\rho_f}} t, \quad (1.1)$$

## 1. INTRODUCTION

---

and when  $t \geq t_r$ :

$$S(t) = \frac{C_v^{0.5} (2 C_a)^{0.25}}{(a \tan\theta/2)^{0.5}} \rho_a^{-0.25} \Delta P^{0.25} D_o^{0.5} t^{0.5}, \quad (1.2)$$

where

$$t_r = \frac{(2C_a)^{0.5}}{C_v} \frac{\rho_f D_o}{a \tan\theta/2 (\rho_a \Delta P)^{0.5}}, \quad (1.3)$$

where  $\Delta P$  is the pressure difference between the fuel and the surrounding gas,  $C_v$  is the velocity coefficient,  $C_a$  the area coefficient,  $\rho_f$  the fluid density,  $\rho_a$  the discharge gas density,  $D_o$  the outlet diameter and  $\theta$  the spray angle. It is important to note from these formulas that in the linear area the penetration is not influenced by the outlet diameter nor the gas density. Whereas in the  $\sqrt{t}$  zone the penetration is affected by the gas density and the nozzle outlet diameter. Finally, in both regions, the penetration is influenced by the injection pressure, though the influence is greater in the linear zone than in the fully developed zone.

Finally, some penetration curves can be found in literature to highlight these two different compartments. Figure 1.9 shows the penetration curves presented in [77] and [72], the two temporal behaviour presented earlier are clearly identifiable.

The penetration curve of the injector used to produce all the results presented below (excepted for the engine measurements) has a relatively long linear behaviour, it favours the wall impingement (which is the worst case scenario for engine applications). Which is good in our case as the spray-wall impingement is at the core of the whole study.

In [53], the influence of pressure on the discharge coefficient  $C_D = \frac{\dot{m}}{A_o \sqrt{2\rho_f \Delta P}}$  [71] is tested (Figure 1.10).  $\dot{m}$  is the injector mass flow rate and  $A_o$  the hole area. It can be seen that for the pressure range we are interested in (20 to 200 bar), the variation of  $C_D$  is around 5% which is relatively small. Though the injectors are not the same, their compartment is really close and the experimental facilities are the same. Consequently, it will be considered that the variation in  $C_D$  for our injector is not a dominant parameter to consider.

In 2015, Giacomo Piccini Leopardi performed two-components PDA measurements of the injector at Loughborough University. Selected results are presented here to give some more knowledge about the spray distribution. The data produced are injectorwise (and not spraywise, Figure 1.11), it means that the two components velocity



### 1.3 Dynamic of droplets and spray impingement

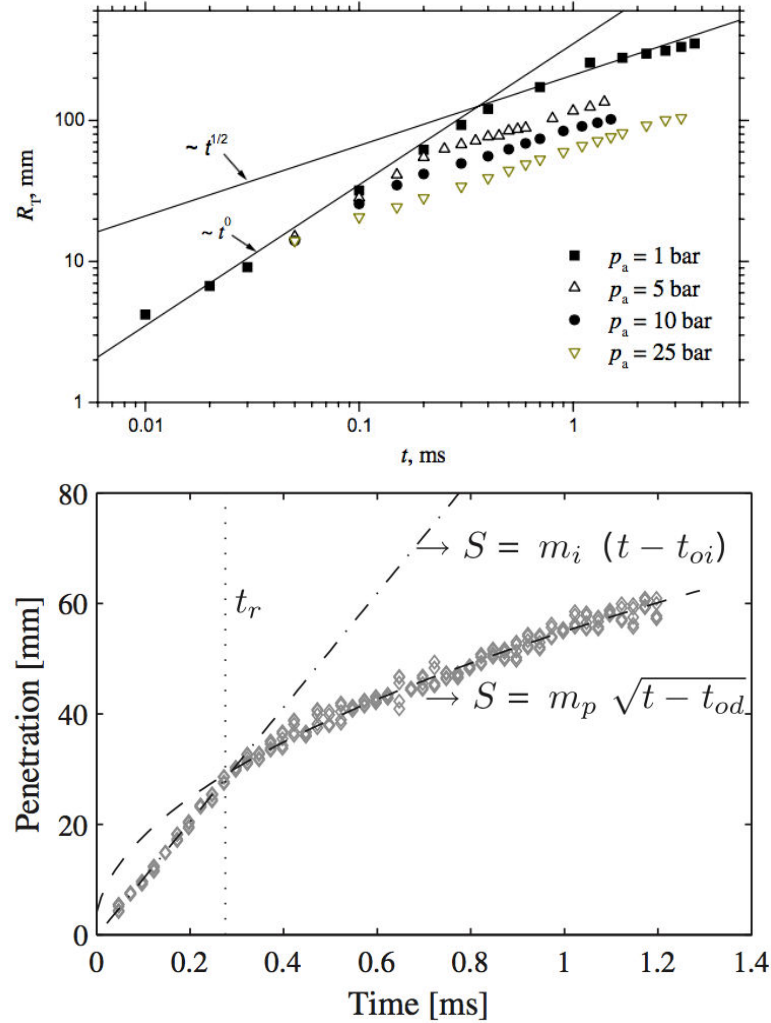


Figure 1.9: Top: Spray penetration, as a function of time at various ambient pressures (injection pressure 1350 bar) [77]. Bottom: Penetration curve and calculation of the penetration parameter [72].

are in the injector axis and orthogonally to this direction. Figure 1.12 shows a picture of the spray during the measurement and the velocity distribution on a point at 40 mm and 100 bar. These results are performed during the steady state of the injection, that is to say without the injection head or tail.

Figure 1.13 shows the calculated Reynolds and Weber (as defined in Table 1.3) number for a measurement point in the spray. Both histograms follow a Weibull distribution

## 1. INTRODUCTION

---

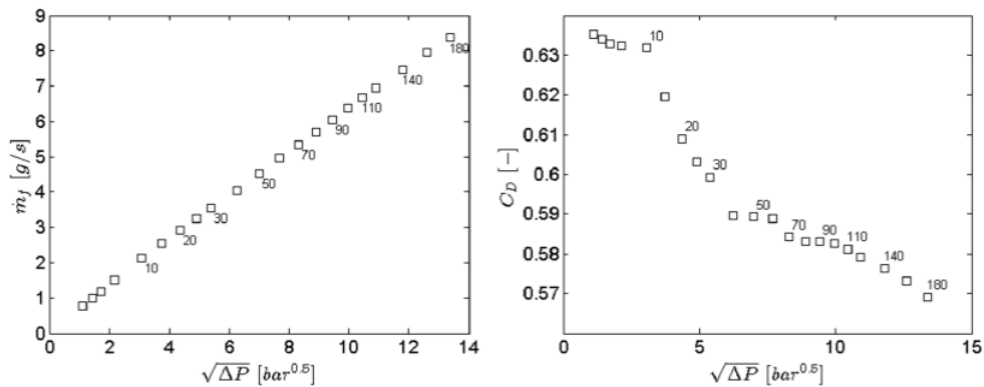


Figure 1.10: Evolution of mass flow rate and discharge coefficient for different injection pressure [53].

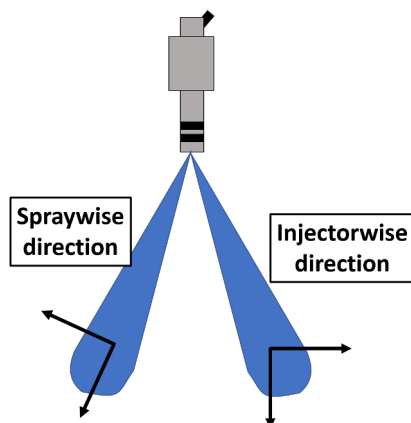


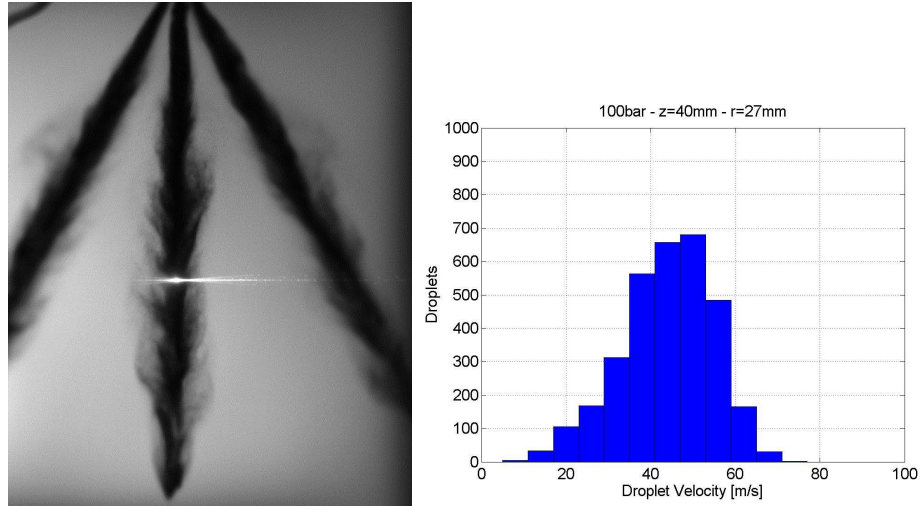
Figure 1.11: Description of injectorwise and spraywise directions.

(often referred as Rosin-Rammler in granulometrie).

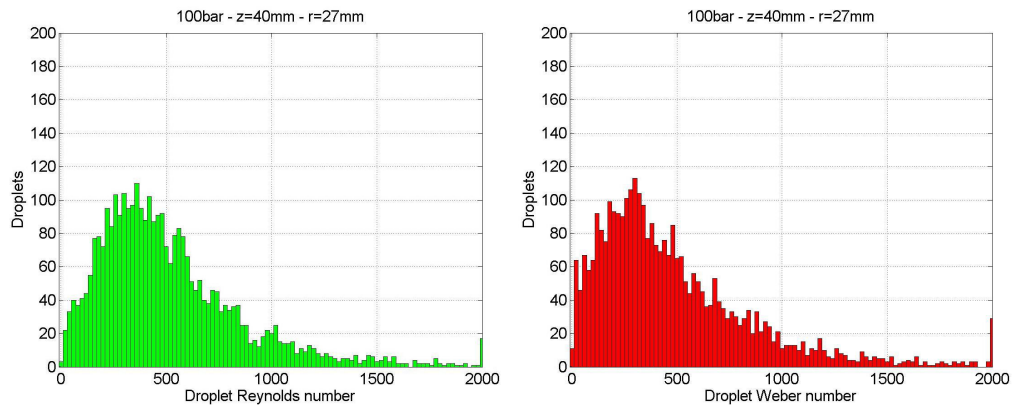
### 1.3.2 Impact regime description

Now that the injector and the spray composition have been presented, a presentation of the droplets outcomes is given. The objective here is not to make a complete review of droplets impacting regimes (as the subject is widely studied, and reviews already exists) but to give the necessary information to the reader for the understanding of spray impingement. Indeed, the literature is quite exhaustive about single droplet impact dynamics in ambient conditions [59]. However, spray-wall impact literature is

### 1.3 Dynamic of droplets and spray impingement



**Figure 1.12:** PDA measurement of the spray, and velocity distribution at 100 bar and 40mm.



**Figure 1.13:** Reynolds and Weber distribution at 100 bar, 40 mm away from the injector (See Table 1.3 for definition).

less detailed, because of the spray, the gas flow, the liquid film and the very numerous re-atomised droplets in the impingement zone which makes the study more complex [32, 37, 38].

The impact regimes for a droplet on a cold (relative to the saturation temperature of the liquid studied), flat, rigid and dry surface are generally separated in four different post-impingement scenarii (Figure 1.14). The details of a drop-wall impingement are very complex, especially when the impact energy of the droplet is high. Though, the

## 1. INTRODUCTION

---

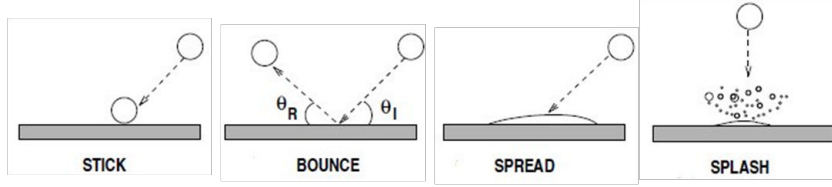


Figure 1.14: Post impingement scenario of single drop impact on cold, rigid and dry wall [5].

four scenarios (stick, rebound, spread and splash) introduced in [5] are most of the time valid:

- **Stick:** When the droplet is really slow, it may just stick to the surface and stop moving (thanks to contact forces).
- **Rebound:** As the impact energy increases, the air layer between the drop and the wall leads to a small energy loss and the drop rebounds.
- **Spread:** When the impact energy gets higher, the droplet is strongly deformed and can spread on the surface. The phenomenon is complex and a precise description can be found in [3, 78]. As a competition between inertia and surface tension starts (dissipation via friction), a new equilibrium can be reached, depending on the surface wettability. At rest, a static contact angle can be defined between the liquid, the wall and the surrounding gas.
- **Splash:** If the impact energy gets even higher, the drop will disintegrate [3, 59, 63, 97, 101] as the inertial forces will overcome capillary effects. The splashing itself can take several forms such as prompt splash, corona splash, receding break-up, partial rebound, finger break-up [3]. A constant consequence of splashing is an atomisation process, the impacting droplets split up. Depending on the scenario, some liquid (smaller drops) can stick or not on the surface.

The variety of droplets size, speed, composition (liquids) is really wide. Hence, dimensionless numbers are commonly used to describe drop-wall interactions. Considering a droplet of diameter  $D$ , normal (to the wall) velocity  $U$ , specific mass  $\rho$ , viscosity  $\mu$  and surface tension  $\sigma$  several dimensionless numbers can be defined. Here the focus is put on only three numbers, which are the Reynolds number  $Re$ , the Weber number

### 1.3 Dynamic of droplets and spray impingement

---

$We$  and the Splashing Criterion  $K$  defined in Table 1.3. The splashing criterion has been first introduced by Stow in 1981 [95], and then confirmed by Mundo in 1995 [63].

Dimensionless number	Description	Definition
Weber number	Inertia / Surface tension	$We = \frac{\rho U^2 D}{\sigma}$
Reynolds number	Inertia / Viscous forces	$Re = \frac{\rho U D}{\mu}$
Splashing parameter	Defines a threshold for splashing regime	$K = AWe^a Re^b$

**Table 1.3:** Notable dimensionless numbers for the study of impacting droplets.  $A$ ,  $a$  and  $b$  are constant that differs between the model and experimental facilities which helped defining the splashing criterion.

For a given droplet with a defined Reynolds and Weber numbers, the impact scenario can be evaluated. In [93, 94] Stanton and Rutland introduced two criterion for the stick/rebound limit and the rebound/spread limit. As these regime only concerns small and slow droplets, the Weber number value is sufficient to describe the impact outcome. For a Weber number  $We \leq 5$  the droplet will stick to the wall and for a Weber  $5 < We \leq 10$  the droplet will rebound. The values presented here vary in literature depending on the experimental set-up, mainly because of surface tension, though, they give a good insight of the frontier (in term of Weber value) between stick and rebound. Finally the frontier between spreading and splashing is defined for droplets with a Weber  $We > 10$ . If the Splashing parameter is below the splashing criterion the droplet will spread, if it is higher the droplet will splash. Studies give different values for the parameters  $A$ ,  $a$  and  $b$  in the splashing parameter (defined in Table 1.3). As an example the values  $A = 1$ ,  $a = 0.5$ ,  $b = 0.25$  and  $K_c = 57.7$  were identified by Mundo in [63] as reported in [25] and will be used in what follows. A summary of the different values for the parameters can be found in [59]. The problem described here, is for supposedly isolated droplets, impacting on dry walls. However

## 1. INTRODUCTION

---

in the case of a spray impacting on a wall, some droplets are facing a dry wall and others a wetted wall. A splashing criterion for wetted surface are also available in [59], but is only valid for single droplets impacting on liquid films (sprays are even more complicated).

Table 1.4 presents, for different positions and pressures, the splashing ratio calculated using the droplet distribution, pretending droplets are isolated. It gives (with the previously defined criterion), between 40% and 80% of droplets (in number) in the splashing regime. These droplets are representing more than 80% in mass, of the spray droplets. Finally, taking as an hypothesis that, for a droplet in the splashing regime, 50% of the mass sticks to the wall and 50% is ejected away from the wall, it then gives that, more or less 50% of the mass impacting on the wall is deposited. This hypothesis is easily arguable, but it is inspired by the model adopted by Bai et al. [5]. Splashing to incident droplet mass ratio  $r_m = m_{splash}/m_{imp}$  "is taken to have a random value evenly distributed in the experimentally-observed range [0.2;0.8] for a dry wall". To have a rough idea of the mass deposited, fixing this ratio to 0.5 seems a fair hypothesis. The calculations presented here use strong hypothesis, as the objective is not to develop again a model of adhered mass using the droplets distributions. But to give to the reader a rough idea of what is happening when the spray is impacting on a plate.

In the definition of the Reynolds and Weber numbers, the velocity normal to the wall has been used. However, here the measurement has been performed in the direction of the injector as presented before. Hence, the deposition rate calculated correspond to piston impingement in a central mounted configuration (Figure 1.5).

	Number ratio		Mass ratio		Mass	
	Non-splash	Splash	Non-splash	Splash	Away	Adhered
40 mm 100 bar	22.2%	77.8%	2.4%	97.6%	48.8%	51.2%
60 mm 100 bar	39.8%	60.2%	6.5%	93.4%	46.8%	53.2%
40 mm 200 bar	48.0%	52.0%	14.8%	85.2%	42.7%	57.3%
60 mm 200 bar	56.9%	43.11%	17.4%	82.6%	41.8%	58.1%

**Table 1.4: Splashing ratio in number and mass computed from the PDA analysis performed on ASTRIDE injector. Adhered mass regroups sticking, spreading and half of splashing droplets. Whereas, away mass correspond to rebounding and half of splashing droplets.**

### 1.3 Dynamic of droplets and spray impingement

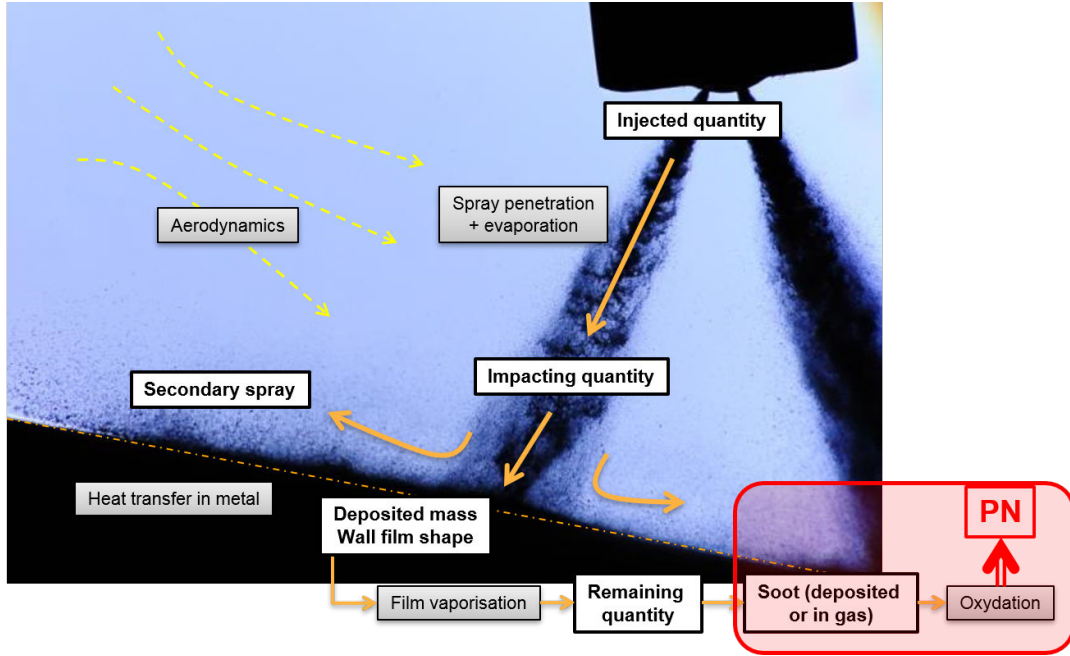
---

This kind of approach gives a good insight of what could happen when a high pressure sprays impacts on a flat wall. Figure 1.15 shows a shadowgraph of a spray impacting on the wall and describes all the events that could happen during this process. As mentioned earlier the first objective is to inject the correct quantity of fuel  $M_{inj}$  (to match the oxygen present in the cylinder). The pressure of injection together with the small size of the engines makes the impingement nearly impossible to avoid. Hence a quantity of fuel  $M_{imp}$  impacts on the wall. Due to air motion and heat transfer  $M_{imp} \leq M_{inj}$  as some drops will not reach the wall and other will vaporise. During the impact, as most of the droplets are in splashing regime, a certain fuel mass  $M_{dep}$  will stick to the wall depending on the wall temperature. While the rest will be reatomised and either deposited on another wall or vaporised, these droplets compose the secondary spray of mass  $M_{secS}$  (it is hard to make the difference between droplets blown away, by the air motion, over the liquid film without reaching the wall, and the reatomised drops).

The mass  $M_{dep}$  due to the incoming mass flux, and momentum provided by the spray will spread over the wall. This deposited mass, is at the core of this PhD thesis and a thorough look at the spreading of the injected liquid will be proposed in Chapter 4. In the mean time, while the mass is depositing, a heat transfer between the spray and the wall establishes, it is important to characterise this heat transfer. The heat flux and the wall temperature are the boundary conditions for the evaporation/vaporisation process of the liquid film (either in the engine or in computational simulations). The heat transfer will be studied in Chapter 5 while the vaporisation of mono and multi-component fuels will be addressed in Chapter 6. Figure 1.15 also highlights the fact that the fuel quantity not vaporised prior to combustion (or lately vaporised, hence badly mixed) will participate to the soot formation. These particles are at the starting point of many studies on injection process, and it is also the case for the present study. The objective is to try to give answers and guidelines in the comprehension of particle generation prior to combustion. For the combustion and post combustion process, another PhD thesis is specially studying the soot generation. It has been started between the PRISME and Continental with Anthony Roque in 2017 [79] and is entitled: "Experimental study of spray-wall-flame interaction on the formation of soot and solid

## 1. INTRODUCTION

---



**Figure 1.15:** Schematic visualisation of spray-wall impingement and the interrogations raised by this phenomenon. Ombroscopy visualisation performed with a high pressure injector, injection pressure is  $100 \text{ bar}$ , injector to wall distance  $13.5 \text{ mm}$  at ambient temperature, light source is a nanolite with an exposure time of  $25 \text{ ns}$ . Courtesy of Continental.

deposit. Application to gasoline direct injection (GDI) engines”. Finally a last PhD thesis with Continental Bangalore entitled: ”Hydrothermal phenomenon in GDI injector nozzle associated with carbon deposit formation” and working specifically on the development of numerical model for the vaporisation of thin liquid films has also been started by Sandeep Mouvanal [61]. The work presented here is, among other things, trying to give some entry data for these two PhD thesis.

This manuscript is decomposed as follows: engine measurements will first be presented in Chapter 2 as a deeper introduction to the spray-wall impingement problem in automotive applications and will also provide precious information about the piston and head surface temperatures. To answer the questions raised during this part, experimental devices will be presented in Chapter 3, as the data studied in the rest of the thesis are produced using these set-ups. In the next chapter, the growth of the liquid film will be tackled: a description of the spreading process, together with the derivation



### **1.3 Dynamic of droplets and spray impingement**

---

of an original model are presented. A discussion on the liquid film thickness and mass deposition is also addressed in Chapter 4. After this, the question of the heat transfer during the spray-wall impact will be detailed in Chapter 5, thanks to the measures performed with a plate instrumented with fast thermocouples. Finally, the vaporisation of the liquid film will be studied in Chapter 6 for mono- and multi-component fuels, before dressing the work conclusions.

## 1. INTRODUCTION

---

## 2

# Engine Measurements

## 2.1 Context

In a real car engine, the operating conditions sweep a really wide range, depending on the location of the car, the season, the fuel used, the user himself and the list goes on. Engine calibration is, by the way, a key task in the automotive industry and many tests and optimisations must be carried before a car can be driven. For instance test are performed in northern Europe in very cold conditions to verify that the car will lit correctly. Indeed the fuel used may have difficulties to vaporise and a good mixture prior to ignition is necessary to run the engine. Also test in deserts are performed in order to avoid problems relative to fuel vaporisation in the injection pipes. Finally test in altitude are also performed in order to see how the engine responds to low atmospheric pressure and lack of oxygen.

The goal of all these tests, is to ensure the good operating of the engine in strongly different conditions. Some of these tests are also realised in artificially heated or cooled chassis dynamometer. Instrumentation of the whole powertrain elements help to diagnose the problems encountered during those tests. The temperature of the engine is a precious data for Original Equipment Manufacturer (OEM). Several techniques are used to measure or predict the engine temperature for all the operating points. The coolant temperature gives a good insight of the engine temperature. However, the use finite element softwares, helps to get local predictions of the temperature in the engine (such as valve temperature, cylinder head temperature or piston temperature).

Since Computational Fluid Dynamics (CFD) is used for engine development, OEM

## 2. ENGINE MEASUREMENTS

---

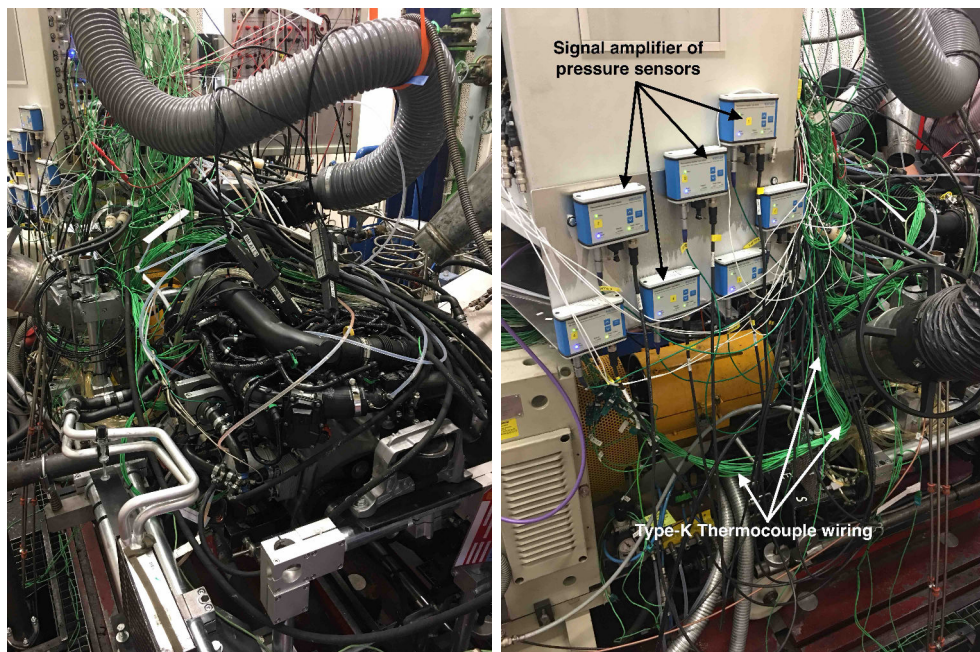
have made great progress in engine optimisation. For instance in [66] the simulation is not used for development phase, but to reduce the time necessary for the calibration of the engine. Thanks to the tools usually used for the dimensioning of the engine at full load, they developed a 1D solution to calibrate the air path. However, in order to continue to ameliorate the simulation quality experimental data are essential. They allow validate the simulation results and the developed models. Experimental data can either be produced in controlled atmosphere or directly by measuring inside the engine.

During this PhD experimental data were mainly produced in a test bench facility presented in Chapter 3. Several experimental devices allow to study the interaction between the spray generated by the injector and a wall. These experimental set-ups are designed to study separately several aspects of the liquid film. The quality and the relevance of the results, for industrial purposes, are not straight forward. Indeed, each experimental set-up is a piece of puzzle, and they need to be arranged in the correct way to provide valuable results.

For all these reasons, a project was started in late 2014 early 2015 at Continental France. It is based on the full instrumentation of a small three-cylinders gasoline engine. Sensors were placed in the intake pipes, exhaust pipes, cylinder head and inside the piston. Combining these data allows to understand the correlation between many parameters, and allows to re-calibrate/modify and improve the models used in the CFD software at Continental. After three to four years of evolution in the project, the campaign has been held by the powertrain team in Toulouse in 2018. Figure 2.1 shows the engine inside the test bench. The engine being tested without the rest of the car it needs many additional devices such as: an electrical generator to start the engine, a cooling system (Figure 2.2) with a pump to replace the radiator and cooling system. An air supply as the engine is aspiring a lot of fresh air, together with an exhaust system in order to collect and treat burned gases etc... In this specific case the engine was instrumented with a tremendous amount of sensor, it explains why the engine is covered by wires, current sensing probes, air conduct and liquid pipes (Figure 2.1).

A non exhaustive list of the sensors implemented specially for the campaign (in addition of the classical sensors used to ensure the safe and correct operation of the engine) is given:

- More than 20 surface thermocouples distributed in the intake pipes, the cylinder head, the piston, the exhaust pipes ...
- Other temperature sensors in the coolant jacket and crank case in order to get water and oil temperature in the engine.
- More than 20 pressure sensors distributed in the intake, the exhaust, the compressor, the combustion chamber ...
- Two gas analysis system and particle count placed respectively before and after the catalyst.

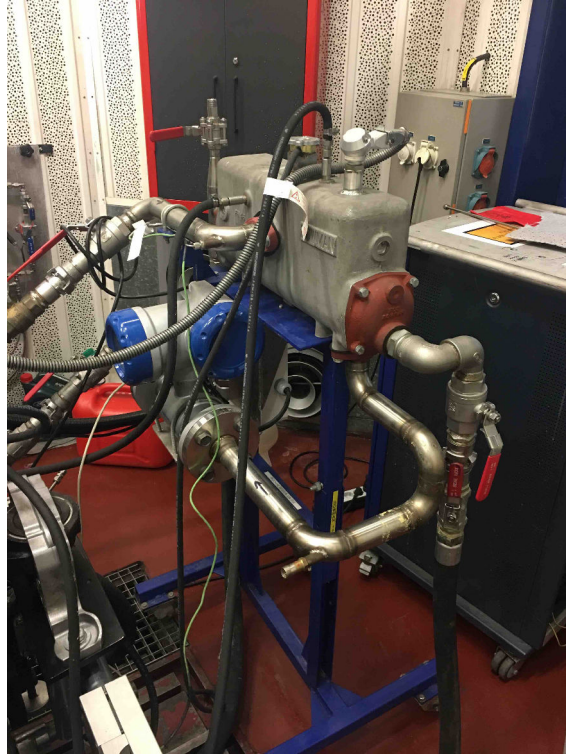


**Figure 2.1:** Pictures of the instrumented engine in the test bench. **Left:** Global view of the engine. **Right:** Vue of amplification devices for pressure sensor distributed in the air system of the engine. Green Type-K thermocouple wires distributed in the air system also visible.

In this Chapter the focus will be laid on the surface thermocouples inserted in the piston of the 2<sup>nd</sup> cylinder of the engine, together with the particle count placed at the exhaust of the engine (before the catalyst). It will help to link the information extracted from the temperature measurement to the emission of particles. It is important to

## 2. ENGINE MEASUREMENTS

---



**Figure 2.2:** Coolant system, it replaces the one in the car, allowing to test the engine in different conditions.

insist on the initial objective of the project, which was to have a global knowledge of the temperatures in the engine, and if possible to have information about piston temperature. Though, a lot of test were performed, just a very small amount of them will be presented here, as they are the most relevant regarding the objectives of this thesis.

### 2.2 Experimental Set-up

Though all the experimental set-ups are available in Chapter 3, the instrumentation of the piston is depicted here because the results are only used in this chapter.

As mentioned before one of the engine pistons as been instrumented with surface thermocouples. They are inserted flush to the surface using the same method as presented in Section 3.4 where more details can be found. However the transmission of the signal is quite different.



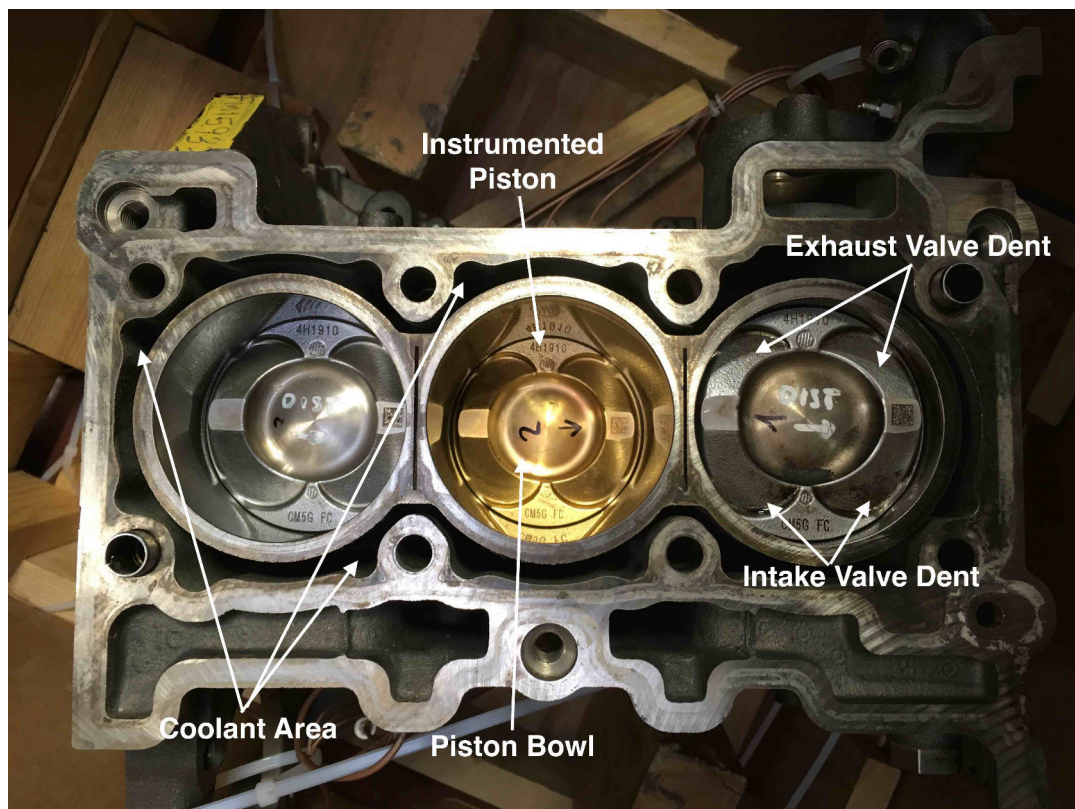


Figure 2.3: Top visualisation of the instrumented engine. The piston in the middle is covered with gold in order to ensure the hot junction of the surface thermocouples (see Figure 3.21).

Figure 2.3 shows the open three-cylinders engine. The golden piston in the center is the one instrumented with thermocouples. The geometry of the piston is also identifiable. The bowl shape in the center of the piston is specific to this engine design, it helps the internal flow during the cycles.

The valves (intake and exhaust) dents are also visible, they allow the piston to fit the contour of the valves at the top dead center, it reduces the volume at the end of compression which helps to increase the compression ratio. In the Otto cycle (or Beau de Rochas cycle, see Figure 2.4), which is the ideal thermodynamic cycle of the four stroke engines [58], the efficiency is directly linked to the compression ratio:

$$\eta = 1 - \frac{1}{r^{\gamma-1}}, \quad (2.1)$$

where  $\eta$  is the efficiency,  $r$  is the compression rate and  $\gamma$  is the heat capacity ratio. Hence

## 2. ENGINE MEASUREMENTS

---

increasing the compression ratio helps increasing the efficiency of an engine.

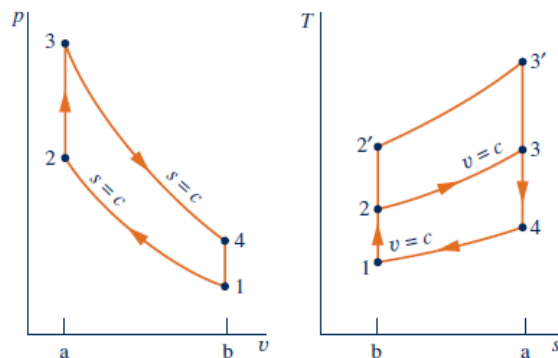


Figure 2.4:  $p-v$  and  $T-s$  diagrams of the air-standard Otto cycle [58]

The part referred as coolant area in Figure 2.3, are the visible parts of the coolant jacket. This is where the cooling liquid is flowing in order to maintain the engine at the good temperature.

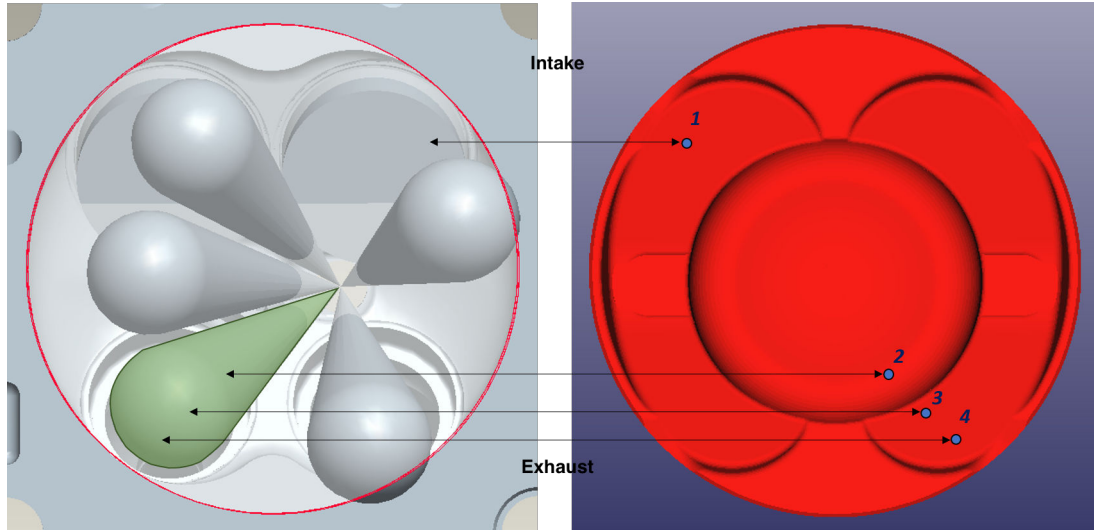
### 2.2.1 Position of the thermocouples

The four surface thermocouples are placed as presented on Figure 2.5 together with respect to the targeting of the injector, even though the spray penetration is known to be perturbed by the air motion (valve jets, tumble, etc...). The first thermocouple (T1) is placed in one of the intake valve dent. This location has been chosen so the thermocouple is supposedly not impacted by any of the injector plumes. The second thermocouple (T2) is located in the bottom of the piston bowl, whereas thermocouple 3 and 4 (T3 and T4) are placed in the exhaust valve dent. These three thermocouples should, depending on the injection timing, undergo spray impingement by one of the injector plume (highlighted in green on Figure 2.5).

The position of these thermocouples have been chosen in order to extract at least two pieces of information which are:

- The surface temperature of the piston during a combustion cycle, for different operating points. It must be reminded here, that this is an important boundary condition for several applications: 0D-1D engine simulations, 3D CFD simulations, spray-wall impingement. Thanks to these measurements, not only will the





**Figure 2.5: Position of the four thermocouples in regard of the spray targeting. Left: Injection targeting looking at the cylinder head. Right: Position of the thermocouples looking at the piston.**

temperature time and range variations be known, but a good idea of the space inhomogeneity will be available.

- The influence of the spray impact on the piston temperature, either during the combustion cycle evolution or for the time average value on stabilised operating point. Regarding the wall film occurrence or lifetime, the mean piston surface temperature is already a key information to know. Nevertheless as will be presented thereafter, spray-wall impingement induces a local decrease of the surface temperature. The local decrease where the wall film is generated may strongly increase the wall film lifetime, and thus, the likelihood of pollutant generation.

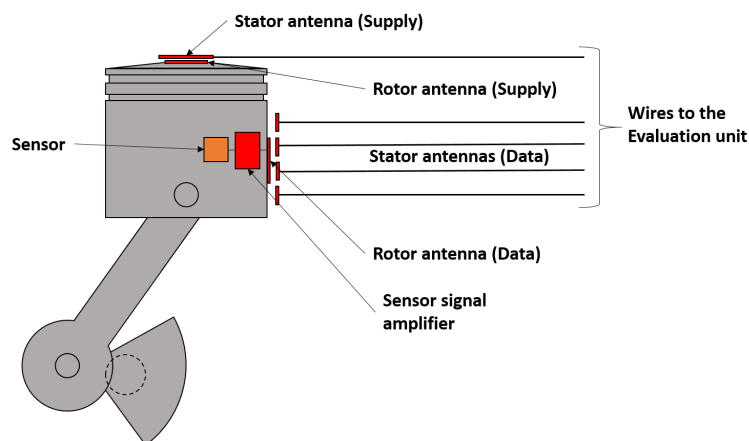
### 2.2.2 Signal Transmission

As the piston is a moving part of the engine (typical piston stroke is around 8 *cm* for this type of engine). It is hard to link the thermocouples to the outside of the engine with wires. The piston is also a lubricated part, which is not suitable for electronics, as oil can splash everywhere. During the elaboration of the project, it has been considered to use wires. However, admitting that they will not break or disconnect due to the high accelerations encountered, the reaction between the oil pool and the thermocouple

## 2. ENGINE MEASUREMENTS

---

whipping the oil surface raised some serious doubts. Finally, the solution envisaged was to use a wireless transmission of the data, Figure 2.6 shows the working principle of the signal transmission. Figure 2.7 shows the piston seen from the bottom, with the signal amplifiers and the thermocouples sheaths.

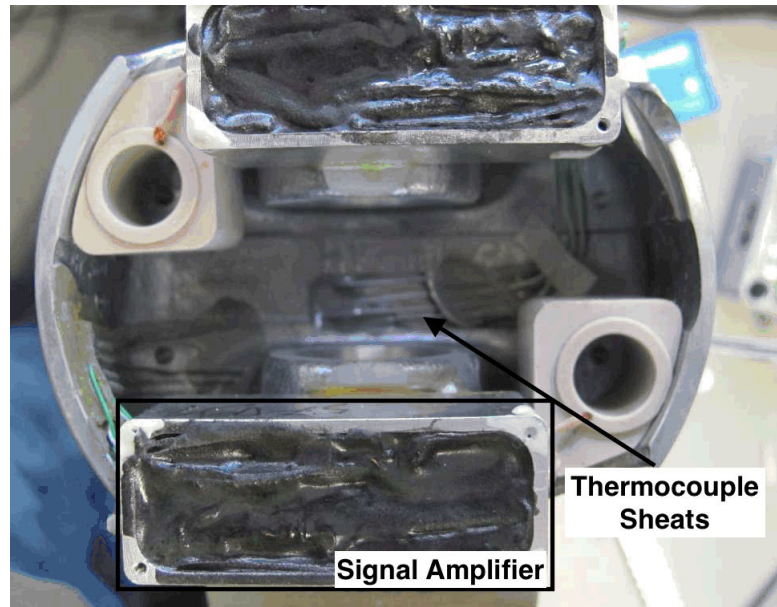


**Figure 2.6: Working principle of the radio transmission of data from the cylinder body to the acquisition line. Source: MANNER Operating manual [55].**

The energy is supplied by the evaluation unit and is transmitted to the sensor signal amplifier at every top dead centre (Supply). Then, the data are radio transmitted from the rotor, at a frequency close to  $700\text{ MHz}$ , to the radio receiver placed on the stator. They are then processed and converted into readable temperatures by the evaluation unit.

### 2.2.3 Cylinder head instrumentation

The cylinder head is also instrumented with 14 thermocouples (see Figure 2.8). The main objective of this instrumentation is once again to validate or improve the data of simulation. The position for the thermocouples has been chosen in order to check the difference of temperature between the three cylinders. But also to see the influence of intake/exhaust on the surface temperatures inside the combustion chamber. Finally it helps having a good idea of the temperature of fresh and burned gases using the wall informations. These thermocouples are not radio-transmitted, type-K wires are used to transmit the signal to the amplification unit. The system is totally depicted in Section 3.4.



**Figure 2.7: Bottom view of the piston, parts of the instrumentation are visible.**

Though the information provided by these thermocouples are really interesting, they will not be detailed here, as it is not in the scope of the study. However, a temperature map for the cylinder head at different operating points is presented Figure 2.14 to show the comparison with piston temperature. After presenting piston and cylinder head temperature map, a study of piston impingement together with two complementary tests are presented.

## 2.3 Results

The results presented here, are first detailing the signal treatment. Then a typical temperature evolution during a combustion cycle is presented, it allows to highlight the remarkable events of an engine cycle.

### 2.3.1 Temperature evolution during a combustion cycle

In order to introduce the results obtained with the surface thermocouples, a first step is to look at the temperature given by one of the thermocouples during one cycle (i.e.  $720^\circ\text{CA}$  which is two rotations of the crankshaft). Figure 2.9 shows the raw signal without any processing. Immediately, two phases can be identified: an elevation of the

## 2. ENGINE MEASUREMENTS

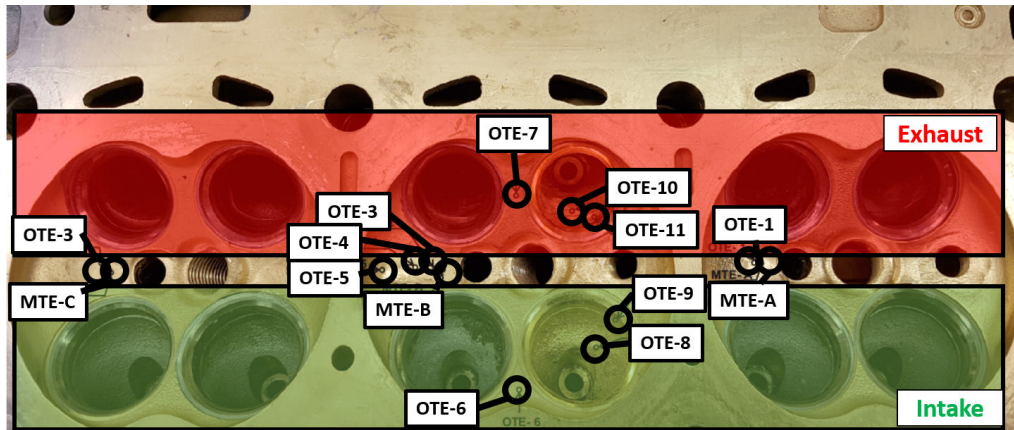


Figure 2.8: Cylinder head instrumentation, green area represents the intake, red area the exhaust. The black circle are thermocouples positions together with their names.

temperature around  $0^\circ\text{CA}$  and then a slow decrease of the temperature. As the studied point is stabilised, the curve start can be juxtaposed next to the curve end in order to imagine the next cycle. The elevation of temperature is due to the combustion process, and it is accompanied with noise.

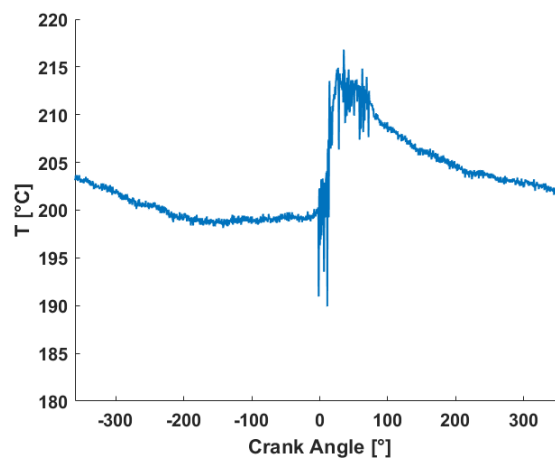
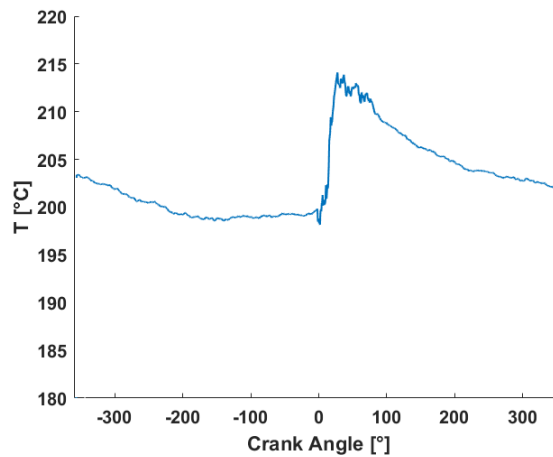


Figure 2.9: Evolution of piston surface temperature during a combustion cycle at 2000 rpm and a BMEP of 10 bar.

In order to reduce the noise a sliding average with a window width of 20 points has been applied (which represents  $4^\circ\text{CA}$ ). Figure 2.10 presents the results after filtering.

The 20 points are replaced with 0, has it does not influence the visualisation of the results, they will later not be displayed, and not taken into account for averaging. The readability of the curve is greatly increased, and though some information might be lost, the shape of the curve is preserved.



**Figure 2.10:** Filtered value of the evolution of piston surface temperature during a combustion cycle at 2000 rpm and a BMEP of 10 bar.

Finally, as automotive engines are repeating cycles many times each second, it is important to look at the cycle-to-cycle variability. Figure 2.11 shows the variation of temperature during a combustion cycle, it is averaged over 1000 cycles and corresponds to the phase average. The standard deviation associated is also displayed in order to evaluate the cycle variations.

The maximum of variability is reached during the combustion phase and the second half of the cycle. This variability is induced by the combustion process, it introduces the biggest time derivative of the cycle which is accompanied with cycle to cycle variability. Also, the post combustion phase is preconditioned by the maximum which is reached at the end of combustion, it is then not surprising to see higher variations in this region. The standard deviation gives a difference of temperature of  $\pm 3^\circ$  which is acceptable.

Other observations can be made on this simple temperature profile, Figure 2.12 highlights the four strokes of the engine and the remarkable events in order to increase the level of comprehension of the cycle temperature evolution.

During the Intake (between  $-360$  and  $-180^\circ$ ) it can be seen that the temperature

## 2. ENGINE MEASUREMENTS

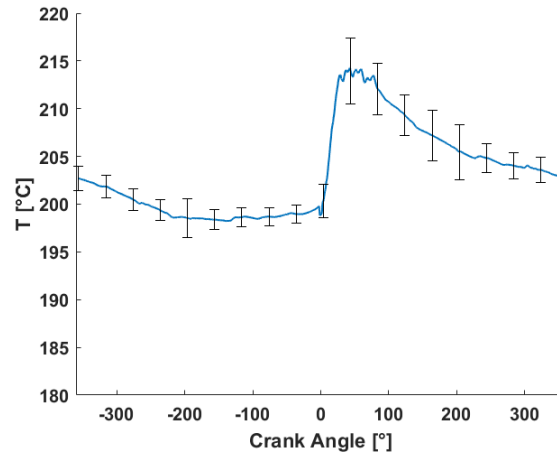


Figure 2.11: Averaged value and standard deviation over 1000 combustion cycles of the evolution of piston surface temperature during a combustion cycle at 2000 *rpm* and a BMEP of 10 *bar*.

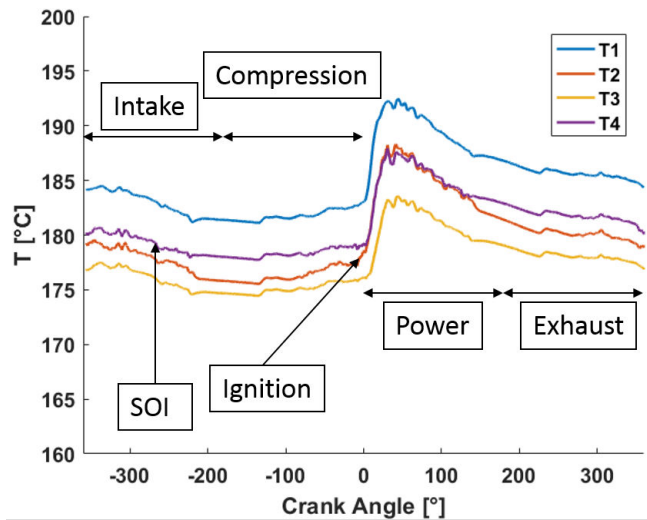


Figure 2.12: Evolution of piston temperature for the four thermocouples. Strokes timing, SOI and ignition presented. Operating point 2000 *rpm* and a BMEP of 10 *bar*.

decreases, it is mainly due by the admission of fresh gases, but also by the global engine cooling ensured by the cooling system. During this phase, the injection also takes place (start at  $-290^\circ$ ), vaporisation of fuel during this phase and also during the beginning

of compression is cooling the fresh gases, though it is not clearly visible on the graphs. Then, the compression phase occurs (between  $-180$  and  $0^\circ$ ), during this phase the valve are closed and the gases start to compress. A slight raise of the temperature is recorded on the surface temperature. At the end of the compression, the spark plug is firing (around  $-7/ -8^\circ\text{CA}$ ): this shift is called the ignition timing advance. It is introduced, in order to optimise the force collected during the power phase.

The compression phase is followed by the power phase. This starts with the combustion of the air/fuel mixture, the expansion of the hot gases pushes the piston in order to rotate the crankshaft. During this phase, the surface temperature is increased by  $15^\circ\text{C}$ . Though this increase may seems small, it is important to keep in mind that the heat transfer between a gas and a wall is not instantaneous, and also the existence of a quenching distance where the flame extinguishes before reaching the wall [74]. The temperature starts to decrease before the end of the power phase, due to engine cooling and also gas expansion. Finally, during the exhaust phase, most of the gases are pushed out and the temperature of the piston keeps decreasing due to engine cooling. A new cycle then follows.

The temperature evolution obtained during a cycle, is physically coherent with what is known to happen in an engine. Besides, it also corresponds with what has been previously found by [42] in 2014. They instrumented the piston of a single-cylinder experimental engine, in order to check the effect of injection pressure, injection timing and a change in engine load on the piston surface temperature. Figure 2.13 shows the temperature variation during a cycle in their piston.

The main difference between the two projects, is the instrumentation of a complete engine in opposition with a research engine. The research engine has many advantages, as it is easier to manipulate and modify, also an optical access is available which helps understanding what happens inside the combustion chamber. However, instrumenting a full engine, though it is more complicated to link a recorded variation to its cause, gives the bigger picture and allows to compare/improve the models developed with simulation softwares. Testing on a full engine, allows to get one step closer to what will happen in a car, specially in term of engine cooling.

## 2. ENGINE MEASUREMENTS

---

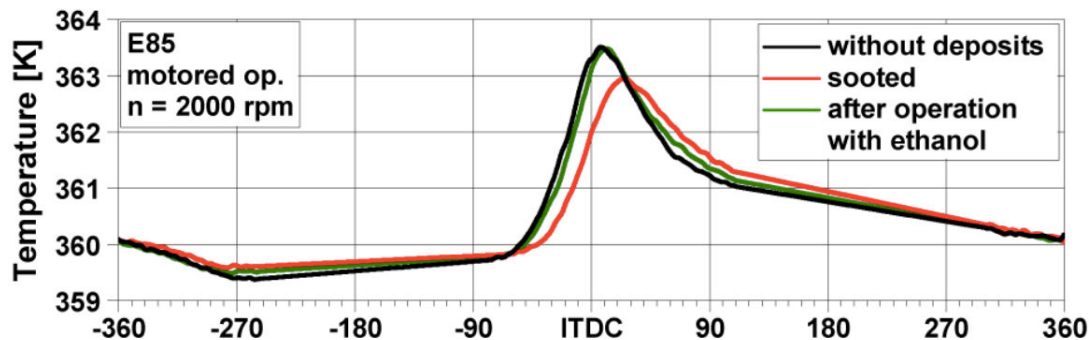


Figure 2.13: Temperature evolution during a combustion cycle [42]. They developed a cleaning process using fuel enriched in ethanol to clean the soot deposit. The deposit includes a delay and reduces the sensitivity of the thermocouple. Such study hasn't be done in the case presented here.

### 2.3.2 Piston temperature map

At the beginning of the project, the ambition was to get, for a wide range of operating points, an average value of the piston temperature. It was motivated by two main reasons, to validate the 0D/1D simulation and to improve boundary conditions for 2D/3D computational fluid dynamics (CFD) simulations and development of liquid deposition models.

To do so the average temperature of the piston has been measured on a range of operating points. The temperature has been measured every 500 *rpm* between 1000 *rpm* and 4000 *rpm* and every 2 *bar* of BMEP (Break Mean Efficiency Pressure) between 2 and 24 BMEP (a second campaign has allowed to increase the number of measures). For each point of the map it takes 4 to 5 minutes to wait for a stabilisation of the engine and perform the data acquisition. However, for confidentiality purposes a part of the map cannot be presented. Only data between 1000 *rpm* and 3000 *rpm* and between 1 *bar* and 12 *bar* are presented. The highest temperature measured on the piston is 265°C.

Figure 2.14 presents the results of the piston temperature map. The average temperature is computed as the mean temperature of the temporal average of the four sensors. The temperature of the piston increases with respect to the engine speed (*rpm*) and also with respect to the engine load. During a combustion cycle the variation of temperature is around 10 to 20°C, however as the rise of temperature last for



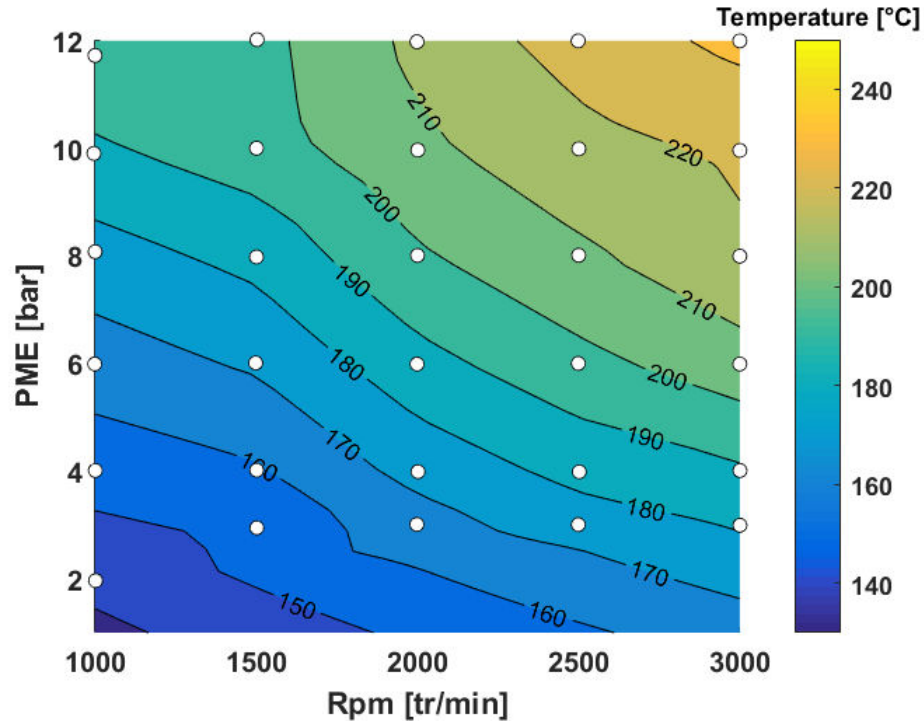


Figure 2.14: Map temperature for the piston. White circles: measured points.

only a quarter of cycle ( $180^\circ$ ), the combustion process does not influence greatly the average temperature over a cycle ( $2 \sim 3^\circ\text{C}$ ). Hence, this temperature is precise enough and can be used as a boundary condition for spray impact simulations.

On this map, the difference of conditions for a fuel impinging on the surface is around  $100^\circ\text{C}$  (from one side of the map to the other), which is in term of physical behaviour, for mono-component fuels huge. Indeed, Table 2.1 shows the saturation temperature, the Nukiyama [67] and the Leidenfrost [49] temperatures for n-heptane, iso-octane and n-decane as presented in [24] **for gently deposited droplets**. Nukiyama and Leidenfrost temperatures are notions relative to lifetime and heat transfer of liquid on hot walls. These notions are detailed in Chapter 6 where the evaporation and vaporisation of liquid film is addressed thoroughly.

Nukiyama and Leidenfrost temperatures are not thermodynamic quantities: though they vary (like the saturation temperature) with respect to pressure, they are also in-

## 2. ENGINE MEASUREMENTS

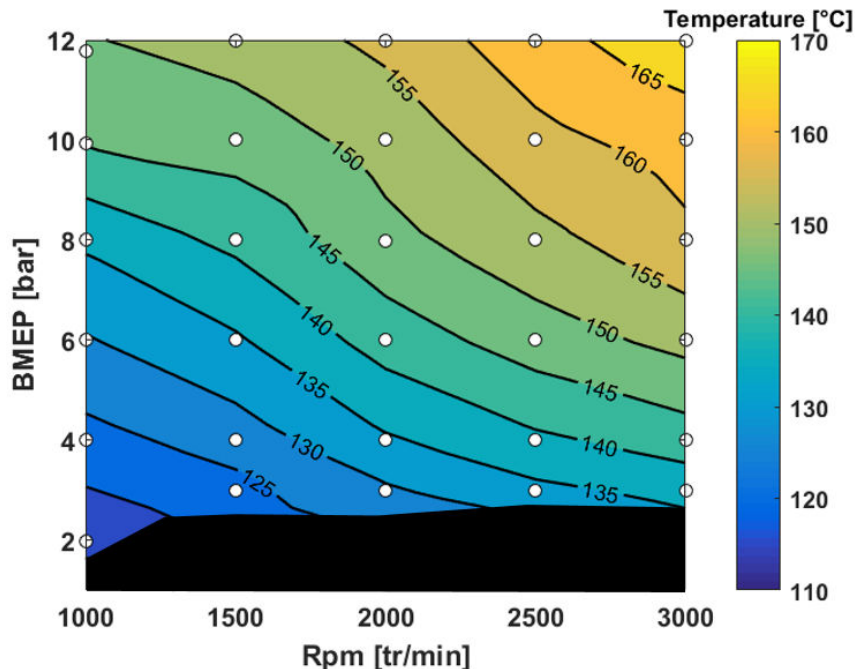


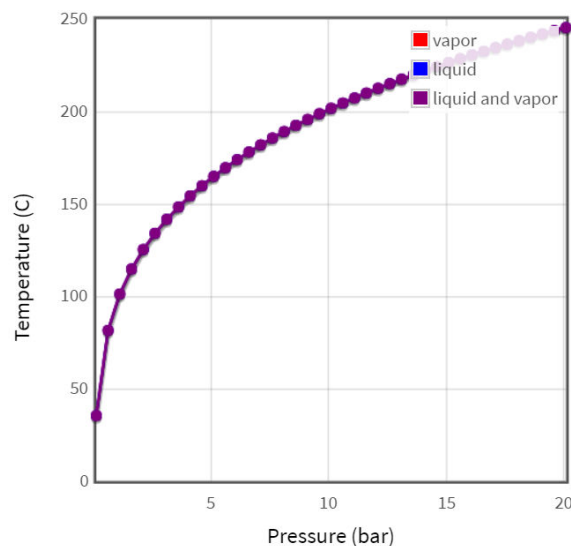
Figure 2.15: Map temperature for the cylinder head. White circles: measured points.

Fuel	Saturation Temperature [ $^{\circ}C$ ]	Nukiyama Temperature [ $^{\circ}C$ ]	Leidenfrost Temperature [ $^{\circ}C$ ]
n-heptane	98	150	210
iso-octane	99	122	190
n-decane	174	210	253

Table 2.1: Characteristic temperature for selected alkanes for gently deposited droplet as depicted in [24] at atmospheric pressure.

fluenced by deposition conditions. The roughness of the wall or the velocity at impact are playing a big role in their definition, transforming these values into vague reference points more than absolute reference. However, as mentioned earlier on the map presented in Figure 2.14, the difference of temperature is greater than  $100^{\circ}C$  from one side to another side of the map. For the three alkanes presented in Table 2.1 a variation of  $100^{\circ}C$  allows to go from sub-saturation temperature to higher than Leidenfrost one, changing the heat transfer and lifetime considerably. To this first level of analysis, one

needs to add the pressure dependency. During the two first strokes of the combustion cycle, the pressure is greatly changing. Depending if the engine is naturally aspirated or turbocharged, the pressure during the intake can vary from 0.5 to 2 *bar*. Then, during the compression phase, pressure up to 20 *bar* can be experienced. As shown in Figure 2.16 the saturation temperature of n-heptane is going from 50°C at 0.2 *bar* to 245°C at 20 *bar*. This is why it is fundamental to have correct boundary conditions for computational fluid dynamics (CFD) in order to correctly simulate the phase change of deposited liquid.



**Figure 2.16: Evolution of saturation temperature for n-heptane for different pressures realistic of engine operating points. NIST database.**

Figure 2.15 shows the temperature map for the cylinder head. On every point, this temperature is lower than the piston temperature (30 to 60°C here). The cooling is higher as it belongs to the engine stator, while the piston belongs to the rotor (creating friction and reducing the "available time" for cooling). It is also important to keep the injector (which is inserted in the cylinder head) at a cool temperature, in order to avoid damaging the inner components. The direction of the gradient of temperature is the same for the piston and the cylinder head. It should be mentioned here, that, despite the very harsh conditions the piston faced, results have been generated for a very large engine speed / load domain. This underlies the quality of the material and of the experimental setup used. Furthermore, temperature measurements with so high

## 2. ENGINE MEASUREMENTS

---

load are particularly rare and thus very precious. As a comparison, the load never exceeds 8 *bar* in the aforementioned experiments in [42].

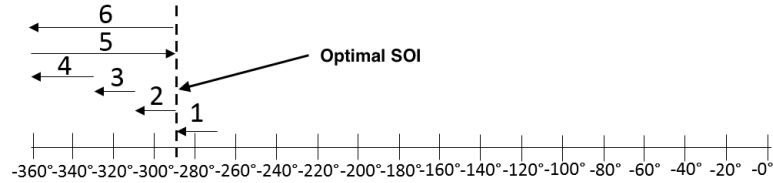
### 2.3.3 Influence of piston impingement

#### 2.3.3.1 Experimental design

In order to characterise the spray cooling on the piston surface, an experimental design has been developed. It consists of advancing the start of injection in order to be sure that the spray and the piston meet each other, and hopefully be able to record a loss of temperature. It is composed as followed:

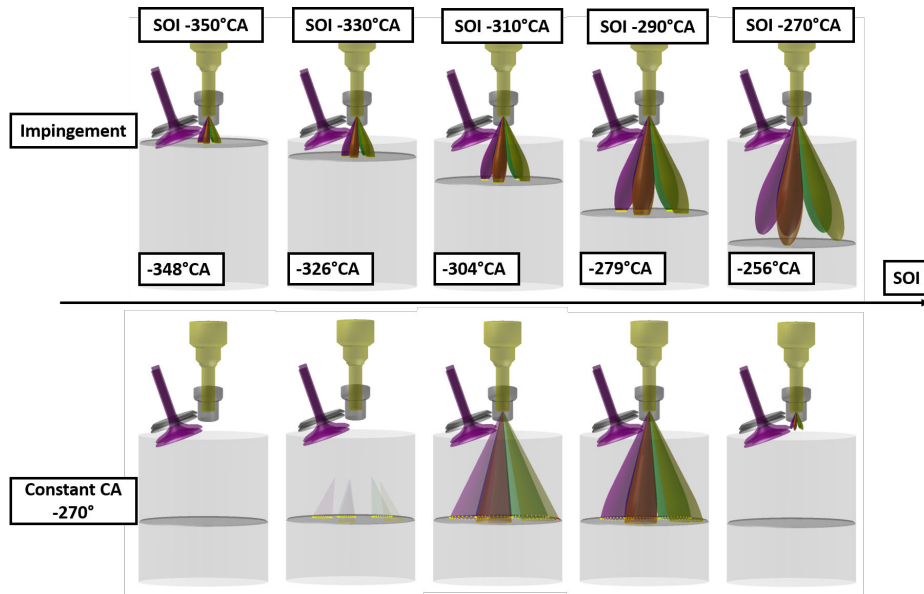
- The reference Start Of Injection (SOI) is taken using the calibration of the Engine Control Unit (ECU). It is assumed that it is the optimal SOI for the car (not only focussed on the minimisation of particle number).
- 6 steps are performed, each one is composed of 500 cycles on the same operating point, a brutal change of SOI and 1000 cycles with the new SOI. The steps of SOI are: optimal + 20 to optimal, optimal to optimal -20, optimal -20 to optimal -40, optimal -40 to Top Dead Center (TDC), and finally TDC to optimal and optimal to TDC. Figure 2.17 displays the different SOI steps.
- During these changes of SOI, it is really hard to change only one parameter while keeping all the other constant. In order to get results that are the most comparable to each other, it has been chosen to impose a constant value for the AI50. The AI50 is the instant where 50% of the integrated area (AI50) of rate of heat release is reached [88]. It also guarantees that the air mass flow remains as constant as possible, as well as the consumption.
- The temperature evolution together with the particle number (PN) are recorded in order to try to link the piston impingement, and supposedly the liquid fuel films with the particulate matter creation.

To give a better visualisation of the SOI effect on the piston impingement, simulations realised with a in-house (IMPACT [29]) software helps visualising the impact of the sprays on the walls of the combustion chamber (Figure 2.18). It is usually used to develop the injector targeting. In the presented case, the growth of spray plumes, and



**Figure 2.17: Timescale and experimental protocol visualisation for the influence of piston impingement.**

the intersection with the wall is only geometrical (no air motion is taken into account and the penetration follows a logarithmic law as presented in [29]). The air motion plays a huge role as presented on a high load point in Figure 2.19, where the fuel sprays is highly deflected by the engine aerodynamics. However, Figure 2.18 gives a good idea of what could happen, and why this experimental design has been developed.



**Figure 2.18: Simulation realised with IMPACT [29] (without aerodynamics) of the effect of SOI on piston impingement. Top: °CA of spray-piston impact. Bottom: Constant 90°CA. Set point 2000 rpm 10 bar BMEP.**

Figure 2.20 shows the typical temperature evolution of the four thermocouples for a SOI of  $-290^{\circ}\text{CA}$ , the optimal SOI is at  $-270^{\circ}\text{CA}$ . The first observation is that the thermocouple 1 gives values relatively higher than thermocouples 2, 3 and 4. This is a first

## 2. ENGINE MEASUREMENTS

---

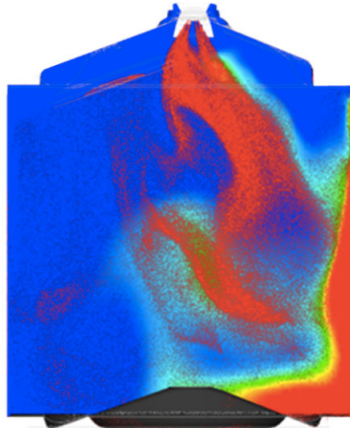


Figure 2.19: Spray deflection simulation in an engine, cylinder wetting.

interesting indication of an existing inhomogeneity in the piston surface temperature.

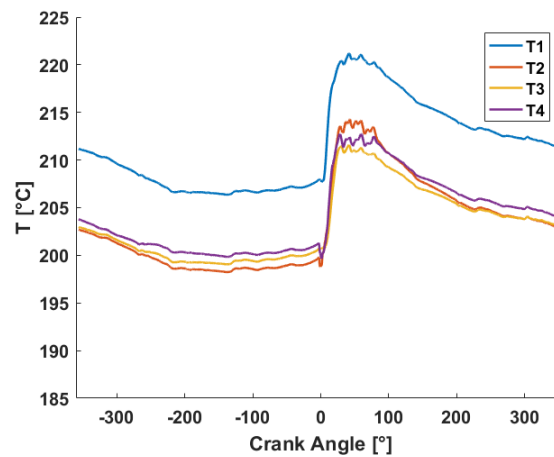


Figure 2.20: Evolution of piston surface temperature for the standard SOI. Set point at 2000 *rpm* and a BMEP of 10 *bar*.

Before trying to give an explanation to this inhomogeneity, it is necessary to check that it is not a measurement deviation induced by the thermocouples or the acquisition chain. To do so, a measurement at the start of the engine has been performed.

### 2.3.3.2 Engine heating

Figure 2.21 shows the temperature evolution, together with the cylinder pressure (in order to track the first ignition of the engine). As the measure needs the rotation of the engine to work the first instants (1 s) gives non relevant values. Indeed, as the water coolant temperature at the beginning of the test is recorded at  $25^{\circ}C$ , every piston temperature recorded below is not relevant. A zoom on the first combustion cycle shows that, before the combustion the four thermocouples gives the same temperature, and the deviation starts from this first combustion. Another view 3 seconds after the first combustion shows that the thermocouples record different temperatures. This behaviour is exactly the same as the one presented in Figure 2.20. Hence, it can be affirmed that the inhomogeneities of temperature measured on piston surface, are not due to measurement issues and reliable.

A first, probable explanation is that, as the temperature inside the engine is not homogeneous, the gradient from cylinder one to three is also present on the piston. Another explanation could be due to the air motion in the cylinder. Indeed the thermocouple 1 is located on the intake side, whereas the three others are placed on the exhaust side. The tumble flow imposed in the engine could cool one side more than the other. A last contribution has been envisaged, the piston is hosed from below by a small oil nozzle, in order to cool it but also to ensure a good lubrication. Depending on the impingement point of the hose, it could cool a side more than the other. To check this a test has been performed.

### 2.3.3.3 Oil pressure effect

The oil injection pressure can be switched from 2 to 4 *bar*, hence increasing the mass flow rate would increase the cooling. After one minute at 2 *bar* of oil pressure it is switched to 4 *bar* (Figure 2.22 and Table 2.2), the cooling is increased when the pressure is raised. However, it does not seem to increase the temperature difference between one side of the piston and the other.

In conclusion, though the reason for this surface gradient is not clearly identified, this simple information is valuable and makes a good validation case for engine thermal simulations. It can also be an interesting information when designing the spray

## 2. ENGINE MEASUREMENTS

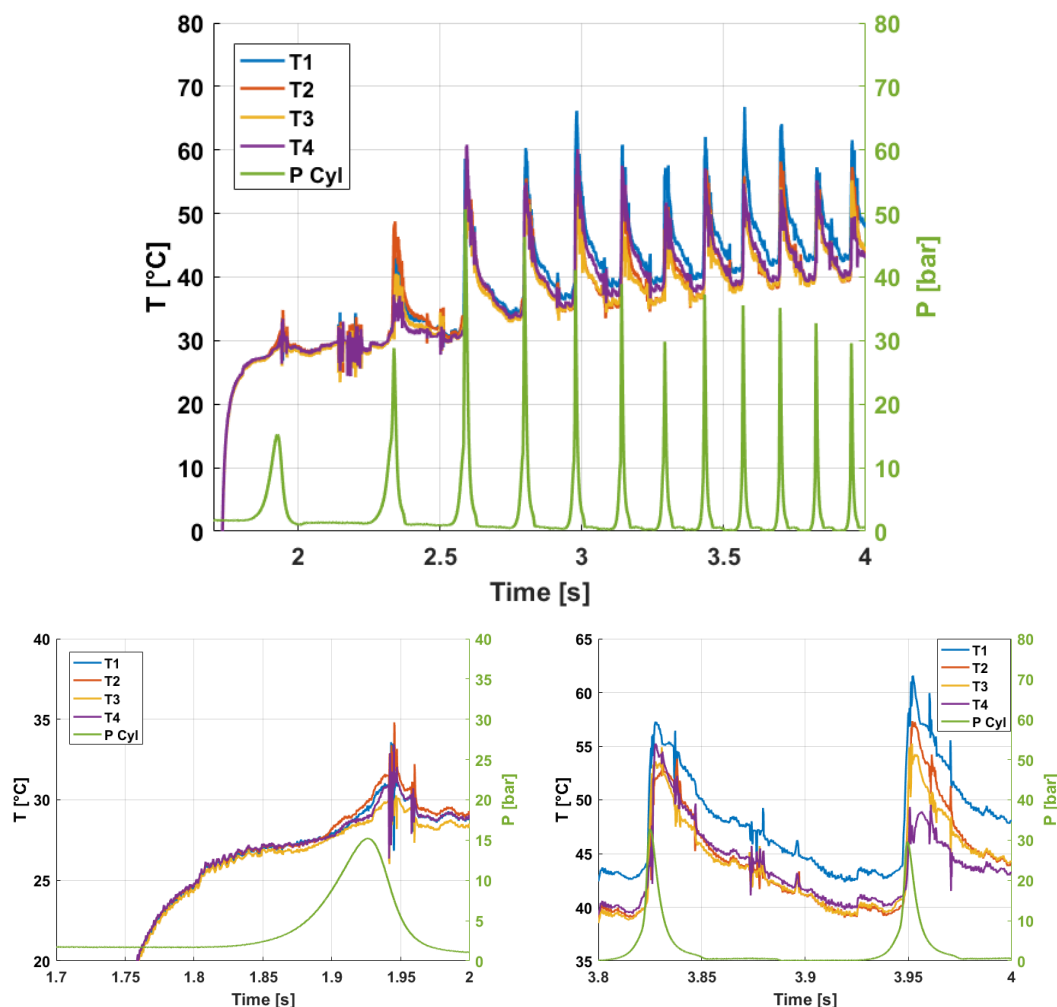


Figure 2.21: Temperature evolution at engine start and cylinder pressure evolution. Engine speed  $\approx 400$  rpm. Top: full temporal evolution. Bottom left: first combustion cycle. Bottom right: Temperature differences established.

targeting (trying to target supposedly hotter surface to favour a quick vaporisation). The four thermocouples show the same behaviour, with the same timing, and the raise and decrease of temperature are all in the same range.

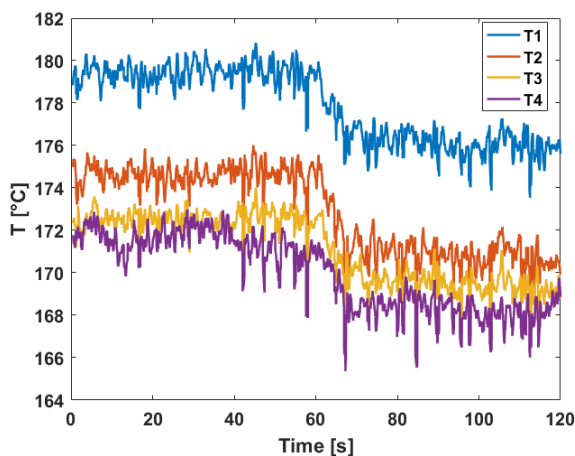
### 2.3.3.4 Start Of Injection effect

Figure 2.23 shows the temperature evolution over a cycle for a SOI of  $-330^\circ\text{CA}$  and  $-360^\circ\text{CA}$  respectively. These two injection timings are really early in the combustion



	2 bar	4 bar	$\Delta T$
T1 [ $^{\circ}C$ ]	179.4	176.0	3.4
T2 [ $^{\circ}C$ ]	174.6	170.5	3.9
T3 [ $^{\circ}C$ ]	172.5	169.3	3.2
T4 [ $^{\circ}C$ ]	171.5	168.2	3.3

**Table 2.2:** Oil pressure test results.  $\Delta T$  is the difference of temperature recorded when switching the oil pressure from 2 to 4 *bar*.



**Figure 2.22:** Effect of oil pressure on piston temperature. Switch from 2 to 4 *bar* is performed at  $t=60$  *s*.

cycle and probably not realistic for a real application, as it is known to lead to pollutant generation. Nevertheless, it is here done on purpose, as the piston is really close to the top dead centre, and spray-piston impingement must occur. Indeed, a decrease of temperature is recorded on thermocouple 2 (which is placed in the bowl of the piston) for both cases, a few degrees after the start of injection. The timing of the loss (which is shifted when the SOI change) clearly indicates that it is due to the spray impingement on the piston surface.

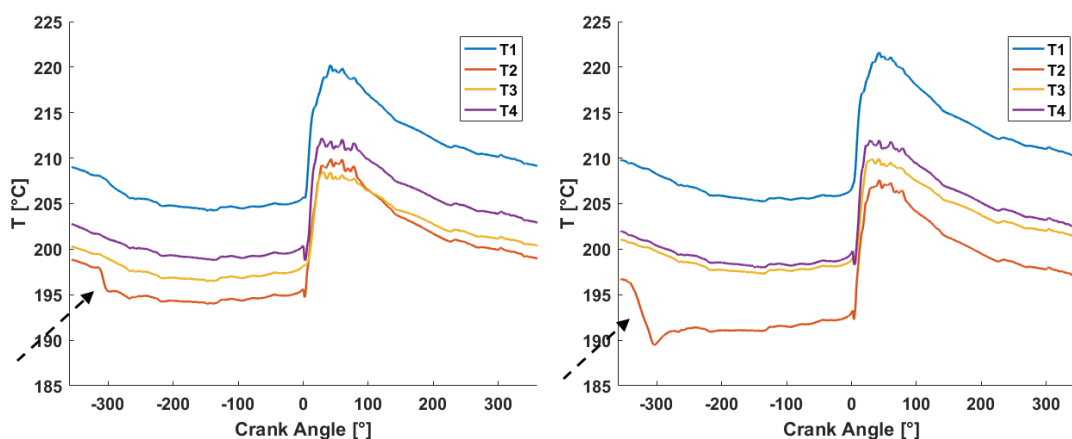
For the case with the SOI at  $-330^{\circ}CA$  referred in Figure 2.23 (Left), the temperature starts to decrease at  $-314^{\circ}CA$  until  $-300^{\circ}CA$ . At this engine speed it represents 1.2 *ms*, during this time the temperature has decreased by  $2.5^{\circ}C$ . The injection duration for this set point is 3 *ms* at 100 *bar* of injection pressure. It is interesting to note the shift between the start of injection and the beginning of temperature loss, it can be explained

## 2. ENGINE MEASUREMENTS

by the spray travel time and eventually by a soot deposit upon the piston surface as studied in [42]. At the start of impingement ( $-314^{\circ}\text{CA}$ ), the piston has almost travelled half a stroke, which represents 3 to 4 *cm* (taking into account that the thermocouple is off-centred). Looking at the typical spray penetration curve at 100 *bar* (Figure 1.8), a travel time can be estimated around 1 *ms* which is really comparable with the  $16^{\circ}\text{CA}$  ( $1.3 \text{ ms}$ ) between the SOI and the start of impingement.

A reason to explain that the temperature loss is shorter than the injection duration is that the thermocouple goes out of the spray impingement area.

Then for the case with the SOI at  $-360^{\circ}\text{CA}$  (Figure 2.23) the temperature starts to decrease at  $-340^{\circ}\text{CA}$  until  $-304^{\circ}\text{CA}$  which makes  $36^{\circ}\text{CA}$  and represents 3 *ms*, that is to say the totality of the injection duration. During this time the recorded temperature loss is  $-7^{\circ}\text{C}$ . Table 2.3 recapitulates this information.



**Figure 2.23:** Evolution of piston temperature for two early injection timing. Left: SOI  $-330^{\circ}\text{CA}$ . Right: SOI  $-360^{\circ}\text{CA}$ . Set point at 2000 *rpm* and a BMEP of 10 *bar*. The arrows highlight the impingement process.

SOI[ $^{\circ}\text{CA}$ ]	Start of impingement [ $^{\circ}\text{CA}$ ]	End of impingement [ $^{\circ}\text{CA}$ ]	$\Delta T[^{\circ}\text{C}]$
-330	-314	-300	-2.5
-360	-340	-304	-7.0

**Table 2.3:** Temperature loss on thermocouple 2 due to spray impingement on the piston, extracted from Figure 2.23.

The loss of temperature recorded is never totally overcome by the heat transfer in the piston, hence the level of thermocouple 2 is below thermocouple 3 and 4 during the whole cycle.

It is quite surprising to see that neither thermocouple 3 nor thermocouple 4 see the spray impact. Two reasons could be envisaged. The first one is that the spray impacts on a small area and the heat removal associated is then very local. In order to study the spatial restriction of temperature loss a special study with the experimental set-up presented in Section 3.4 has been performed. The fixed positions of the thermocouples and injector, together with the strong aerodynamic forces (intensity is varying depending on operating points) that are deflecting the injector plumes, makes the aiming of the thermocouples with the sprays a complex task.

The second reason, is that the valve dent on the piston, where the two thermocouples are placed, acts as a shield and protects the thermocouples from spray impingement. More information and interpretation will be provided in Chapter 5 and 6.

The engine has been instrumented with a particle counter (AVL particle counter (APC)) in order to correlate the particle emissions with the tested parameters. Figure 2.24 shows the full campaign of SOI steps. It displays, for each SOI, the level of particles generated. The first thing to note is the logarithmic scale of the graph. Indeed, when the quality of the combustion is poorer, the number of created particles increases tremendously. The variation of emission during the jump from  $-270^\circ$  to  $-290^\circ$ , and  $-290^\circ$  to  $-310^\circ$  are small compared to the jump from  $-310^\circ$  to  $-330^\circ$  and  $-330^\circ$  to  $-360^\circ$ . This is critical for the OEMs and their providers. The exponential increase of PN is responsible for the difficulties encountered during the homologation cycles. In the jump between  $-310^\circ$  and  $-330^\circ$  the particles are multiplied by one hundred. If the engine stays too much time at such level of particle generation, it cannot pass the homologation cycles. This is why the automotive industry is looking carefully at the steep gradients that could occur during an homologation cycle. Many levers are tested to reduce their occurrences, especially during transients. One of the most critical factor is the spray penetration reduction. While the recent raise in fuel injection pressure implies a better atomisation and air / fuel mixing, the raise of liquid momentum increases the spray velocity and the likelihood of spray impingement. Therefore, injector manufacturers

## 2. ENGINE MEASUREMENTS

have improved the design (hole conicity, counter-bores, etc) and defined new injection laws (multiple injections) to reduce overall penetration.

Then it can be noted that, the minimum number of particles is not recorded for the optimal SOI, but for a SOI of  $-310^{\circ}\text{CA}$ . One reason is the fact that, the engine is often optimised in term of fuel consumption as long as particulate matter are maintained below a threshold. The behaviour presented in [40] (Figure 1.4) in the introduction is confirmed: there is a window (Zone B) where the injection process must be performed in order to avoid particle generation.

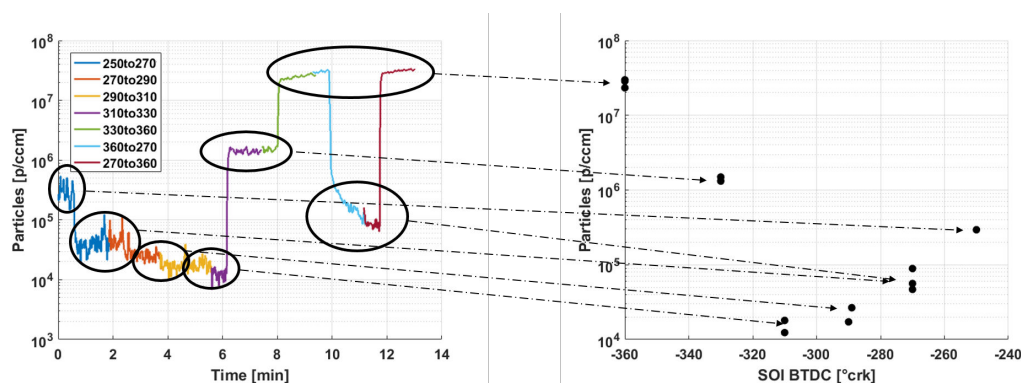


Figure 2.24: PN generation for different SOI. Left: SOI steps and time evolution of particle generation. Right: PN level as a function of the SOI.

### 2.3.3.5 Conclusion

The main goal of this experimental design was to study the piston impingement thanks to the surface thermocouples. It has been identified that: when the injection is started really early in the cycle, a huge number of particles are generated. In the same time piston impingement is recorded thanks to the loss of temperature of thermocouple 2. It is clear that the piston impingement is responsible of this temperature increase.

By reaching the piston, the spray starts to generate a liquid film, due to the relatively small surface of contact (compared to millions of droplets flowing in the combustion chamber) the liquid film evaporate late (if it completely vaporises). This late vaporisation timing, reduces the quality of the fuel/air mixture and generates a lot of particles during the combustion phase.

It has also been noted that the heat removal seems really local and is quite small (2 to 10°C). In order to address all these questions many experimental set-ups have been developed during this PhD. The goal is to study separately the different aspect observed in here in order to improve the knowledge level around spray/wall impingement.

## 2.4 Acknowledgment

The data produced and presented in this Chapter are deeply linked to the great work performed by Hans Nuglisch who coordinated the project during its early phase. But also, Jean-Jacques Saves and Rémy Truquet who took in charge the design of most of the tests and their specifications, and supervised during a month all the tests at the engine test bench. Finally, Nicolas Lamarque contribution is also remarkable, either for the original idea, the test designs, or the positioning of the thermocouples.

## 2. ENGINE MEASUREMENTS

---

# 3

## Experimental Methods

In this work many different experimental set-ups have been used. Indeed as the work focuses on four different aspects which are: (i) a qualitative description of spray impingement, (ii) a modelling of film spreading due to spray impingement (ii) a modelling of the heat transfer associated and (iv) a study of the vaporisation rate of mono and multicomponent liquid films. It has been necessary to use and develop many different experimental set-ups, sometimes together or independently. This is why a description of all the experimental set-ups and methods is proposed, before studying the campaigns and the modelisation based on the experimental data produced.

### 3.1 Fuel preparation system

For all the experimental set-ups presented below, the fuel preparation system is the same it was already present at Continental. A full description follows, complementary informations can be found in [53].

It can be divided in two different parts, the fuel feeding part and the electronic/control part. The fuel is stocked in a fuel tank, a pipe connects it to a low-pressure pump. The fuel is then transmitted to high pressure pump via a heat-exchanger filled with cold water ( $4^{\circ}C$  water running through the whole Continental facility). The high pressure pump is driven by an electrical engine which is piloted by a computer to vary the pressure between 15 and 250 bar. Once the fuel is pressurised a high-pressure line transmits the fuel to the injector. The fuel not used is going back to the fuel tank in a closed circuit, the heat exchanger purpose is to avoid the heating of the liquid due to multiple

### 3. EXPERIMENTAL METHODS

---

passages through the pressure system. The fuel tank is equipped with a low-level sensor to avoid discharging the pump, and a temperature sensor. The power unit that runs the pressure pumps is composed of a 12 V and 48 V, the electrical engine that drives the high pressure pump is using three-phase current.

Concerning the control part of the fuel preparation system it is mainly composed by a computer running a National-Instrument card, and a Solenoid driver box (ECU Engine Control Unit) from continental that generates the signal to open and close the injector. The NI card works with a in house LabView software, the principal features are:

- A control of the electrical engine, together with a pressure sensor to provide the required pressure to the injector
- A signal management interface, designed to command the ECU and several other devices such as the light triggering, the camera triggering, etc...
- Definition of the injection duration, cadency etc...

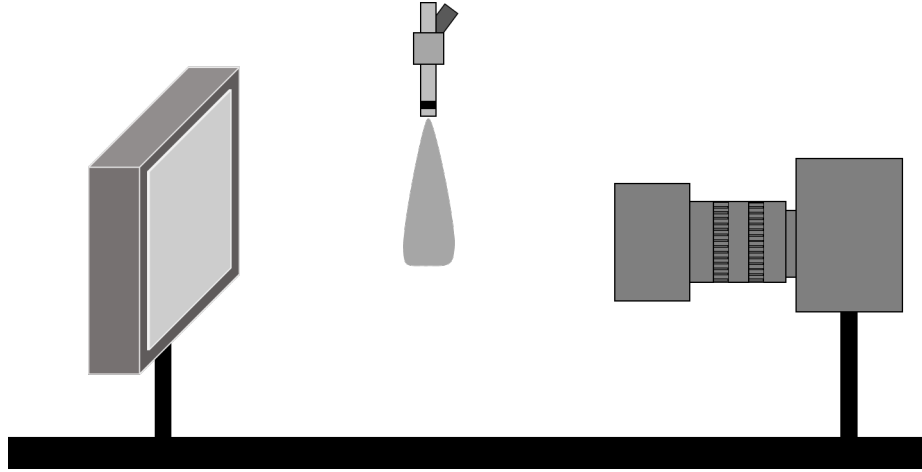
Finally the injector itself which generates, thanks to its geometrical characteristics, the fuel sprays that will be used in all the experiments. The injector principal characteristics of the ASTRIDE injector has been presented in Chapter 1.

## 3.2 Shadowgraphy

The shadowgraphy is a method that consists in illuminating the observed object or flow (here a spray), in order to project the shadows either on a screen or a camera. The light can either be pulsed at every image or continuous (laser, LED, flash). In the case presented here the light used is a steady high intensity EFFILUX-LED panel that is placed in front of the camera. Between the light and the camera the injector is placed and it is ensured that the spray generated by the injector stays in the focal field of the camera. Since the droplets size is small enough, they appear as black dots and the spray is black. Figure 3.1 depicts the experimental set-up.

The method can be used to observe the free spray (without impingement) to obtain its characteristics such as spray angle, spray penetration, or to study the impact of the spray. The impact generates a cloud of droplets that makes the impact region difficult





**Figure 3.1: Working principle of Shadowgraphy, the object observed is placed between a light source and the camera.**

to observe. However, it is very useful to study the secondary spray (numerous droplets organised in a spray and leaving from the impingement area) propagation.

Contrast and brightness issues are encountered when working with shadowgraphy. However the one addressed here is the sharpness of the image specially due to the exposure time. Indeed as the droplets are travelling at high speeds ( $\approx 100 \text{ m/s}$ ) the exposure time needs to be adapted in order to freeze the image. Two different possibilities exist, one is to use a camera that allows the shutter to open and close very fast (i.e. in less than  $0.02 \text{ ms}$ ) and to have enough light collected during this time. The other one is to have a triggered source of light that can flash during the opened time of the shutter. Histograms in Figure 3.2 depict the two cases. In both histograms the exposition time is  $0.02 \text{ ms}$ , however one is piloted by the shutter speed and the other one by the light speed.

A simple calculation with droplets moving at  $100 \text{ m/s}$  during  $0.02 \text{ ms}$  gives a travelled distance of  $2 \text{ mm}$ . Depending on the magnification and the captor size, this kind of images can be clear or not. To illustrate this, Figure 3.3 shows two pictures of the same spray, one performed with a LED panel illuminating continuously, the other one with a laser pulsing at  $10 \text{ ns}$ . Pressure of injection is constant and magnification is almost the same in the two cases. These two pictures are close-up visualisations of the spray (i.e. close to the injector tip). It is the part of the flow with fastest droplets. On

### 3. EXPERIMENTAL METHODS

---

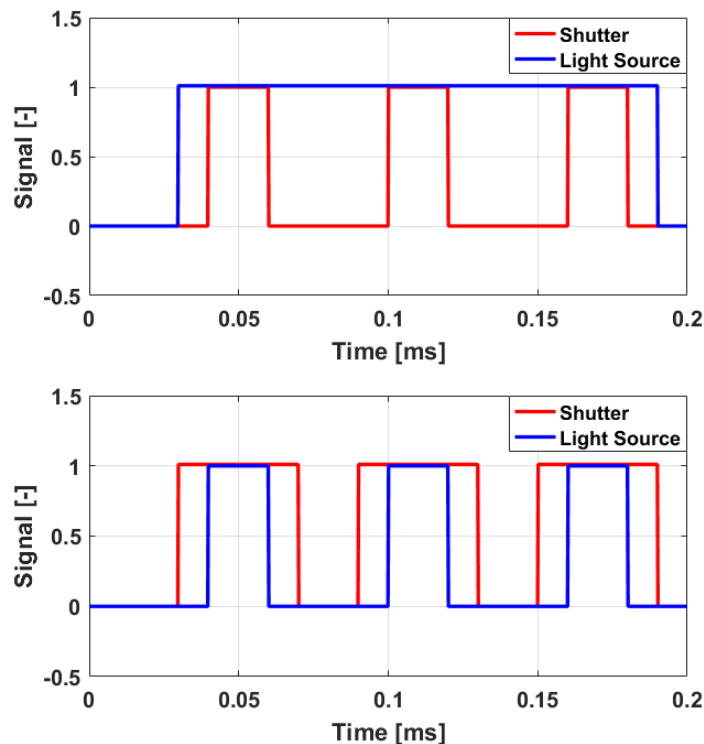
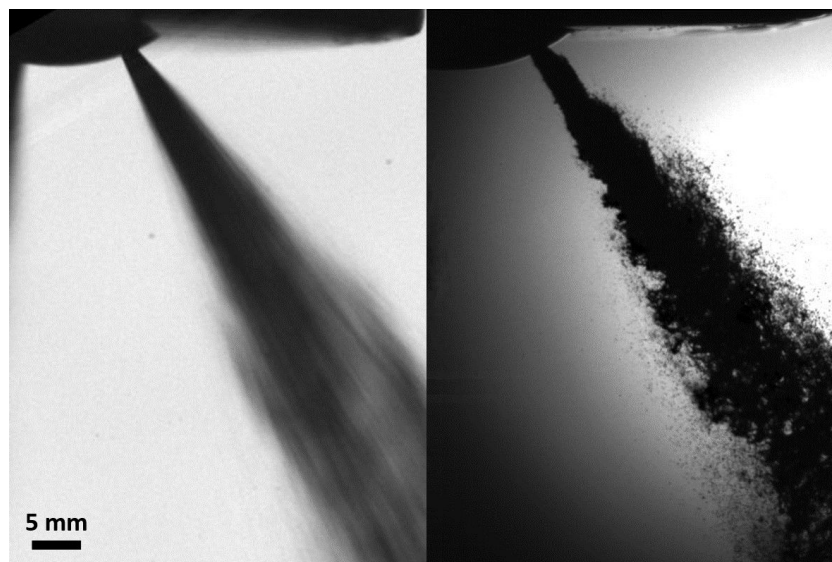


Figure 3.2: Two different histograms showing how to achieve a  $0.02 \text{ ms}$  exposure time. Top: Continuous light used with a "fast" shutter. Bottom: Pulsed light used with a "slow" shutter.

the left hand side (LED panel with exposure time of  $7.5 \mu\text{s}$ ) the droplets displacement during the exposure time, is too fast to freeze them. However, on the right hand side a laser pulses light during  $10 \text{ ns}$  allows the freezing of the flow. Droplets appear distinctly and local analysis can be performed. Both pictures are extracted from  $25000 \text{ fps}$  movies, and it highlights the difference of picture quality that can be made with the same camera. Finally, it is important to underline that depending on what one wants to analyse, the adaptation of the experimental set-up is necessary. For comparison of spray angle between injectors, a reflex camera with a LED panel would give very good results.



**Figure 3.3:** Close up shadowgraphy visualisation of 100 bar injection with two different light sources. Left: Continuous LED panel. Right: Pulsed Laser. Courtesy of Continental

### 3.3 RIM

The RIM method was already in use at Continental, however some modifications such as the use of an aluminium plate or a sapphire plate (as presented in the followings) have been made during the PhD thesis.

#### 3.3.1 Measurement principle

To visualise the wall film and its spreading, it is really helpful to observe it from below because of the large number of droplets impinging upon the plate. The impact of the spray on the plate generates a lot of droplets going in all directions. Hence, it is really complicated to perform a direct, non-invasive, observation of the liquid film generated by the spray (Figure 3.4).

The principle of the RIM method can be visualised on Figures 3.5 and 3.6.

The impingement plate is a 5mm-thick circular sanded quartz plate (Kirchheim optics) with a 60mm diameter. A circular aluminium holder has been designed to allow visualisation from the bottom of the plate. It also allows to fix a heating collar and, hence, heats the plate up to 250°C. The heating system is therefore composed of a

### 3. EXPERIMENTAL METHODS

---



Figure 3.4: GDI spray impinging upon a smooth plate. Fuel pressure is 100bar.

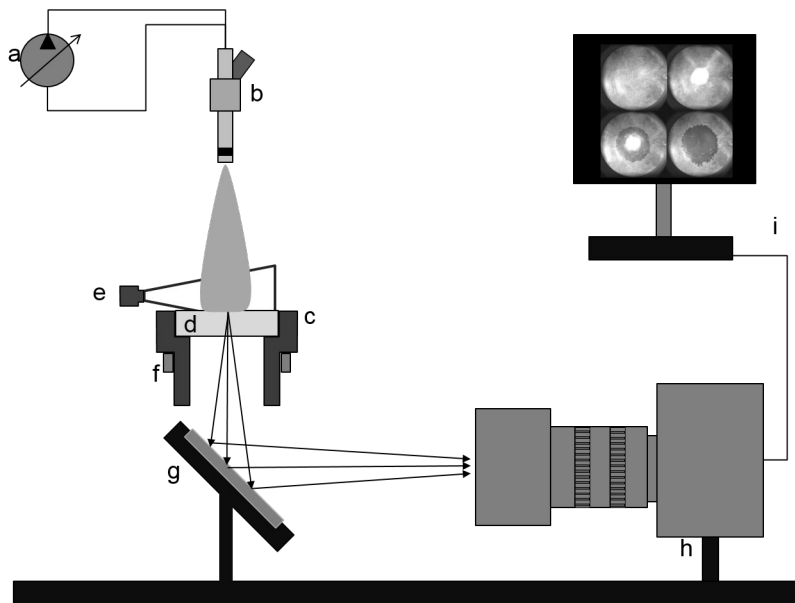
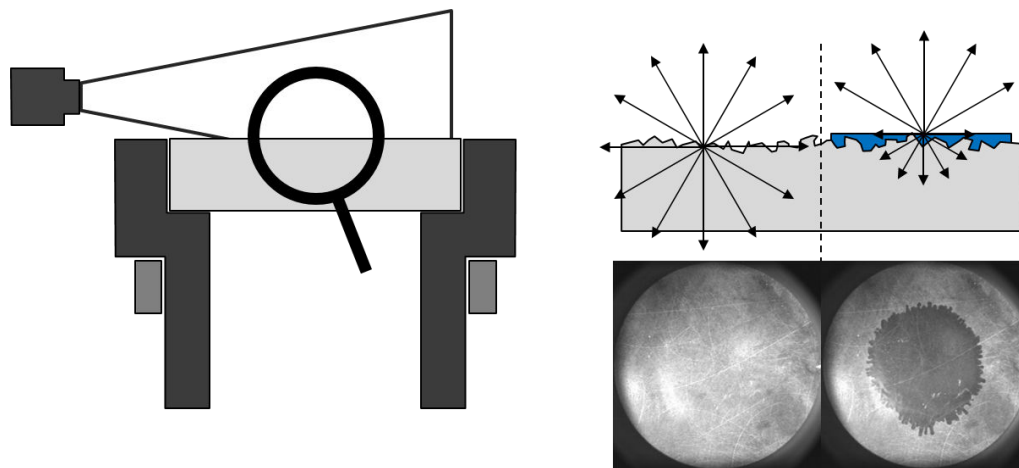


Figure 3.5: Sketch of the Refractive Index Matching experimental setup;  
a) High-pressure pump b) GDI injector c) Plate holder d) Impinging plate  
e) Light source f) Heating collar g) Mirror h) High-Speed Video camera i)  
Computer.

thermocouple, fixed on the element to heat, a PID controller and a heating collar. The accuracy of the system is  $0.5^{\circ}\text{C}$  and both the injector and the impingement plate can



**Figure 3.6:** Principle of RIM measurement. **Left:** Grazing Light illuminating a transparent plate; **Right:** Modification of light path caused by wetting

be heated independently at a specific temperature.

A fixation rail allows to support the plate holder and, in the same plan, a holder for a mirror. The mirror is tilted at  $45^\circ$  to redirect the light to the camera.

The High-Speed Videocamera is a Phantom V1210 with a CMOS sensor. The sample rate used is 20kHz, with an exposition time of  $10 \mu\text{s}$ . It is connected to a 60mm Nikon objective.

The RIM method is well described in [45, 54, 100]. A rough transparent plate is illuminated at grazing angle by an optical fibre connected to a LED spot. As liquid is filling the troughs on the impingement plate, the light ray paths are changed and the wetted surface transmits less light than the dry surface (Figure 3.6). The name of the method comes from the optical property of the quartz, its refractive index is close to the one of alkanes used in this experience. After a fine calibration of the measure (Section 3.3.3) the grey level can be linked to the thickness of the liquid film [18, 54]. Though this method has many advantages, and specially its cost, it has some defaults that will be presented in Section 3.3.4.

### 3.3.2 The impingement process observed with the RIM method

In order to understand the strengths of the method a complete description of the impingement process is proposed.

### 3. EXPERIMENTAL METHODS

---

Figure 3.7 displays the early stage of injection, first the tip of the spray plume is visualised. The white colour as mentioned before is due to Mie scattering. Once the spray tip impacts the plate, a white corona develops: it is the secondary spray that is propagating over the plate. If spatial and temporal resolution are high enough it is possible to track and study the secondary spray (Figure 3.8). The white corona that develops is not the liquid film, it is the front of the secondary spray flowing out of the impingement area.

Then the first droplets starts to wet the plate.

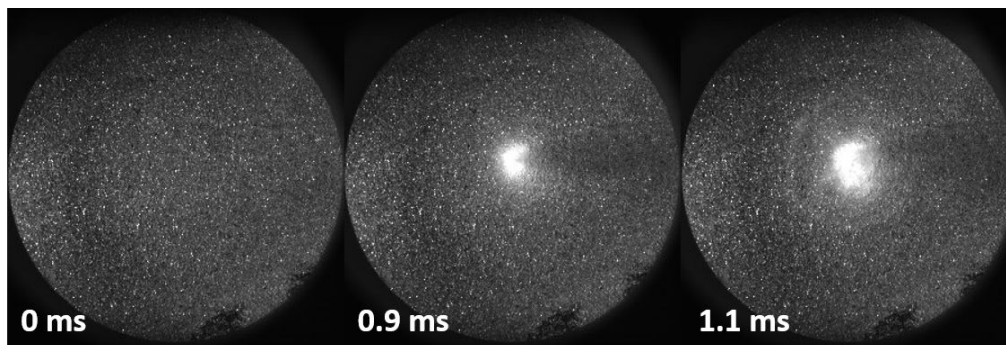


Figure 3.7: Early injection process of n-heptane at 200bar, injection duration 5ms, wall temperature  $25^{\circ}C$  . Left: Before spray impingement. Centre: Spray tip reaching the plate. Right: Secondary spray developing and starts of wetting.

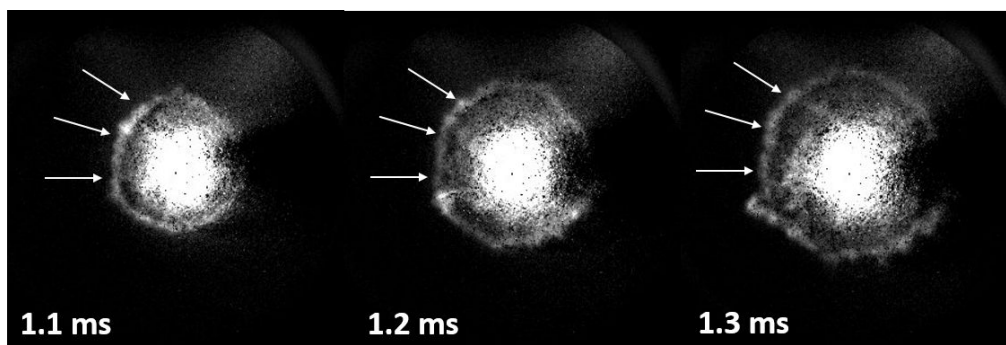
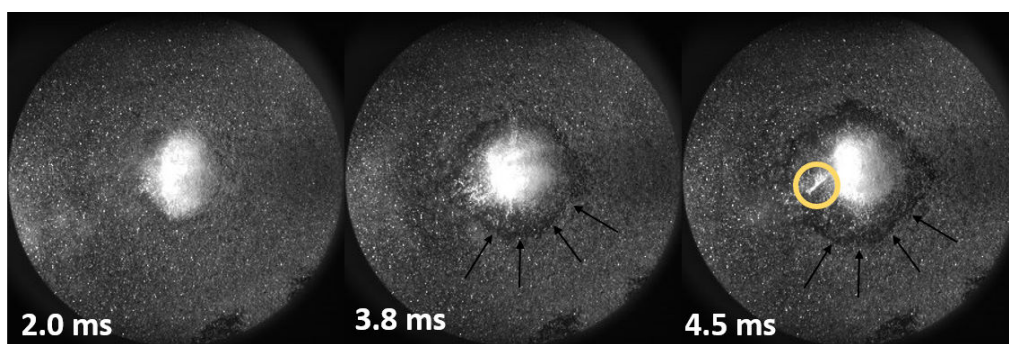


Figure 3.8: Background subtracted images of secondary spray propagation during injection process of n-heptane at 200bar, injection duration 5ms, wall temperature  $25^{\circ}C$  . White arrows highlights the secondary spray corona.

Figure 3.9 displays the spreading of the liquid film ( $0.7\text{ ms}$  later than Figure 3.8, the

secondary spray corona is already blown out the picture frame). After the first droplets have wetted the surface, the liquid film starts to spread. As the impingement area is messy due to spray Mie scattering, the edges of the liquid film are hard to observe. Though after some time (0.5 to 2 *ms* depending on the injection conditions) the liquid film clearly appears. It allows to track the edges, and also to observe some reatomised droplets flowing over the plate.



**Figure 3.9:** Steady state during injection process of n-heptane at 200bar, injection duration 5ms, wall temperature  $25^{\circ}C$ . Left: Mie scattering of the spray. Centre: Spreading phase. Right: Droplets reatomisation. Black arrows highlight the liquid film edge, yellow circle shows some droplets reatomisation.

Figure 3.10 shows the end of injection. Once the injection has stopped, the liquid film is still spreading and some droplets are still reaching the plate. It takes several milliseconds for all the droplets suspended in the air above the plate to get out of the field of view (either depositing or being blown out). After all the entrapped bubbles have disappeared, if the method has been correctly calibrated (see section 3.3.3) a global measure of the liquid film thickness can be performed. The spatial sensitivity of the method depends on three main parameters which are, the image resolution, the roughness levels and the filtering used during the post treatment.

### 3.3.3 Calibration of the RIM method

As stated before, if the method is used to get the film liquid thickness (and not only to track its edges), a calibration that links the grey levels to the thickness is necessary. We follow here the same procedure as in [18, 54, 100]. To do so, a known volume of liquid is deposited on the plate. Figure 3.11 illustrates the calibration process. A precision

### 3. EXPERIMENTAL METHODS

---

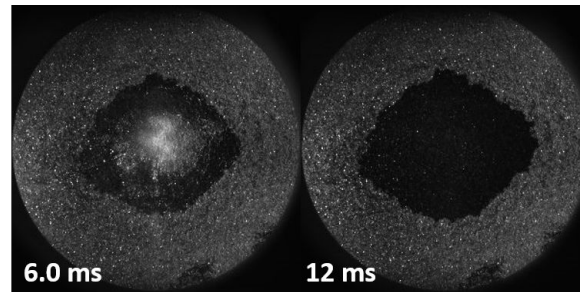


Figure 3.10: Late injection process of n-heptane at 200bar, injection duration 5ms, wall temperature 25°. Left: Late droplets reaching the plate (white area in the middle of the liquid film). Right: After injection process.

pipette from Eppendorf suited for biology work is used. The area together with the grey level is measured and as the volume is known, it gives one calibration point. This is performed with several volumes and different concentration mixtures.

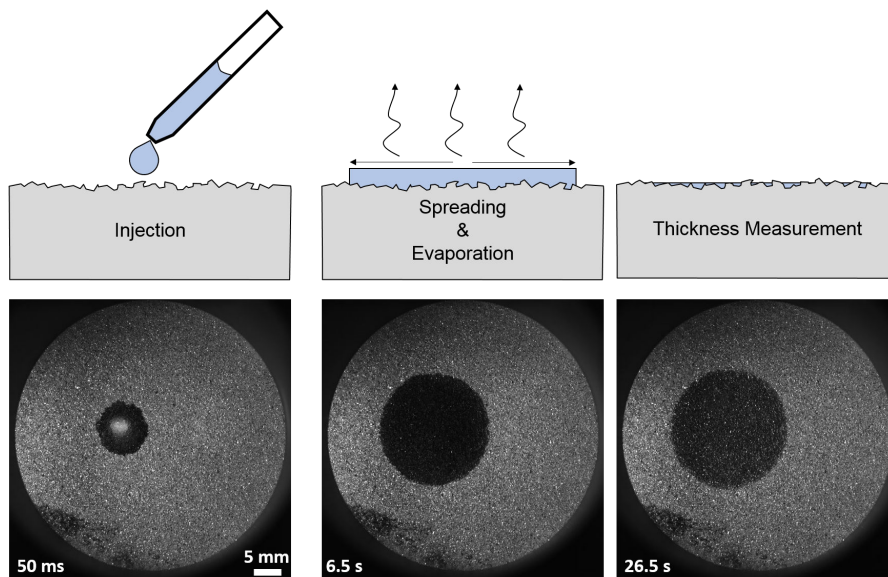


Figure 3.11: Calibration process of RIM method.

The fuel used is a mix of n-heptane and n-dodecane, ranging from 5% (vol/vol) of n-dodecane up to 60% (vol/vol). n-Heptane is used to help the n-dodecane to spread properly. Indeed, due to its surface tension, pure n-dodecane takes a lot of time to spread (in Chapter 4 the effect of fuel surface tension will be neglected, as the time



scale of the events are dozens of milliseconds and during this time surface tension effect are not significant). Figure 3.12 shows how a calibration point is obtained. Repeating the same process with different concentrations of n-dodecane and different injected volumes allows to generate a calibration curve (Figure 3.13).

To obtain a calibration point, one must wait for the n-heptane to vaporise completely. Considering that the n-dodecane does not vaporise in cold conditions (i.e.  $T_w = 20^\circ C$  and  $T_{amb} = 20^\circ C$ ), when the n-heptane has disappeared, the grey level is only due to the presence of n-dodecane. It can be written that:

$$\Omega = A e, \quad (3.1)$$

hence as the volume  $\Omega$  is known and the area  $A$  is measured, the thickness  $e$  of the liquid film can be linked to the mean grey level of the spot. Which is added on the calibration curve. The deviation from a constant area and grey level at long times (see Figure 3.12) is not due to vaporisation but to film spreading that lasts for a very long time because of gravity.

The normalised grey level (Eq. 3.2) presented in Figures 3.12 and 3.13, is obtained by subtracting the background (first image of the movie  $B$ ) to the image  $I$ . Dividing by the background. It allows to keep the image levels  $v$  between 0 and 1 for convenience purpose, in particular dividing by the background dampen some of the inhomogeneities. However, as float numbers are used it becomes heavier to manipulate. For a 12-bit camera,  $I \in \llbracket 0, 4095 \rrbracket$  and  $B \in \llbracket 0, 4095 \rrbracket$ , which gives  $v \in [0, 1]$ :

$$v = \frac{B - I}{B} \quad (3.2)$$

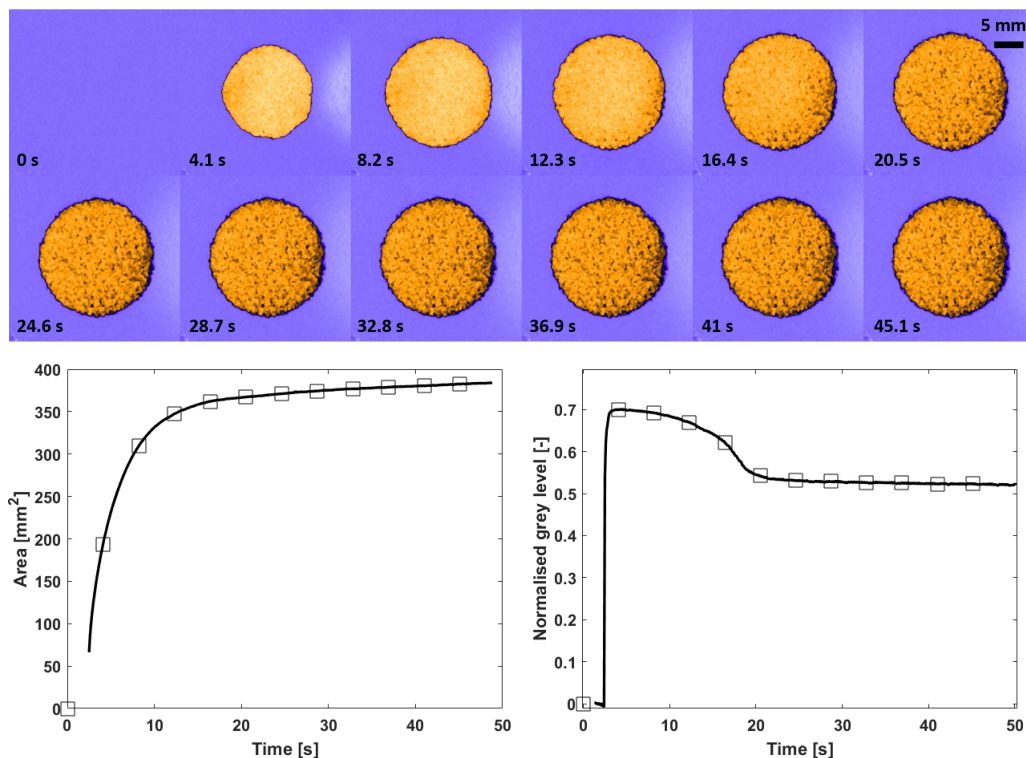
Once the calibration points are all performed and post processed an exponential fit is used to get a continuous calibration law of the form:

$$e = a \exp(b v) \quad (3.3)$$

where  $e$  is the liquid film thickness,  $v$  is the pixel normalised value and  $a$  and  $b$  are fitting constants. Different fitting functions are used in [54, 100] for the calibration law.

On Figure 3.13, two calibration curves are displayed: two different positions of injector were used (as presented Figure 3.28). The angle between the centre of the spray and the plate is changed, however the spray travelling distance is kept constant.

### 3. EXPERIMENTAL METHODS



**Figure 3.12: Calibration process for RIM measurement. Injection of  $4\mu L$  of 20% dodecane fuel. Top: Liquid film evolution. Left: Area evolution with respect to time. Right: Evolution of liquid film grey level.**

The reason for these differences is because the injector body (and its holder) reflects a part of the light towards the plate. When the injector position is changed, the plate lighting also changes and must be taken into account, hence a new calibration is needed. The difference between the grey level and the associated thickness is important. For a normalised grey level of 0.8, the film thickness is  $5.10\ \mu m$  on  $90^\circ$  whereas it corresponds to a thickness of  $8.6\ \mu m$  when the injector is positioned for a  $60^\circ$  impingement. Due to these non negligible differences, because of the exponential fit of the curve (even when working with normalised grey levels), it is necessary to perform a new calibration when a device is added or moved on the experimental set-up. It is advised to be careful when touching at the experimental set-up, because performing a new calibration is time consuming.

The plate used for the RIM measurements together with the plate use in the RIM Alu method (Section 3.3.6) have been characterised by Giacomo Piccinni using an

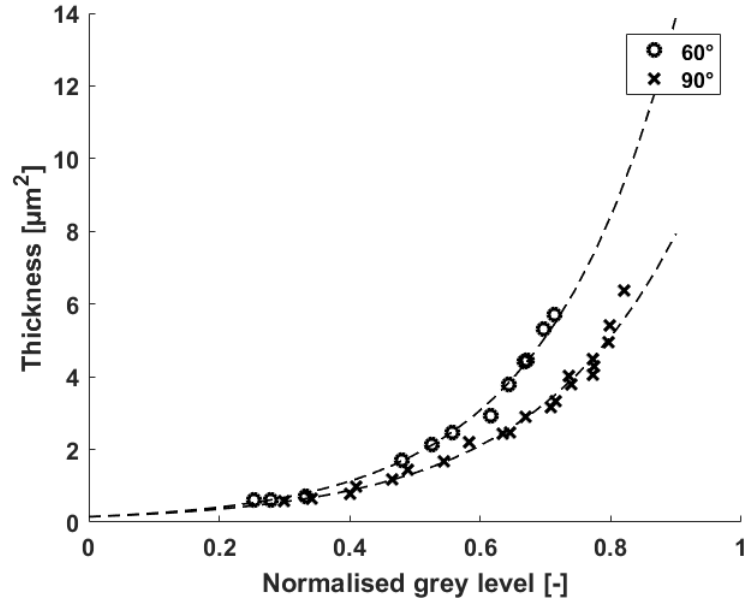


Figure 3.13: Calibration curves for two different impingement angle

ALICONA profilometer. The statistics of the plate roughness are summarised in Table 3.1:

	Quartz 1	Quartz 2	Alu 1	Alu 2	Alu 3
Ra [ $\mu m$ ]	6.77	20.22	5.42	11.51	16.28
Rq [ $\mu m$ ]	8.45	24.36	6.86	14.66	20.59
Rp [ $\mu m$ ]	30.09	52.50	41.02	63.06	71.66
Rv [ $\mu m$ ]	-36.75	-71.29	-44.46	-64.23	-82.65
Rt [ $\mu m$ ]	66.84	123.79	85.48	127.3	154.3

Table 3.1: Amplitude parameter of plate roughness used in the different experimental methods. The arithmetical mean deviation  $R_a$ , the profile root mean square  $R_q$ , the maximum peak height  $R_p$ , the maximum valley depth  $R_v$  and the maximum height of the profile  $R_t$  are common description parameters used to characterise surface roughness.

### 3. EXPERIMENTAL METHODS

---

#### 3.3.4 On the drawbacks and limits of the RIM method

The RIM method present many advantages presented in Section 3.3.2, and specially its cost which is small compared to other methods. A rough estimation of the cost is 3 to 5 k€ it comprises a camera, a light source, an optical guide, some supports to holds the different devices, a mirror and the sanded quartz plate. Using a reflex camera is sufficient to get instantaneous records of the liquid film, though a high speed video camera can be used (increasing tremendously the cost of the method). It has some drawbacks that will be addressed below. Most of authors have stressed on the advantages without mentioning the difficulties that could arise when applying the method.

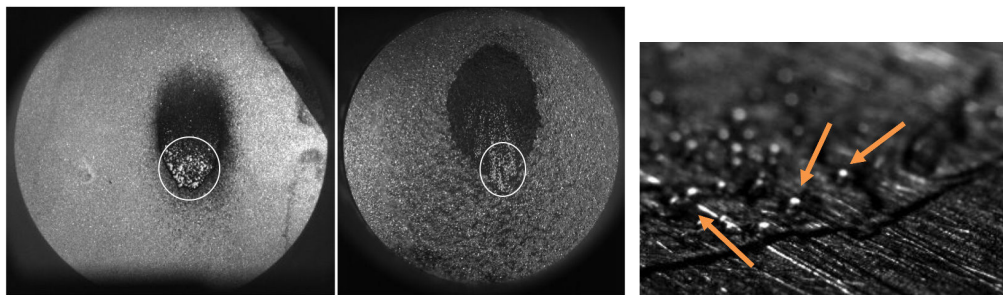
The first drawback is not directly due to the method itself but to the material used to perform the index matching. Typical refractive index values for alkanes used with this method are ranging between 1.38 and 1.41. In order to match these refractive indices, a common choice is to use Quartz (Fused Silica), with a refractive index around 1.47 for white light wavelengths. Although it gives excellent results and good grey level contrast when wetted, the differences between thermal properties of quartz and metals used to produce engines are very different. Heat conductivity of Fused Silica is  $1.38 \text{ W/m.K}$ . For Aluminium it is between 100 and  $300 \text{ W/m.K}$ , around  $50 \text{ W/m.K}$  for Steel and  $80 \text{ W/m.K}$  for Iron. Usually automotive engine are made out of aluminium for the piston and the cylinder head, the cylinder can be in steel.

Thanks to the good contrast provided by the method, tracking the edge of the liquid film after the end of injection is really convenient (useful to get the liquid film lifetime). However, as the heat transfer are much smaller for the quartz than for the aluminium, the liquid film lifetime is not relevant of what could be measured in an engine. Questions also arise on the capacity of the quartz to locally maintain the prescribed heat while the liquid film is spreading, and particularly under hot conditions.

When working with a hot plate another issue can be encountered: if the temperature of the wall is higher than the saturation temperature of the fuel, boiling occurs. The formation of vapour bubbles is modifying the light path and bright zones appear (Figure 3.14). These bright areas locally change the grey level, as explained before, grey level is linked via the calibration to film thickness. In other words, when bubbles are present, the calibration is no longer valid. It is worth to note that depending on the camera resolution and the wall temperatures, bubbles may not appear clearly, but they still

exist and deviate the ray paths. Hence, in any case, film thickness is probably strongly underestimated and calibration is not valid anymore.

The same issue is encountered during the injection process, even in cold cases. Indeed for some injection conditions, some air bubbles are entrapped between the quartz and the liquid film (Figure 3.14). It also leads to the apparition of bright spots. Therefore, one needs to wait for these bubbles to vanish to perform the thickness measurement. The time needed for the method to converge to a "coherent" grey level will later be called the convergence time of the method. The term coherent is used here to illustrate the fact that not all the grey level is transferable to fuel film thickness when bubbles are entrapped. This is also the case when, at the end of injection, a cloud of droplets is still present above the plate, they are often referred as late or re-depositing droplets in papers [52]. However, more than their mass contribution to the liquid film, it is Mie scattering that they induce, which disturbs the measure.



**Figure 3.14:** Left: Boiling bubbles developing in the liquid film. Middle: Entrapped bubbles during injection process. Right: Direct visualisation of liquid film surface soon after the end of injection. Arrows indicate bubbles.

This convergence time can be quite long compared to the injection time. If the user of the method wants to know precisely the film thickness at the end of injection, it is likely that the values will be underestimated, due to the previously addressed issues. Results presented in Section 4.3 shows a convergence time of 1 to 4 seconds before being able to perform a mass evaluation.

Another issue that has been discussed by [18] is the saturation of the method. Figure 3.13 shows that the thickness is growing exponentially with respect to the normalised grey level. When the liquid film becomes too thick, the material is saturated, and the method is no longer sensitive to change in thickness. For an aluminium plate (method

### 3. EXPERIMENTAL METHODS

---

discussed later in Section 3.3.6) the value as previously been characterised in [30] and it is around 30% of the Roughness level  $R_a$  (arithmetical mean deviation of the assessed profile) of the material. In the case of quartz this value seems closer to 50% of the  $R_a$ .

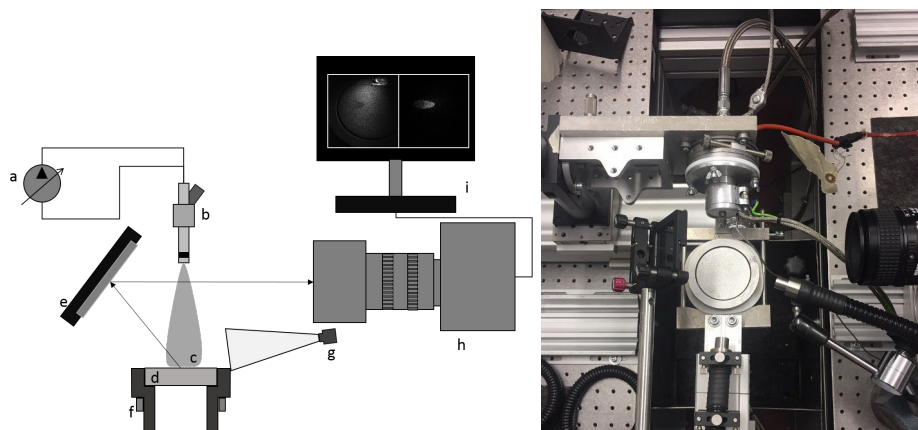
#### 3.3.5 RIM method with Sapphire

It has been mentioned before that the thermal conductivity of the quartz is one of the default of the method. To circumvent this, a sapphire plate can be used. Its thermal conductivity is around  $23 W/m.K$  which is 15 times higher than quartz and 2 to 8 times less than metals presented before. However as the sapphire is much harder than quartz, it is difficult to sand it to the desired roughness. A smooth plate is then used: it is sanded in order to perform liquid film visualisation but the roughness level is less than  $1 \mu m$ . Hence, the method is no longer capable of thickness measurement as liquid film thickness (5 to  $20 \mu m$ ) is bigger than roughness level. It also allows to eliminate the wall roughness as an influencing factor for film spreading. The characterisation of the sapphire roughness has been performed with the help of an Atomic Force Microscope and is presented in Section 3.7.

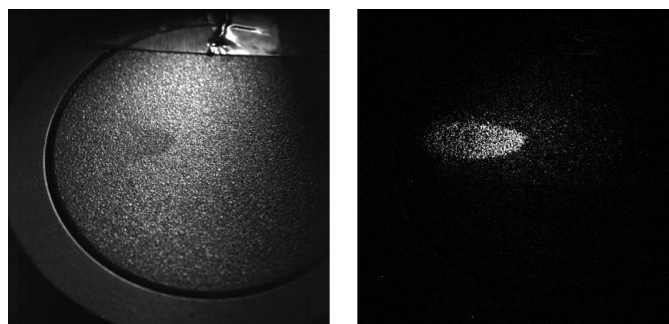
#### 3.3.6 RIM method with Aluminium

A last modification of the RIM method will be presented. This method will be called RIM Alu in the following. The experimental set-up is almost the same, but the quartz plate is replaced by a aluminium rough plate. The position of the mirror is no longer the same as light does not go through aluminium. For contrast and film visualisation the optical fibre position is also modified. Figure 3.15 shows the modification brought to the experimental set-up.

This method as been developed by [96], and the principal advantage of the method is that the heat transfer is now correctly addressed. The metal (i.e. aluminium) used in the engines can be used in the experimental set-up, and it will allow to reproduce the heat transfer experienced in an engine. In theory this method is also calibratable, as mentioned before and thickness lower than 30% of the  $R_a$  can be measured. However, this calibration has not been performed in this work. Figure 3.16 shows how is visualised the liquid film on the aluminium plate. It highlights the fact that background subtraction greatly increases the visualisation of the liquid film.



**Figure 3.15:** RIM Alu set-up. Left: a) High-pressure pump b) GDI injector c) High-pressure spray d) Aluminium plate e) Mirror f) Plate holder g) Light source h) High-Speed Video camera i) Camera. Right: Picture of the experimental set-up.



**Figure 3.16:** Visualisation of liquid film with RIM Alu method. Left: Raw image of liquid film. Right: Background subtracted image of the liquid film.

Though this method is not using the "Index Matching" properties, as the working principle and the core of the method is the same. To summarise, three different types of plates were used to perform RIM visualisation, Figure 3.17 shows the three plates together.

### 3. EXPERIMENTAL METHODS

---

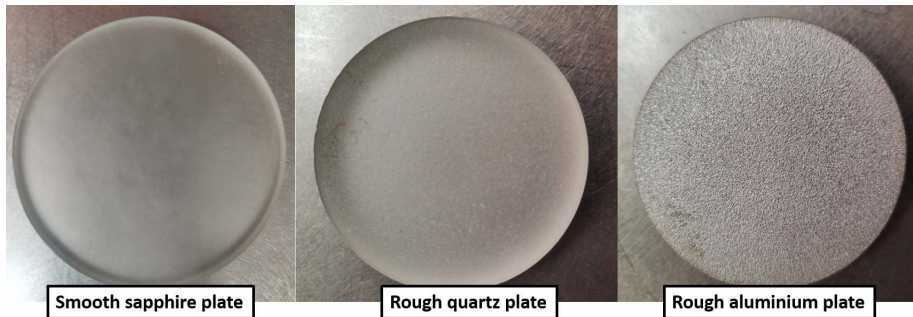


Figure 3.17: Top visualisation of impingement plates used to perform RIM methods.

#### 3.4 Fast Thermocouple Measurement Plate

The fast thermocouple measurement set-up is divided in four different parts, which are:

- The instrumented plate
- The zero degree correction device
- The amplification system
- The acquisition system

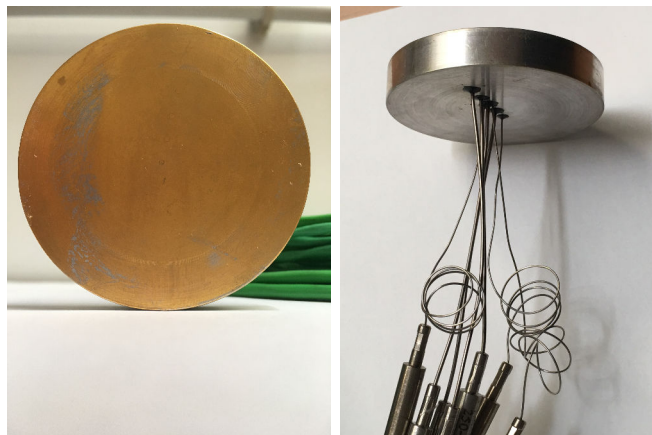


Figure 3.18: Left: Top view of the instrumented plate with gold coating. Right: Side view of the instrumented plate with apparent thermocouples.

The instrumented plate is a 60 *mm* diameter and 10 *mm* thick aluminum plate inserted with 7 type-K thermocouples. Four of them are surface thermocouples with



### 3.4 Fast Thermocouple Measurement Plate

fast response time. Holes were drilled in the plate, and thermocouples were inserted. The end of the probes were cut, so that the surface of the thermocouple is flush with the plate. A thin gold layer is deposited on top of the surface in order to ensure the hot junction of the thermocouples (see Figure 3.18). The plate has been build-up by the University of Rostock in Germany. The three other thermocouples are inserted one at 5 mm and two at 0.1 mm below the surface of the plate, and they have a slower response time. The three slower thermocouples were not exploited, their use was only to ensure the plate is at the set temperature. The position of the thermocouples can be seen on Figure 3.19 and 3.20.

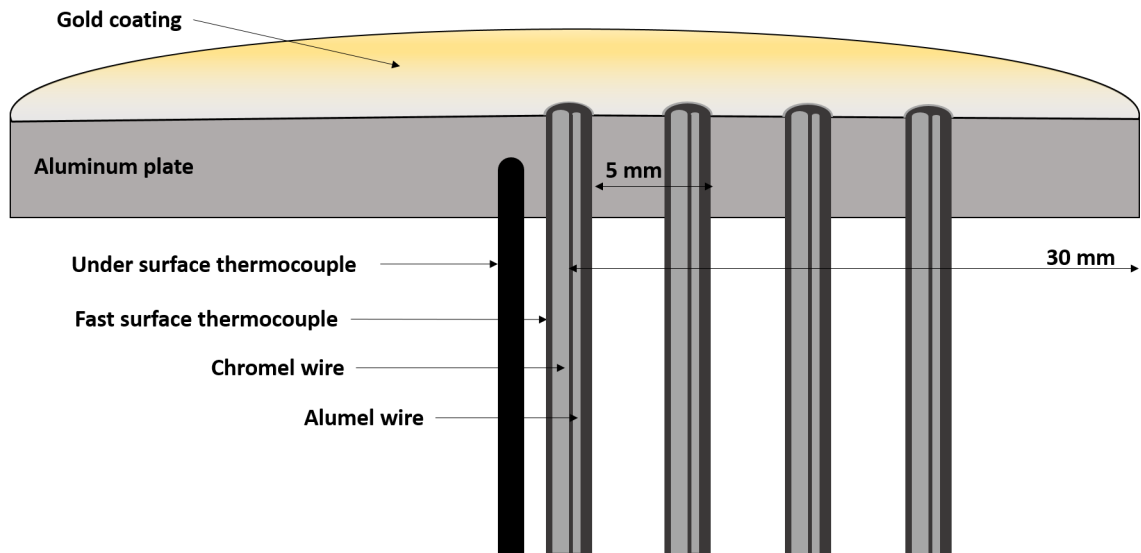


Figure 3.19: Side cut of the thermo-instrumented plate.

Thermocouples are made by the association of two different metals, at the junction of the metals a current is generated with a certain voltage (few  $mV$ ), due to Seebeck effect [87] (Figure 3.21). Each couple of metals gives a different potential for a given temperature (choosing the right couple helps to get more temperature sensitivity for a given study). However, when trying to connect the thermocouple to an acquisition system, copper wires are generally used. At the two ends of the thermocouple (i.e. Metal 1/Copper and Metal 2/Copper), two new couples of metal are therefore created, with new potential generations. The junction used to measure the temperature (Metal 1/Metal 2) is called the hot junction, whereas these two new junctions

### 3. EXPERIMENTAL METHODS

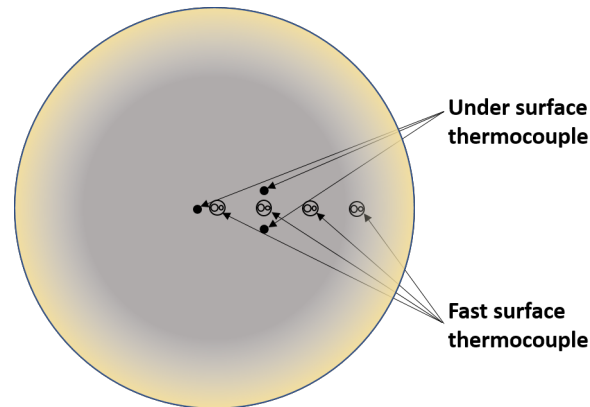


Figure 3.20: Top view of the instrumented plate.

(Metal 1-2/Copper) are called the cold junctions. In order to get accurate results, a compensation of the cold junctions needs to be performed.

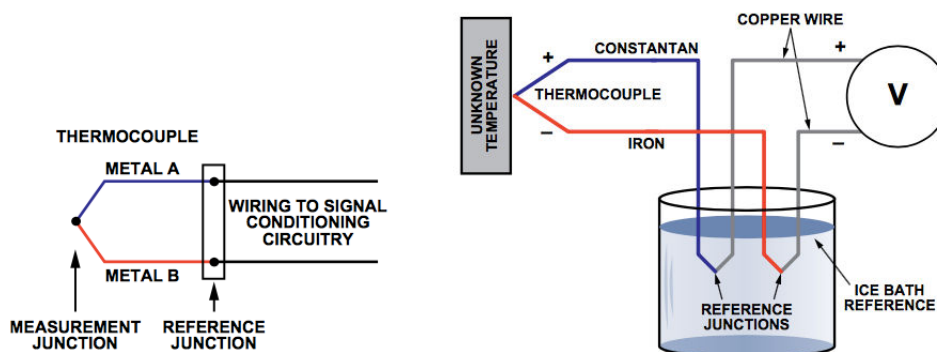


Figure 3.21: Left: Working principle of thermocouple. Right: Working principle of zero degree compensation in the case of iron-constantan couple [19].

Several techniques exist and are presented in [19]. In this experiment the zero degree compensation has been chosen. The method is rather simple, the two cold junctions (Chromel/Copper and Alumel/Copper for a type-K thermocouple) are placed in a ice bath (at  $0\text{ }^{\circ}\text{C}$ ). As the potential generated by the cold junctions is zero at  $0\text{ }^{\circ}\text{C}$ , it allows to read via copper wires the potential associated to the measured temperature (Figure 3.21). The main drawback of this method is the difficulty to maintain water at  $0\text{ }^{\circ}\text{C}$  all the time. So, in this experiment, the zero degree compensation is composed by a OMEGA-TRCIII ice point Calibration Reference Chamber which ensures that

6 wells suited for the insertion of Temperature reference probes (which contains the two cold junctions) are maintained at exactly  $0\text{ }^{\circ}\text{C}$  (freezing temperature of distilled deionised water at atmospheric pressure). Two OMEGA-TRCIII ice points were used in order to cool the 7 thermocouples.

As the signal is travelling through copper wire an amplification is performed. It allows to reduce the signal to noise ratio. Moreover, as the signal is multiplied by 100, it helps neglecting the Seebeck effect that could occur with other metal/metal junction in the acquisition line.

The amplification system consists in an OMEGA-OM5-BP-16-C backpanel, together with OMEGA-OM5-WMV-50A-C analog voltage input modules. The backpanel is a circuit board, where different modules can be plugged. The OMEGA-OM5-WMV-50A-C is converting the  $-50$  to  $+50\text{ mV}$  input signal to a  $-5$  to  $+5\text{ V}$  output signal. A type-K thermocouple generates a current of  $-6.458\text{ mV}$  at  $-270\text{ }^{\circ}\text{C}$  and  $54.886\text{ mV}$  at  $1373\text{ }^{\circ}\text{C}$ . These values are amplified thanks to the voltage modules. It allows to measure temperature ranging between  $-270$  and  $1233\text{ }^{\circ}\text{C}$ . The signal is then transmitted to an acquisition system.

The backpanel is powered by a  $5\text{ V}$  DC power unit. The signals can be read after passing through a break-out box. Everything has been embedded in a box in order to simplify the connecting and the use of the device. This experimental device is used to measure temperature ranging between  $20$  to  $400\text{ }^{\circ}\text{C}$ . Consequently the temperature range provided by the method is wide enough (cf Figure 3.22) as the plate will not be heated higher than  $200\text{ }^{\circ}\text{C}$ .

Various acquisition systems and interfaces can be used, in this case an ETAS-ES 1000 has been chosen, because it allows to record up to 16 signals at a frequency of  $10\text{ kHz}$  (see Figure 3.23). Another argument is that it is a system commonly used in the automotive industry for the vehicle measurements, hence available at Continental. It is necessary to use this acquisition system with the software ETAS-INCA developed by ETAS.

### 3.5 X and Y translation

An issue experienced while using the thermocouple plate was the spatial discretisation offered by the thermocouples. Indeed, the impingement area of the spray is hardly more

### 3. EXPERIMENTAL METHODS

---



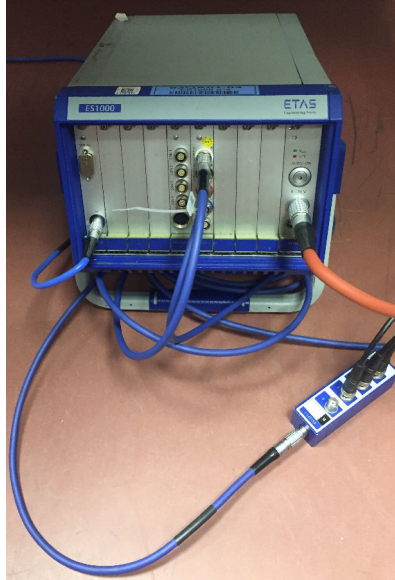
**Figure 3.22:** Top Left: Overview of the amplification system, in green the back-panel, in blue the amplification modules. Top Right: Break-out box. Bottom Left: Exit panel with BNC connections. Bottom Right: 5 V Power unit.

than a circle of 1 *cm* of diameter. As each thermocouple is separated by 5 *mm* from its neighbour the discretisation is not satisfying enough. To circumvent the problem, two translation plates were screwed on the pillar that holds the thermocouple plate. It allows to have a micrometric precision in two dimensions (the resolution aimed is millimetric, however it is possible to perform a better discretisation). The measures are then reassembled in order to generate 2-D temperature maps. Figure 3.24 shows the translation plates, used to perform the 2D measurement.

### 3.6 Interferometric Measurement Device

The interferometric measurement device is an optical point sensor that comes together with a controller. It is developed by STIL S.A, the optical sensor (referred as optical pen in the following) is linked to the sensor by an optical fibre. It guides the light from a halogen lamp in the controller to the optical pen. Several pens can be used with the

### 3.6 Interferometric Measurement Device



**Figure 3.23:** ETAS-ES 1000 used as acquisition surface for thermocouple signals.



**Figure 3.24:** Translation plate used to displace the thermocouple plate. Manual linear stage NEWPORT M-UMR 8.51.

same controller. However, in this work, only the OPILB is used. It allows to measure thickness of transparent medium between  $0.4$  and  $90 \mu m$ . Table 3.2 recapitulates the characteristics of the optical pen.

The working distance of  $42 \text{ mm}$  needs to be kept constant, the spot size (light point where the measure is performed) is  $32 \mu m$  in diameter. A working angle between the

### 3. EXPERIMENTAL METHODS

	Working distance [mm]	Max Slope [°]	Spot diameter [ $\mu m$ ]	Min thick. [ $\mu m$ ]	Max thick. [ $\mu m$ ]
OPILB	42	5.2	32	0.4	90

Table 3.2: Optical pen measurement characteristics. STIL S.A.

light beam and the measured sample needs to be kept lower than  $5.4^\circ$ , to ensure enough light is collected back in the sensor (Figure 3.25).

Two methods are combined in the interferometric device: Confocal Imaging and Spectroscopic Analysis of White Light Interferogram (SAWLI [82]). The difference of optical path between the two surfaces of the sample (i.e. the air/fuel and fuel/aluminum interfaces) generates interferences. A spectral analysis of the interferogram is made after passing through a pinhole that acts as a spatial filter (Figure 3.25). The analysis gives access to the thickness of the liquid film between the two interfaces.

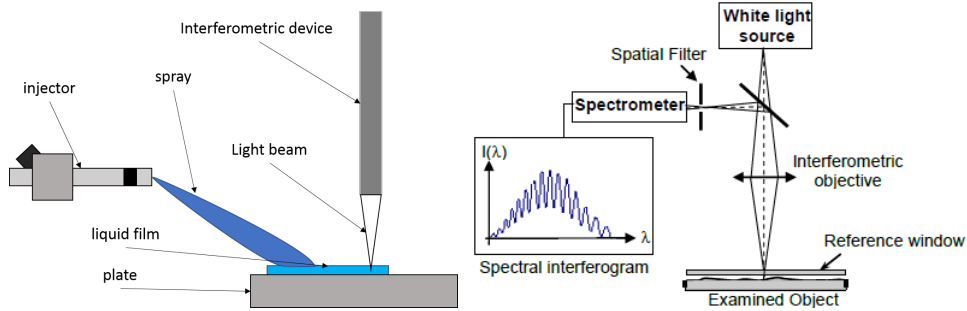


Figure 3.25: Left: Positioning of optical pen for film thickness measurement. Right: Measurement principle of confocal interferometric device. Here the device measures the distance between a plate and a sample not the thickness of a liquid film (STIL-DUO user manual).

The quality of the results mainly depends on the ability to maintain the optical pen as orthogonal as possible to the measured surface. The light being emitted and collected by the same device (confocal) together with the constraint imposed by interferences are responsible of this necessity of orthogonality. The reflectivity of the observed surface also plays a role in the quality of the measurement, a metallic plate reflects more light than a quartz plate to the sensor. The controller allows to modify the sample rate from  $1\text{ Hz}$  to  $1000\text{ Hz}$ , however depending on the light collected the highest frequency might not be used. This device is meant to be used with a translation plate, that will

ensure orthogonality while moving. However here only a holder places the optical pen on top of the measured liquid film and orthogonality is yet not perfect. Also due to the working conditions (unsteady liquid films, rough plate, vapour generation in hot conditions) the signal gets noisier and quality is too poor below  $3 \mu m$ .

### 3.7 Atomic Force Microscopy

In order to characterise the roughness of the sapphire plate (using finger touch tells that it is  $\leq 2\mu m$  of average roughness) an Atomic Force Microscope (AFM) present at the Institutue of Fluid Mechanics of Toulouse (IMFT) facility has been used. Using a probe placed at the very end of a cantilever, it is possible to record the vertical microscopic motion of the probe with a great accuracy. Then a height map or profile of the scanned zone can be generated. During this campaign the JPK NanoWizards AFM has been used and 15 linear samples have been scanned (back and forth). The collected data together with their statistics are displayed in Table 3.3. Figure 3.26 shows two different visualisation of two sampled profiles. The first (Top) visualisation shows the local variation of the sample height, however the second (Bottom) shows the variation with the same scale for  $x$  and  $y$  axes. It highlights the fact that though the surface seems very un-even, it is in fact very flat and smooth at a millimetric scale.

<b>Sapphire plate</b>	$R_a[\mu m]$	$R_p[\mu m]$	$R_v[\mu m]$	$R_t[\mu m]$
Roughness	0.43	11.2	4.80	6.4

**Table 3.3: Roughness parameters obtained with an AFM microscope on the sapphire plate**

The average roughness  $R_a$  of  $0.43\mu m$  is small compared to the liquid films studied later ( $> 5\mu m$ ), hence the sapphire plate will be called "smooth sapphire plate" in the following, specially in comparison with the quartz and aluminium plates presented in Table 3.1.

### 3. EXPERIMENTAL METHODS

---

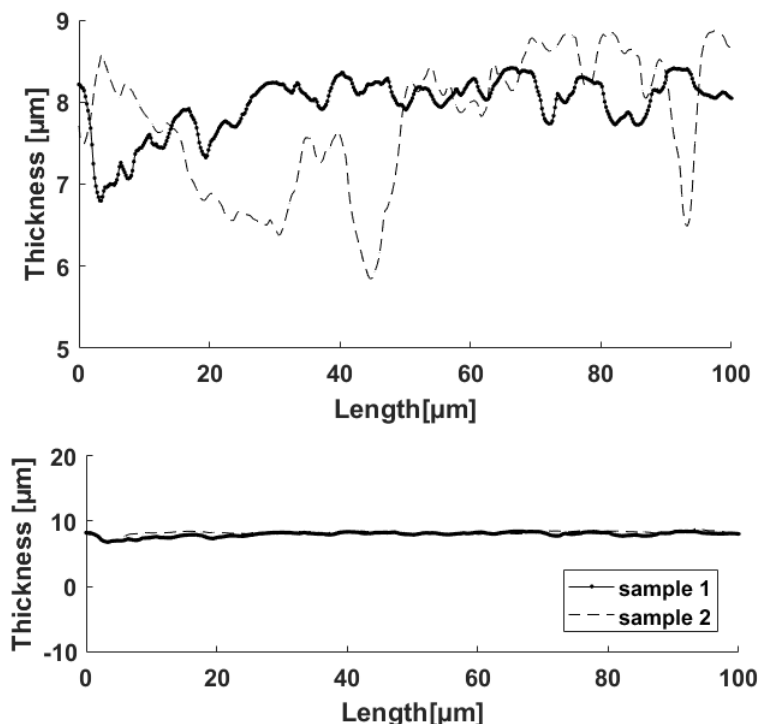


Figure 3.26: Two different visualisations of profiles sampled with AFM. Top: Zoom on sapphire trough and crest. Bottom: Same horizontal and vertical scales. The thickness presented here, is a height variation in relatively to the position of the probe.

### 3.8 Injector Position

In the engine the injector is inserted in the cylinder head and does not move at all, however, has several holes are generally drilled and the piston is moving the variability of spray to wall distance and angle is quite large. In order to cope with the different experimental set-ups presented earlier, it is necessary to be able to move the injector accurately. To do so two translations and three rotations plates are used and they allow to position the injector correctly in three dimensions, and to align the spray plume with the plate. Figure 3.27 shows the material used. In the rest of the work a convention for the angle of impingement will be adopted, it is described in Figure 3.28. When the spray impacts the plate orthogonally the angle is set at  $90^\circ$  and when the injector is positioned horizontally the angle between the plume axis and the plate is  $30^\circ$ . This



### 3.8 Injector Position

range of angle is representative of what can be encountered in real engine either for piston or cylinder impingement.

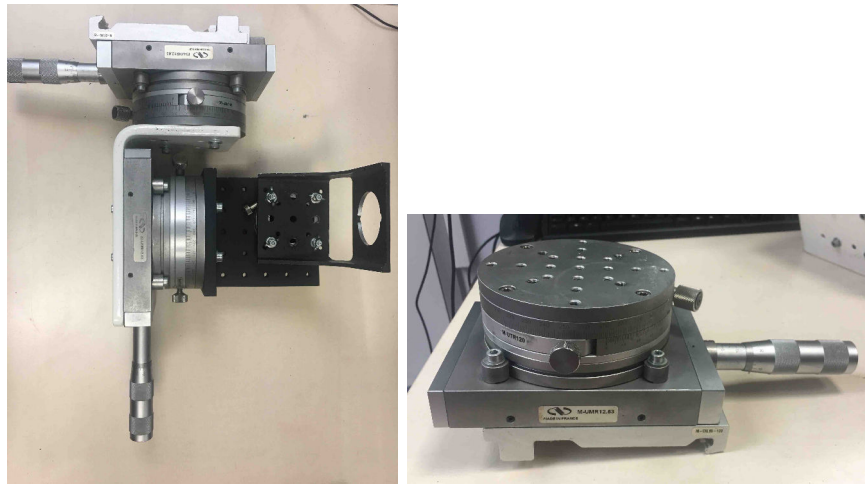


Figure 3.27: Translation and rotation plate allowing the correct positioning of the injector. NEWPORT M-UMR12.63 and M-UTR120 material

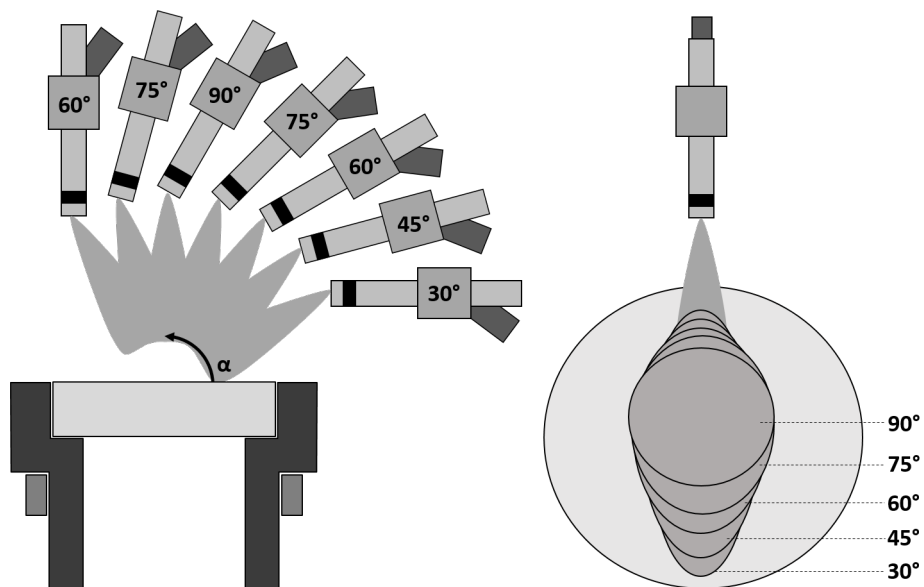


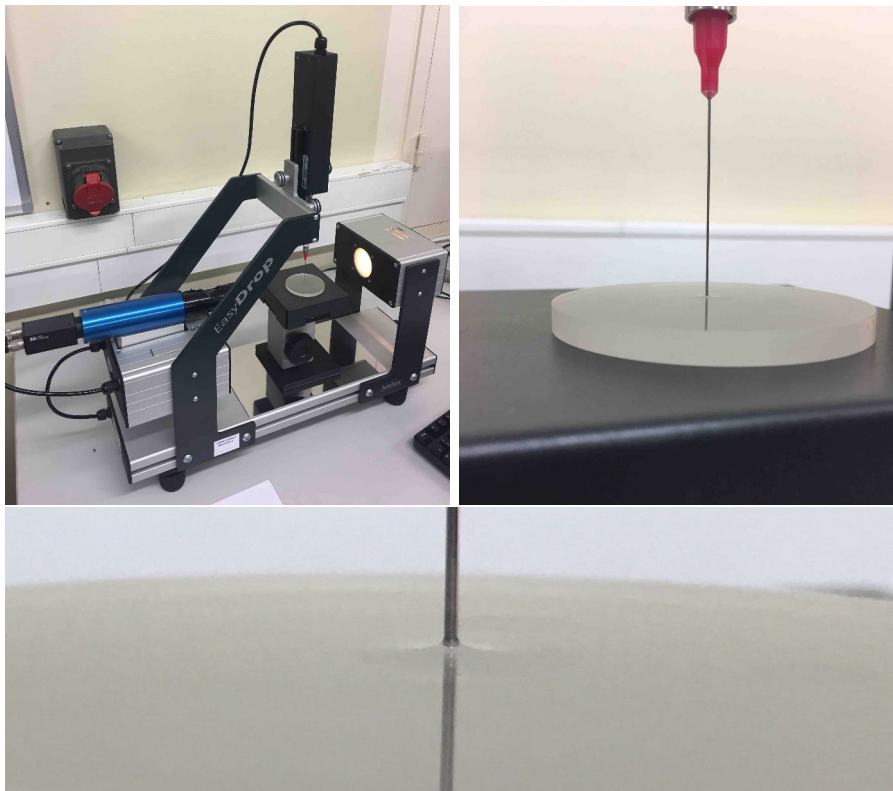
Figure 3.28: Left: Side vision of the impingement angle definition. Right: Top vision of the impingement angle definition.

### 3. EXPERIMENTAL METHODS

---

#### 3.9 Goniometry

In order to check the advancing and receding angles between decane and sapphire a goniometer has been used at the IMFT. Figure 3.29 displays the experimental set-up. A syringe is used to deposit a decane drop on the plate. Then using a microscopic lens, a camera is recording the angle during the spreading of the decane drop (moving the syringe piston drives the drop either in the advancing or receding regime). For the couple decane/sapphire the angle were found to be  $\theta_a = 11 \pm 2^\circ$  and  $\theta_r = 3 \pm 2^\circ$  for the advancing and receding angles respectively.



**Figure 3.29:** Goniometer set-up for the advancing and receding angles of n-decane on a sapphire plate.

#### Conclusion

All the experimental set-ups used in this work have been presented in this chapter. The fuel preparation system is common for all the experiments as it is necessary to

pressurise the fuel in the injector and hence to produce the spray. The RIM method and its derivatives are non intrusive methods used to observe the liquid film and/or measure its thickness. The fast thermocouple measurement plate gives information about the heat transfer, and the temperature profile on the wall surface. The interferometric measurement device developed by STIL allows to have a local evolution of the liquid film thickness during the evaporation process. Altogether these methods help to have a global macroscopic description of the impingement process.

One of the main difficulties encountered while working with the experimental set-ups is the availability of the material and the room. Indeed, as the experimental facility was provided by Continental Automotive and some other (sometimes unexpected) campaigns ordered by or for customers (internal or external) had often to be performed as a priority. Depending on the schedules, some parts of the set-ups were not available, delaying or shortening the planned campaigns of the present PhD thesis. Moreover, it happened during the post-processing that some data were eventually missing (by mistake, or by the desire to explore further in one direction / increase a database). Unfortunately, once a given set-up has been disassembled, it was sometimes very complicated to reproduce exactly the same experimental set-up. For all these reasons, the data presented in the following may sometimes appear mismatched, as some expectations have evolved during the three years of the PhD thesis and the final decision was rather to share results from complete campaigns in this document.

### 3. EXPERIMENTAL METHODS

---

# 4

## Liquid Film Spreading

### Contents

---

<b>1.1</b>	<b>General Context . . . . .</b>	<b>1</b>
<b>1.2</b>	<b>About injection process and engine working . . . . .</b>	<b>7</b>
<b>1.3</b>	<b>Dynamic of droplets and spray impingement . . . . .</b>	<b>10</b>
1.3.1	Injector and spray description . . . . .	10
1.3.2	Impact regime description . . . . .	14

---

In this chapter the main objective is to derive a model for the wall film spreading. As it has been presented in the Introduction, with direct injection liquid films formation on the walls of the combustion chambers are identified as major contributors of pollutants generation. Hence being able to predict the quantity deposited by an injector is really valuable for injector designers. Many CFD models for film generation and motion have been developed [5, 22, 25, 43, 60, 64, 69, 94, 97, 98, 103]. Most of them are based on a Lagrangian approach to describe the spray but also the film. Generally the numerical models are fed by experimental data to improve their accuracy. Simulation produce good results, however their cost is relatively high, and due to the high variability of operating points of an engine it is not possible to rely only on numerical simulations. The originality of the model presented bellow lies in its simplicity. The model uses simple momentum and mass balances to predict the spreading rate of the liquid film generated by the injector. As the model is really light, it can be easily implemented in a tool to optimise and accelerate the design phases of injector makers.

## 4. LIQUID FILM SPREADING

---

For simplicity purpose, the spreading of liquid film generated by orthogonal impingement will be first presented (it allows to make a symmetry hypothesis). It gives the foundations of the model, then a parametrical variation is presented in order to test the model robustness. Based on the same considerations a model for non-orthogonal impingement will be proposed. Indeed, though orthogonal impingement does happen in the combustion chamber, non-orthogonal impacts are more likely to happen. Finally, thickness evaluations using the RIM method will be presented, as both the liquid film area and the thickness are important parameters.

### 4.1 Orthogonal impingement film spreading

This part of the PhD thesis (Section 4.1.1 to 4.1.3) has been submitted to Physical Review Fluids and is currently under revision.

#### 4.1.1 Results

##### 4.1.1.1 Film spreading description

An example of film spreading is depicted in Figure 4.1 for an injection time  $T_i = 6\text{ms}$ , a fuel pressure  $P_i = 100\text{ bar}$  and a distance  $z = 50\text{ mm}$ . Using the software Fiji [84] and several image processing tools, it is possible to track the liquid film edge and, hence, determine the time evolution of the film surface area. As observed, the film area is almost circular during all the spreading process.

Figure 4.2 presents the area evolution of the liquid film corresponding to the images reported in Figure 4.1. It displays the average of 5 repetitions, together with error bars, which represent the typical standard deviation observed in our experiments. This shows the good repeatability of the injection, the spray wall impingement and the film spreading. In what follows, error bars will not be displayed for the sake of clarity.

During the early stage of injection, the first droplets are piling up to create a liquid film. The contour of this liquid film is difficult to identify because of a strong Mie scattering from the spray. This is why the first measurement point is taken 1ms after the impact of the first droplets on the plate. Once this liquid film is created, it is spreading and the edge of the film can be tracked. As shown in Fig. 4.2, the spreading can be separated into two main phases: the film spreading observed during the injection and a relaxation phase following the closing of the injector needle. As the impingement

## 4.1 Orthogonal impingement film spreading

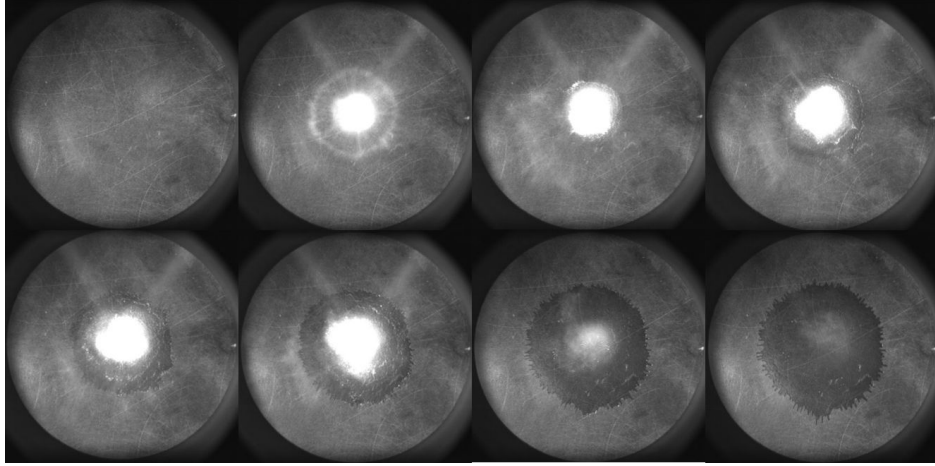


Figure 4.1: Images of a film spreading as visualized from bottom on the RIM setup.  $P_i = 100$  bar  $T_i = 6$  ms and  $z = 50$  mm. Images are displayed every 1.25 ms.

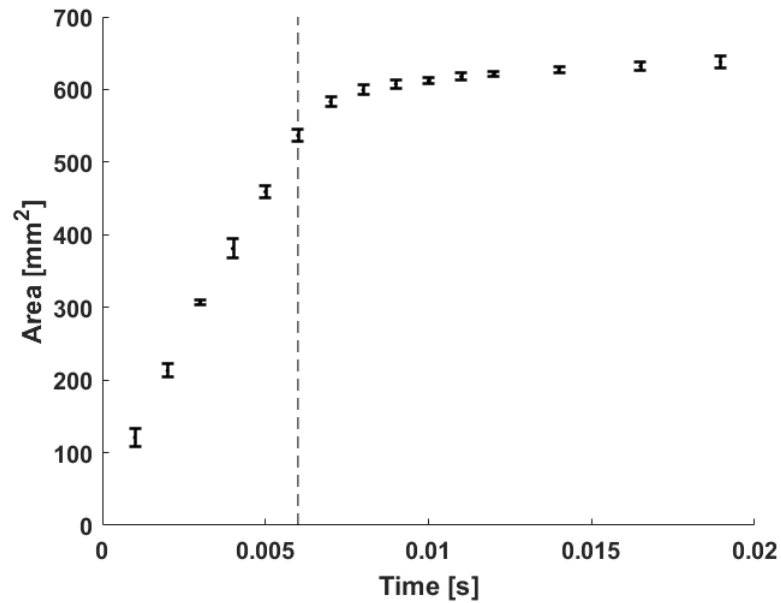


Figure 4.2: Time evolution of the liquid film area. Experimental conditions:  $T_i = 6$  ms,  $P_i = 100$  bar,  $z = 50$  mm. The vertical dashed line indicates the end of injection.

is orthogonal to the plate, the spreading rate is almost the same in all directions and the mean film shape is almost a circle. During the spreading phase, the liquid film

#### 4. LIQUID FILM SPREADING

---

area is observed to grow linearly with respect to time. After the end of injection, the film dynamics changes. It still continues to slowly grow for some moments, due to its inertia. This last phase will be called the relaxation phase.

As can be observed in Figure 4.1, digitations develop at the edge of the liquid film. The so-called digitations look like fingers disturbing the regular shape of the liquid film edge but their size always remains much smaller than the film radius. Inserts of Figure 4.3 shows a magnification of these digitations, for the three pressure of injection considered (50, 100, 200 bar). Increasing the injection pressure promotes the apparition of the fingers. The digitations wavelength has been determined as follows. After the end of injection, the number of digits on several portions of the liquid film is recorded. The number of fingers is then extended to the full liquid film front assuming that the instability development is the same in all directions. Hence, it gives a wavelength  $\lambda$  that is normalised by the corresponding mean film perimeter  $2\pi R$ . This normalised digitation wavelength is reported in Figure 4.3 as a function of the injection pressure. A power law of the form  $\lambda/R \propto P_i^{-1/3}$  is observed. Such behaviour can be related to the apparition of fingers on a liquid film flowing down a plate. In this situation, the liquid driving is controlled by  $\rho g \sin \alpha$  where  $\alpha$  is the slope of the surface and the wavelength of the growing instability follows the power law  $\lambda \propto (\rho g \sin \alpha)^{-1/3}$  [33, 90]. The same power law is here observed with the pressure of injection  $P_i$  that drives the film expansion.

An other feature identified during the spreading is the apparition of waves while the liquid film is propagating, as can be observed in Figure 4.4 for different injection conditions. High-pressure sprays are turbulent and thus a place where many micro and macroscopic motions are created [21, 27]. A well known consequence of the spray inner-motion is the so-called droplet clustering [21, 92]. By looking carefully at the movies, it becomes quite clear that the waves are generated by the spray inhomogeneities and oscillations that impact the film surface (see Figure 3.4). These waves propagate at a velocity larger than the spreading velocity. For each pressure, the velocity of the waves flowing over the liquid film have been tracked for different radial positions. The relative wave velocity is obtained by subtracting the film speed at the wave position. In Figure 4.4 the relative velocity of several waves is displayed for  $P_i = 100$  bar. The wave velocity is found in the range 1 to 15 m/s. The maximum value is observed close



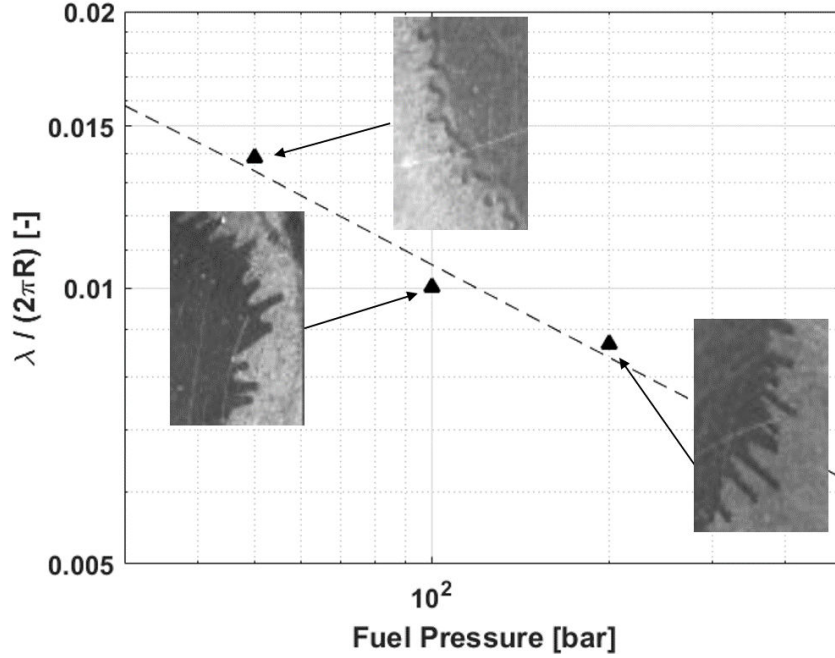


Figure 4.3: Evolution of digitation wavelength with respect to fuel pressure for  $T_i = 6\text{ms}$  and  $z = 50\text{mm}$ . The dashed line represent the power law  $P_i^{-1/3}$ .

to the impact zone and then it decays following a  $r^{-1/2}$  evolution as expected for planar radial waves.

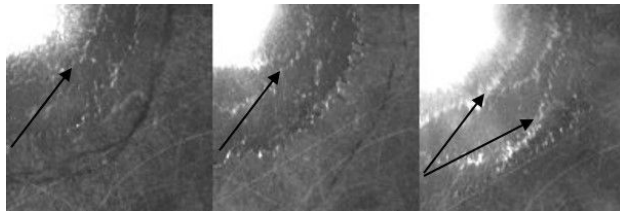


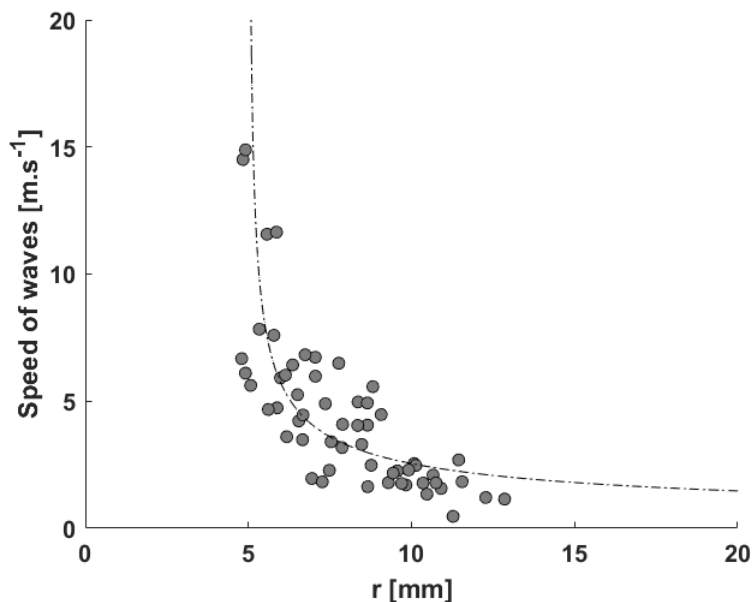
Figure 4.4: Detail of surface waves for different injection conditions for  $T_i = 10\text{ms}$  and  $z = 50\text{mm}$ . Left to Right: 50, 100, 200 bar.

#### 4.1.1.2 Effect of the injection duration

Figure 4.6 presents the influence on the film spreading of the injection duration  $T_i$  for the injection pressure fixed to 100 bar and the distance  $z = 50\text{mm}$ .  $T_i$  is varied from 2 to 12 ms. The two phases (spreading and relaxation) are observed for the 6 different

## 4. LIQUID FILM SPREADING

---



**Figure 4.5: Evolution of film surface waves speed with respect to their radial position  $r$ . Experimental conditions  $P_i = 100$  bar,  $T_i = 10$  ms and  $z = 50$  mm. The curves represent a  $r^{-1/2}$  evolution expected for a planar radial wave.**

injection durations. The curves clearly collapse during the spreading phase showing a good control of the injection and the repeatability of the experiments. The final film area is obviously found to increase with the duration time. The relaxation phase seems to increase with  $T_i$ . This point will be analyzed in more details in the following.

### 4.1.1.3 Effect of the injection pressure

The effect of the injection pressure on the film spreading can be observed in Figure 4.7. The two distinct phases in the spreading process are confirmed whatever the injection pressure. The spreading rate is clearly depending on the injection pressure. Not only does raising the injection pressure increase the spray momentum, but it also raises the injected mass that has to spread. It is then not surprising that the spreading rate increases with injection pressure, while the global behaviour of the film spreading remains the same.

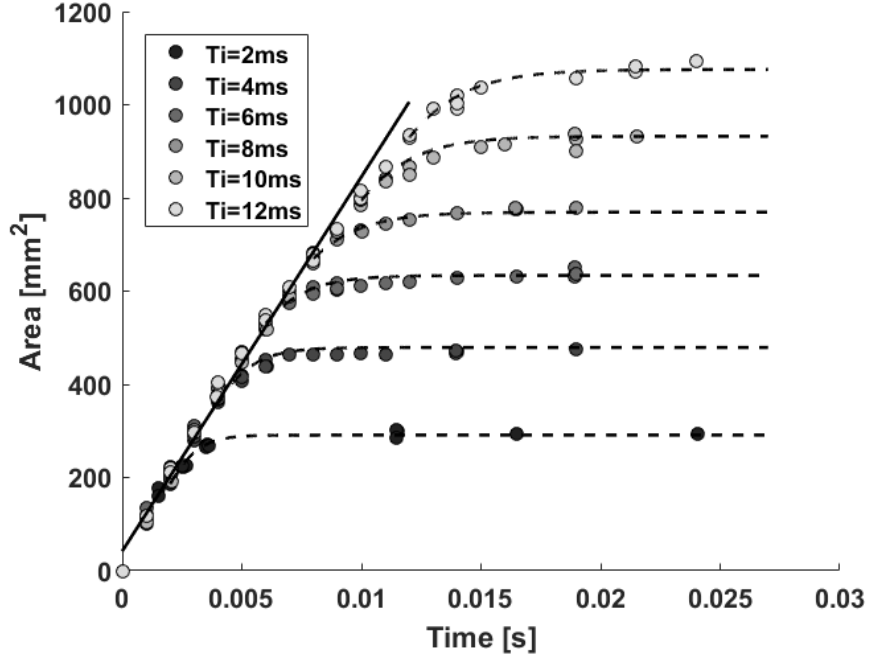


Figure 4.6: Liquid film area for different injection times. Experimental conditions  $P_i = 100$  bar and  $z = 50$  mm. Continuous Line: Eq. 4.6, Dashed line: solution of Eq. 4.10.

#### 4.1.1.4 Effect of the Injector to wall distance

The injector-wall distance  $z$  has been varied from 20 mm to 65 mm. The corresponding effect on the film spreading area is therefore reported in Figure 4.8 for  $P_i = 100$  bar. The same behavior is observed for the three pressure 50, 100 or 200 bar. Film spreading is unchanged when the injector is either closer or further to the impingement plate. This is not a trivial result because, when increasing the distance, the jet is expected to expand and change the impact area on the plate. However for the injector considered here the jet expansion is relatively moderate as illustrated in the image shown in Figure 3.4. As a consequence the area of impact  $A_o$  is almost constant for the different position  $z$  considered. The mean value  $A_o = 42$  mm<sup>2</sup> is very close to the value of the mean area of the jet for  $z$  between 20 mm to 65 mm. The variation of  $A_o$  with respect to  $z$  is small enough to both observe the same behavior and spreading rate as shown in Figure 4.8.

## 4. LIQUID FILM SPREADING

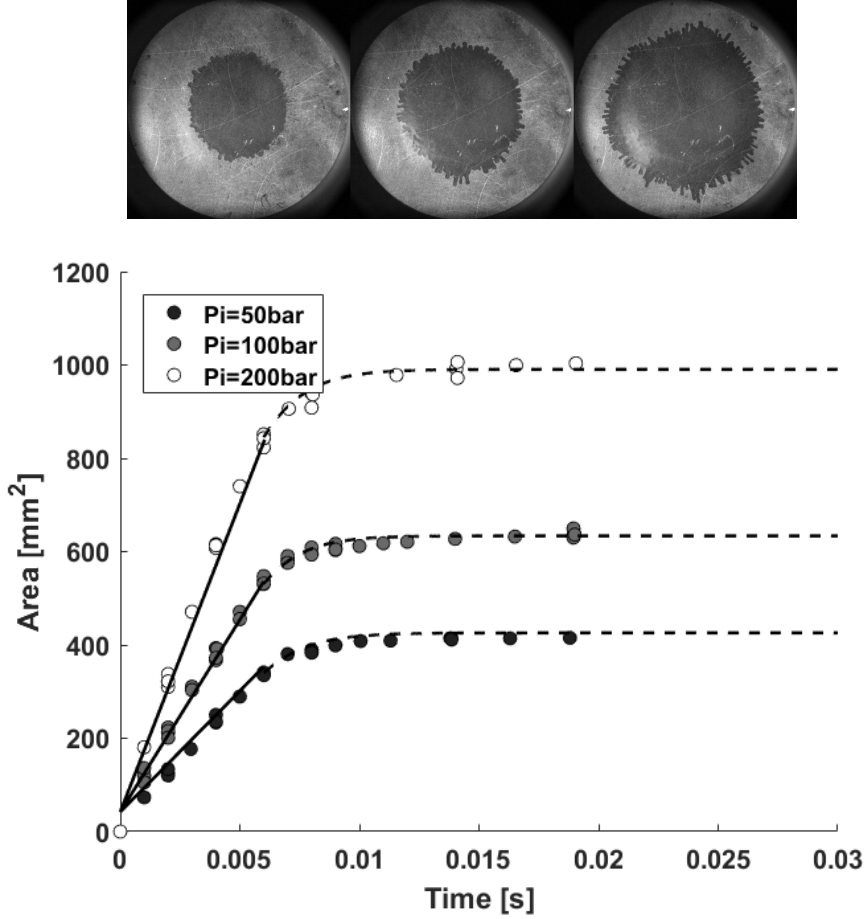


Figure 4.7: Liquid film area for different injection pressures. Experimental conditions  $T_i = 6$  ms,  $z = 50$  mm. (top) film at the end of the injection from left to right for  $P_i = 50, 100$  and  $200$  bar. (bottom) Time evolution of the film area. Continuous Line: Eq. 4.6. Dashed line: solution of Eq. 4.10.

### 4.1.2 The spreading phase

As well underlined in [38], spray-wall impingement is a very complex phenomenon, with many interactions between the incoming droplets and the perturbed film surface. The attention is first drawn to the film propagation, while the injector is open. The film shape is simplified to a puddle or a pizza shape, with a uniform thickness  $e$  as shown in Figure 4.9. Mass conservation in the film can then be written as:

$$\frac{d\pi R^2 e}{dt} \approx K_m Q, \quad (4.1)$$

## 4.1 Orthogonal impingement film spreading

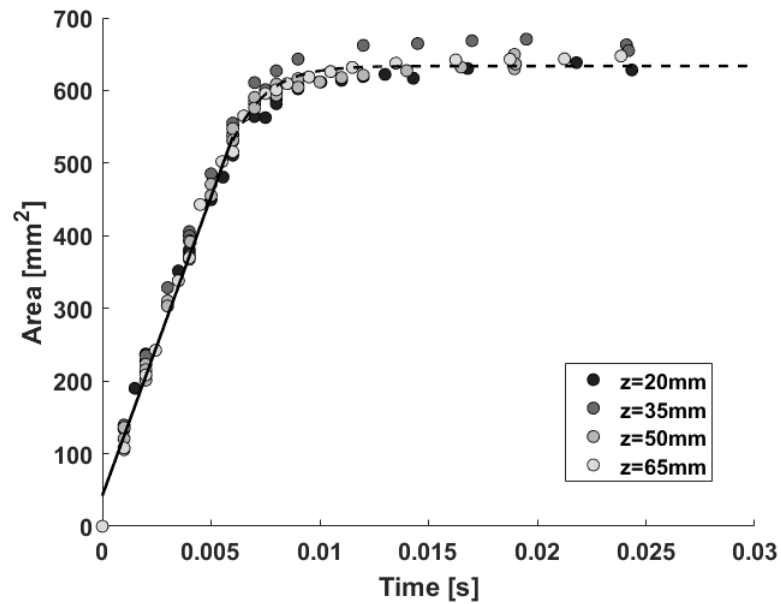


Figure 4.8: Liquid film area for different injector-wall distances. Experimental conditions  $T_i = 6$  ms,  $P_i = 100$  bar. Continuous Line: Eq. 4.6, Dashed line: solution of Eq. 4.10.

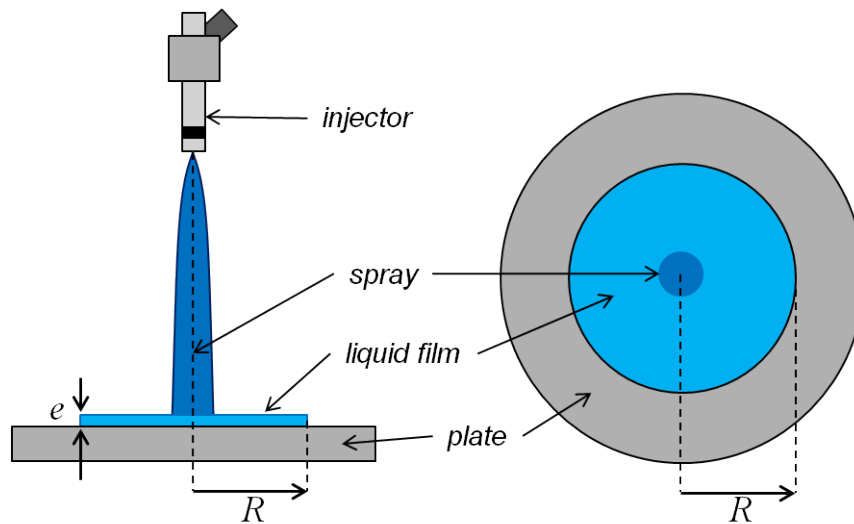


Figure 4.9: Sketch of the modeled problem. The film thickness is supposed to be homogeneous.

#### 4. LIQUID FILM SPREADING

---

where  $Q$  stands for the injection discharge of the injector and  $K_m$  represents the injected mass that contributes to the film.  $K_m = 1$  corresponds to an injected mass totally transferred into the film. From equation 4.1, we get the following relation between  $R$  and  $e$

$$\pi R^2 e \approx K_m Q t \quad (4.2)$$

Considering that the pressure gradient induced by the jet impact is balanced by viscous friction, the momentum balance in the film can be simplified to:

$$\frac{\Delta P}{R} \approx \frac{\eta \dot{R}}{e^2} \quad (4.3)$$

The pressure of the jet at impact is directly connected to the pressure of the injector. Thus, we propose to relate the driving pressure in the film  $\Delta P$  to the injector pressure  $P_i$  through a transfer function  $K_P$  such that  $\Delta P \approx K_P P_i$ . Combining relations 4.2 and 4.3, the evolution of the radius with the parameters of the problem is

$$R^2 \propto P_i^{1/3} Q^{2/3} \eta^{-1/3} t, \quad (4.4)$$

showing a linear evolution of the film area in time in agreement with the experimental results presented above, while a constant film thickness is obtained

$$e \propto \eta^{1/3} Q^{1/3} P_i^{-1/3}. \quad (4.5)$$

The evolution of the surface area is reported as a function of  $P_i^{1/3} Q^{2/3} \eta^{-1/3} t$  in Figure 4.10. As shown, all the evolutions are almost collapsing on a single curve showing the relevance of the proposed modeling. As discussed before, the initial area for the film  $A_o$  is almost the same for all the cases and can be related to the mean value of the jet expansion for the distances  $z$  considered (from 20mm to 65mm). In particular, equation (4.4) is able to reproduce the influence of the pressure injection on the film spreading for a large range of pressure.

A quantitative description of the film area can be provided considering the transfer coefficients  $K_m$  and  $K_P$ , for the injected mass contributing to the film and for the driving pressure for the film spreading, respectively. The corresponding dependancies of the surface area and the film thickness are given by

$$\pi R^2 = \pi R_0^2 + \left( \frac{2\pi K_m^2 K_P P_i Q^2}{\eta} \right)^{1/3} t, \quad (4.6)$$

$$e = \left( \frac{\eta K_m Q}{2\pi K_P P_i} \right)^{1/3}, \quad (4.7)$$

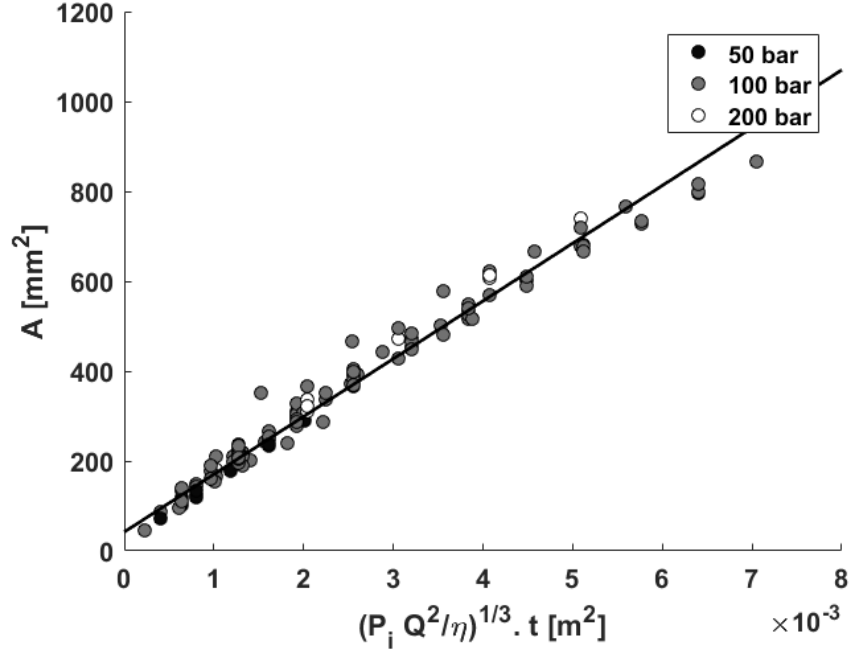


Figure 4.10: Evolution of the film surface as a function of  $P_i^{1/3} Q^{2/3} \eta^{-1/3} t$  for all the experiments presented above. Line: Equation 4.6 (see the text for the value of  $K_P$  and  $K_m$ )

showing that the area of the film formed at the end of the injection is

$$A_i - A_o = \pi R_i^2 - \pi R_o^2 = \left( \frac{2\pi K_m^2 K_P P_i Q^2}{\eta} \right)^{1/3} T_i. \quad (4.8)$$

Few studies have been able to determine the mass of liquid injected that effectively contributes to the film under similar conditions of pressure, temperature and mass flow rate. In [86], iso-octane is injected at 150bar in a vessel heated at  $80^\circ C$  and the injected mass is 21.7mg over 6 holes. The deposited mass for one hole is around 1.4mg which corresponds to a value  $K_m = 0.39$ . In [41], Diesel is injected at 190bar by a one hole injector in non-vaporizing conditions at the distance  $z = 50$  mm for single injection. It is found that the mass recovered on the plate is around 50% of the injected mass, and 75% of this mass contributes to the liquid film resulting in the value  $K_m = 0.37$ . Finally, based on these two studies, the value  $K_m = 0.38$  is considered for the following discussion.

## 4. LIQUID FILM SPREADING

---

The value of  $K_P$  is deduced from our experiments considering the evolution reported in Figure 4.10. From the slope of the general trend,  $K_P$  and  $K_m$  are connected through the relation  $K_m^2 K_P \approx 3.38 \cdot 10^{-4}$ . Considering  $K_m = 0.38$  one obtains  $K_P = 2.34 \cdot 10^{-3}$ . This value can be discussed considering a simple pressure force conservation in the jet as  $\Gamma_{injector} P_i \approx \Gamma_{impact}^2 P_{impact} = \Gamma_{impact} K_P P_i$  where  $\Gamma$  is here the jet cross section. Thus  $K_P$  can be roughly related to the jet cross section ratio as  $K_P \approx \Gamma_{injecteur}/\Gamma_{impact} \approx 10^{-3}$  in agreement with the above value deduced from Figure 4.10. Relation 4.6 is now reported in Fig. 4.6, 4.7 and 4.8 with  $K_P = 2.34 \cdot 10^{-3}$  and  $K_m = 0.38$ . As shown, the spreading phase is accurately described for all the experiments. In particular, the effect of the injection pressure is well reproduced (see Fig. 4.7).

Having estimated  $K_P$  and  $K_m$  for the present injection conditions, it is now possible to have an estimation of the film thickness. Considering relation 4.7, the thickness is  $e = 19, 15$  and  $12 \mu\text{m}$  for  $P_i = 50, 100$  and  $200$  bar, respectively.

The value of the film thickness, together with the thickness evolution with respect to injection pressure, are consistent with experiments reported for liquid films under similar injection conditions [41, 85, 86].

The normalized area  $A^* = (A - A_o)/(A_i - A_o)$  is finally reported as a function of the normalized time  $t/T_i$  in Figure 4.11 for all the cases considered. The experiments performed for different pressures, distances and durations of injection are all collapsing on the  $y = x$  line, showing the relevance of the proposed modeling.

### 4.1.3 Relaxation phase

After the end of injection, the liquid film continues to spread even if the source of momentum has been shut down. It has been previously referred as the relaxation phase. The relaxation phase has been observed for all the injection conditions. The radius increase during this phase ranges between 15% to 30%.

Once the injection is stopped, the liquid film volume  $\Omega_i = \pi R^2 e$  can be considered as constant. During the relaxation, the film momentum is dissipated by viscosity in the film so that the momentum equation satisfied in the film writes

$$\ddot{R} \sim -\frac{\nu}{e^2} \dot{R} \quad (4.9)$$

where  $\nu = \eta/\rho$  is the kinematic viscosity. From Eq. 4.9, the characteristic time of the relaxation phase is then  $\tau = e^2/\nu$ . Considering the order of magnitude of the film



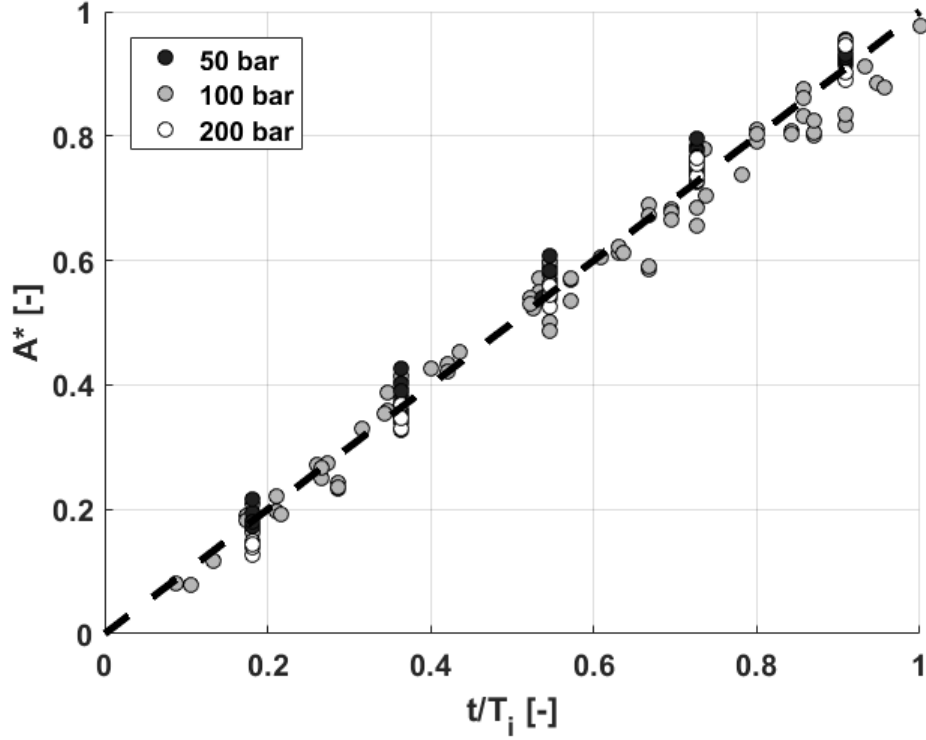


Figure 4.11: Evolution of the dimensionless area  $A^* = (A - A_o)/(A_i - A_o)$  versus the dimensionless time  $t/T_i$  for different injection durations and pressures.

thickness ( $15\mu\text{m}$ ), we get  $\tau \approx 0.4$  ms in agreement with the relaxation phase observed in the above figures. Combining the mass and momentum conservation, one gets the following equation for the film radius during the relaxation phase:

$$\ddot{R} = -C \frac{\nu \dot{R} R^4}{\Omega_i^2} \quad (4.10)$$

where  $C$  is a parameter that a priori needs to be adjusted for the different conditions of injection. Considering the initial values of the film radius  $R_i$  and velocity  $\dot{R}_i$  for the relaxation phase as the values of  $R$  and  $\dot{R}$  at the end of injection ( $t = T_i$ ), this equation can be solved to obtain the film radius evolution once the injection is stopped. The corresponding evolutions are reported in Fig. 4.6 for different injection times and in Fig. 4.7 for the three pressures of injection considered. As shown in the figures, the relaxation phase is remarkably reproduced by the solution of equation 4.10. The corresponding values of the parameter  $C$  that gets a correct fitting of the experiments

## 4. LIQUID FILM SPREADING

---

are reported in Table 4.1. Note that the parameter  $C$  has the same order of magnitude for all the considered cases. It is observed to decrease when increasing the pressure injection.

$P_i$ [bar]	$T_i$ [ms]	$R_i$ [mm]	$\dot{R}_i$ [m.s <sup>-1</sup> ]	$C$ [-]
50	6.0	10.4	0.7	2.71
100	2.0	8.0	1.80	2.17
100	4.0	10.7	1.22	2.07
100	6.0	13.0	0.75	1.97
100	8.0	14.9	0.55	1.73
100	10.0	15.9	0.65	1.58
100	12.0	17.8	0.59	1.48
200	6.0	16.4	0.81	1.23

**Table 4.1:** Value of the parameter  $C$  for different pressures of injection and injection durations.

### 4.1.4 Effect of fuel type

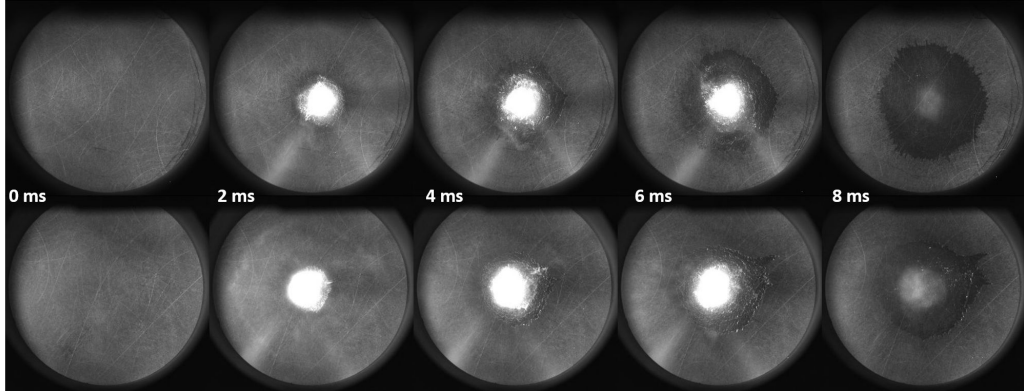
The model developed earlier is calibrated using experimental measures performed with n-decane. However, it is interesting to know if the previous conclusions hold true using another liquid. The main reason is that gasoline<sup>1</sup> is composed of dozens of compounds (Figure 6.7). Another is also to be able to make injection with another fuel (the cost of n-decane is higher than for n-heptane and both are present in regular gasoline). Two impingement processes are displayed in Figure 4.12. The first liquid is n-heptane, the second n-decane, the injection pressure is 100 bar, the wall temperature 20°C and the injection duration 6 ms. It is interesting to note that the n-decane film edge is less apparent. This is because of the volatility of the fuel. It is lower than n-heptane, and the small quantity of sparse droplets reaching the plate further than the continuous liquid film, evaporate for n-heptane and do not for n-decane. Then, as the surface is wetted by these sparse droplets, it appears darker than the dry sapphire and makes

---

<sup>1</sup>Gasoline but other fuel like diesel, or new generation fuels like E22 or E85 are all composed of many different species.

## 4.1 Orthogonal impingement film spreading

the visualisation (contrast) of the liquid film more complicated (the quantity of fuel deposited by these droplets is negligible compared to the liquid film volume).



**Figure 4.12: Impingement process of different fuel on sapphire plate.**  $T_i = 6$  ms,  $P_i = 100$  bar  $z = 50$ mm  $T_w = 20^\circ\text{C}$ . **Top: n-heptane spreading. Bottom: n-decane spreading.**

Figure 4.13 shows the difference in spreading for n-heptane and n-decane for the same conditions of injection. Exactly the same behaviour as presented before is identified:

- A linear evolution of the wetted area with respect to injection duration:  $A \propto t$ .
- Waves propagating over the liquid film with a velocity which decays as :  $r^{-1/2}$ .
- Once the injection has stopped, a relaxation of the liquid film is recorded.
- The liquid film development is accompanied by a digitation formation (less visible for n-decane as the contrast worse than for n-heptane because of sparse droplets deposition).

Cold conditions (ambient temperature) are used in order to maximise the differences between both fuels. Indeed when n-decane is heated its physical properties (density, viscosity, saturation pressure) are changing and it tends to get similar to n-heptane. The n-heptane has a higher spreading rate than the n-decane and also a bigger maximum area (Table 4.2). The difference of spreading rate between  $73 \text{ mm}^2/\text{ms}$  and  $80 \text{ mm}^2/\text{ms}$  is 9 % whereas the difference in final area  $560 \text{ mm}^2$  and  $650 \text{ mm}^2$  is 14 %. The principal justification of this behaviour is the difference of viscosity between the two fluids.

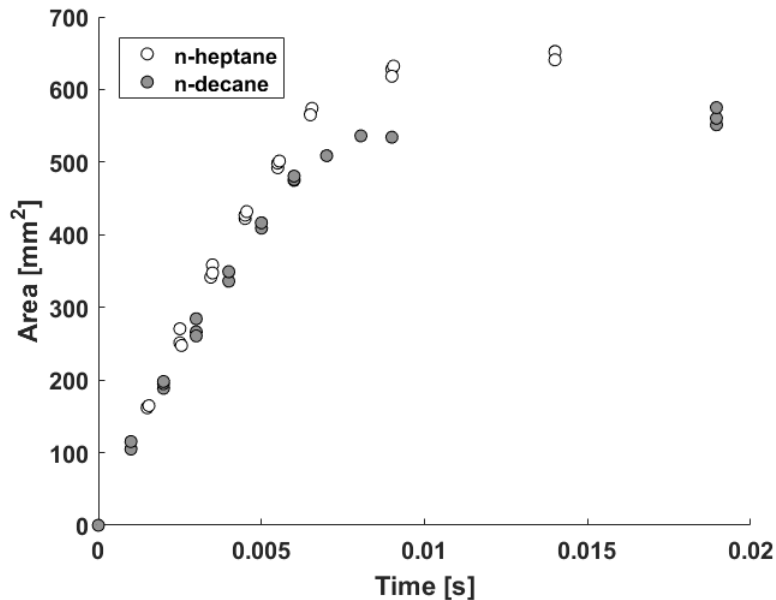
#### 4. LIQUID FILM SPREADING

---

However, replacing (in the model) the n-decane viscosity with the one of n-heptane is not conclusive. In section 4.1.6 where the effect of temperature (which changes the viscosity and density of n-decane) is discussed, the comparison between model prevision (using the viscosity variation) and experimental data is presented.

Plate	Spreading rate [ $mm^2/ms$ ]	Area @6 ms [ $mm^2$ ]	Final Area [ $mm^2$ ]
n-heptane	80	520	650
n-decane	73	480	560

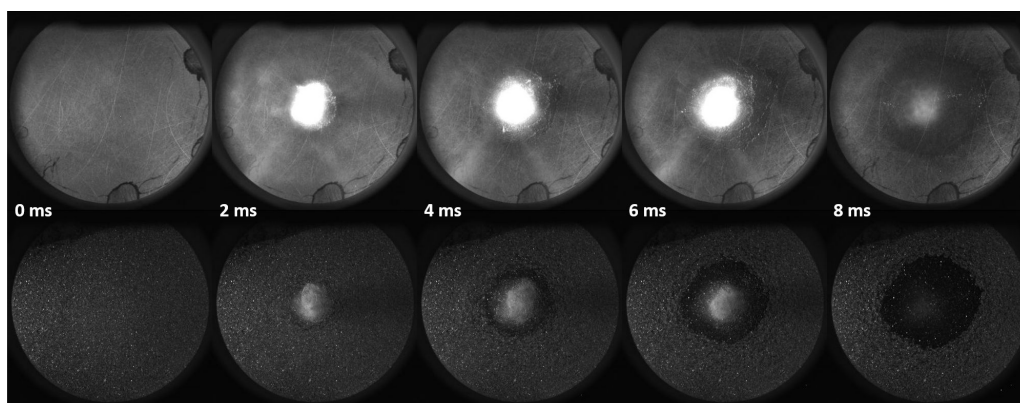
**Table 4.2:** Spreading differences between n-heptane and n-decane in the same experimental conditions.



**Figure 4.13:** Area evolution of n-heptane and n-decane. Injection conditions  $T_i = 6$  ms,  $P_i = 100$  bar  $z = 50$ mm  $T_w = 20^\circ$ C.

### 4.1.5 Roughness effect

The results and modelling presented earlier were all derived from experiments made on a smooth sapphire plate. However, though the cylinder (which is also prone to wetting) is a smooth surface, the piston roughness is higher and can vary even more due to sooting and coking of the surface (measurement of roughness on coked piston is available in Appendix (Section 8.1)). Hence, it is interesting to study the spreading on plates with different roughness. Figure 4.14 shows the difference of impingement process in the same injection conditions but with a different roughness. A complete study of wall spreading on rough wall as been presented at the ILASS conference of 2017 [45]. Globally the same behaviour is observed for both plate. The liquid film is first difficult to identify due to the size of the impingement area. Then, it is easier to visualise the liquid film and it starts to grow. The waves and digitations involved in the process described in Section 4.1.1 are still present. Their observation is harder to perform and the magnitude of these phenomena seems reduced due to roughness effect.

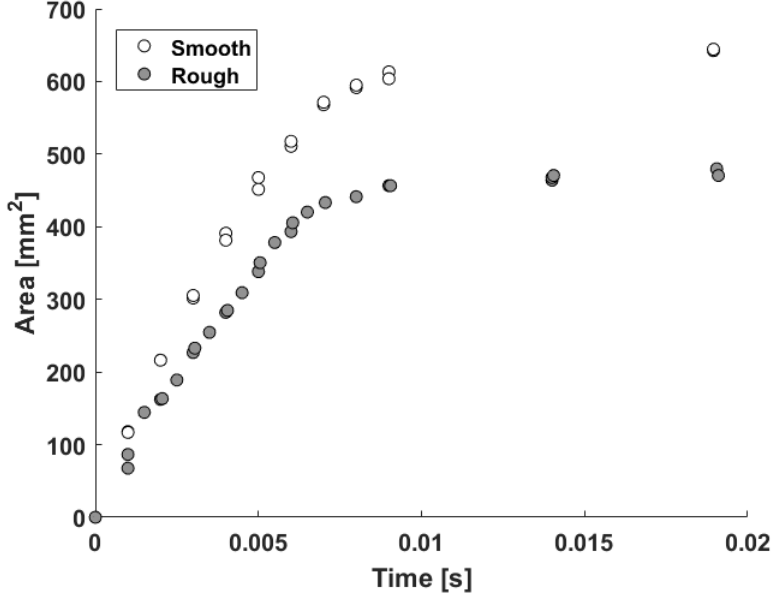


**Figure 4.14: Impingement process on different roughnesses plate.  $T_i = 6$  ms,  $P_i = 100$  bar  $z = 50$ mm  $T_w = 20^\circ\text{C}$ . Top: Smooth sapphire plate. Bottom:  $R_a = 20\mu\text{m}$  quartz plate**

Figure 4.15 shows the area evolution of the liquid film for both plates. The spreading rate and the final area of the liquid film is higher for the smooth plate, as one would have guessed. However, the linear growing rate is present for both cases and the relaxation phase too. The linear spreading on rough plate has been identified and modelled in [45] and the version for smooth plate presented earlier is an updated version of the work presented at the ILASS in 2017.

#### 4. LIQUID FILM SPREADING

---



**Figure 4.15:** Area evolution of n-decane on two different plate, a smooth sapphire plate and a rough  $R_a = 20\mu m$  quartz plate. Injection conditions  $T_i = 6$  ms,  $P_i = 100$  bar  $z = 50$ mm  $T_w = 70^\circ\text{C}$ .

The difference of spreading rate is more than likely due to a higher dissipation of momentum on the rough plate rather than the smooth one and, maybe, in a lower extend, because of a bit less deposited mass (more splashing because of the roughness). The liquid spreading over the plate has to circumvent the obstacles imposed to it (troughs and crests). A way to model this is to correct the viscosity of the fuel in order to take into account the dissipation induced by the wall geometry such as:

$$\frac{\Delta P}{R} \approx \frac{(\eta_l + \eta_w) \dot{R}}{e^2}, \quad (4.11)$$

where  $\eta_l$  stands for the liquid viscosity and  $\eta_w$  for the wall correction. A more convenient way to write this would be to write  $\eta_w = K_\eta \eta_l$ . Finally, Equation 4.12 rewrites:

$$\frac{\Delta P}{R} \approx \frac{\eta_l(1 + K_\eta) \dot{R}}{e^2}. \quad (4.12)$$

The spreading rate for the rough plate is  $66.6 \text{ mm}^2/\text{ms}$  whereas it is  $85 \text{ mm}^2/\text{ms}$  for the smooth plate which is 22 % less. The final area for the rough case is  $475 \text{ mm}^2$

## 4.1 Orthogonal impingement film spreading

---

and  $640 \text{ mm}^2$  or 26 % (Table 4.3).

Plate	Spreading rate [ $\text{mm}^2/\text{ms}$ ]	Area @6 ms [ $\text{mm}^2$ ]	Final Area [ $\text{mm}^2$ ]
Rough Quartz	66.6	405	475
Smooth Sapphire	85	515	640

**Table 4.3: Spreading differences between smooth and rough plate in the same experimental conditions.**

In this case the value of  $K_\eta$  gives a value of 1.08, meaning that the dissipation induced by the material roughness is of the same order of magnitude of the viscous dissipation.

The motivation for the use of roughness (despite the fact that, works on rough plates were anterior to the one on smooth plates) is that it allows in some conditions (described in Section 3.3.4) to get the mass deposited on the plate. Indeed, and as presented in [45], the RIM methods allows, once it has converged, to get the local liquid film thickness. By making assumptions on the mass evaporated during the convergence time, the deposited mass at the end of injection can be estimated.

### 4.1.6 Effect of wall and fuel temperature

In this section, the last parametrical variation for orthogonal impingements is presented. Here, the temperature is varied from  $22^\circ\text{C}$  to  $120^\circ\text{C}$ , the injector and the plate are heated at the same temperature. In this range of temperature, the n-decane used has not yet reached its saturation temperature, which is  $174^\circ\text{C}$  at atmospheric pressure (as presented in Table 2.1). Hence, the liquid film is supposed to experience only an increasing evaporation rate without entering in the boiling window. However, the temperature variation is still relatively important and the effects are numerous:

- On the fluid properties, it modifies the density, the viscosity, the surface tension...  
Table 4.4
- On the mechanical properties of the injector.

#### 4. LIQUID FILM SPREADING

---

Temperature [°C]	Density [kg.m <sup>-3</sup> ]	Dynamic Viscosity [.10 <sup>-4</sup> Pa.s]	$P_{sat}$ [Pa]
22	729	8.86	146
50	707	6.10	880
70	691	4.87	2538
90	676	3.99	6338
120	651	3.05	20184

**Table 4.4: Selected n-Decane properties at variable temperature.**

- The atomisation, and volumetric flow rate of the injector are also modified (as a consequence of the aforementioned effects)

Controlling and having an exact knowledge of the modifications induced by the temperature variation is complicated. However, in the same way as what have been presented earlier, the objective is to take global consideration in order to model the liquid film spreading in different conditions.

Figure 4.16 shows the liquid film for different fuel and wall temperatures (22°C, 70°C, 90°C and 120°C) at 100 bar for an injection duration of 6 ms. At a first glance, the difference of contrast appears to be really important. It is due, as mentioned before, to the evaporation of sparse droplets deposited further than the liquid film edge. Moreover, the digitation wavelength seems to decrease when the temperature is raised, and the fingers look longer (it is not studied here as the focus is put on the spreading rate of the liquid film, but the decrease in viscosity and surface tension could explain this behaviour). Figure 4.17 shows the evolution of the liquid film area for the set of tested temperatures. Once again, the linear growth of the liquid film is validated (proving the robustness of the model). The relaxation phase is also identifiable. Finally, increasing the temperature tends to increase the spreading rate up to a certain temperature. When the temperature is raised from 90°C to 120°C, the spreading and the total area start to decrease. It is believed that at this point, evaporation (either at the liquid film surface and during the travel of the spray) is balancing the beneficial effect of temperature (the viscosity of the fluid decreases with respect to the temperature).



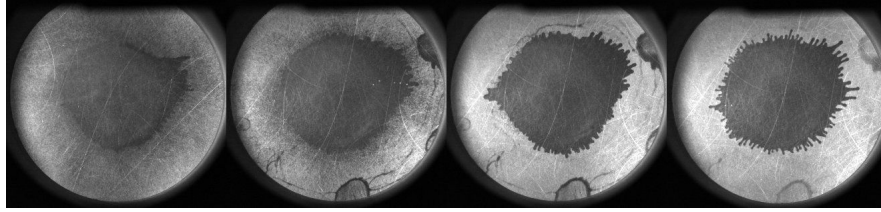


Figure 4.16: Liquid film visualisation 5 ms after the end of injection. From left to right, 22°C, 70°C, 90°C, 120°C. Injection conditions,  $T_i = 6 \text{ ms}$ ,  $P_i = 100 \text{ bar}$ .

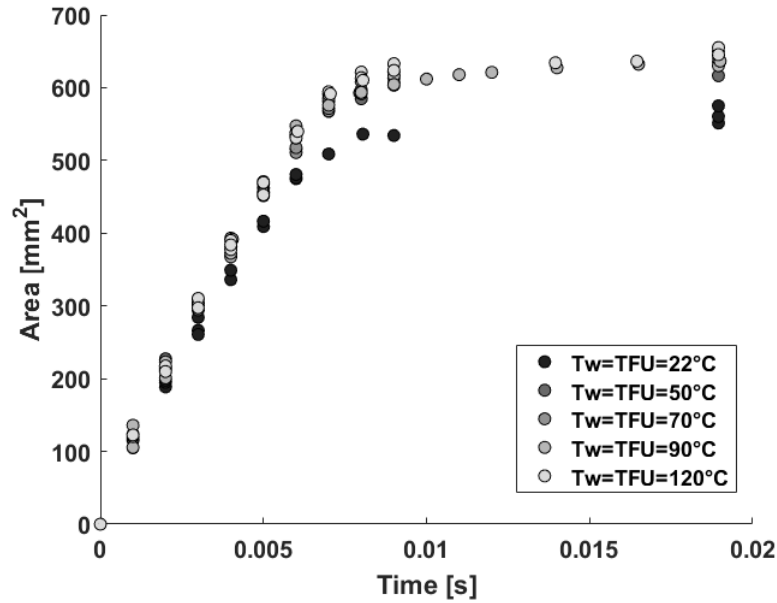


Figure 4.17: Area evolution for different temperature (injector and wall temperature set at the same level). Injection conditions,  $T_i = 6 \text{ ms}$ ,  $P_i = 100 \text{ bar}$ . For some temperature less measurement point are performed, when the measurement were done the focus was on the spreading phase and not on the relaxation phase.

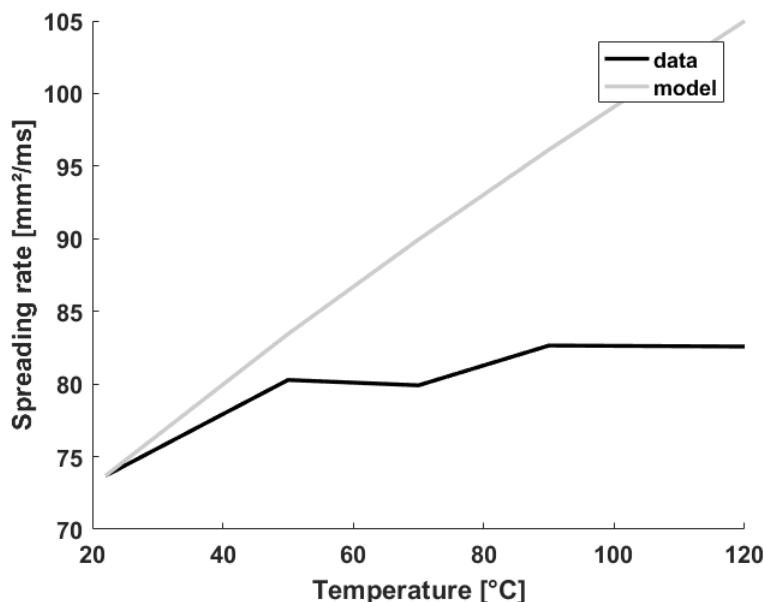
The mass flow rate of the injector variation between 22°C and 120°C has been measured using a test tube as presented in [53] and found to be below 4%. It will then be considered constant in what follows.

The model presented Eq. 4.8, indicates that the variation of the spreading rate is proportional to  $\eta^{-1/3}$ . However, correcting the spreading rate using only the viscosity value at the prescribed temperature does not explain all the variations of spreading

#### 4. LIQUID FILM SPREADING

---

rate (Figure 4.18).



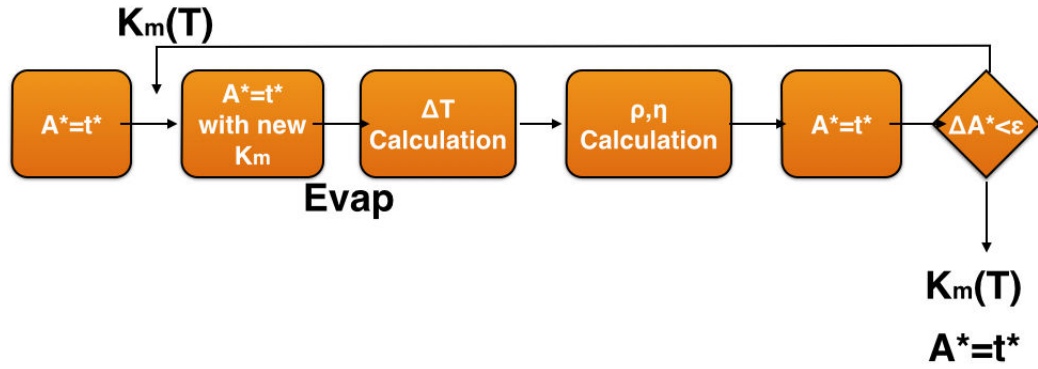
**Figure 4.18:** Effect of viscosity on spreading rate. Comparison between experimental data and power law  $\eta^{-1/3}$  as presented by the spreading model.

A tentative of modelling has still been proposed. As the change of viscosity due to temperature is overestimating the spreading rate, correcting the viscosity with a more realistic film temperature has been tried. Indeed, during the travel time of the spray, a part of the injected quantity is vaporised. The model proposed is rather simple, it will be assumed that at 22°C (the lower temperature we tested), there is no evaporation. However, at higher temperatures, evaporation occurs. The assumption is that all the energy needed for the phase change is taken from the remaining fuel in the spray. This energy cools the fuel, and viscosity is calculated at the new spray temperature, which is the impact temperature (the density is also corrected as the discharge of the injector  $Q = \dot{m}/\rho$  varies with  $\rho$  the fluid density). As mentioned before the mass flow rate  $\dot{m}$  is considered as constant.

The vaporised quantity is described using the coefficient  $K_m$  defined previously in Section 4.1. In order to estimate the vaporised quantity and the "new" temperature of the liquid film, an iterative algorithm is proposed. The algorithm objective is to optimise the value of  $K_m$ , so that the model gives the best evaluation of the liquid

## 4.1 Orthogonal impingement film spreading

film area (i.e. the dimensionless area evolution with respect to the dimensionless time follows the equation  $x=y$ ). Figure 4.19 depicts the algorithm principle. The initial value of  $K_m$  is first fixed (for the present case 0.38 is used as it is the value presented earlier), then the vaporised mass is calculated (on the first step there is no vaporisation as  $K_m = 0.38$  at all temperatures). The liquid properties are then calculated, at the new temperature. New values for the dimensionless area  $A^* = (A - A_o)/(A_i - A_o)$  (derived from Equation 4.8) are calculated, and depending on the results a new value of  $K_m$  is proposed. At, the second step the value of  $K_m$  is not the same for all temperatures, hence the vaporised mass is calculated with the difference between  $K_m$  at  $22^\circ C$  and  $K_m$  at the tested temperature. The algorithm then goes on until convergence.



**Figure 4.19: Working principle of the algorithm used to optimise  $K_m$ .** Where  $\Delta A^* = A^*(n + 1) - A^*(n)$ .

Figure 4.20 shows the value of the dimensionless area before and after optimisation. Whereas, Figure 4.21 shows the value of  $K_m$  and the variation induced on the spray temperature at impact. The value obtained for  $K_m$  are a bit higher than what has been used to calibrate the model at  $90^\circ C$ . However, it indicates that 42.5% of the injected mass participate to the liquid film instead of 38% so the results of the previously presented model are still valid (a rapid calculation gives a variation of 7% in term of spread area). It also shows that the dimensionless area is closer to the experimentally measured area for a wide range of temperature. It also shows that the temperature of the liquid, when impacting on the plate is reduced by almost  $30^\circ C$  when the injection is made at  $120^\circ C$ . This is quite interesting because significant, and even if we have

## 4. LIQUID FILM SPREADING

no validation of the temperature of the spray at the impact, it seems obvious that it cannot remain at the injection temperature.

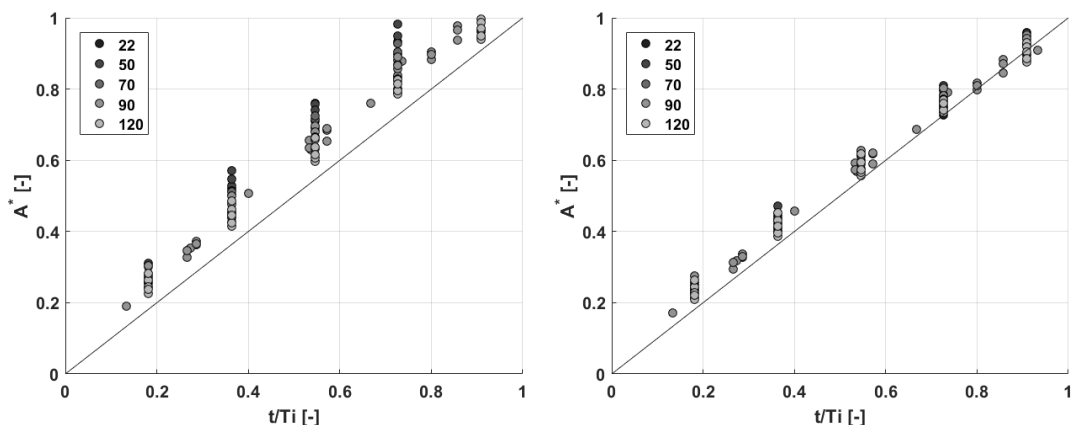


Figure 4.20: Dimensionless area of n-decane liquid film for different injection duration (2, 4, 6, 8, 10 and 12 *ms*), different injection pressure (50, 100, 200 *bar*) and different temperatures (22°C, 70°C, 90°C, 120°C). Left: Before optimisation on the coefficient of mass deposition  $K_m$ . Right: After optimisation on the coefficient of mass deposition  $K_m$ . Black line represents  $y = x$  equation.

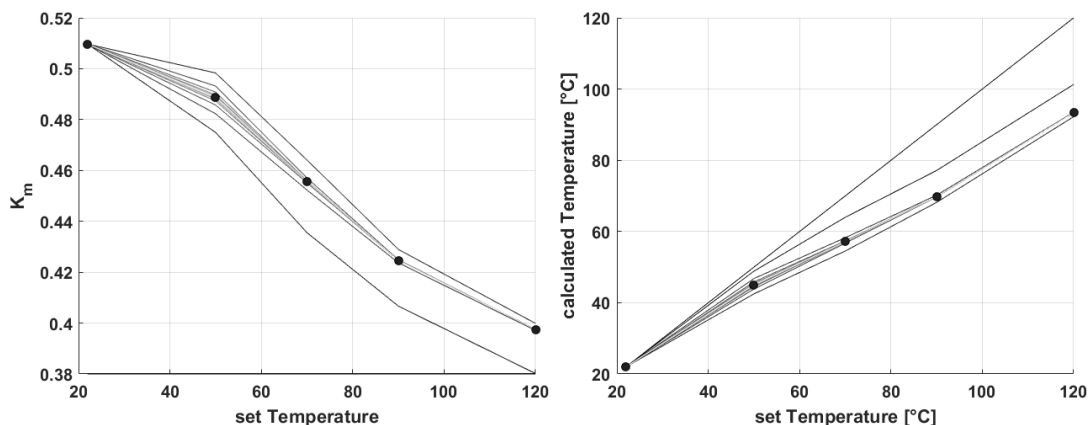


Figure 4.21: Effect of the algorithm on  $K_m$  and the fuel temperature at impact. Left: Evolution of the mass deposition coefficient  $K_m$  with respect to injection temperature. Right: Evolution of the temperature of the spray at impact versus its temperature at the nozzle exit. Black lines present some iterations of the model. Black dots present the converged values.

To summarise, though this algorithm slightly changes the constant  $K_m$  derived during the modelling of the liquid film spreading, it also enforces the interest of the proposed model, as the observations made on the spreading phase are still valid. However, it raises one question, which is: "At which temperature does the spray impact the wall?" . Answering this question is not an easy task. The next chapter will focus on the wall temperature during and after the impingement of the spray, and it might help to understand what is happening here. Now, the spreading during non-orthogonal impingement will be presented.

## 4.2 Non-orthogonal film spreading

In the previous section, an original complete model for the orthogonal impingement has been successfully derived and calibrated based on experimental observations and measurements. The model also works with different fuel types and temperatures, and wall roughnesses. However, spray impingement for automotive applications is more likely to happen with an angle different from  $90^\circ$ . Taking this into account, even if the model developed helps to predict the wetted area, studying the angle dependency<sup>1</sup> is, for sure, very valuable for automotive industry.

### 4.2.1 Results

#### 4.2.1.1 Film spreading description

Figure 4.22 shows an example of film spreading for an impingement angle of  $60^\circ$  (Figure 3.28), the injection duration is  $T_i = 6 \text{ ms}$ , the fuel pressure  $P_i = 100 \text{ bar}$  and the travelling distance  $z = 50 \text{ mm}$ . The plate used is the quartz plate with an average roughness  $R_a = 20.22 \mu\text{m}$  presented in Table 3.1.

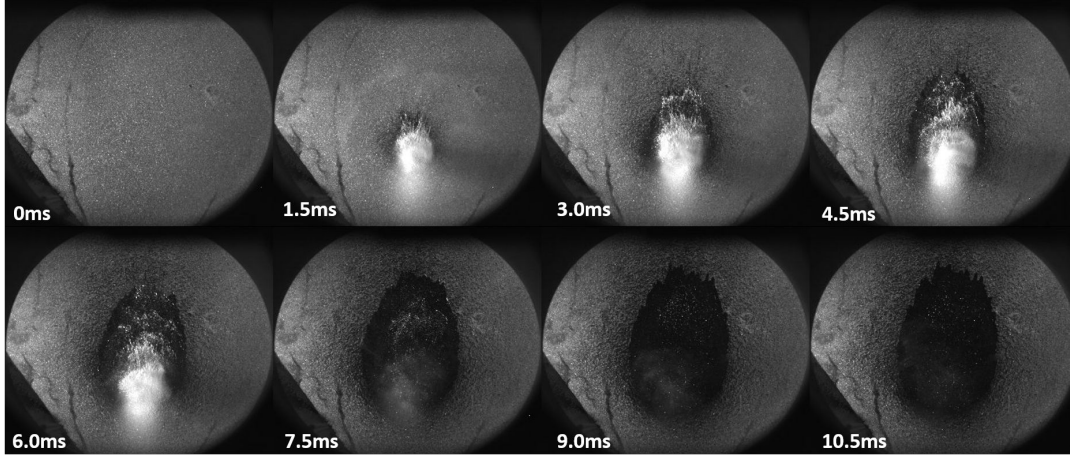
At the beginning of the impact process (first 1.5 ms), the spray is reaching the plate and the first droplets start to wet the plate. As the mass is accumulating in the impact region, it starts spreading in all directions. However, as the spray is reaching the plate with an angle different than  $90^\circ$ , it appears that the liquid film spreads rather in one direction. This side of the liquid film will then be referred as the front of the liquid film. In the other hand, the opposite direction will be referred as the back of the liquid film. The white area on the picture is produced by Mie scattering of droplets

---

<sup>1</sup>Impingement angle has been defined in Section 3.8

#### 4. LIQUID FILM SPREADING

---



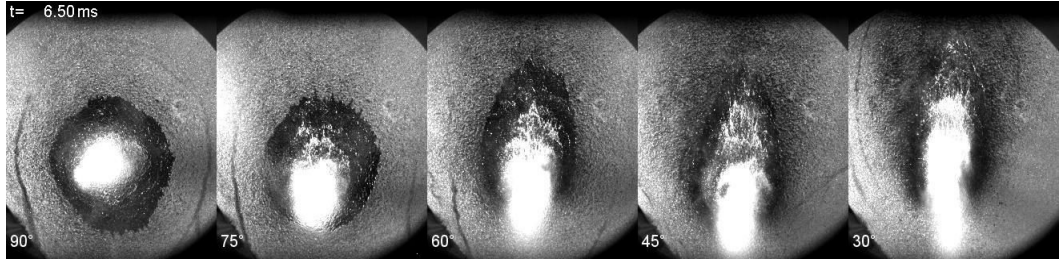
**Figure 4.22:** Image of film spreading of n-decane on a quartz plate, with an impingement angle of  $60^\circ$ .  $P_i = 100$  bar,  $T_i = 6$  ms and  $z = 50$  mm.

laying just on top of the plate (i.e. not wetting yet the plate) due to lighting at grazing angle. These droplets helps to identify the impact zone of the spray. Waves flowing on top of the liquid film are also observable; it has already been presented for orthogonal impingement and [50] also observed these waves for conditions more or less similar. [50] studied the causality between spray inhomogeneities and surface wave generation. Finally, at the end of injection, the apparition of fingers is recorded. This has also been observed by [50] and for orthogonal impingement, the normalised wave length  $\lambda/R$  of fingers apparition has previously been linked to the injection pressure  $P_i$ . The power law  $\lambda/R \propto P_i^{-1/3}$  is consistant with the apparition of fingers at the tip of a liquid film flowing on a inclined surface ( $\lambda \propto (\rho g \sin \alpha)^{-1/3}$  [33, 90]). Depending on the impingement angle and the material roughness, entrapped bubbles are also recorded. After some resting time, the bubbles vanishes and liquid is replacing gas entrapped. Finally, the shape of the liquid which is greatly influenced by the preferential direction induced by impact angle is assimilable to an egg or an ellipse.

The measures presented here were performed on rough plate, as one of the objectives was to study the effect of the angle on the deposited mass.

Figure 4.23 shows the evolution of the fuel film shape with respect to the impingement angle. When reducing the impingement angle, the liquid film gets longer and narrower. This is caused by a momentum flux, which is directed more and more along

the tangential direction and less in the normal direction. However, the shape of the liquid film is still oval. In order to describe this shape and its evolution, the liquid film will be assimilated to an ellipse with varying eccentricity, as will be explained further on. Figure 4.24 shows (for each impingement angle), the evolution of the liquid film



**Figure 4.23: Evolution of liquid film shape with respect to impingement angle at 6.5 ms after start of injection.  $P_i = 100$  bar,  $T_i = 6$  ms and  $z = 50$  mm.**

area with respect to time. During the injection duration, the area grows linearly with respect to time. This behaviour has already been presented and studied in the orthogonal impingement section. Though, the fact that it is still the case with non orthogonal impingement, is a very interesting property. The difference either in terms of spreading rate or in maximal area is small (14% in spreading rate and 13% in term of total area).

### 4.2.2 The spreading phase

Thanks to the use of Fiji [84], it is possible to track the edge of the liquid film, to get its center of mass and also to fit an ellipse to the selected area. The fitting function ensures that the ellipse and the liquid film have the same area. Figure 4.26 shows how the elliptic shape fits to the liquid film area. Using the properties of an ellipse (centre, major and minor axes), it allows to determine the position of the focus relatively to the centre (an ellipse is defined with two focus, hence, the one situated in the impingement area is the one we are taking care of). Tracking the focus position shows that, though it moves a bit, it stays inside of the impingement area (white region on RIM visualisation) (Figure 4.25). It is important to note that for the first millisecond, after the start of impingement, it is difficult to track the liquid film edge. The focus of the ellipse can then be associated with the impingement area.

Figure 4.27 presents the different characteristics of an ellipse, where  $O$  is the center,  $F$  one of the two focus and  $a$  and  $b$  are respectively the major and minor semi-axes.

#### 4. LIQUID FILM SPREADING

---

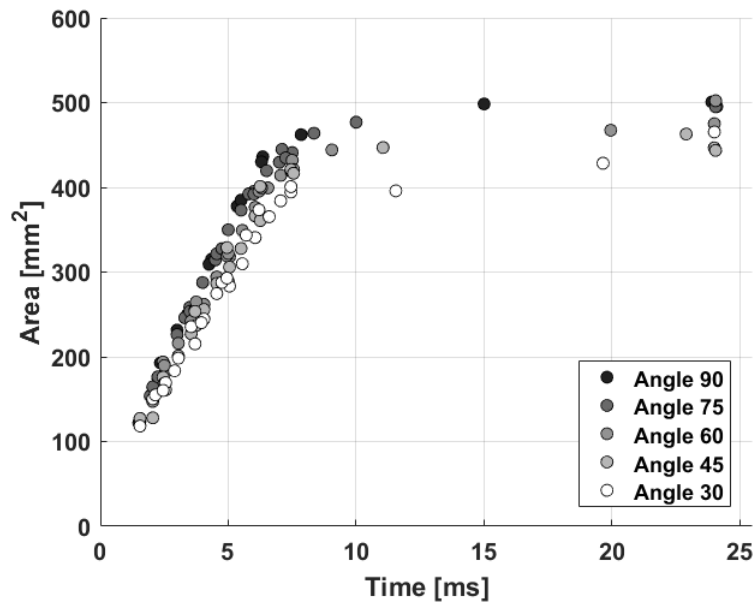
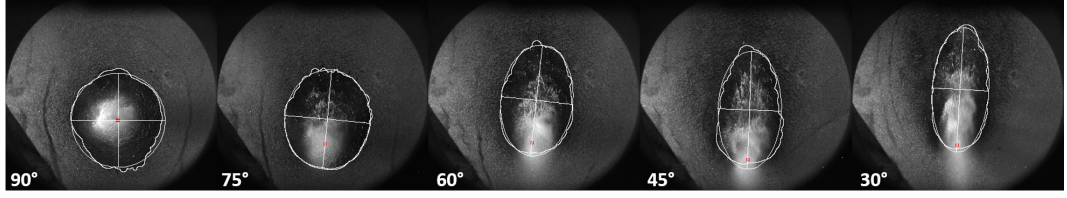


Figure 4.24: Time evolution of the liquid film area for several impingement angle. Experimental conditions:  $T_i = 6$  ms,  $P_i = 100$  bar,  $z = 50$  mm.



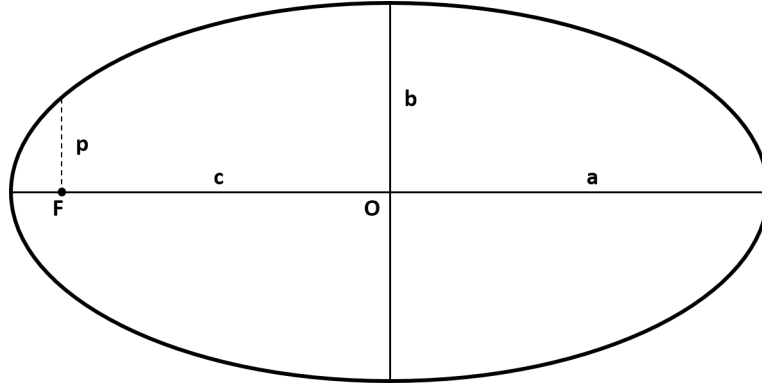
Figure 4.25: Evolution of ellipse focus position on time averaged image, the white area in the centre is the impingement area. Red squares present the position of the focus through time. White line displays the edge of the liquid film at the end of injection. Impingement angle is  $60^\circ$ .





**Figure 4.26:** Visualisation of liquid film edges together with ellipse contour and axes at a given time (5 ms after start of injection). Injection pressure  $P_i = 100$  bar, injection duration  $T_i = 6.0$  ms.

$c$  is the distance between the center and the focus, and  $p$  is the semi-latus rectum (or parameter) of the ellipse. Finally, the eccentricity of the ellipse, which is a key parameter in the definition of the ellipse shape, is defined as  $\epsilon = \sqrt{a^2 - b^2}$ .



**Figure 4.27:** Description of the parameters of an ellipse.

It allows to define several quantity that will be studied:  $a + c$  which is the distance between the focus and the front on the liquid film,  $a - c$  which is the distance between the focus and the back of the liquid film and  $p$  the distance between the focus and the side of the liquid film. The term front, back and side are chosen because it seems legitimate that the liquid film will spread in the preferential direction of the spray. The distances  $c$  and  $p$  can be calculated using the value of  $a$  and  $b$  obtained with Fiji.

The liquid film is assimilated to an ellipse of semi-major and minor axis  $a$  and  $b$  with a uniform thickness  $e$ , the mass balance writes:

$$\frac{d\pi abe}{dt} \approx K_m Q, \quad (4.13)$$

#### 4. LIQUID FILM SPREADING

---

$Q$  is the injection discharge of the injector,  $K_m$  stands for the effective injected mass that contributes to the liquid film (if  $K_m = 1$  the mass is integrally transferred to the liquid film). Equation 4.13 allows to derive a relation between  $a$  and  $b$  (the ellipse parameters) and  $e$  the thickness:

$$\pi a b e \approx K_m Q t. \quad (4.14)$$

The momentum balance is projected on the three main directions of the problem (i.e. Front  $f$ , Back  $b$  and side  $s$ ):

$$\begin{cases} \frac{\partial P}{\partial X} \Big|_f = \eta \frac{\partial^2 v_f}{\partial z^2} \\ \frac{\partial P}{\partial X} \Big|_b = \eta \frac{\partial^2 v_b}{\partial z^2} \\ \frac{\partial P}{\partial Y} \Big|_s = \eta \frac{\partial^2 v_s}{\partial z^2}, \end{cases} \quad (4.15)$$

where  $v_f = \frac{d(a+c)}{dt}$ ,  $v_b = \frac{d(a-c)}{dt}$ ,  $v_s = \frac{dp}{dt}$ . Equation 4.15 can be rewritten as:

$$\begin{cases} \frac{P_i}{(a+c)} \approx \frac{1}{e^2} \frac{d(a+c)}{dt} \\ \frac{P_i}{(a-c)} \approx \frac{1}{e^2} \frac{d(a-c)}{dt} \\ \frac{P_i}{p} \approx \frac{1}{e^2} \frac{dp}{dt} \end{cases} \quad (4.16)$$

$\Delta P$  the pressure in the liquid film is linked to the injection pressure using the coefficient  $K_P$  as a transfer function from the injector to the liquid film, such as  $\Delta P \approx K_P P_i$ . Assuming that the thickness is constant during the injection timing Equation 4.16 rewrites in a very simple way:

$$\begin{cases} (a+c)^2 \propto t \\ (a-c)^2 \propto t \\ p^2 \propto t \end{cases} \quad (4.17)$$

Equation 4.17 implies that the three quantity defined before are also growing linearly with respect to the injection duration, for each impingement angle. The linear behaviour highlighted by Equation 4.17 is presented in Figure 4.28 and 4.29. The linear evolution of the ellipse descriptors is confirmed by experimental data, indeed for  $(a+c)^2$ ,  $(a-c)^2$  and  $p^2$  the linear behaviour is retrieved, for all the angles tested here. Figure 4.24 showed that the area of the liquid film is proportional to the injection duration ( $A \propto t$ ). However, now it also indicates that the spreading is remarkably linear

in all the directions originating from the focus of the ellipse (assimilated at the impact point).

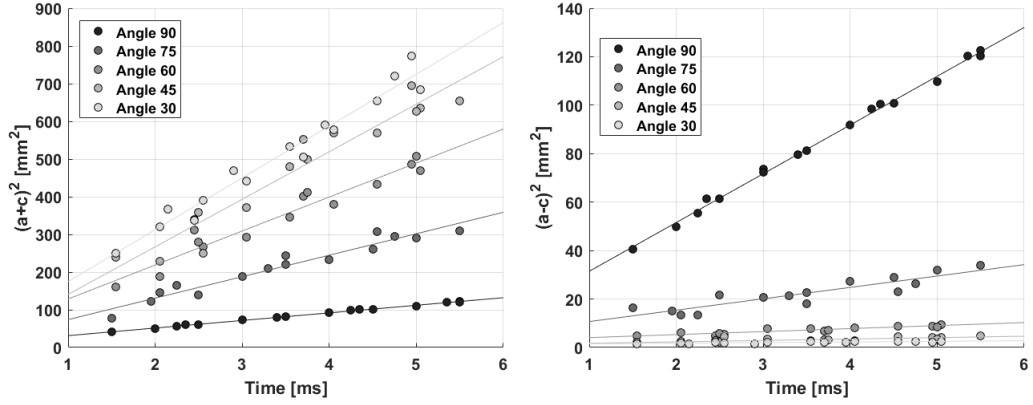


Figure 4.28: Temporal evolution of ellipse descriptors  $(a+c)$  and  $(a-c)$  parameters for several angles.  $P_i = 100 \text{ bar}$ ,  $T_i = 6 \text{ ms}$ .

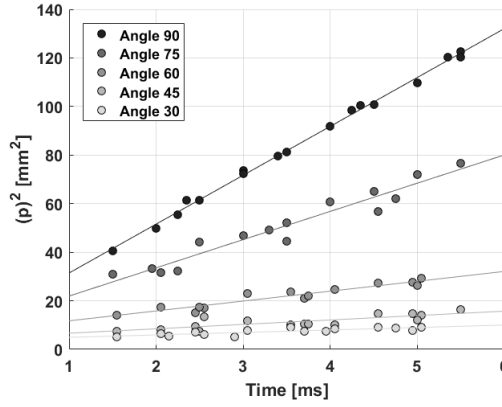


Figure 4.29: Temporal evolution of ellipse descriptor  $p$  for several angles.  $P_i = 100 \text{ bar}$ ,  $T_i = 6 \text{ ms}$ .

### 4.2.3 Angle dependency

The eccentricity of the ellipse associated to the different liquid films varies with respect to the angle of impingement. Figure 4.30 shows how it varies for different angles during the injection process. However, it can be noted that, for a given impingement angle, the eccentricity is slightly increasing during the injection.

#### 4. LIQUID FILM SPREADING

---

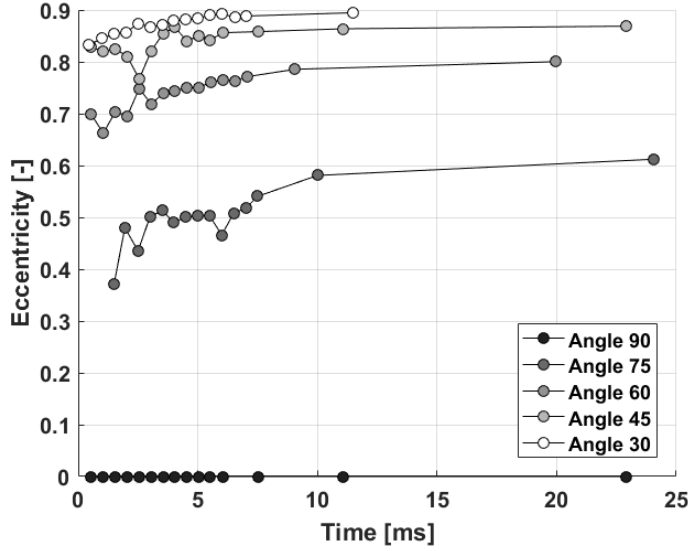


Figure 4.30: Temporal evolution of the liquid film eccentricity for different impingement angle. Injection pressure  $P_i = 100$  bar, injection duration  $T_i = 6$  ms.

On the other hand, from one impingement angle to another (i.e. a variation of  $15^\circ$ ), the eccentricity variation is greater than the augmentation during the injection process. Hence, eccentricity will be considered as constant for each impingement angle, as it is a good descriptor of the liquid film shape.

Figure 4.31 shows the evolution of the eccentricity with respect to impingement angle, a simple modelling of the eccentricity variation is also proposed and displayed in Figure 4.31:

$$\epsilon = \sqrt{\cos\theta} \quad (4.18)$$

Using the experimental data, fitting functions for the evolution of the spreading rates for  $(a + c)^2$ ,  $(a - c)^2$  and  $p^2$  are proposed:

$$\begin{cases} (a + c)^2 &= 20.(1 + 2 \cos\theta)^2 t \\ (a - c)^2 &= 20.(1 - \cos\theta)^2 t \\ p^2 &= 20.(1 - 1.3 \cos\theta)^2 t \end{cases} \quad (4.19)$$

Figure 4.32 and 4.33 shows the comparison between the fitting functions and the experimental values. The factor in front of  $\cos\theta$  results from the projection of the forces in

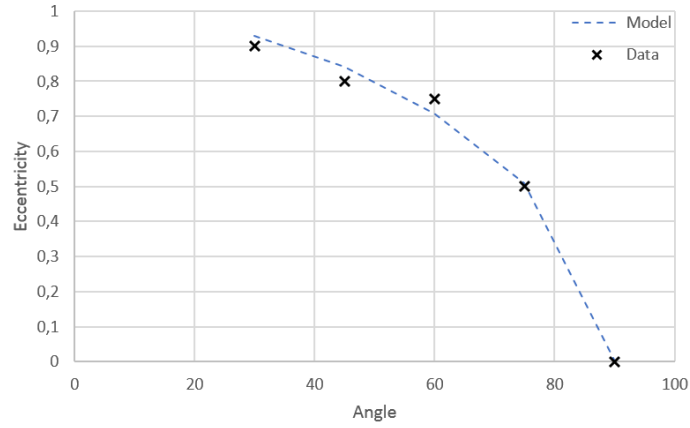


Figure 4.31: Eccentricity evolution for different impingement angle, together with the fit proposed Equation 4.18.

the different directions. Indeed, it is positive towards the head of the liquid film (which further increases the spreading rate) and negative for the side and back propagation directions (which reduces the spreading rate).

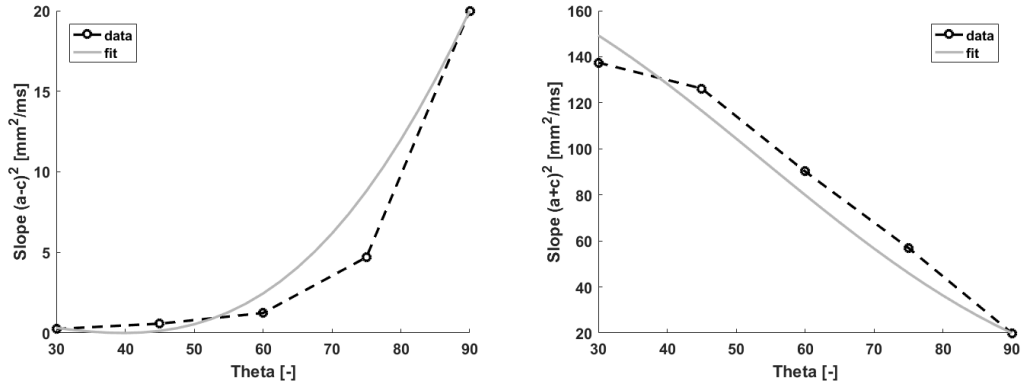


Figure 4.32: Evolution of the spreading rate for the head  $(a + c)^2$  and back  $(a - c)^2$  of the liquid film, together with the fit proposed in Equation 4.19.

A simple model has here been proposed to describe the spreading of liquid films generated by a plain conic spray impinging upon a wall in non-orthogonal conditions. As for orthogonal impacts, the linear behaviour of the area evolution is retrieved for all the angles, waves flowing over the liquid film and digitations at the leading edge of the

## 4. LIQUID FILM SPREADING

---

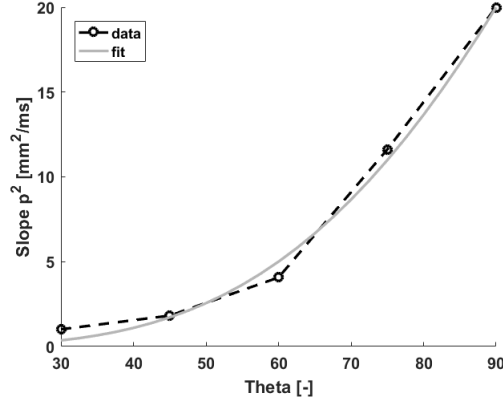


Figure 4.33: Evolution of the spreading rate for the side  $p^2$  of the liquid film, together with the fit proposed Equation 4.19.

liquid film have been observed once again. In appendix, we propose a more complete way to derive the equations previously presented, with more details and a link with the present results.

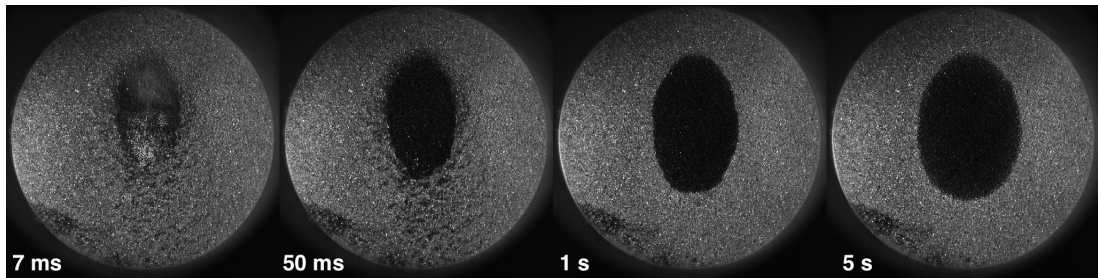
### 4.3 on the thickness of spreading liquid films

In this section will be presented some thickness and mass measurements obtained using the RIM method described in section 3.3. It immediately follows the spreading in orthogonal and non orthogonal conditions (as an evaluation of film thickness using the injection parameter as been presented). But it also follows the Section 3.3.4 on the drawbacks of the RIM method. The objective is to get the best from the performed measurements. However, it will also stress on the limits of the method.

Thickness measurement have been performed for three impingement angles  $90^\circ$ ,  $60^\circ$  and  $45^\circ$  and three pressures  $50 \text{ bar}$ ,  $100 \text{ bar}$ ,  $200 \text{ bar}$ . The injection duration has been adapted in order to always inject the same mass ( $T_i = 4.24 \text{ ms}$  at  $50 \text{ bar}$ ,  $T_i = 3.0 \text{ ms}$  at  $100 \text{ bar}$  and  $T_i = 2.12 \text{ ms}$  at  $200 \text{ bar}$ ).

The first thing that needs to be highlighted is that on the quartz plate, there is another spreading that occurs for longer time. Spreading during the injection and the relaxation at the end of injection has been modelled. Both phenomenon are occurring at the  $ms$  scale. However, a third spreading is also happening, but it takes several seconds to appear and is most likely due to gravity and surface tension effects at the

contact line. Figure 4.34 shows the liquid film for an impingement angle of  $45^\circ$ , at the end of injection ( $7\text{ ms}$ ), after the relaxation ( $50\text{ ms}$ ) and at respectively 1 and 5 seconds after the end of injection. It can be seen that the liquid film has slowly continued to spread. Modelling this spreading phase is not on the scope of this work, as it totally gets out of the typical duration of engine cycles.



**Figure 4.34: Liquid film visualisation on quartz plate at several time after start of injection.**  $P_i = 100\text{ bar}$ ,  $T_i = 6\text{ ms}$ .

As stated in the section on the limitations of the method (Section 3.3.4, the RIM presents a saturation (due to the roughness level). Figure 4.35 shows the average thickness evolution over the wall film and it can be seen that the maximum of thickness is recorded 1 or 2 seconds after the start of injection. This is physically not possible as the liquid film is still spreading (Figure 4.36) while some film mass has probably already been lost. It would mean that the liquid film mass is increasing during this spreading time, while there is no more spray (or even droplets) impacting this late. The reasons to explain this mass increase a long time after the end of injection are multiple:

- The grey level due to entrapped bubbles (or late droplets scattering light) leads to underestimation of the thickness just after the end of injection.
- The method seems to be sensitive only when the thickness is below  $5\text{ }\mu\text{m}$  (saturation of the method).

Finally, a mass estimation is presented (Figure 4.37), using the average thickness and area evolutions. It shows that the maximum of mass is reached 2 to 5 s after the injection. Once again, this seems really questionable but it is coherent with what is reported in [44, 52], though some valuable results can be proposed. It shows, that the liquid film lifetime and thickness (for the three angles) decreases with respect to the

#### 4. LIQUID FILM SPREADING

---

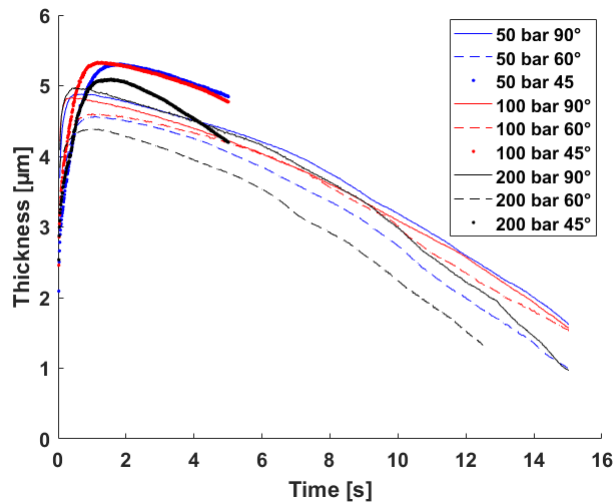


Figure 4.35: Average thickness evolution for three different impingement angles ( $90^\circ$ ,  $60^\circ$  and  $45^\circ$ ) and pressures (50 bar, 100 bar, 200 bar). The mass injected is kept constant in all the injection scenario.

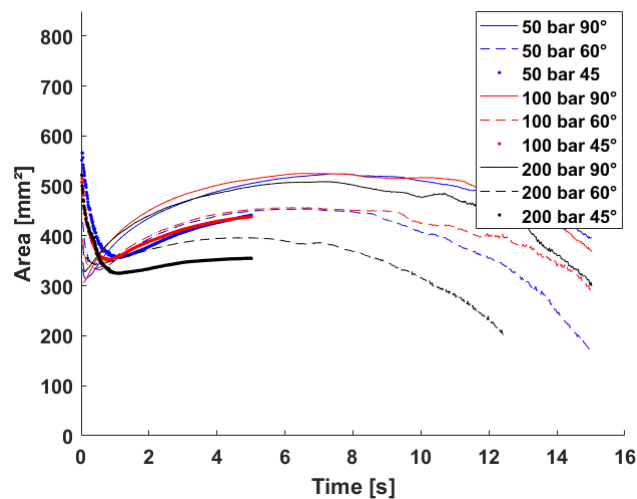
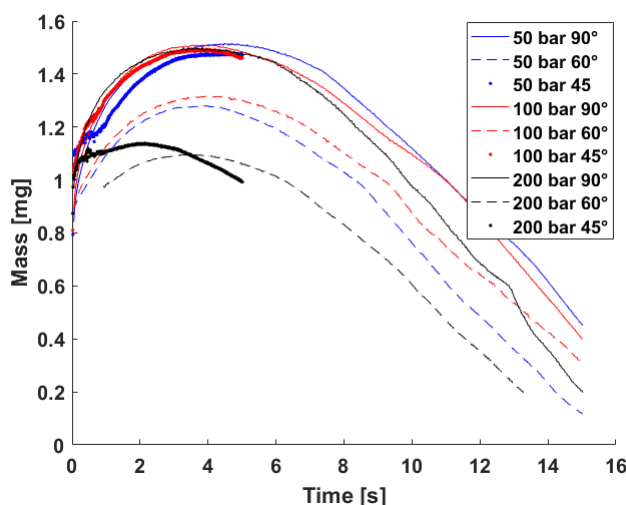


Figure 4.36: Area evolution for three different impingement angles ( $90^\circ$ ,  $60^\circ$  and  $45^\circ$ ) and pressures (50 bar, 100 bar, 200 bar). The mass injected is kept constant in all the injection scenario. During the first  $ms$  the area is highly overestimated due to image detection algorithm that has difficulties to differentiate the liquid film and the sparse droplets.



injection pressure (at least for high pressure injection). This is in accordance with the model and what has already been reported in literature [41, 45, 86]. It also seems that increasing the impingement angle increases the lifetime of the liquid film (it is hard to affirm this as at an impingement angle of  $45^\circ$ , the data are incomplete).



**Figure 4.37:** Mass evolution for three different impingement angles ( $90^\circ$ ,  $60^\circ$  and  $45^\circ$ ) and pressures (50 bar, 100 bar, 200 bar). The mass injected is kept constant in all the injection scenario.

An estimation of  $K_m$  can be proposed as the injected mass is known, and it gives a value for  $K_m$  (again several seconds after the end of injection) between 0.15 and 0.23 (i.e. 15% and 23% of the injected mass has been deposited). This value is in good accordance with the one used to calibrate the model ( $K_m = 0.38$ ) as one needs to keep in mind that some of the deposited mass has vaporised during the 2 to 5 s before the maximum of mass is reached.

## 4.4 Conclusion

This chapter has described the spreading process of a liquid film over a flat wall for many different injection conditions, Table 4.5 gives a summary of the experimental campaigns performed. Injection duration, injection pressure, fuel influence, wall roughness influence, injection temperature and impact angle have been considered (pressure variation up to 350 bar have been performed, for confidentiality reasons they are not presented

#### 4. LIQUID FILM SPREADING

---

here, the model is still valid at such injection pressures). A modelling of the spreading rate and the relaxation phase as been presented for the orthogonal impingement and extended for the spreading rate for a non orthogonal impact has also been derived. The developed model is robust, indeed it integrates all the effect that has been considered during the study. It has also raised the question of the vaporisation during the travel time of the spray, and the real temperature at the impact. Finally, thickness evaluation for several injection conditions have been proposed.

Campaign	Injection Pressure $P_i$ [bar]	Injection Duration $T_i$ [ms]	Distance $z$ or $d$ [mm]	Temperature $T_{Fu}$ [°C]	Impingement Angle $\theta$ [-]	Fluid	Wall Roughness $\varepsilon$ [ $\mu$ m]	Commentary
PRF	50-100-200	2-4-6-8-10-12	20-35-50-65	90	90	n-decane	smooth Sapphire	<ul style="list-style-type: none"> <li>• <math>A \propto t</math> smooth</li> <li>• Relaxation phase</li> <li>• <math>K_m</math>, <math>K_p</math> value</li> </ul>
EFMC Thickness RIM Thickness iso-mass	100	6	50	90	90-75-60-45-30	n-heptane	15 $\mu$ m Quartz	• $A \propto t$ for any angle
	50-100-200	6	50	20	90-75-60-45-30	n-heptane	15 $\mu$ m Quartz	• Split of momentum balance
	50-100-200	4, 24-3, 00-2, 12	50	20	90-75-60-45-30	n-heptane	15 $\mu$ m Quartz	• Thickness angle dependency
Roughness Effect	100	6	50	20	90	n-decane	smooth Sapphire 15 $\mu$ m Quartz	<ul style="list-style-type: none"> <li>• <math>A \propto t</math> rough</li> <li>• Shear stress increases due to roughness</li> <li>• Spreading rate decreases with roughness</li> </ul>
Fluid and Temperature effect	100	6	50	20	90	n-heptane n-decane	Smooth	• $\mu$ and $\rho$ taken into account
Temperature Effect	100	6	50	20-50-70-90-120	90	n-decane	Smooth	• Variation of $\rho$ and $\mu$ with T
Low pressure	10-20 30-40	15-15 12-10	50	70	90	n-decane	smooth Sapphire	• $K_m$ evap
ILASS	50-100-200	2-3-4-6	50	20	90	n-heptane	15 $\mu$ m Quartz	• Global Verification of the model

Table 4.5: Overview of the experimental campaigns performed on film spreading topics.

#### 4. LIQUID FILM SPREADING

---

# 5

## Heat Transfer Modelling

### Contents

---

<b>2.1</b>	<b>Context</b>	<b>23</b>
<b>2.2</b>	<b>Experimental Set-up</b>	<b>26</b>
2.2.1	Position of the thermocouples	28
2.2.2	Signal Transmission	29
2.2.3	Cylinder head instrumentation	30
<b>2.3</b>	<b>Results</b>	<b>31</b>
2.3.1	Temperature evolution during a combustion cycle	31
2.3.2	Piston temperature map	36
2.3.3	Influence of piston impingement	40
<b>2.4</b>	<b>Acknowledgment</b>	<b>49</b>

---

### 5.1 Context/Introduction

Engine measurements presented in Chapter 2 have highlighted the fact that piston temperature greatly varies depending on the engine operating point. It has also shown that the piston temperature can be strongly and locally impacted by the spray impingement. The use of the fast thermocouple measurement plate is to determine in what extend it is possible to reproduce the results in a more controlled atmosphere. This will lead to a parameter control, easier to perform than in a real engine where lots of parameters are connected to each other. Indeed in the engine, pressure and temperature are varying through a cycle. A lot of parameters are corrected depending on the engine speed and

## 5. HEAT TRANSFER MODELLING

---

load (such as injection pressure, injection duration, opening and closure of valve timing etc...). In order to get rid of the connection between all these parameters a study in a controlled atmosphere (out of the engine) is performed. The fast measurement of temperature variation due to spray impingement has already been performed by [2] in 1993 and by [75] in 2002. However, in the followings a presentation of 2D variation of the temperature, and a large parameter variation will be presented. Such parameter variation can be used as a database to increase the knowledge and the performance of CFD codes. A modelling of the heat exchanges between the spray and the plate is later proposed based on a temperature variation and flux reconstruction.

### 5.2 Spray wall heat transfer description

The experimental results presented here were all produced with the fast thermocouple measurement plate. The general reproducibility and repeatability of the injection process is correct, and shot to shot variability is small. However, the acquisition line of thermocouple signal generates noise on the signal. To increase the quality and robustness of the results noise is filtered out.

#### 5.2.1 Data processing

Figure 5.1 presents three different plots for the same operating point. The first one present the raw results, no filtering is performed and only one repetition is displayed. The second one present a moving average over 10 points ( $2\text{ ms}$  as the sample rate is  $0.2\text{ ms}$ ). Finally, the last curve presents the average of 10 repeats for the same injection conditions together with the standard deviation. The experimental conditions are,  $100\text{ bar}$  and  $6\text{ ms}$  for the injection pressure and the duration with wall temperature of  $100\text{ }^\circ\text{C}$  and the injector temperature of  $20\text{ }^\circ\text{C}$ . The distance travelled by the spray is  $50\text{ mm}$  and the impingement is performed with  $60^\circ$ .

The processing of the curve increases its readability. Indeed, it dampens the shot to shot variation induced by the injection system, and allows to filter the noises transmitted or produced by the acquisition line. Though the temporal and thermal position of the minimum ( $\pm 3^\circ$  and  $\pm 0.1\text{ ms}$  is affected by the post-processing, it can be estimated that the error introduced by the post processing is lower than  $10\%$  of the raw data, and it greatly increases the measure robustness and readability.

## 5.2 Spray wall heat transfer description

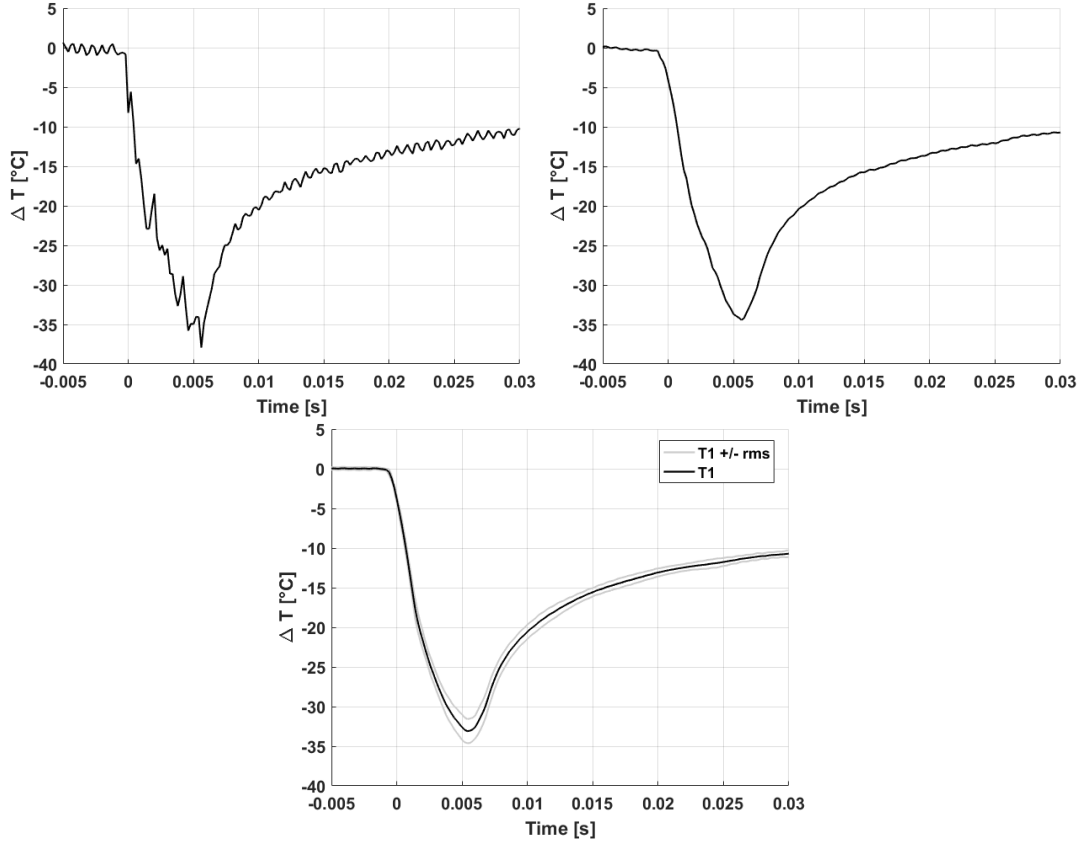
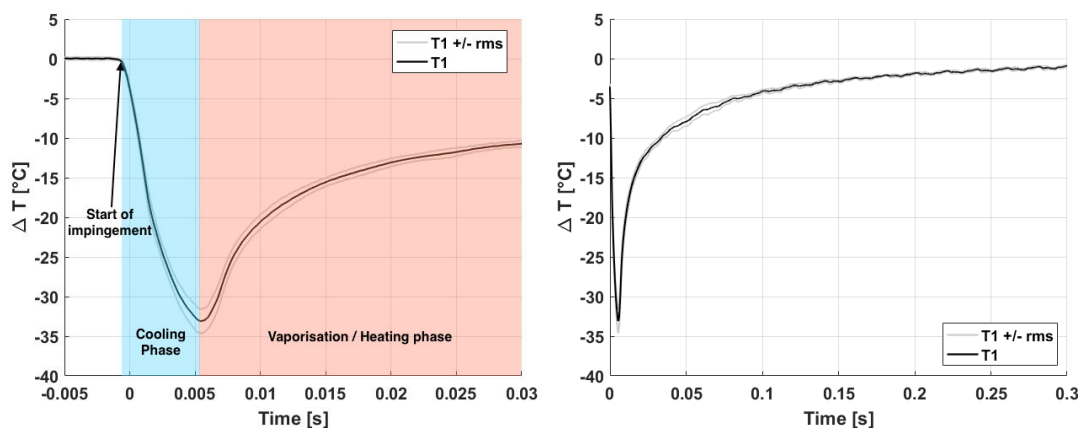


Figure 5.1: Fast surface thermocouple measurement for n-heptane impingement. Injection duration 6 ms, injection pressure 100 bar, wall temperature 100°C, fuel temperature 30 °C and injector to wall distance 50 mm. Left: Raw data with sample rate of 0.2 ms. Centre: Filtered data with 2 ms moving average. Right: Averaged measure over 10 repeats for the same injection conditions.

Figure 5.2 shows the effect of spray impingement on a hot plate. The conditions of injection are the same as presented above. As soon as the spray reaches the plate, the temperature starts to decrease. The temperature reaches its minimum when the injection process stops (6 ms after start of impingement), then the temperature evolves to reach its initial value. During the heating phase, vaporisation of the liquid film occurs. For these experimental conditions it takes up to 300 ms for the temperature to reach one degree below the initial temperature. In section 1.2 a time allowed for vaporisation of 20 ms has been defined, in the present case the piston temperature is

## 5. HEAT TRANSFER MODELLING

still  $12^{\circ}\text{C}$  below its initial value. Hence, for simulation the wall temperature before injection cannot be taken as the boundary condition for fuel film vaporisation.<sup>115</sup>



**Figure 5.2:** Fast surface thermocouple measurement for n-heptane impingement. Injection duration 6 ms, injection pressure 100 bar, wall temperature  $100^{\circ}\text{C}$ , fuel temperature  $30^{\circ}\text{C}$  and injector to wall distance 50 mm. Left: Physical description during the impact. Right: Temperature evolution focussed on the heating phase.

The objective of the study is to analyse the effects of the different injection parameters, to characterise the spatial dependency of the heat removal, propose some interpretations and to develop a simple model able to explain the different results.

### 5.2.2 Detailed description

Figures 5.1 and 5.2 illustrates the effect of the spray impingement on the plate temperature. A fine description of the process is now presented. The spray is composed of small droplets travelling at high speed and carrying with them a high density of latent heat. When reaching a hot wall, heat is transferred from the wall to the spray. This transfer has several components, the convection of gas and liquid over a hot wall, the heating of the adhered fuel up to the temperature of the plate. Finally the phase change, with enhanced contact interface due to droplets splashing, is probably the main component of this heat transfer. As the droplets reach the surface, they suck heat from the plate and the temperature starts to drop. Temperature keeps decreasing during the whole injection process, and reaches a minimum at the end of injection. When the



minimum is reached and the injection is stopped the temperature slowly reaches its initial value, two phenomenon are here competing. Heat conduction of the surrounding metal (in order to smooth the gradients of temperature in the material), and fuel film evaporation or vaporisation (depending on the plate temperature and fuel saturation temperature) that keeps cooling the surface of the plate from above.

### 5.2.3 2D Temperature map

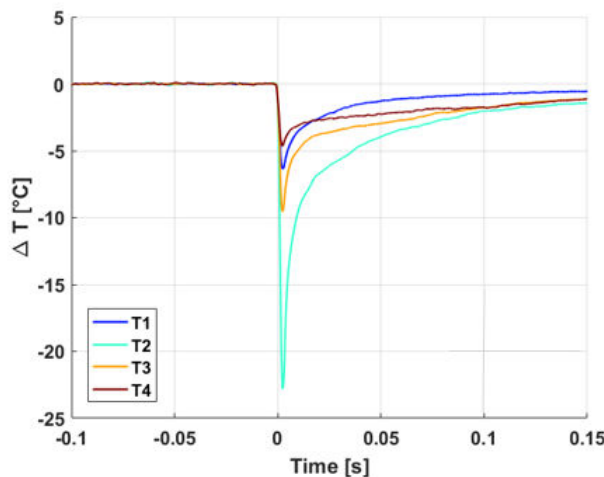
As presented in section 3.4 the distance between two thermocouples is 5 *mm*, this distance is quite large with respect to the liquid film size (around 2 *cm* for the films presented earlier), and the spatial dependency of the heat removal is a major interest. Indeed, in the chapter on engine measurements (Chapter 2), a loss of temperature of 7°C was recorded, and one question arose: is it the maximum loss, or could it be worse, some millimetres away?

To illustrate this some data produced when the experimental set-up was tested for the first time (i.e December 2016) are displayed (Figure 5.3), where  $T1$  to  $T4$  are respectively the temperature of thermocouple 1 to 4. Immediately it appears that (the spray positioned so the liquid film covers the four thermocouples) the loss of temperature is sensibly different on the four thermocouples. It raises the question of the minimum of temperature. Is it localised (in this case) between thermocouple 2 and 3, or the minimum is correctly recorded by thermocouple 2. The temperature of thermocouple 1 is crossing the one of thermocouple 4 during the heating phase, as the impingement is performed non orthogonally thermocouple one is in the back of the liquid film whereas thermocouple 3 and four are in the head of the liquid film (head and back as defined in Section 4.2).

Hence, in order to obtain the thermal footprint of the spray and be sure not to miss some information, a slight modification of the experimental set-up as been made. Two 1-D mechanical translation plate (with 0.01 *mm* of accuracy) are used to move the instrumented plate in two dimensions. The final discretisation obtained using the translation plates is 1 *mm*, which is 5 times more than the one of the thermocouple plate.

## 5. HEAT TRANSFER MODELLING

---



**Figure 5.3:** Simultaneous temperature variation of the four thermocouples, for an impingement angle of  $60^\circ$ . Wall temperature is  $100^\circ\text{C}$ , fuel temperature is  $30^\circ\text{C}$ , injector-wall distance is  $50\text{ mm}$  and injection pressure and duration are  $100\text{ bar}$  and  $2.12\text{ ms}$ .

### 5.2.3.1 Orthogonal Impingement

Figure 5.4 displays the temperature evolution for orthogonal impingement ( $\Delta T = T_w - T_{init}$ ), the temperature field is assumed axisymmetric for orthogonal impingement, hence translation is performed in only one direction. The wall temperature is set to  $100^\circ\text{C}$  and fuel temperature is  $50^\circ\text{C}$ , the maximum temperature drop is  $\Delta T = 23.8^\circ\text{C}$ . This temperature is reached  $6\text{ ms}$  after the start of impingement, which corresponds to the injection duration. Figure 5.5 shows a radial cut on the temperature map. It can be seen that it is almost symmetrical, which justifies the axisymmetry. This, despite the jet not being perfectly symmetrical. However, the main information is that 28 % ( $-6.6^\circ\text{C}$ ) of the maximum drop is recorded  $5\text{ mm}$  away and only 10 % ( $2.4^\circ\text{C}$ )  $1\text{ cm}$  far from the impingement point. This means that the temperature (and heat) removal is very local.

In term of heat removal it is interesting to note that, as it is quite important at the impingement location, the boundary condition for evaporation/vaporisation is different from the one imposed before injection. For a given fuel injected on a wall at a temperature slightly higher than its boiling temperature, the wall surface temperature will actually be lower than the boiling temperature. Hence, heat transfer will be modified

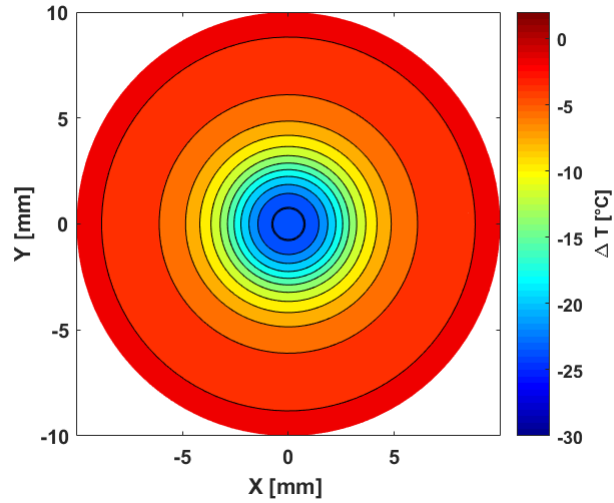


Figure 5.4: Temperature map for orthogonal impingement. Wall temperature is  $100^{\circ}\text{C}$ , fuel temperature is  $50^{\circ}\text{C}$ , injector-wall distance is  $50\text{ mm}$  and injection pressure and duration are  $100\text{ bar}$  and  $6\text{ ms}$ .

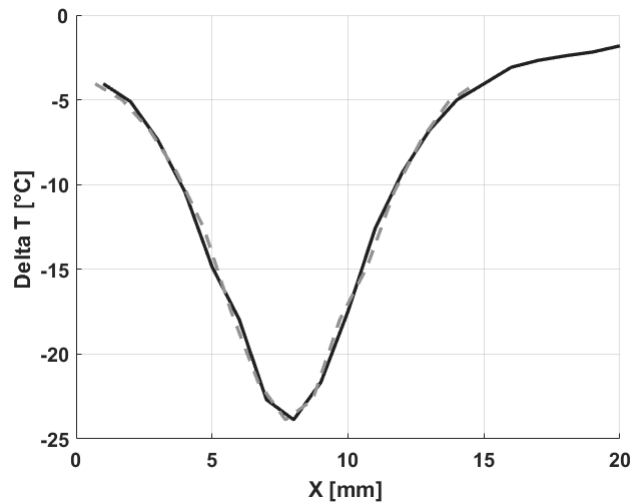


Figure 5.5: Temperature profile generated by orthogonal impingement. Continuous and dashed line are the same data mirrored to assess symmetry of the profile. Same conditions as Figure 5.4.

and it has to be taken into account for modelling or simulation, indeed vaporisation time could greatly differ depending on the prescribed boundary conditions. These time and spatial temperature variations are valuable inputs for validation and development

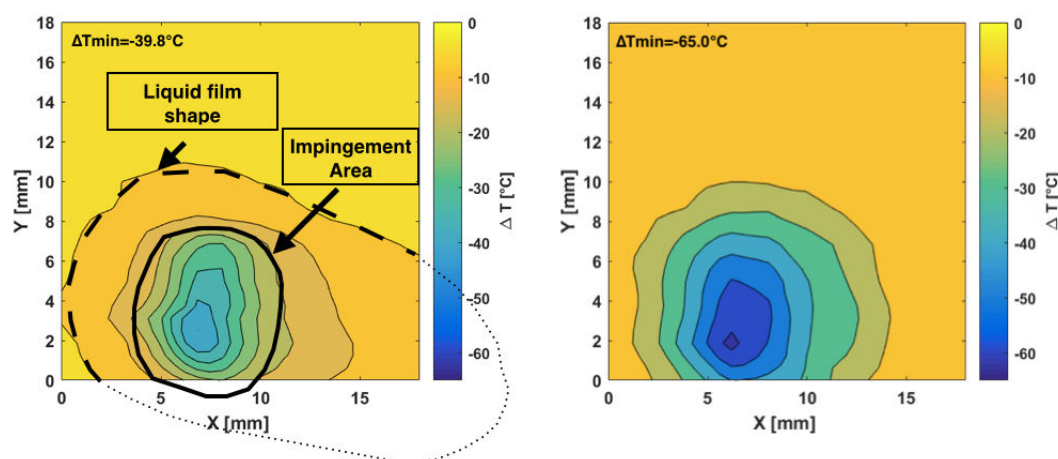
## 5. HEAT TRANSFER MODELLING

---

cases in CFD.

### 5.2.3.2 Non orthogonal impingement

Non orthogonal impingement have also been tested, for this visualisation the two translations were performed, as no symmetry can be assumed a priori. Figure 5.6 shows two 2D temperature maps for spray impacting with  $60^\circ$ . The injection conditions are kept constant except the wall temperature that is  $100^\circ\text{C}$  in the first case  $150^\circ\text{C}$  in the second case.

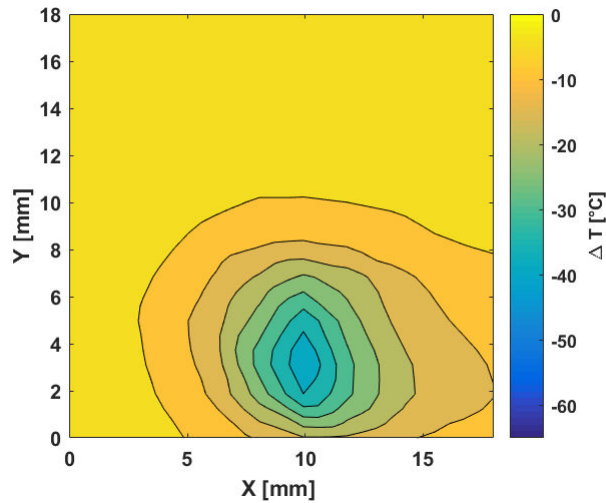


**Figure 5.6:** 2D Temperature map for  $60^\circ$  impingement angle, injection duration  $6\text{ ms}$ , fuel temperature  $30^\circ\text{C}$ , injection pressure  $100\text{ bar}$  Left: Wall temperature  $100^\circ\text{C}$ . Right: Wall temperature  $150^\circ\text{C}$ .

Looking carefully at the two maps presented in Figure 5.6 highlights one main difference, in the spreading direction of the liquid film, a temperature decrease can be seen at  $100^\circ\text{C}$  (a small dissymmetry is visible, it can come from the spray itself which is not perfectly symmetric, or from a bad positioning of the injector). Whereas at  $150^\circ\text{C}$ , the spray footprint has a more circular shape. It seems that the central, part cooled by the spray impingement is still observed (and almost circular at  $150^\circ\text{C}$ ). However, the elliptic shape in the spray propagation direction, which is seen at  $100^\circ\text{C}$ , does not appear at  $150^\circ\text{C}$ . These differences could be explained by the residence time of the liquid film, the shape recalls the one of liquid films with non-orthogonal impingement at lower temperature (observed with RIM set-up in Section 4.2). At a temperature

## 5.2 Spray wall heat transfer description

close to boiling point, the liquid film has the time necessary to recover the wall and then vaporise, whereas at higher temperature the liquid film vanishes instantaneously. In other words, two zones can be distinguished, the one cooled by the spray and the one cooled by the liquid film. Another angle ( $45^\circ$ ) has been tested at  $100^\circ\text{C}$  and the conclusions are roughly the same (Figure 5.7).



**Figure 5.7: 2D Temperature map for  $45^\circ$  impingement angle, injection duration 6 ms, fuel temperature  $30^\circ\text{C}$ , injection pressure 100 bar and wall temperature 100.**

Finally, an other campaign (unfortunately not complete) showed that for orthogonal impingement at a distance of 50 mm, injection duration of 6 ms, injection pressure of 100 bar (that is to say the same conditions as in Figure 5.6 (Left) and 5.7) the maximum of temperature drop reached is  $-46.2^\circ\text{C}$ . For an impingement angle of  $30^\circ$  it is  $-39.8^\circ\text{C}$  and for an impingement angle of  $45^\circ$  it is  $-39.9^\circ\text{C}$ . Hence, the orthogonal impingement has a greater cooling ability than non orthogonal impingement. The difference between impingement at  $30^\circ$  and  $45^\circ$  is not significant to conclude.

The two dimension maps, either for orthogonal or non-orthogonal impingement, showed that the temperature decrease is really local. Hence, assuming that the conditions are comparable it means that the temperature loss of  $7^\circ\text{C}$  recorded in the engine can be the witness of a temperature drop way more important (30 to  $60^\circ\text{C}$ ). If so, it implies that the conditions for the liquid film vaporisation will be highly unfavourable.

## 5. HEAT TRANSFER MODELLING

---

However, these results need to be moderated. Indeed in the engine the piston is moving, hence the impingement area moves at the piston surface, it will spread the heat loss. Also, the injection duration are usually shorter than what has been tested here. It is also important to keep in mind that the pressure is varying in the engine, and either favourable (low pressure) or unfavourable (high pressure) can be experienced. Finally, in the engine the air motion is important whereas in the experimental facility the air motion is only induced by the spray displacement (the measured are performed in open atmosphere in a room of  $30\text{ m}^2$ , the only source of convection is from the security ventilation duct, several meters away from the injection area). The air motion will increase the heat transfer coming from above the piston.

This being said, the conclusion is that the temperature loss of  $7^\circ\text{C}$  recorded in the engine is more than likely greater than this value. However, the temperature loss recorded on the thermocouple plate are probably an upper bound of what is experienced in the engine.

A parameter variation is now presented, in order to characterise the individual effects of the injection parameters on the heat exchange between the spray and the wall.

### 5.3 Parameter Variations

In order to understand the influence of the injection parameters on the spray's temperature removal, each parameter have been tested separately and conclusion on cooling behaviour will be proposed. The experimental measures presented here come from different experimental campaigns (orthogonal/non orthogonal, long injection time, short injection time...) which were led with different objectives. The conclusions on the influence of each parameter are derived from data coming from the same experimental campaign to avoid ambiguities between the results. Hence, comparing the minimum of temperature observed from one section to the other is not advised as the spatial variation of the heat removal is really local (as presented before) and discrepancies could occur.

### 5.3.1 Injection duration effect

Figure 5.8 shows the temperature loss on one thermocouple for different injection duration (i.e. more mass injected). Two conclusions can be drawn from this graph, the first one is that, when injection duration is raised the temperature removal increases. The second one is that the curves seems to follow the same path, and the curve shape is the same for all the curves. Meaning that there is no change in the physical phenomenon causing the cooling.

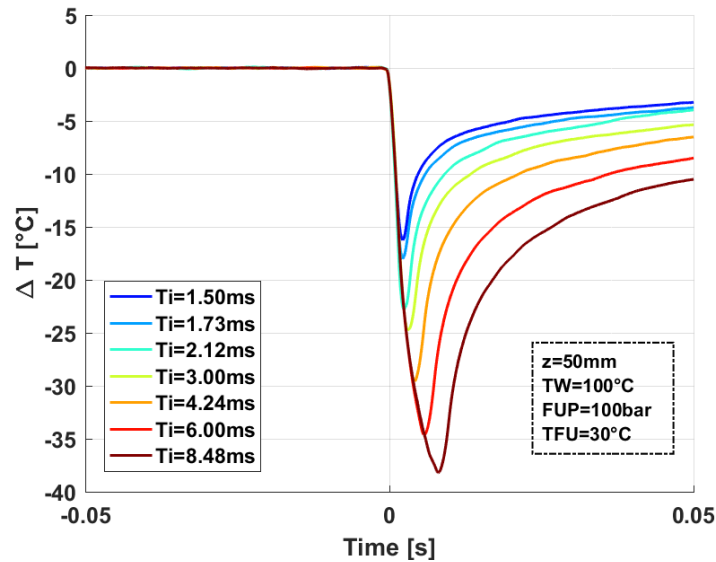


Figure 5.8: Effect of injection duration on wall cooling. Injection pressure 100 bar, wall temperature 100°C, fuel temperature 30°C, injector to wall distance 50 mm.

### 5.3.2 Pressure effect

In order to check the effect of pressure, it is necessary to ensure that the same mass of fuel is injected. As the discharge of the injector is proportional to the square root of  $\Delta P$ , raising the pressure by a factor two implies dividing the injection duration by  $\sqrt{2}$  to keep the same injected mass (considering that the discharge coefficient  $C_D$ [71] is constant). Figure 5.9 shows the effect of pressure on the temperature profile. The first

## 5. HEAT TRANSFER MODELLING

---

$T_i[ms]$	$\Delta T [^{\circ}C]$
1.50	-16.1
1.73	-18.1
2.12	-20.4
3.00	-24.7
4.24	-29.6
6.00	-34.6
8.48	-38.2

**Table 5.1: Effect of injection duration on wall cooling.**

observation, is that the peaks are shifted in time, obviously this is due to the injection duration, which changes. The minimum of temperature is reached for  $\Delta P = 100bar$ , however the difference of  $\Delta T$  is around  $4^{\circ}C$  in the whole range of pressure tested. This difference is relatively small, and it is not possible to conclude with these informations on the cooling ability of the spray at different pressure. The widths of the peaks tend to indicate that, at lower pressures, the plate needs more time to go back to the initial temperature. However, to ensure this, it is necessary to look at the energy removed by the spray during the impingement process, this will be performed in Section 5.4

### 5.3.3 Wall temperature effect

The effect of wall temperature on  $\Delta T$  has been tested for four different temperatures 50, 100, 150 and  $200^{\circ}C$  with n-heptane. Figure 5.10 displays, for two different pressures, the effect of wall temperature. The main conclusion is that the drop of temperature augments with respect to the wall temperature increase, it is also interesting to note that the minimum of temperature is reached at the same time, confirming that the minimum temperature is systematically reached at the end of injection. It also confirms the fact that the impingement process controls the cooling phase. Finally, a change in shape can be identified for the two injection pressures when  $T_w = 150^{\circ}C$  during the heating phase.

Figure 5.11 shows pictures of the vaporisation of the liquid film at  $150^{\circ}C$ . In the movie it appears clearly that a nucleation site is attached just on top of the thermocouple. It can be ensured that this behaviour is linked to the nucleation site as it



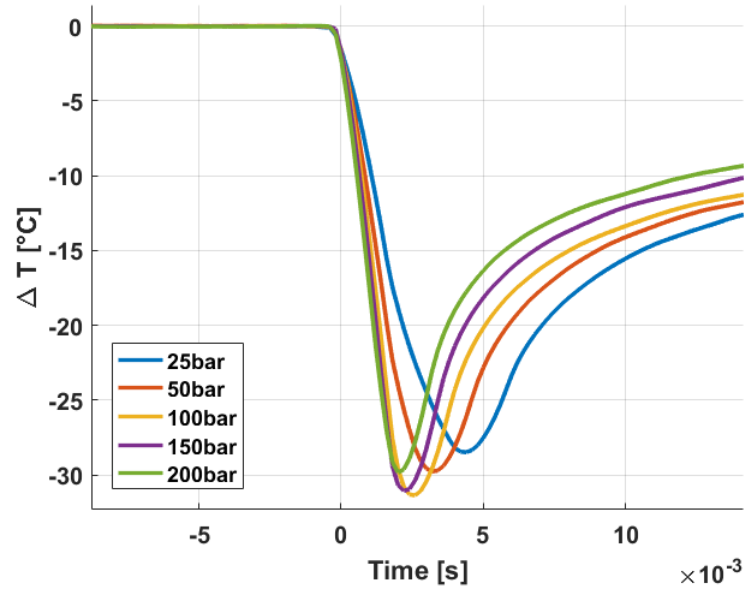


Figure 5.9: Effect of injection pressure. Wall temperature  $100^{\circ}\text{C}$ , fuel temperature  $30^{\circ}\text{C}$ , injection duration variable (i.e. constant mass), injector to wall distance  $30\text{ mm}$ .

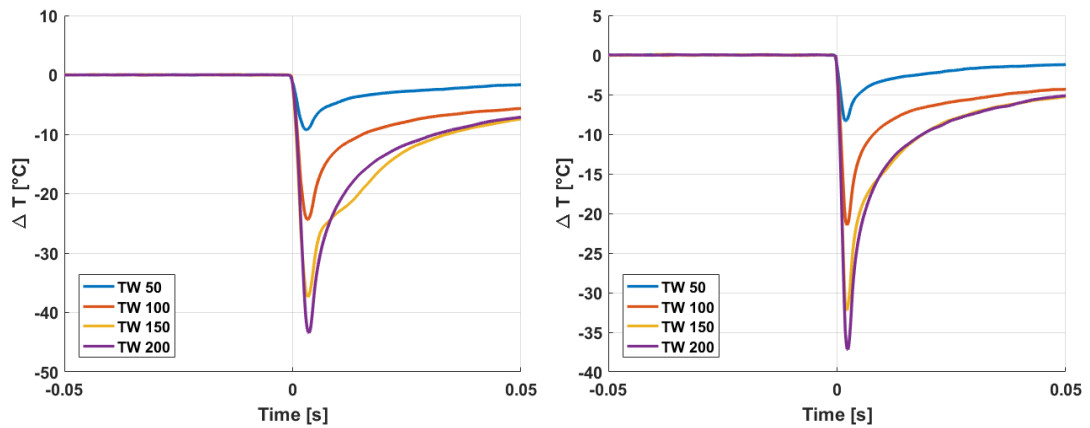


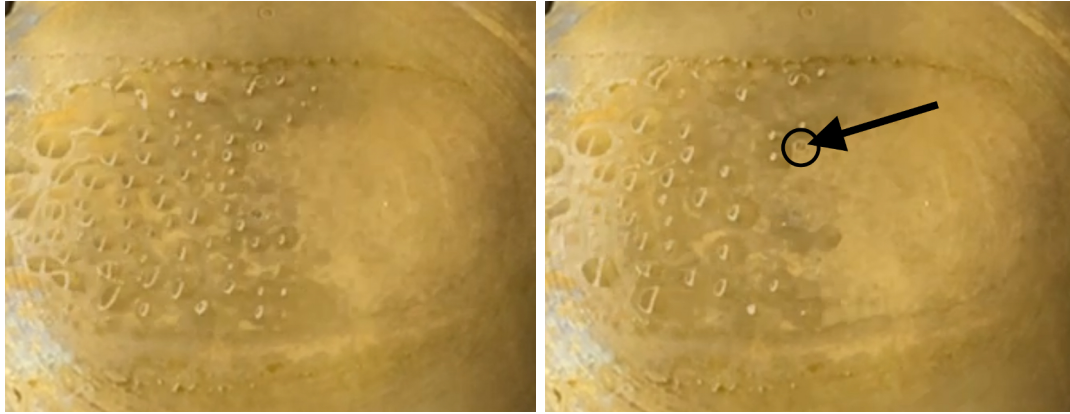
Figure 5.10: Effect of wall temperature, fuel temperature  $30^{\circ}\text{C}$ . Left: injection pressure  $P_i = 50\text{ bar}$ , injection duration  $T_i = 3.0\text{ ms}$ . Right: injection pressure  $P_i = 200\text{ bar}$ , injection duration  $T_i = 1.5\text{ ms}$

only appears when the temperature is between  $100^{\circ}\text{C}$  and  $150^{\circ}\text{C}$ . Moreover, this phenomenon does not appear at every injection, and looking at the thermocouple signal

## 5. HEAT TRANSFER MODELLING

---

clearly links the shape of the temperature curve to the nucleate boiling.

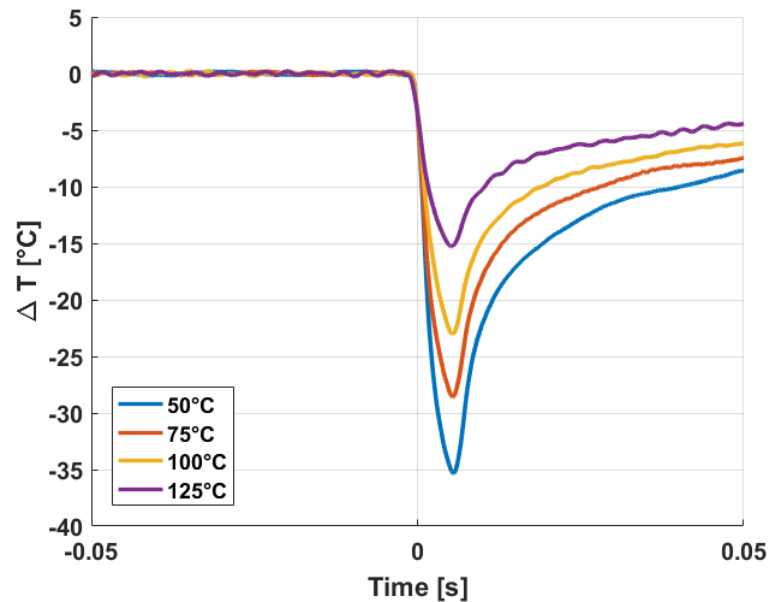


**Figure 5.11: Nucleate boiling on the thermocouple for injection temperature of 150°C. Left: nucleation site attached. Right: thermocouple visible without nucleation. Arrow and circle highlight the thermocouple position.**

### 5.3.4 Fuel Temperature effect

Figure 5.12 shows the effect of fuel temperature, the temperature of the injector being fixed at a constant temperature in order to study the effect of fuel temperature. Several observations are interesting to note. The first one is that when the fuel temperature is raised, the temperature removal decreases. This is easily guessable, as the difference of temperature between the wall and the spray gets lower, hence the heat transfer is less powerful. However, when the temperature of the fuel is higher than the wall temperature, the surface is still cooled by the spray. This result is still valid when the fuel temperature is larger than the saturation temperature of the fuel, as shown in Figure 5.12. Indeed, n-heptane saturation temperature is 98°C and cooling is still recorded when the injector is heated at 125°C. This observation recalls what has been discussed for the film spreading at variable temperature. Indeed, it has been said that: the temperature at the impact is likely to be colder than the one imposed at the nozzle exit. Several explanations can be proposed. The first one is the structure of the spray itself. The spray is composed by fuel but also by the surrounding air entrained by the fuel motion. In this case, the air is at ambient temperature so the impacting spray gets cooled by the surrounding air (it has not been taken into account in section 4.1.6 as it is complicate to estimate the heat transfer between the droplets and the

air, but also to evaluate the exact quantity of air entrained by the spray). The second explanation is the vaporisation of the fuel during the travel time of the spray. Due to the high temperature of the fuel and the speed of the droplets a part of the injected fuel vaporises before reaching the plate, this endothermic phenomenon is also responsible of spray cooling. One observation that is still interesting is that once again the minimum of temperature is reached at the same time which correspond to the end of injection process.



**Figure 5.12: Effect of fuel temperature. Wall temperature  $100^{\circ}\text{C}$  , injection pressure  $P_i = 100 \text{ bar}$ , injection duration  $T_i = 6.0 \text{ ms}$**

#### 5.3.5 Injector to wall distance

The last parameter varied is the injector to wall distance. More than the injector to wall distance it is the travel distance of the spray that is studied. Figure 5.13 depicts the effect of distance. It is clear that when the injector gets closer to the wall the temperature drop increases. Two main arguments are in favour of this phenomenon, the first one is the impinged quantity, the second one is the speed of the droplets. When reducing the distance between the injector and the wall, the time available for the droplets to vaporise is also reduced. The quantity of fuel to vaporise is greater

## 5. HEAT TRANSFER MODELLING

---

which helps to cool the surface. The other factor that might be important is the speed of the droplets. Indeed as the spray slows down with the travelling distance, the energy transmitted during the impact is smaller and then cooling is less efficient.

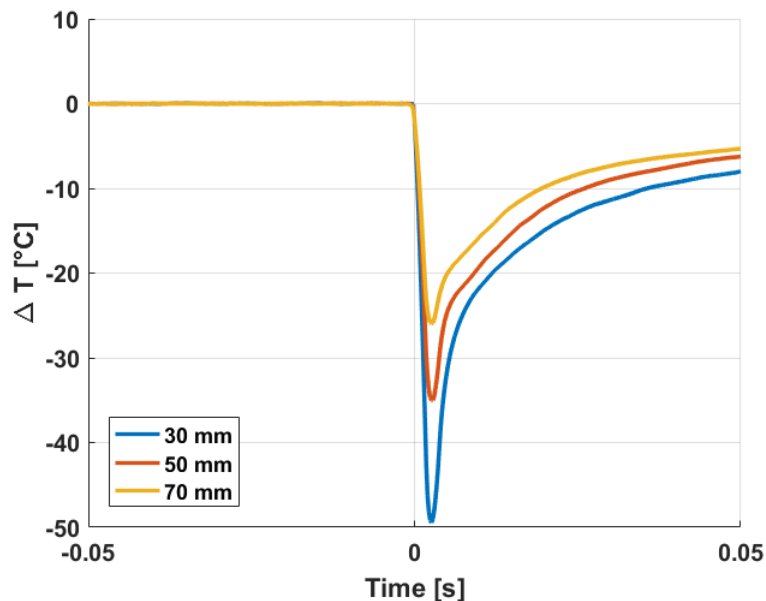


Figure 5.13: Effect of spray travelling distance, wall temperature  $150^{\circ}\text{C}$ , fuel temperature  $30^{\circ}\text{C}$  and injection pressure  $P_i = 100 \text{ bar}$ , injection duration  $T_i = 2.12 \text{ ms}$ .

### 5.4 Flux Calculation

The time evolution of the surface temperature has been recorded thanks to the fast surface thermocouples. These data, in spite of their raw utility, can be used to calculate the heat flux removed from the plate by the spray impingement. To perform this flux calculation a method presented in [75] is used. The method is based on the assumption that the heat conduction in the plate is one-dimensional in the direction normal to the wall. The temperature gradient for comparable experimental setup are:

- In [56], the radial gradient is estimated at  $10^3 \text{ K/m}$  whereas the orthogonal gradient is estimated at  $10^5 \text{ K/m}$

- In [2], the radial gradient is estimated at  $18K/mm$  whereas the orthogonal gradient is estimated at  $257K/mm$

In this work it is possible to estimate these gradients thanks to the thermocouple that are inserted in the depth of the wall film. One thermocouple is inserted at  $0.1mm$  below the surface, and only half a millimetre away from one of the surface thermocouple. Thanks to the map presented in Figure 5.6 it is possible to get the vertical gradient without correcting for the  $0.6 mm$  distance between the thermocouples. It gives for the plate heated at  $150^\circ C$  a vertical gradient of  $4.5 \times 10^5 K/m$  and a radial gradient of  $5.2 \times 10^3 K/m$ . The two orders of magnitude between the gradients allows to validate the hypothesis of 1D heat conduction.

The method used to reconstruct the flux has been developed by [75] and is applied to the data produced with the fast thermocouple instrumented plate. As the problem is considered one dimensional the heat equation writes:

$$\frac{\partial \theta}{\partial \tau} = \frac{\partial^2 \theta}{\partial \xi^2} \quad (5.1)$$

with  $\theta$  the temperature deficit of the surface,  $\delta$  the wall thickness,  $\tau = ta/\delta^2$  the dimensionless time and  $\xi = z/\delta$  the dimensionless distance. The boundary conditions before impingement writes as follows:

$$\begin{aligned} \theta(\xi, 0) &= 0, \\ \theta(0, t) &= \vartheta_s(t) - \vartheta_\delta = \theta_s(t), \\ \theta(1, t) &= 0. \end{aligned} \quad (5.2)$$

The instantaneous heat flux can be calculated thanks to the surface variation of wall temperature:

$$\dot{q}'' = -\frac{\lambda}{\delta} \cdot \frac{\partial \theta}{\partial \xi}(0, \tau), \quad (5.3)$$

where  $\lambda$  is the thermal conductivity of the material. Using Laplace transformation the equations can rewrite as:

$$s\bar{\theta}(\xi, s) - \theta(\xi, 0) = s\bar{\theta}(\xi, s) = \frac{\partial^2 \bar{\theta}}{\partial \xi^2} \quad (5.4)$$

$$s\bar{\theta}(\xi, s) = \bar{\theta}_s(s) \cdot \frac{e^{-p\xi} - e^{p(\xi-2)}}{1 - e^{-2p}} \quad (5.5)$$

## 5. HEAT TRANSFER MODELLING

---

$$\frac{\partial \bar{\theta}}{\partial \xi}(0, s) = -\bar{\theta}_s(s)p \cdot \frac{1 + e^{-2p}}{1 - e^{-2p}} \quad (5.6)$$

Using Taylor expansion, transformation tables given in [10] and convolution theorem the wall heat flux can be determined as:

$$\dot{q}''(\tau) = \frac{\lambda}{\sqrt{\pi} \cdot \delta} \int_0^\tau \frac{d\vartheta_s}{d\tau^*}(\tau^*) \cdot \frac{1}{\sqrt{\pi(\tau - \tau^*)}} \times \left( 1 + 2 \sum_{n=1}^{\infty} e^{-(n^2/(\tau - \tau^*))} \right) d\tau^* , \quad (5.7)$$

where  $\vartheta_s$  is the surface temperature measured. The problem is solved using numerical schemes for small value of  $\tau$ . The whole expression of the heat flux can be rewritten as:

$$\dot{q}''(\tau_i) = 2 \frac{\lambda}{\delta} \sqrt{\frac{\Delta\tau}{\pi}} \sum_{k=0}^{i-1} \left( \left( \vartheta'_{S,k} + \vartheta''_{S,k} \Delta\tau \left( i - \frac{2k+1}{2} \right) \right) \times R_{i,k} - \vartheta''_{S,k} \frac{\Delta\tau}{3} S_{i,k} \right) \quad (5.8)$$

with

$$R_{i,k} = (i - k)^{1/2} - (i - k - 1)^{1/2} \quad (5.9)$$

$$S_{i,k} = (i - k)^{3/2} - (i - k - 1)^{3/2} \quad (5.10)$$

Full details of the methodology can be found in [75]. Applying this method to the data produced with the instrumented plate allows to calculate the heat flux induced by the spray impingement on the wall. In [56, 75] the conductivity used is the one of the thermocouple material which is mainly composed of Nickel. In [2] it is not clear which material property are used to calculate the heat flux, it is stated that "  $k_w$ ,  $\rho$ ,  $C_p$  are the thermocouple conductivity, density, and specific heat of the wall respectively". Figure 5.14 shows the heat flux calculation together with the transient temperature distribution at the surface associated. Here the physical properties of the aluminium are used for the computation of the heat fluxes.

This figure teaches a lot. First the order of magnitude of the cooling proposed by the spray is huge  $20 \text{ MW} \cdot \text{m}^{-2}$ . Indeed sprays are one of the most dense system in term of cooling ability. Figure 5.15 shows in a logarithmic scale the heat transfer coefficient associated with various cooling systems [89]. The shape of the heat flux is also interesting: it can be seen that the maximum is not reached at the end of injection but earlier. This is due to the difference of temperature between the spray and the wall that is decreasing with the injection duration. The curve of heat flux is also offset in

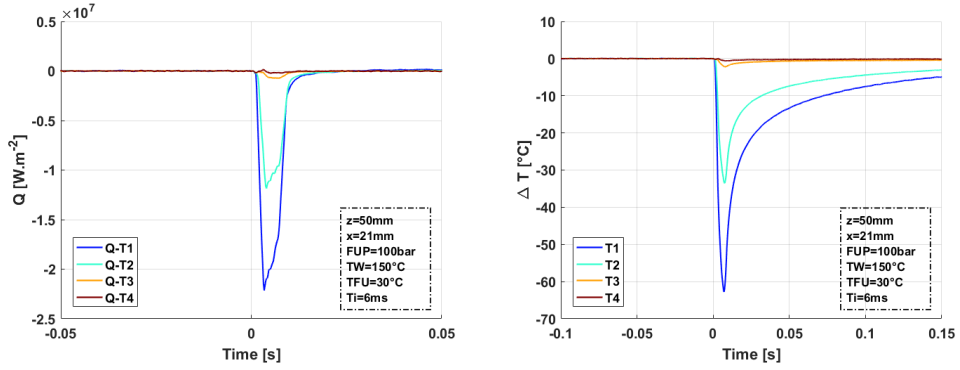


Figure 5.14: Heat flux and temperature temporal variation.

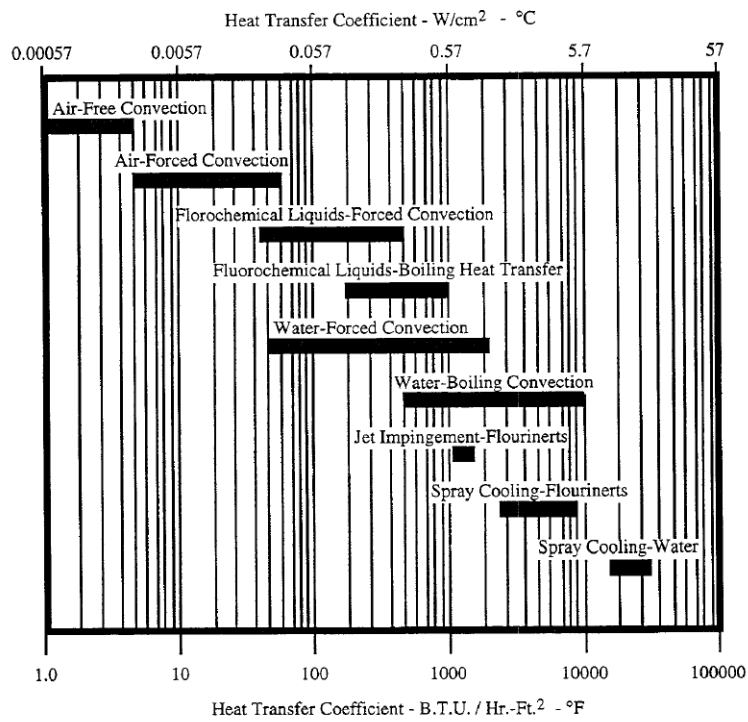


Figure 5.15: Heat transfer coefficient variation [89]

time, the process starts around 1.5 *ms* after the start of impingement and also last 1.5 *ms* more than the injection duration.

Here the heat transfer is really local, as 5 *mm* away from the first thermocouple, only half of the heat flux is remaining. Comparing these data with what [2, 56] found

## 5. HEAT TRANSFER MODELLING

is really interesting, indeed the order of magnitude is comparable, and the shape of the heat flux temporal variation also (Figure 5.16)

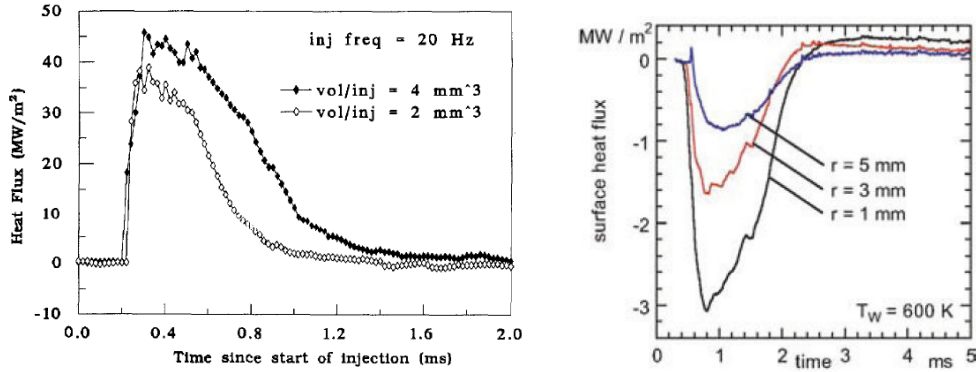


Figure 5.16: Heat flux calculation of Arcoumanis [2] and Meingast [56].

### 5.5 Heat exchange modelling

One of the objective of this section is to provide a model for the heat transfer in the wall, in order to substitute it to experimental data. In the mean time, the objective is not to code a temperature solver, as plenty of them already exist, and due to the high variability of engine working points, using classical CFD methods is probably too expensive. Indeed, even a simple 1D finite difference or element solver, in the normal direction to the surface would be a burden as far as the computational time. The temperature variations being limited to a small domain, it implies a very fine mesh, hence a very limited time step or the use of implicit (and yet expensive) time marching method in time.

For the resolution of the 1-D temperature profile in a wall with a constant heat flux density  $q_w''$  the solution is:

$$T_w = T_i + 2 \frac{q_w''}{k} \sqrt{\frac{\alpha t}{\pi}}, \quad (5.11)$$

where  $T_w$  is the wall temperature,  $T_i$  the initial wall temperature and  $\alpha$  the thermal diffusivity of the material. As the equation temperature is a linear Partial Differential Equation (PDE), solutions can be superimposed. For instance, in order to get the temperature solution when a constant heat flux (of intensity  $\varphi_0$ ) is imposed for a finite



time  $t_i$ , shifting two Heaviside signals with opposite signs such as:

$$q_w''(t) = \varphi_0 H(t) - \varphi_0 H(t - T_i), \quad (5.12)$$

gives the following solution for the wall surface temperature:

$$T_w = T_i + 2\frac{\varphi_0}{k}\sqrt{\frac{\alpha t}{\pi}} - 2\frac{\varphi_0}{k}\sqrt{\frac{\alpha(t - T_i)}{\pi}}. \quad (5.13)$$

In order to get the wall surface temperature for every form of heat flux density, discretising the flux with a piecewise constant will perfectly works. It gives the following temperature solution:

$$T_w(n) = T_i + \frac{2}{k}\sqrt{\frac{\alpha\Delta t}{\pi}} \left\{ \sum_{l=0}^N q_w''(l) \left( \sqrt{n-l+1} - \sqrt{n-l} \right) \right\}, \quad (5.14)$$

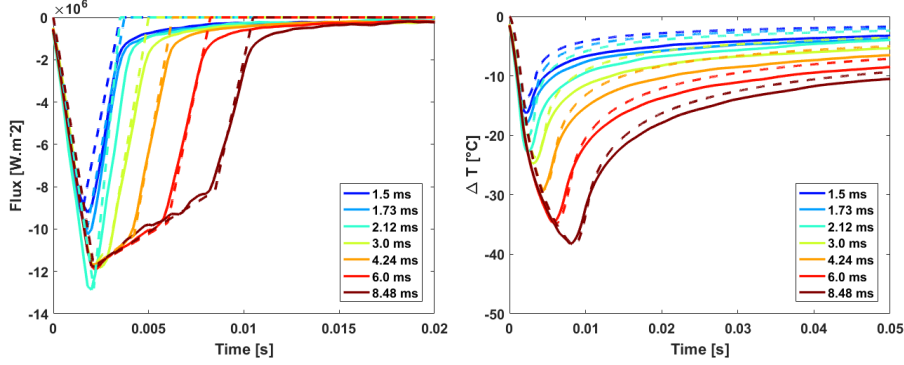
with  $T_w(n)$  the wall surface temperature at the  $n$ -th time iteration.

To check the accuracy of the model proposed here, the heat flux associated with the case presented Figure in 5.8 is tested (variable injection duration). From the experimental data obtained with the thermocouple plate, the heat flux has been calculated using the method presented in [75]. The heat flux density profile is then simplified, depending on the injection duration, it is either approximated by a triangular shape or a quadrilateral shape. It is then discretised with a piecewise constant profile (discretisation size is  $0.005 \text{ ms}$ ). The results are presented in Figure 5.17. The minimum of temperature is correctly predicted by the method and the global shape of the temperature evolution is well respected. However, there is during the heating phase a shift between the model and the data, heating seems to be a little overestimated by the model. It is more than likely due to the very simple shape that has been used for the heat flux approximation. Indeed, on Figure 5.17 (Right), while some heat flux is still visible on the experimental data, the choice for the model makes it zero a bit too early.

In an attempt to get even closer to what is really happening during the impact of the spray, a slightly different heat flux density model is finally presented. The objective is to find a model for the heat transfer coefficient  $h$  induced by the injection. The wall heat flux density is written as follows:

$$q_w'' = h(T_w - T_f), \quad (5.15)$$

## 5. HEAT TRANSFER MODELLING



**Figure 5.17:** Heat flux and temperature temporal variation experiment vs model. Dashed line presents the model and plain lines presents the experimental data. Injection condition  $P_i = 100 \text{ bar}$ ,  $T_w = 100^\circ\text{C}$  and fuel temperature is  $30^\circ\text{C}$ .

where  $T_f$  is the fuel temperature. Though a discussion on the effective temperature of the spray at the moment of impingement has been introduced earlier, here  $T_f$  is assumed constant and equal to the injection temperature. Also, it has been presented in Section 5.3.4, that even when  $T_f > T_w$ , the wall temperature still decreases due to spray impingement. This new model will take into account that, when the wall temperature has started to decrease, then the heat flux density will also decrease. In practice, to calculate the heat flux density  $q_w''$  at time  $n$ , the wall temperature at the time  $n - 1$  is used.

As the injection process presents transient phases such as the opening, the closure and the travelling of the spray the proposition for the heat transfer coefficient shape is to use a trapezoid (Figure 5.18). Indeed, the rising and falling edge before and after the flat top are charged to represent the transients mentioned earlier .

Depending on the injection duration, the width of the flat top gets longer or shorter (for really short injection the trapezoid will shrink into a triangle). The quality of the results obtained for the temperature prediction is really satisfying. It is hard to differentiate the results presented in Figure 5.17 made with discretisation of the flux calculated with the experimental data, and the results presented Figure 5.19 based on the heat flux density presented Equation 5.15. The new heat flux takes into account the variation of the wall temperature, it is clearly visible on the shape on the heat flux curve.

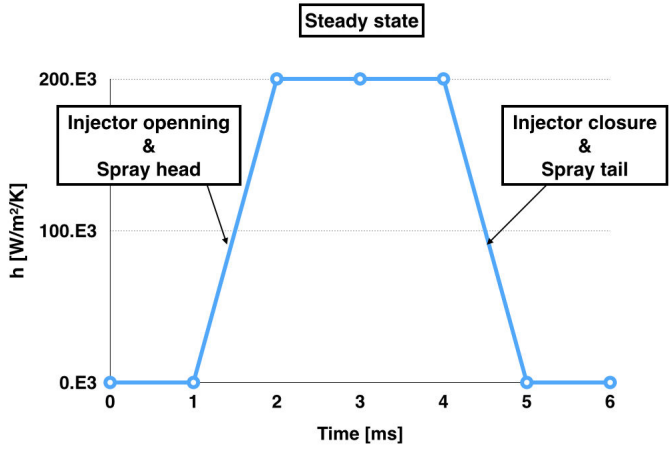


Figure 5.18: Proposed shape for the heat transfer coefficient.

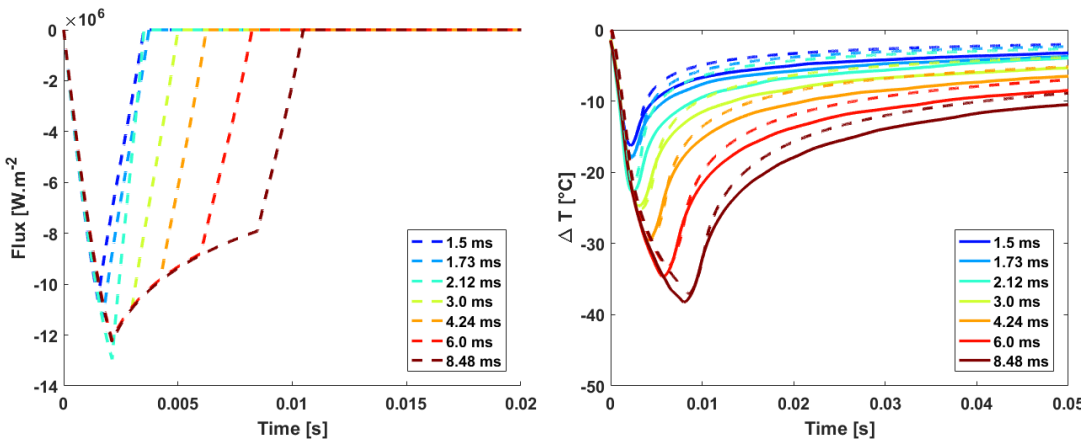


Figure 5.19: Evolution of heat flux and wall temperature for variable injection duration. Dashed line present the model, plain line the experimental data. For sake of clarity experimental data are not shown on the flux curve. Injection condition  $P_i = 100 \text{ bar}$ ,  $T_w = 100^\circ\text{C}$  and fuel temperature is  $30^\circ\text{C}$ .

Finally, Figure 5.20 shows the evolution of the heat transfer coefficient  $h$  introduced Equation 5.15 for different injection durations. When the injection duration is increased, the heat transfer coefficient  $h$  reaches its maximum value of  $2.4 \cdot 10^5 \text{ W.m}^{-2}.\text{K}^{-1}$  and the triangular shape turns into a trapezoidal shape.

Being able to characterise, for some defined injection parameters (pressure, mass,

## 5. HEAT TRANSFER MODELLING

---

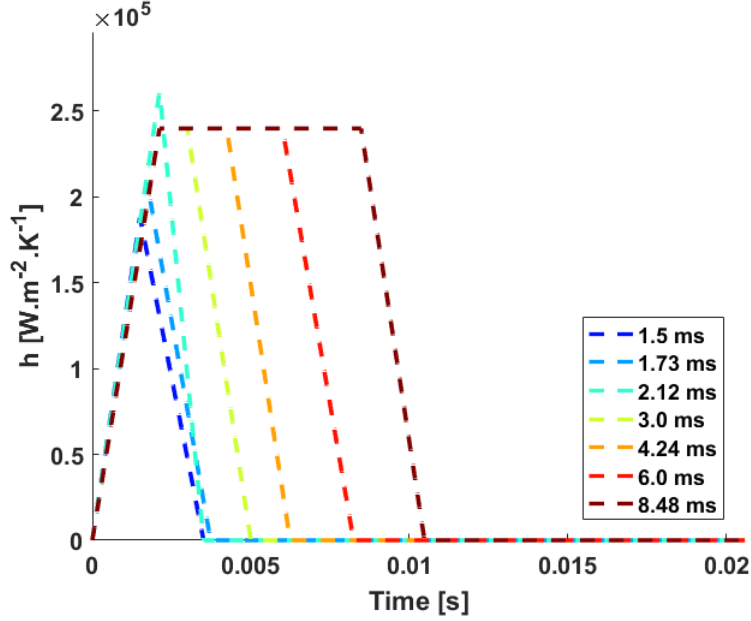


Figure 5.20: Evolution of the heat transfer coefficient  $h$  for different injection duration. Injection condition  $P_i = 100 \text{ bar}$ ,  $T_w = 100^\circ\text{C}$  and fuel temperature is  $30^\circ\text{C}$ .

temperature), several injectors will allow to compare them.

### 5.6 Conclusion

In this chapter the temperature evolution together with the heat transfer induced by spray-wall impingement has been studied thanks to the experimental device presented in Section 3.4. 2D temperature maps have been made, and they give precious data on the spatial variation of the heat loss. It has introduced a new vision on the measures performed in the instrumented engine, the temperature variations on the piston could be more important than what has been measured. The wall temperature variation is really fast during the cooling as the heat flux density is very important due to the high speed and volatility of the droplets. During the heating phase the temperature variation is much slower, it has some consequences on the vaporisation rate of the liquid film. A simple descriptive but precise model has been derived, it allows a posteriori to compute the value of the heat transfer coefficient  $h$  and will allow more parametrical variations in the future.

# 6

## Vaporisation in the vicinity of hot walls

### Contents

---

<b>3.1</b>	<b>Fuel preparation system . . . . .</b>	<b>51</b>
<b>3.2</b>	<b>Shadowgraphy . . . . .</b>	<b>52</b>
<b>3.3</b>	<b>RIM . . . . .</b>	<b>55</b>
3.3.1	Measurement principle . . . . .	55
3.3.2	The impingement process observed with the RIM method . .	57
3.3.3	Calibration of the RIM method . . . . .	59
3.3.4	On the drawbacks and limits of the RIM method . . . . .	64
3.3.5	RIM method with Sapphire . . . . .	66
3.3.6	RIM method with Aluminium . . . . .	66
<b>3.4</b>	<b>Fast Thermocouple Measurement Plate . . . . .</b>	<b>68</b>
<b>3.5</b>	<b>X and Y translation . . . . .</b>	<b>71</b>
<b>3.6</b>	<b>Interferometric Measurement Device . . . . .</b>	<b>72</b>
<b>3.7</b>	<b>Atomic Force Microscopy . . . . .</b>	<b>75</b>
<b>3.8</b>	<b>Injector Position . . . . .</b>	<b>76</b>
<b>3.9</b>	<b>Goniometry . . . . .</b>	<b>78</b>

---

In this chapter some considerations about evaporation and vaporisation of mono- and multi-components fuels will be addressed. It will strengthen the significant role of the wall surface on the liquid film lifetime.

### 6.1 Evaporation of isolated droplets

The aim of this section is not to do a complete study of the vaporisation of single droplets, as the liquid film is at the core of the study. However, as many thin film evaporation models are rather close to the single droplet models, it is important to give some knowledge about droplet vaporisations. The book written by Sirignano [91] presents thoroughly the heating and vaporisation of steady and moving droplets. Several models with and without inner droplet motion are presented and discussed together with single and multicomponent liquid droplets.

The evaporation of single droplets is quite complex and the problem gets even more complex when impacting on a hot/very-hot wall. However, it exists some models that manage to describe these phenomenon. In [12] Castanet studies the effect of temperature on the impact of droplets. Due to the development of a vapour cushion, because of vaporisation, the impact mechanism is modified compared to impact on a cold wall.

Finally, though the physics of single impacting droplets is fairly well understand as stated in [7] (Figure 6.1), extending the models and physical descriptions to sprays is not easy. A rough description of these topics will be presented before presenting the experimental results of liquid film evaporation.

	Dry Surface		
	Single Drop	Multiple Drops	Spray / Film
Single Phase Cooling Regime			
Nucleate Boiling			
Film Boiling			


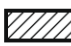

 Well understood/ Analytic solution	 Semi-empirical	 Purely empirical
---	--	--

Figure 6.1: Summary of state of the art in terms of cooling regimes [7].

### 6.1.1 Droplets in gas

In [91] the theory of isolated droplet vaporisation, heating and acceleration is addressed, together with the complications induced when the liquid is composed by several species. It is also tackled by several authors [14, 15, 39, 99]. The simplest model is the constant droplet-temperature model, it allows to derive the  $d^2$  law. This law states that the diameter of the droplet decreases linearly with time due to vaporisation:

$$d^2 \propto t, \tag{6.1}$$

where  $d$  is the diameter of the droplet and  $t$  is the time. The vaporisation rate [ $m^2.s^{-1}$ ] involved is depending of the density of the gas at the surface and far away, the diffusion coefficient and the density of the droplet liquid. Its value is positive in case of condensation and negative in case of vaporisation.

When the operating conditions gets more complex, the  $d^2$  law is no longer valid despite of the robustness of the model. However, it is still possible to correctly predict the evolution of the droplet size and its lifetime using models such as infinite liquid-conductivity model, or spherically symmetric transient droplet heating model (the temperature is no longer homogeneous, but spherically symmetric). Finally, a vortex model for droplet heating (Figure 6.2) and the Navier-Stokes solution can be envisaged as mentioned by [91]. In a nutshell, for single component droplets, a tremendous number of models is available depending on the conditions encountered by the droplet. Increasing the number of components in the vaporising liquid also increases the number of equations to solve and the complexity of the models. Diffusion coefficient, concentrations, saturation pressure of each species should be taken into account which makes the resolution of the problem even harder. Even if single droplet vaporisation or condensation is nowadays well understood, it is still an active experimental and numerical research topic.

### 6.1.2 Droplets gently deposited on a wall

The vaporisation of single component droplets at the contact of a wall is greatly depending on both the wall temperature and the saturation temperature of the fuel. Three temperatures can be identified in the vaporisation process at wall contact. The saturation temperature  $T_{sat}$  at which boiling initiates, the Nukiyama temperature [67]  $T_{Nuk}$  at

## 6. VAPORISATION IN THE VICINITY OF HOT WALLS

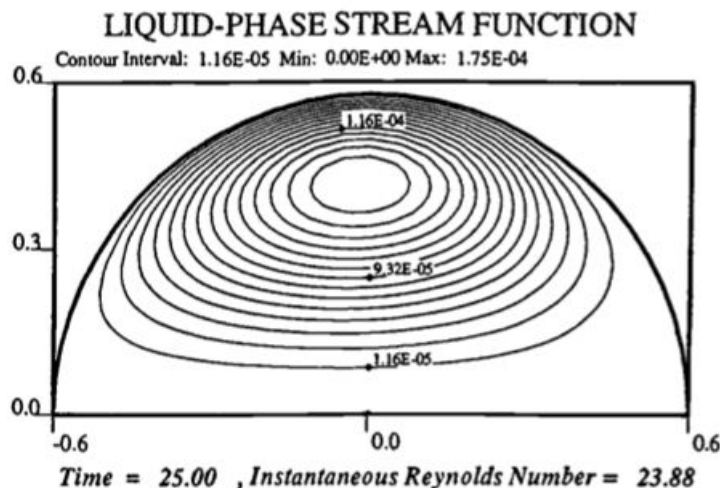


Figure 6.2: Simulation of streamlines inside a bubble flowing through gas by Chiang et al.[13].

which the heat flux is maximal (and the droplet lifetime minimum). Finally while continuing raising the temperature the Leidenfrost temperature [49]  $T_{Lei}$  is reached. The heat flux is now lower than at  $T_{Nuk}$  and is now minimal, hence the droplet lifetime is maximal. This behaviour is due to the establishment of a vapour cushion between the fuel and the wall due to the high vaporisation rate. Once this layer of vapour is formed it isolates the fuel from the wall, and it causes the heat flux to decrease. Figure 6.3 from [59] illustrates the droplet lifetime of single droplet together with the heat flux curve. In a nutshell, when raising the wall temperature, the survive time first decreases, then increases and it finally starts to decrease again.

This behaviour is encountered either in droplet vaporisation or pool vaporisation and it is of high concern in heat exchangers. Indeed, if a vapour cushion establishes between the coolant and the cooled surface, its temperature will start to increase tremendously and it can be very destructive for the heat exchanger.

In [76] the vaporisation of isolated droplet in film boiling conditions (i.e. above  $T_{Lei}$ ) is studied. The droplet is gently deposited on a hot wall and it seats on its vapour cushion. Modelling of the gas flow between the wall and the droplet is necessary to estimate the vapour cushion thickness. It is found that this thickness is proportional to  $(T_w - T_{sat})^{1/4}$  and ranges from 10 to 100  $\mu m$ . The study of impacting droplets is now addressed.



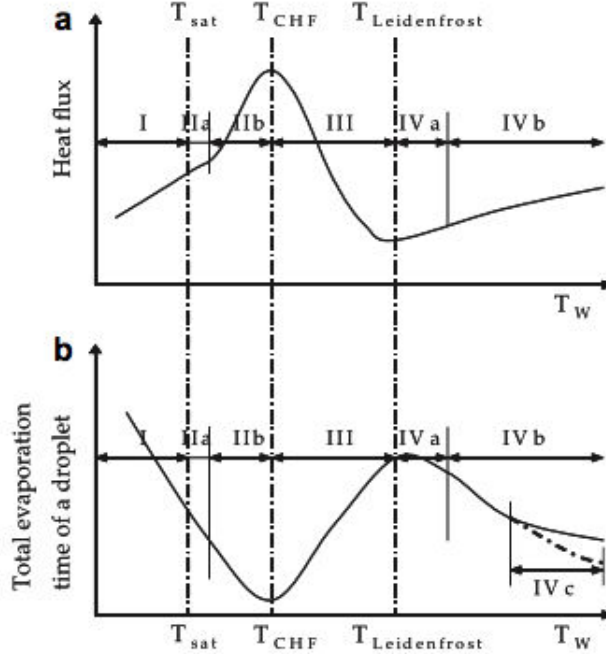


Figure 6.3: Heat flux evolution and droplet lifetime curve with respect to wall temperature. Case of gently deposited droplets,  $T_{CHF} = T_{nuk}$  [59].

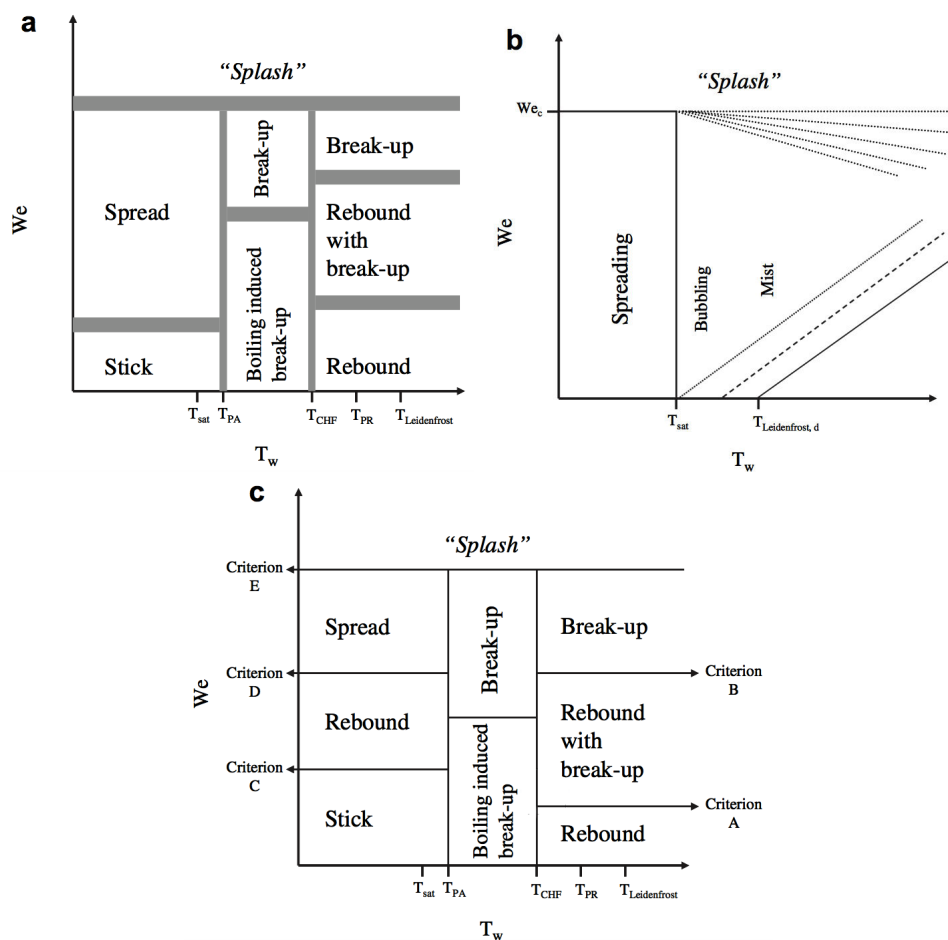
### 6.1.3 How it modifies the impact of droplets on a wall

The impact of droplets on a flat wall has already been discussed in Section 1.3.2 and the vaporisation of single droplets too in Section 6.1. However, the combination of vaporisation and impact is not trivial as the temperature of the wall modifies the impact kinematics. Indeed, what is true in "cold" conditions is no longer true when a droplet faces a hot wall [12]. As mentioned before for gently deposited droplets, at Leidenfrost temperature, a vapour cushion develops and augments the vaporisation time. Though there are some differences between quiescent and impacting droplets, the vapour layer may develop and it can modify the impact regimes [102].

Several studies have proposed a description and a modelling of impact regimes in hot conditions [4, 48, 76]. Even though, they offer a globally similar picture, there are still some discrepancies. For instance, the criteria used to define the boundary temperatures differs, whereas in [4, 48] the definition is only based on the morphology of droplets during the impact. Whereas in [76] the reference temperatures of the liquids are used, as mentioned in [59]. Figure 6.4 illustrates the different behaviours, depending

## 6. VAPORISATION IN THE VICINITY OF HOT WALLS

on several parameters. It is essential to keep in mind that many parameters have to be taken into account such as liquid properties, topography, impact angle, wettability and effusivity of the surface [59], that makes the impact of droplets on a hot wall a very rich and complex subject.



**Figure 6.4: Overview of droplet global representations of the impact regimes and transition conditions for a dry heated wall. (a) Bai and Gosman [4]; (b) Rein [76]; (c) Lee and Ryu [48]. As presented in [59].**

The understanding of droplet impact on hot wall is thoroughly studied. For instance in [11] the impact of droplets onto a smooth wall in Leidenfrost conditions is studied. They present a model for the spreading and the flow inside the lamella (droplet shape due to the deformation at impact) for a range of Weber and Reynolds numbers (defined in Chapter 1). However, even with a perfect comprehension of the problem for single

## 6.2 Evaporation of mono/multicomponent liquid film (When $T_{wall} \leq T_{sat}$ )

droplet impacts, the link between single droplets and spray impingement is not straight forward [7, 38], especially while working with hot walls (Figure 6.1).

The objective of this very small literature review, was to make a reminder of the differences between single droplets and spray, indeed sprays cannot be treated only as a summation of individual droplets. But also, to insist on the supplementary difficulty that comes when working with hot walls. Some of these difficulties are: several new break-up regimes, new rebound zones due to the apparition of Leidenfrost effects, evaporation and the heat transfer involved.

## **6.2 Evaporation of mono/multicomponent liquid film (When $T_{wall} \leq T_{sat}$ )**

### **6.2.1 Why studying evaporation**

In this part, evaporation of liquid films on aluminium plate are studied. Measures produced with the RIM-alu (Section 3.3.6) experimental setup and the STIL measurement device (Section 3.6) will be analysed but before it is necessary to understand why talking about evaporation for internal combustion engines.

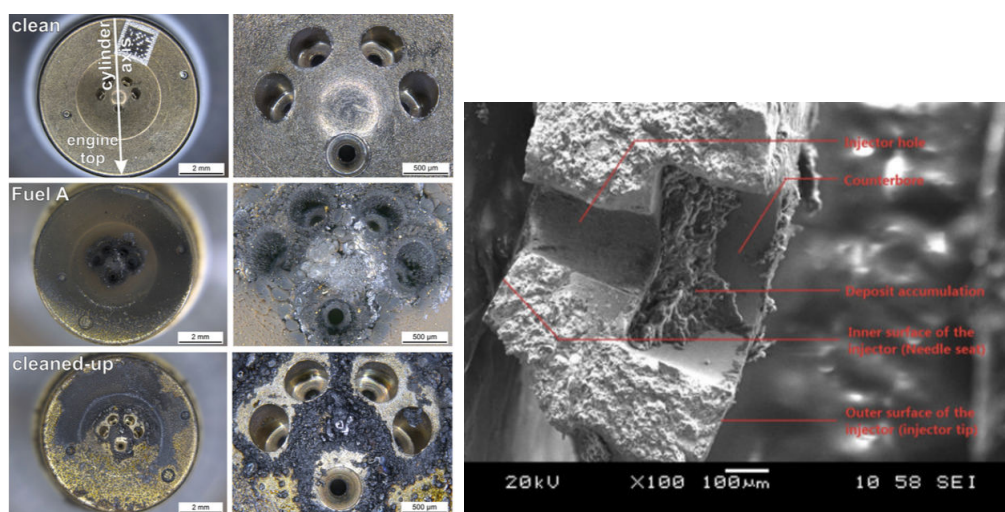
In the engine, particularly in the combustion chamber, the temperature is non homogeneous and unsteady. In the worst case scenario when the engine is still cold (not long after engine start), liquid films are deposited in the cold regions and heat flux is not strong enough to initiate boiling.

The injector tip is a cold part in the combustion chamber and due to purge issues it is sensible to tip wetting [28] (Chapter 1 & 2). This liquid film encounters evaporative conditions and is of great concern for injector maker. If the liquid film does not vaporise before the ignition, bad combustion occurs and it leads to injector coking. It corresponds to carbon deposits that covers the tip of the injector and can modify the injector properties. Indeed coking have effects on nozzle cavitation due to geometrical modification of the injector holes (Figure 6.5), it can also modify the repeatability of injection and increase penetration, increasing the risks of wall film generation.

During cold start not only the injector tip, but also the whole combustion chamber is cooler than in normal combustion. In this case, the liquid film is not boiling, but rather in the evaporative conditions.

## 6. VAPORISATION IN THE VICINITY OF HOT WALLS

Finally, gasoline being a mixture of hundreds of components, one must have a look to the distillation curve (see Figure 6.6 extracted from [9]). This distillation curve is presented for three variants of a gasoline with 91 anti knock index (AI). Which corresponds to a regular Sans Plomb 95 in France or Regular unleaded in Europe. The two other variants are 91AI fuel with respectively 10%(vol/vol) and 15%(vol/vol) of methanol mixed in.



**Figure 6.5: Images of Injector coking: Right [36] Cleaned, fouled and cleaned up injector. Left [30] SEM image of a coked injector hole**

The detailed composition of the fuel can be found in Figure 6.7. There are 37 different compounds with a number of carbon atoms ranging from 6 to 10, with cyclic and acyclic formations. This variability of molecules is responsible for the smooth and continuous distillation curve. As stated in Chapter 2, the temperature of the piston is ranging from  $140^{\circ}\text{C}$  to  $270^{\circ}\text{C}$  in stabilised conditions (i.e not taking into account when the engine starts) and the temperature of the cylinder head which is colder is ranging between  $110^{\circ}\text{C}$  and  $170^{\circ}\text{C}$  in regular use of the engine. This confirms that, conditions below boiling must be encountered for certain engine conditions, for part or total of gasoline compounds. If evaporative conditions are met in the engine, it is legit to study evaporation. Though, as the evaporation is a slow process (compared to boiling), it is more than likely that liquid films experiencing these conditions will not vaporise within the time limit allowed. It is necessary to state it before studying the evaporation of liquid films.

## 6.2 Evaporation of mono/multicomponent liquid film (When $T_{wall} \leq T_{sat}$ )

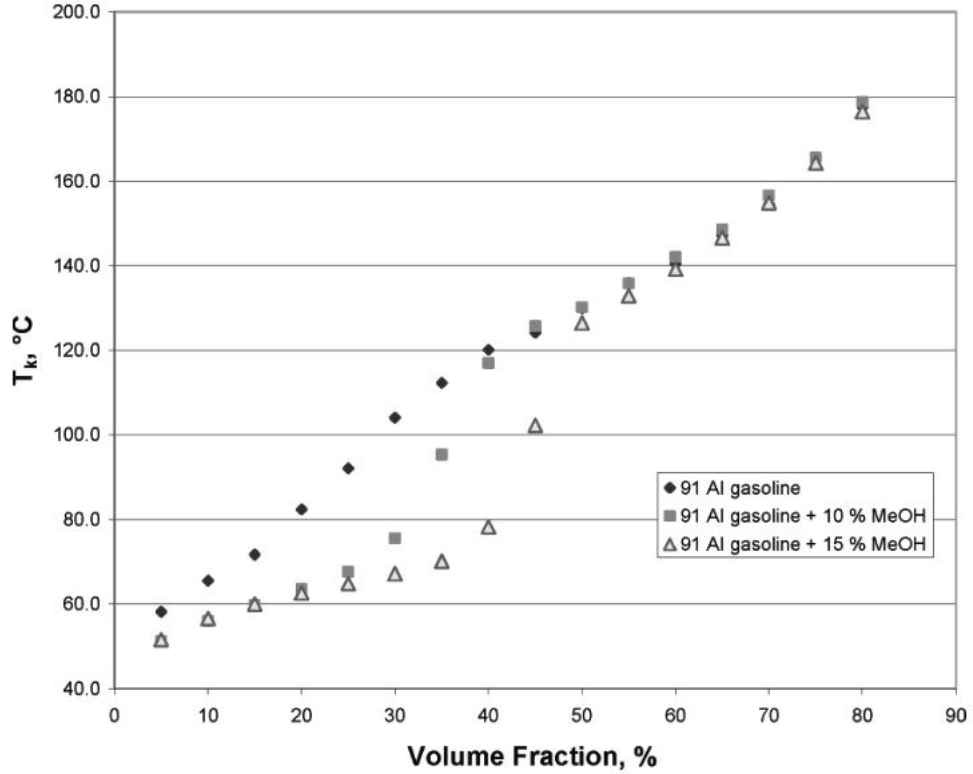


Figure 6.6: Distillation curve for 91AI fuel, 91AI fuel + 10% methanol, 91AI fuel + 15% methanol [9]

### 6.2.2 The different fuels surrogates

In this part evaporation of thin liquid film is studied, three different multicomponent fuels are used. The first one has been previously used by [42]. Its composition is available in table 6.1 and will be referred as surrogate  $n^{\circ}1$ .

Fuel		n-hexane	iso-octane	n-decane
Density	$[kg/m^3]$	661	699	721
Saturation temp.	$[K]$	342	372	447
Dynamic viscosity	$[Pa.s]$	3.26e-04	2.06e-03	9.20e-04
Mass fraction	$[-]$	0.35	0.45	0.2

Table 6.1: Properties of Surrogate  $n^{\circ}1$  at 20°C

## 6. VAPORISATION IN THE VICINITY OF HOT WALLS

compound	% composition (mol/mol)	compound	% composition (mol/mol)
0.025% distillate volume fraction			
2-methyl butane	23.4	<i>n</i> -heptane	2.4
2-methyl pentane	17.6	2,3,3-trimethyl butene	0.7
<i>n</i> -hexane	7.7	toluene	18.6
benzene	5.1	ethyl benzene	1.0
methyl cyclopentane	16.1	1,4-dimethyl benzene	3.8
2,2,3,3-tetramethyl butane	3.8	1,2-dimethyl benzene	0.9
45% distillate volume fraction			
2-methyl pentane	1.0	toluene	31.7
3-methyl pentane	0.7	<i>n</i> -octane	0.8
<i>n</i> -hexane	1.4	ethyl benzene	4.5
2,2-dimethyl pentane	1.6	1,4-dimethyl benzene	15.6
benzene	9.3	1,2-dimethyl benzene	4.8
2,2,3,3-tetramethyl butane	4.0	propyl benzene	0.7
<i>n</i> -heptane	3.6	1-ethyl-2-methyl benzene	3.0
2,3-dimethyl hexane	1.7	1,3,5-trimethyl benzene	0.8
2,3,4-trimethyl pentane	9.4	1,2,3-trimethyl benzene	0.5
3-ethyl-2-methyl pentane	1.2	1,2,4-trimethyl benzene	2.5
2-methyl heptane	1.5		
80% distillate volume fraction			
toluene	1.1	indane	1.6
ethyl benzene	2.9	1-methyl-4-propyl benzene	3.1
1,4-dimethyl benzene	12.9	1-ethyl-2,4-dimethyl benzene	4.0
1,2-dimethyl benzene	6.5	1-ethyl-3,5-dimethyl benzene	9.9
1,2,3-trimethyl benzene	1.7	2-ethyl-1,3-dimethyl benzene	1.3
propyl benzene	2.7	1-methyl-3-(1-methylethyl) benzene	1.3
1-ethyl-2-methyl benzene	15.1	2-ethyl-1,4-dimethyl benzene	2.4
1,2,4-trimethyl benzene	6.5	<i>x,y</i> -diethyl benzene	0.3
1-ethyl-4-methyl benzene	3.4	<i>x,y</i> -diethyl benzene	1.1
1,3,5-trimethyl benzene	20.7	<i>x,y</i> -diethyl benzene	1.5

Figure 6.7: Composition of AI91 gasoline from [9]

The second and third surrogate have been developed for the study of soot generation at the university of Orléans. The surrogate  $n^{\circ}2$  composition is presented in table 6.2.

Fuel		<i>n</i> -hexane	iso-octane	Toluene	1-Methylnaphtalene
Density	[ $kg/m^3$ ]	661	699	870	1001
Saturation temperature	[ $K$ ]	342	372	384	517
Dynamic viscosity	[ $Pa.s$ ]	3.26e-04	2.06e-03	5.9e-04	-
Volume fraction	[-]	0.103	0.473	0.311	0.111

Table 6.2: Properties of Surrogate  $n^{\circ}2$  at  $20^{\circ}C$

The 1-Methylnaphtalene has been chosen because of its ability to generate particles during combustion. The results of the study carried out by Anthony Roque are available

## 6.2 Evaporation of mono/multicomponent liquid film (When $T_{wall} \leq T_{sat}$ )

in [80].

Finally the third surrogate is composed as presented in Table 6.3.

<b>Fuel</b>		<b>n-hexane</b>	<b>iso-octane</b>	<b>Dodecane</b>
Density	$[kg/m^3]$	661	699	745
Saturation temp.	$[K]$	342	372	491
Dynamic viscosity	$[Pa.s]$	3.26e-04	2.06e-03	1.34e-03
Volume fraction	$[-]$	0.103	0.786	0.111

**Table 6.3: Properties of Surrogate  $n^{\circ}3$  at  $20^{\circ}C$**

In the third surrogate the Toluene, which can be used to track iso-Octane in Laser Induced Fluorescence (LIF) [26], and the 1-Methylnaphtalene used as a tracer for n-undecane or n-dodecane [6, 35] have been replaced by iso-Octane and Dodecane.

### 6.2.3 Experimental results

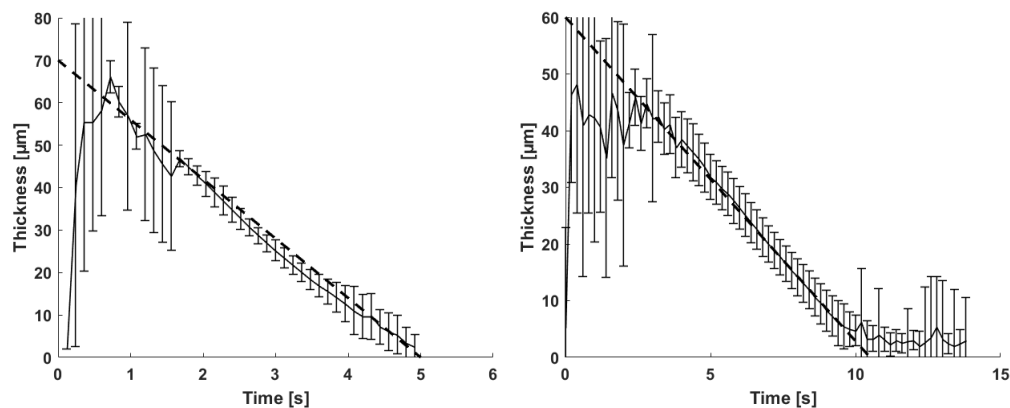
Using the STIL device, measurements of the liquid film thickness evolution with respect to time are possible. The injection is performed with an angle of  $30^{\circ}$  as depicted in Figure 3.25. Figure 6.8 and 6.9 shows the evaporation of liquid film of pure n-Hexane, n-Heptane, n-Decane and iso-Octane.

The difficulty of the measurement stays in the quality of the liquid-vapour interface and the frequency of acquisition. Indeed, if the plate is too hot, ebullition starts and the flatness of the interface is difficult to ensure, as well as the number of interface that can increase (Figure 6.10). Both phenomena are responsible of the reduction of quality and repeatability of the vaporisation process.

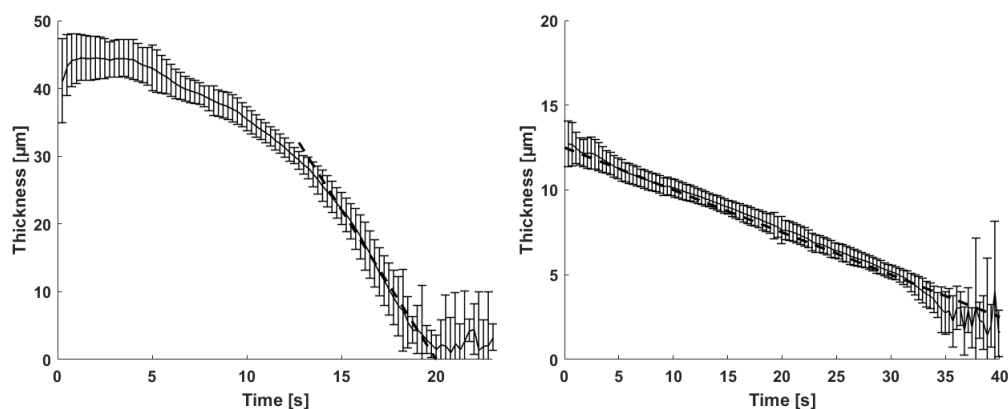
Another issue is the acquisition frequency of the STIL device. It can be raised up to 1kHz if the quality of the signal is good enough, but using it at a frequency of 400Hz increases the measurement quality. Hence a vaporisation time of 20ms will be represented by 8 points. Due to all these difficulties, it has been decided to use the STIL only in evaporation conditions and not for boiling of liquid films. Also the injection pressure is 10 *bar*, as the quantity of available surrogate were small, hence an air-pressurised vessel has been used. It partly explains that the film thickness are greater

## 6. VAPORISATION IN THE VICINITY OF HOT WALLS

---



**Figure 6.8: Fuel film thickness evolution. Left: hexane liquid film with  $T_w = 23^\circ\text{C}$ . Right: heptane liquid film with  $T_w = 30^\circ\text{C}$ . Dashed line illustrate the identified linear behaviour of the film thickness evaporation.**



**Figure 6.9: Fuel film thickness evolution. Left: iso-octane liquid film with  $T_w = 23^\circ\text{C}$ . Right: decane liquid film with  $T_w = 50^\circ\text{C}$ . Dashed line illustrate the identified linear behaviour of the film thickness evaporation.**

than the one presented in Chapter 4. The figures 6.8 and 6.9 present the average of 10 repetitions together with error bars. The dashed line represents an arbitrary linear fit that is representative enough of the vaporisation process. Vaporisation rates [ $\mu\text{m}/\text{s}$ ] are then obtained based on the slopes of the dashed lines. Table 6.4 summarises the vaporisation rates of the different alkanes mentioned before. They increase with respect to the wall temperature, and it also highlights the difference of volatility in the components of a commercial gasoline (Figure 6.7).



## 6.2 Evaporation of mono/multicomponent liquid film (When $T_{wall} \leq T_{sat}$ )

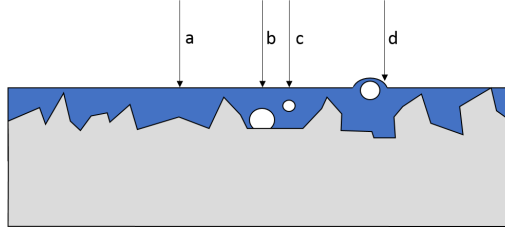


Figure 6.10: Schematic vision of STIL measurements. The arrows present possible positions for the measurement in case of nucleate boiling. Position a: no problem encountered. Position b: thickness might be underestimated because of the bubble presence. Position c: too many interfaces to perform a correct measurement. Position d: the surface curvature makes the measurement impossible.

Temperature	n-hexane	n-heptane	iso-octane	n-decane
23°C	14	-	4.14	-
30°C	-	5.714	6.36	-
40°C	-	14.29	-	-
50°C	-	-	-	0.25
70°C	-	-	-	0.824

Table 6.4: Summary of vaporisation rate for Alcanes [ $\mu m/s$ ]

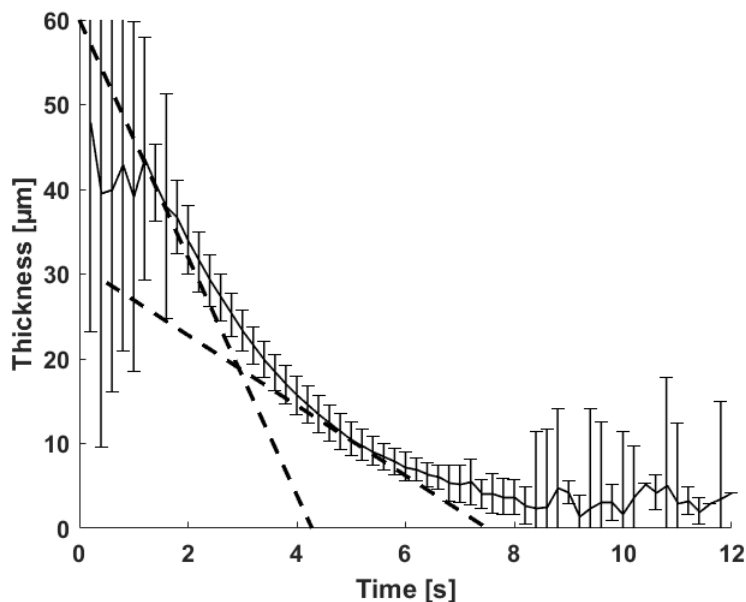
Figure 6.11 shows the vaporisation for a two compounds fuel composed of 50% hexane and 50% iso-octane at 23°C. The vaporisation rate of each component is superimposed in order to compare the evaporation of a two components fuel with the evaporation of each compound taken individually.

The vaporisation curve for the 3 first seconds is well described by the rate of vaporisation of hexane alone. In the same way the 4 last seconds seems well described by the behaviour of pure iso-octane.

The purpose of these measures is to evaluate and show the benefits and limitations of the STIL device, illustrate how slow the evaporation process is with respect to engine characteristic times and give data in order to calibrate a numerical model developed by S.Mouvanal et al in [62] (available in Appendix) to predict the lifetime of mono and multi component liquid films. The full model is detailed in the paper together with

## 6. VAPORISATION IN THE VICINITY OF HOT WALLS

---



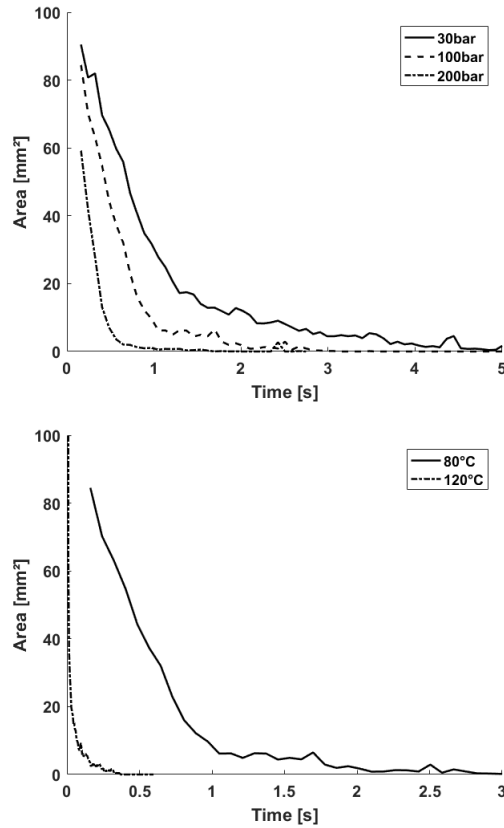
**Figure 6.11: Fuel film thickness evolution. hexane/iso-octane liquid film with  $T_w = 23^\circ C$  . Dashed line presents the vaporisation rate of single components superimposed in order to compare mono- and multi-components vaporisation behaviours.**

the results for surrogate 1 and allows to have good approximations and previsions of vaporisation times of multicomponent alkane fuels.

The RIM Alu method has been used to produce data for the vaporisation of surrogate fuels 2 and 3. To do so, injection was performed on the aluminium plate. As the liquid film modifies the light path, via background substitution it is possible to use the grey level information to track the presence or absence of liquid film. Figure 3.16 shows typical liquid film visualisation together with the background substracted image. Figure 6.12 shows the evolution of the liquid film area for different injection conditions. The surrogate used here is surrogate 3, the temperature of injection are respectively  $80^\circ C$  and  $120^\circ C$ . The pressure of injection are 30 bar, 100 bar and 200 bar and the injection duration is adapted so the same mass is always injected. The effect of temperature and pressure appear clearly. Indeed, increasing the temperature reduces the liquid film lifetime but increasing the injection pressure also reduces the liquid film lifetime. This last remark confirms the observations realised in chapters 4 and 5: a

## 6.2 Evaporation of mono/multicomponent liquid film (When $T_{wall} \leq T_{sat}$ )

higher pressure leads to thinner films and spray cooling is less (for a given injected mass), which leads to a hotter wall. A multicomponent behaviour is also identified, the liquid film area starts to decrease at a certain rate, then it slows and a second rate can be identified. It is important to note that for short times ( $< 0.2 - 0.3$  s) the detection algorithm used, encounters difficulties to correctly evaluate the liquid film area. Hence, the beginning of the curves is not presented here.



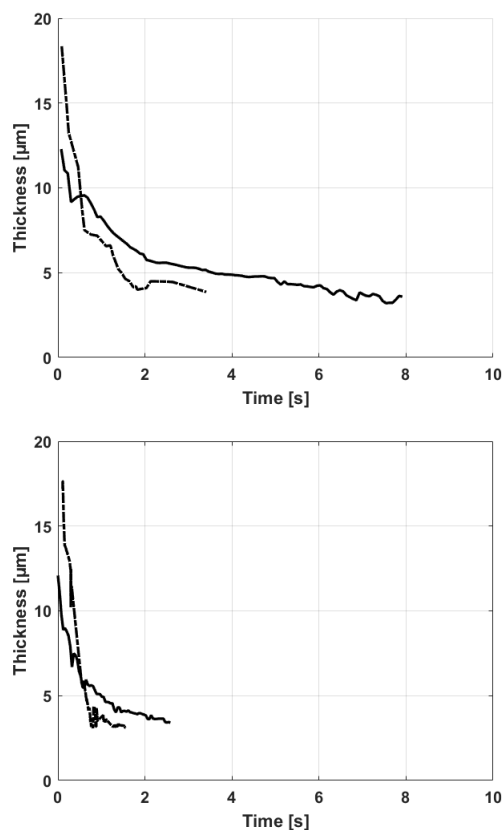
**Figure 6.12:** Area evolution for Surrogate 2 fuel film injected on Aluminium plate. Left: Wall temperature  $T_w=80^\circ C$ . Right: Injection pressure  $P_i = 100$  bar.

Finally, in order to compare surrogate 2 and 3 the thickness measurement with STIL at  $80^\circ C$  has been performed. Figure 6.13 shows for two injection pressures the behaviour. Below  $4 \mu m$  the quality of the signal is not good enough so the curves have been cut. For both fuels, a two step behaviour in the thickness evolution is identified, and it seems that the vaporisation rates for the long time are roughly equivalent. The

## 6. VAPORISATION IN THE VICINITY OF HOT WALLS

---

objective was, to say if studies made with surrogate 2 are comparable with studies made with surrogate 3. At low temperature such as the one tested (i.e.  $80^{\circ}\text{C}$ ) it is really hard to conclude. However, for higher temperatures, it is likely that both surrogates will vaporise at the same time scale.



**Figure 6.13:** Thickness evolution for surrogate 2 and 3 for a wall temperature  $T_w = 80^{\circ}\text{C}$ . Left: injection pressure  $P_i = 30$  bar. Right: injection pressure  $P_i = 100$  bar.

### 6.3 Hot walls (When $T_{wall} \geq T_{sat}$ )

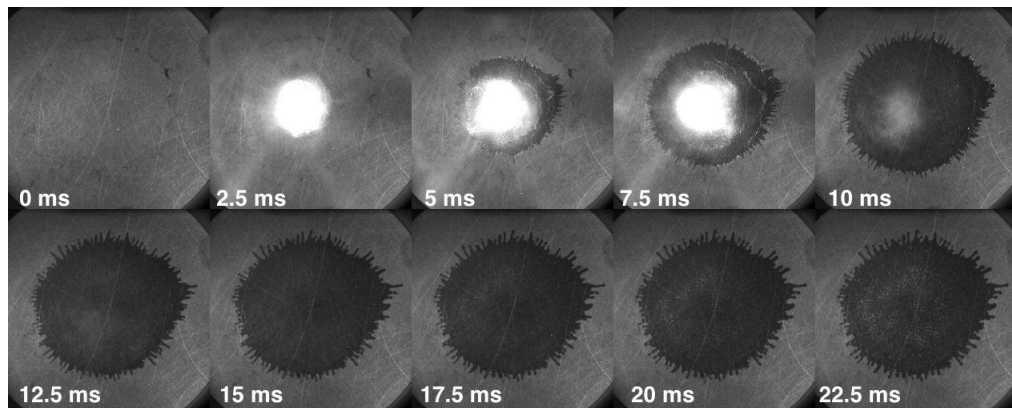
In this section, is presented the evolution of the liquid film on hot walls. It has been presented before that on cold walls the liquid film will take a long time to disappear (too long at the engine timescale). Hence, the question that arises is what will happen to the liquid film when facing a hot wall? Experimental observations together with

descriptions are presented. Only interesting scenarii provided to inform the reader of what has also been observed at high temperature during the PhD thesis.

### 6.3.1 Decane boiling on quartz plate

In this section the impact of n-decane high pressure spray is reported. With the exception of the temperatures, everything is similar to the orthogonal impingement cases presented in Chapter 4. They were not included there, because of the strong influence of vaporsation in the present cases. The wall temperature is varying between  $150^{\circ}C$ ,  $180^{\circ}C$  and  $210^{\circ}C$ . The injection temperature is respectively  $150^{\circ}C$ ,  $180^{\circ}C$  and  $180^{\circ}C$ . Indeed, for safety reasons, the injector temperature was kept below  $200^{\circ}C$ . The saturation temperature of n-decane is  $174^{\circ}C$  in atmospheric conditions. Thus, an impact just below (Figure 6.14), around (Figure 6.15) and above (Figure 6.16) the saturation temperature are depicted respectively.

Below the saturation temperature, the liquid film is still present  $22.5\ ms$  after the start of injection, and de-wetting in the middle of the liquid film starts to happen. Around the saturation temperature, the liquid film is almost evaporated after  $22.5\ ms$ ,

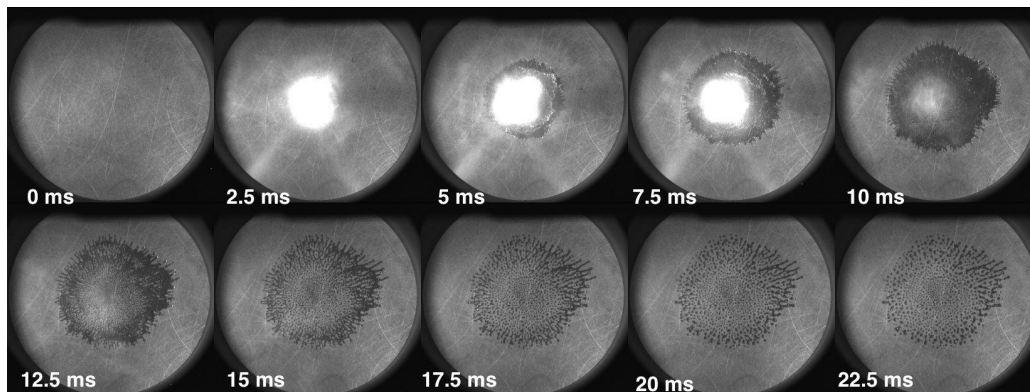


**Figure 6.14: Liquid film evolution for orthogonal impingement. Wall temperature  $T_w = 150^{\circ}C$ , injection temperature  $T_{FU} = 150^{\circ}C$ , injection duration  $T_i = 6.00\ ms$  and injection pressure  $P_i = 100\ bar$ .**

and presents some holes. Some bubbles, signs of vaporisation are also experienced (however they are more easily identifiable on movies than images). Finally, above the saturation temperature, strong boiling is experienced, mainly outside the impingement area. This can be linked with the data produced in Chapter 5. Indeed, the impingement

## 6. VAPORISATION IN THE VICINITY OF HOT WALLS

---



**Figure 6.15: Liquid film evolution for orthogonal impingement. Wall temperature  $T_w = 180^\circ C$ , injection temperature  $T_{FU} = 180^\circ C$ , injection duration  $T_i = 6.00$  ms and injection pressure  $P_i = 100$  bar.**

area is much cooler (especially here, because sapphire is used instead of aluminium), and the wall temperature is probably below the saturation temperature of n-decane. On the other hand, outside of the impingement area, the temperature is higher and nucleation starts in the liquid film. It is also interesting to note that the impingement zone is dry before the peripheral zones. One possible explanation is that, after the end of injection the mass spreads radially increasing the mass to vaporise on the film edges, while probably decreasing the film thickness at the centre. A last visualisation is proposed Figure 6.17 a zoom is here proposed at 15 ms (really representative of engine timescale) for the three temperatures. It can be noted that at these temperatures the liquid film has almost vanished at  $180^\circ C$  and  $210^\circ C$ , especially noting that this is performed with sapphire, it can be estimated that the vaporisation is faster on aluminium. Hence, in these conditions the liquid film is less a problem than in the cases presented at the beginning of the chapter.

These results were obtained with temperature near the saturation temperature. Experimental data significantly above this threshold were not performed for safety reasons. Shadowgraphy of impacts with a more volatile fuel on aluminium plate at higher temperatures (with respect to the saturation temperature), are now proposed.

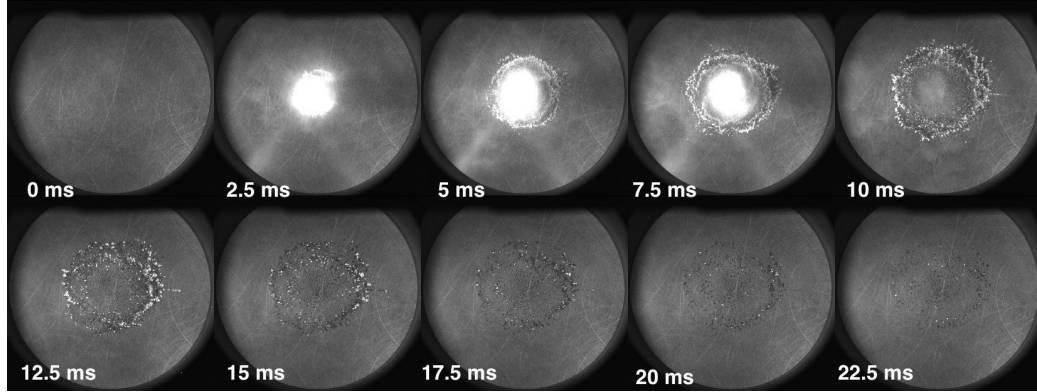


Figure 6.16: Liquid film evolution for orthogonal impingement. Wall temperature  $T_w = 210^\circ C$ , injection temperature  $T_{FU} = 180^\circ C$ , injection duration  $T_i = 6.00$  ms and injection pressure  $P_i = 100$  bar.

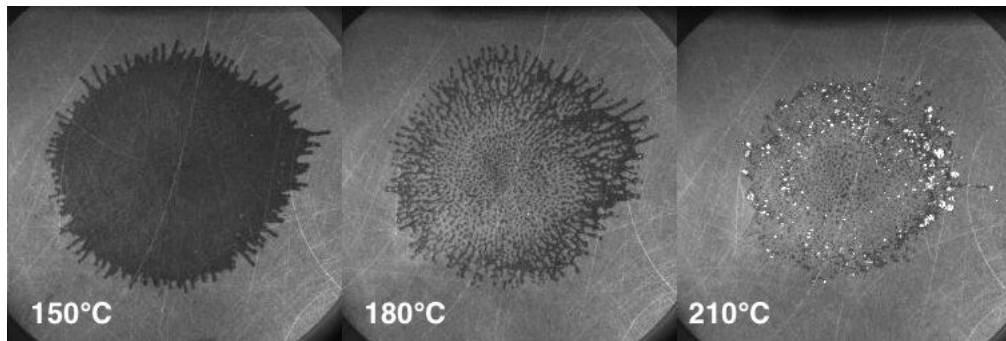


Figure 6.17: Zoomed visualisation of a n-decane film 15 ms after the start of injection for different plate temperature. Injection duration  $T_i = 6.00$  ms and injection pressure  $P_i = 100$  bar.

### 6.3.2 Shadowgraphy of impact on bowl shape

Inspired from the piston geometries of direct injection engines, an aluminium plate has been built. The dimensions of the plate are 3.5 cm long, 3 cm wide and the distance between the bottom of the bowl and the top is around 1 cm. Figure 6.18 shows a side picture of the plate.

High pressure injections, for the same injection conditions, but with two different plate temperatures were performed. The fuel used for this campaign is n-heptane, and it has a saturation temperature of  $98^\circ C$ . The impacts were performed at  $130^\circ C$  and  $200^\circ C$ . Just to give an order of magnitude heptane Nukiyama and Leidenfrost

## 6. VAPORISATION IN THE VICINITY OF HOT WALLS

---

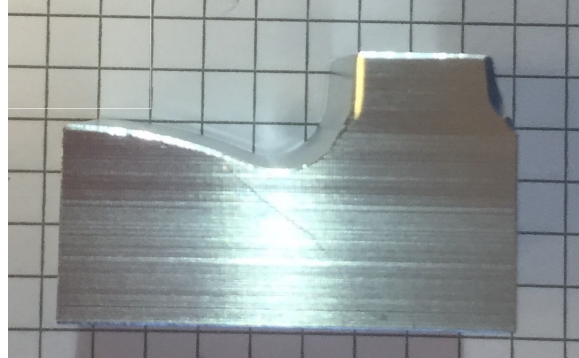


Figure 6.18: Aluminium plate mimicking a bowl shape. Length 3.5 cm, width 3 cm, height 1 cm (between bottom and top of the bowl).

temperature (for gently deposited droplets) are respectively  $150^{\circ}\text{C}$  and  $210^{\circ}\text{C}$  [24].

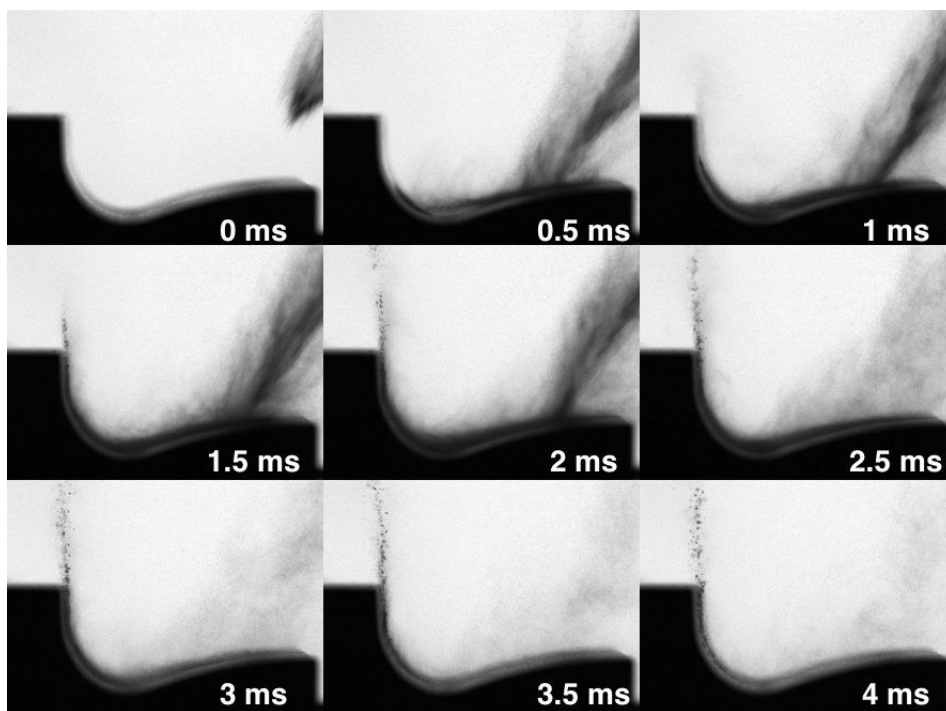
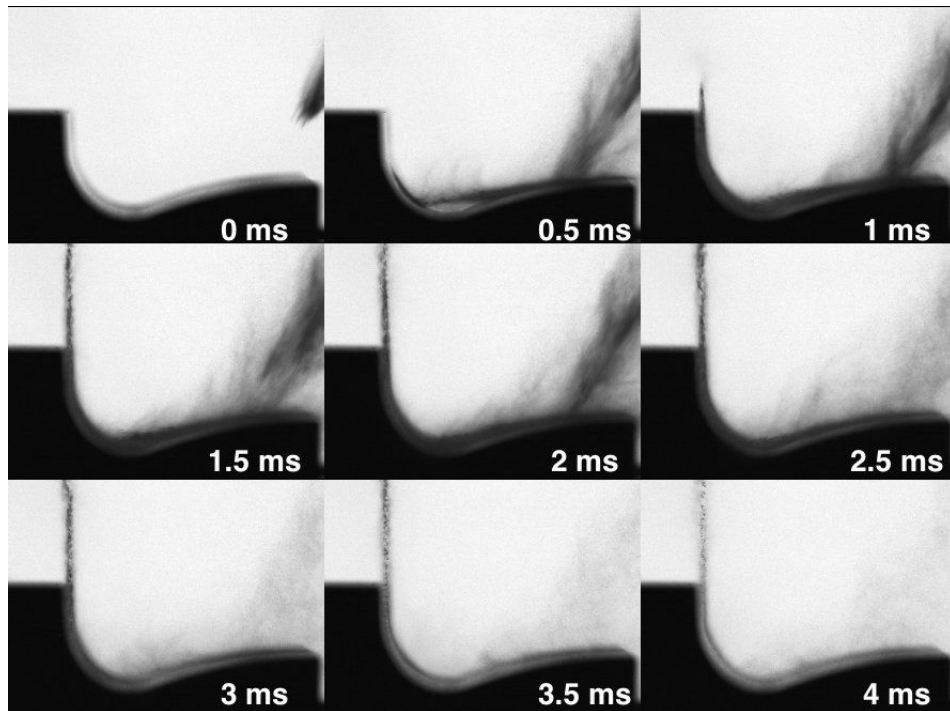


Figure 6.19: Shadowgraphy of spray impinging on a hot wall, bowl shape geometry. Wall temperature  $T_w = 130^{\circ}\text{C}$ , injection duration  $T_i = 2.12\text{ ms}$  and injection pressure  $P_i = 100\text{ bar}$ .

Figure 6.19 shows the development of the liquid film and secondary spray for a wall temperature of  $150^{\circ}\text{C}$ . It has to be compared with Figure 6.20 where the wall



temperature is  $200^{\circ}C$ . Indeed, for the colder conditions some droplets at the edge of the bowl starts to appear after  $1.5\ ms$ . Whereas for the hot case they appear after  $1.0\ ms$ . It also seems that the quantity leaving the edge of the bowl is more important for the hotter case. Several interrogations arise: what is the mass, size and velocity of these droplets? From the visualisations available here, it seems that the speed of the droplets increase with respect to the wall temperature as well as their size (probably because of thermal atomisation [7]), Leidenfrost effect are experienced at  $200^{\circ}C$ , also the mass leaving the plate seems more important at  $200^{\circ}C$  than at  $150^{\circ}C$ . Using, the frame-rate and the spatial resolution of the camera some rough estimations were performed. Droplets up to  $150\ \mu m$  to  $200\ \mu m$  were observed. The velocity of these big droplets is estimated between  $8\ m.s^{-1}$  and  $10\ m.s^{-1}$ . Finally some ligaments were also observed at the edge of the bowl shape.



**Figure 6.20: Shadowgraphy of spray impinging on a hot wall, bowl shape geometry. Wall temperature  $T_w = 200^{\circ}C$ , injection duration  $T_i = 2.12\ ms$  and injection pressure  $P_i = 100\ bar$ .**

In an engine configuration, these droplets are immediately directed towards the cylinder head which is colder than the piston (as presented in Chapter 2). These

## 6. VAPORISATION IN THE VICINITY OF HOT WALLS

---

droplets of consequent size are actually experiencing the conditions envisaged in Section 6.1, the size of these droplets being consequently more important than the characteristic size of the droplets generated by the injector, it seems that they represent a potential issue for the achievement of the air/fuel mixture.

Wetting the spark plug is probably the worst scenario as the flame will probably not develop or the spark plug could be damaged.

### 6.4 Conclusion

In this chapter the use of two new experimental methods have been presented. Though many limitations were identified while using the interferometric device, it has proven good repeatability and accuracy in evaporative conditions. It gets more complicate to use when getting closer to the saturation temperature. However, it helped to study the behavious of multi-component fuels and calibrating a model for the evaporation of thin liquid films. In the mean time, the use of an aluminium plate to perform the "RIM method" has been tested. Though the thickness evaluation available with quartz has been lost (in [96] they managed to get the liquid film thickness on aluminium) it gives a trustable value for the lifetime of the liquid film. Indeed, using an aluminium plate corrects one of the main aspects that are non satisfying with the classical RIM performed on quartz. Finally, some visualisation at high temperature have been performed and they raise some new questions. RIM performed at high temperatures, showed that the evaporation during the spreading is no longer negligible when getting close to the saturation temperature. However, a modification of spreading models presented in [8, 46] with a sink term could probably be derived inspired by what is already done for boiling in [24, 34, 51]. The shadowgraphy performed at high temperatures (close to Leidenfrost temperature), witness eventual issues that could be encountered for these regimes. Indeed, avoiding the evaporative conditions is one of the main concern, however impacting in Leidenfrost conditions (too hot) is probably not satisfying either. A thorough study of the problem could help to conclude whether or not the consequences are important.

# Conclusion

## Contents

---

<b>4.1</b>	<b>Orthogonal impingement film spreading . . . . .</b>	<b>82</b>
4.1.1	Results . . . . .	82
4.1.2	The spreading phase . . . . .	88
4.1.3	Relaxation phase . . . . .	92
4.1.4	Effect of fuel type . . . . .	94
4.1.5	Roughness effect . . . . .	97
4.1.6	Effect of wall and fuel temperature . . . . .	99
<b>4.2</b>	<b>Non-orthogonal film spreading . . . . .</b>	<b>105</b>
4.2.1	Results . . . . .	105
4.2.2	The spreading phase . . . . .	107
4.2.3	Angle dependency . . . . .	111
<b>4.3</b>	<b>on the thickness of spreading liquid films . . . . .</b>	<b>114</b>
<b>4.4</b>	<b>Conclusion . . . . .</b>	<b>117</b>

---

Liquid film generation, propagation and vaporisation as well as the heat transfer involved have been studied during three years for this PhD thesis. The main objective was to increase the detailed knowledge about liquid films in combustion chambers for the automotive industry. Thanks to the industrial facilities present at Continental Automotive, it has been possible to perform various experimental measurements. From the thickness evaluation of a thin liquid film to the high-speed surface temperature acquisition of piston temperature in a fully instrumented engine. In this engine, the effect of the Start Of Injection (SOI) on the liquid film impingement and the link with

## 7. CONCLUSION

---

particle matter generation (though it is a known behaviour for direct injection engines) was observed using a thermo-instrumented piston. Only a few research works performed with an instrumentation of the piston with thermocouples have been published so far, and the observation of piston temperature over an extended range of operating points (up to 2500 *rpm*-24 *bar*, or 4000 *rpm*-20 *bar*) is of great interest for the simulation teams at Continental Automotive or their partners. It has raised many interrogations on the mass of the liquid deposit, the heat exchanges accompanying the spray impact (as a decrease of temperature has been recorded up to 7°C on one of the thermocouples), and the lifetime of this fuel film.

In a tentative of answering these questions, the general problem of spray-wall impingement has been divided in several sub-problems. Together with this division, different experimental set-ups have been used. The RIM method, which was already in use at Continental was thoroughly used, and some modifications and ameliorations have been provided. In the mean time, a method using thermocouples inserted in an aluminium plate has been developed. It has allowed to treat the heat transfer involved during the spray-wall impingement process. Finally, the development of a new measuring technique via the use of an interferometric pen (STIL OPILB), helped estimating the liquid film thickness in evaporative conditions of thin mono- and multi-component liquid films (down to 3 to 4  $\mu m$ ).

The first fuel film characteristic to be addressed is the generation of the liquid film itself, and more particularly its spreading. An original, model has been derived to describe the phenomenon. The robustness of the approach is one of its strengths, as it is valid for a wide range of injection duration, injection pressure, wall temperature, wall roughness, impingement angle, and fuel composition. Many models for liquid film generation exist, however, most of them use Lagrangian approach, Lagrangian particles of fluid stick and spread over the wall which generates the fuel film. The CFD methods are expensive, and due to the high variability of the engine working points, a fine parametric study remains a hard task (many calculations and post-processing steps). This is where the principal quality and originality of the model stay: it is a global and simple analytical model based on mass and momentum balances. It manages to explain the most of film spreading and trends versus parameter variations, while being very cheap in term of computation time (algebraic formulas). Thickness evaluation for different pressure and angle has also been presented confirming the model trends.

---

Unfortunately it was not possible to perform the measure during the spreading phase of the liquid film.

Then, the heat transfer between the spray and the wall has been tackled. Thanks to the thermo-instrumented plate, the heat removal and temperature drop induced by the spray-wall impact has been observed. The heat transfer spatial dependency is very local. Therefore, it has given a different view on the engine measurements: the piston cooling is probably even stronger than what has been measured. The database developed with the different parameter variations can be used as validation cases for CFD and Conjugate Heat Transfer (CHT) spray-wall impingement models. Finally, the heat transfer has been modelled and an injector (or spray) heat transfer coefficient has been introduced. Increasing the knowledge about this coefficient would be highly appreciable to better characterise spray cooling.

The last part of liquid film study that has been tackled is its vaporisation. Two innovative methods have been developed. The STIL interferometric device gives interesting results regarding the liquid film thickness in evaporative conditions, either for mono- or multi-component fuels. However, it has shown some strong limitations in boiling regimes. In the mean time, the RIM method has been modified, and using an aluminium plate, it allows to correctly take into account the properties of piston materials. Thanks to image processing, tracking the liquid film area allowed to get the fuel film lifetime in realistic conditions (even when nucleate boiling starts). A qualitative study on film spreading, in hot conditions and very hot conditions, was finally presented and rose new questions for liquid film impingement. The mass leaving the piston after impingement can, in adverse conditions, be a source of new problems. A quantitative study of this mass would be of great interest in future works.

The PhD thesis has brought its contribution to the link between engine and experimental research. Database, and test cases for computational research and understanding on liquid films have been done together with new or improved experimental set-ups. Hopefully it will help to continue increasing the scientific knowledge around liquid films generated by high pressure sprays. Either in term of deposition and heat transfer or in term of pollutant and emission generation.

Follows-up on this rich topic can be envisaged, a deeper investigation of multi-components fuels would be very interesting. Also the effect of multi-injection strategies on the film spreading and impingement heat transfer could ameliorate the knowledge

## 7. CONCLUSION

---

on these phenomenon. Modelling the evaporation during the liquid film spreading in hot conditions by adding a sink term in the equations is a promising approach and deserve to be tested. Finally, LES simulations during the impact and spreading of the liquid film would help to ameliorate the comprehension of the phenomenon involved during the spray wall impingement.

## 8

# Appendix

### 8.1 Roughness measurement on coked piston

Measurement performed with an ALTISURF workstation on a coked piston. The coking of the piston increases the piston roughness.

Porosity of the soot deposit is often questioned as it can adsorb some fuel during impingement.

## 8. APPENDIX

---

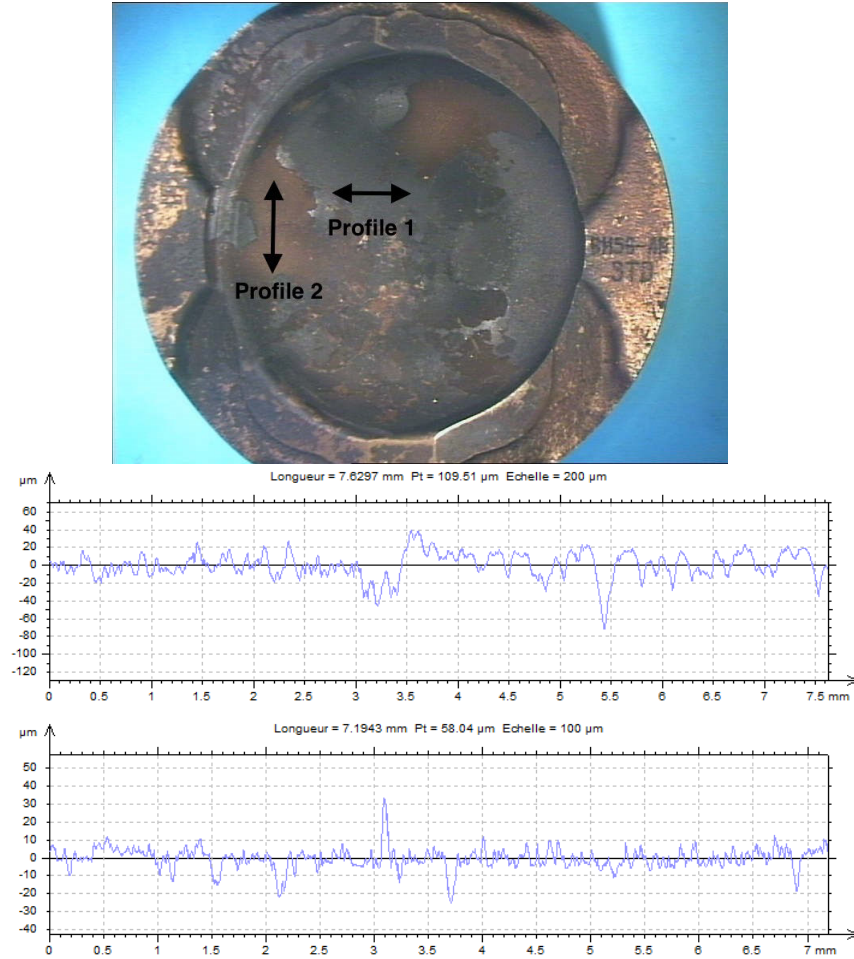


Figure 8.1: Coked piston visualisation together with the roughness measurements performed on a coked zone. Top: piston visualisation. Centre: roughness measurement in the non coked zone. Bottom: roughness measurement in the coked zone

### 8.2 Additional material on the non-orthogonal spreading of liquid film

The liquid film is assimilated to an ellipse with a constant thickness  $e$ , a semi-major and -minor axes  $a$  and  $b$ . Using the definitions from Chapter 4, the mass balance writes again:

$$\frac{d\pi abe}{dt} \approx K_m Q, \quad (8.1)$$



## 8.2 Additional material on the non-orthogonal spreading of liquid film

---

$Q$  is the injection discharge of the injection, while  $K_m$  stands for the effective injected mass that contributes to the liquid film. Eq (8.1) enables to write:

$$\pi a b e \approx K_m Q t. \quad (8.2)$$

The ellipse relations are the following, with the same definitions as in chapter 4:

$$\begin{aligned} a + c &= a(1 + \epsilon), \\ a - c &= a(1 - \epsilon), \\ p &= a(1 - \epsilon^2). \end{aligned}$$

The momentum equation is projected in the three main directions (front  $f$ , back  $b$  and side  $s$ ) as indicated in Chapter 4.

$$\frac{\partial P}{\partial x_f} = \eta \frac{\partial^2 v_f}{\partial z^2}, \quad (8.3)$$

$$\frac{\partial P}{\partial x_b} = \eta \frac{\partial^2 v_b}{\partial z^2}, \quad (8.4)$$

$$\frac{\partial P}{\partial y} = \eta \frac{\partial^2 v_s}{\partial z^2}, \quad (8.5)$$

and  $v_f = d(a + c)/dt$ ,  $v_b = d(a - c)/dt$  and  $v_s = dp/dt$ . The previous system can be approximated following the same philosophy as in Chapter 4. Here, it is clear the pressure term is now a combination of a tangential and an orthogonal contributions. Therefore, one expects, of course, to have different momentum sources, depending on the direction.

$$\frac{\Delta P_1}{a + c} \approx \frac{\eta}{e^2} \frac{d(a + c)}{dt}, \quad (8.6)$$

$$\frac{\Delta P_2}{a - c} = \frac{\eta}{e^2} \frac{d(a - c)}{dt}, \quad (8.7)$$

$$\frac{\Delta P_3}{p} = \frac{\eta}{e^2} \frac{dp}{dt}, \quad (8.8)$$

## 8. APPENDIX

---

The exact nature of  $\Delta P_n$ ,  $n \in \{1, 2, 3\}$  is not discussed here but we suppose it can be written:  $\Delta P_n = K_n P_i$ ,  $i \in \{1, 2, 3\}$ , where  $P_i$  is the injection pressure and  $K_n$  corresponds to the transfer function from the injector to the liquid film.

In what follows, we only detail the derivation for  $a + c$ , the other two are then straightforward.

The next step corresponds to the elimination of  $e^2$ . To do so, Eq (8.2) is used, replacing first  $a$  and  $b$  by  $a + c$  and factors depending on the eccentricity  $\epsilon$ . The definition of the square of thickness is then:

$$e^2 = \frac{K_m^2 Q^2 (1 + \epsilon)^4 t^2}{\pi^2 (a + c)^4 (1 - \epsilon^2)}. \quad (8.9)$$

Injecting the previous in the equation of  $a + c$  leads to:

$$(a + c)^5 \frac{d(a + c)}{dt} \approx \frac{K_m^2 K_1 P_i Q^2 (1 + \epsilon)^4}{\eta \pi^2 (1 - \epsilon^2)} t^2. \quad (8.10)$$

This finally gives for  $a + c$ ,  $a - c$  and  $p$ :

$$a + c \approx \Lambda_1 \left( \frac{(1 + \epsilon)^4}{(1 - \epsilon^2)} \right)^{1/3} t, \quad (8.11)$$

$$a - c \approx \Lambda_2 \left( \frac{(1 - \epsilon)^4}{(1 - \epsilon^2)} \right)^{1/3} t, \quad (8.12)$$

$$p \approx \Lambda_3 (1 - \epsilon^2)^{1/3} t, \quad (8.13)$$

with:

$$\Lambda_n = \left( \frac{2K_m^2 K_n P_i Q^2}{\pi^2 \eta} \right)^{1/3},$$

The equations derived for the orthogonal case naturally rise from these equations as  $\epsilon \rightarrow 0$ . Remains how to express  $K_1$ ,  $K_2$  and  $K_3$  from the experimental measurements first, and, eventually from the spray characteristics. In chapter 4, some fits have been found using the experimental measurements. Introducing the following notations, it is then convenient to make a link between the results from Chapter 4 and the present model.

### 8.3 Evaporation of thin liquid film of single and multi-component hydrocarbon fuel from a hot plate

---

Let us introduce  $\beta_n$  such that:

$$(a + c)^2 \propto \beta_1 t \quad (8.14)$$

$$(a - c)^2 \propto \beta_2 t \quad (8.15)$$

$$p^2 \propto \beta_3 t \quad (8.16)$$

$$(8.17)$$

Then we have  $\beta_n = 20 (1 + \alpha_n \cos \theta)^2$  according to chapter 4. Recalling that  $\epsilon = \sqrt{\cos \theta}$ .

Combining with the model shown in this appendix, it then enables to express  $K_n$  with respect to  $\beta_n$ :

$$K_1 = \left[ \frac{(1 - \epsilon^2)}{(1 + \epsilon)^4} \frac{\eta \pi^2}{K_m^2 P_i Q^2} \right] \beta_1^3, \quad (8.18)$$

$$K_2 = \left[ \frac{(1 - \epsilon^2)}{(1 - \epsilon)^4} \frac{\eta \pi^2}{K_m^2 P_i Q^2} \right] \beta_2^3, \quad (8.19)$$

$$K_3 = \left[ \frac{1}{1 - \epsilon^2} \frac{\eta \pi^2}{K_m^2 P_i Q^2} \right] \beta_2^3.$$

Hence, this complete derivation describes the spreading only with the injection parameters and the geometrical observations on the film shape.

### 8.3 Evaporation of thin liquid film of single and multi-component hydrocarbon fuel from a hot plate

Paper written between Continental Toulouse and Continental Bangalore during the PhD thesis of Sandeep Mouvanal and Quentin Lamiel.



ELSEVIER

Contents lists available at ScienceDirect

## International Journal of Heat and Mass Transfer

journal homepage: [www.elsevier.com/locate/ijhmt](http://www.elsevier.com/locate/ijhmt)

## Evaporation of thin liquid film of single and multi-component hydrocarbon fuel from a hot plate

Sandeep Mouvanal<sup>a,b</sup>, Quentin Lamiel<sup>b,c</sup>, Nicolas Lamarque<sup>b</sup>, Jerome Helie<sup>b</sup>, Axel Burkhardt<sup>b</sup>, Shamit Bakshi<sup>a,\*</sup>, Dhiman Chatterjee<sup>a</sup><sup>a</sup> Department of Mechanical Engineering, Indian Institute of Technology Madras, Chennai, Tamil Nadu, India<sup>b</sup> Continental Automotive GmbH, Siemensstrasse 12, 93055 Regensburg, Germany<sup>c</sup> Institut de Mécanique des Fluides de Toulouse (IMFT) – Université de Toulouse, CNRS-INPT-UPS, Toulouse, France

## ARTICLE INFO

## Article history:

Received 4 April 2019

Received in revised form 11 June 2019

Accepted 17 June 2019

## Keywords:

Evaporation

Liquid film

Single component

Multi-component

Hydrocarbon fuel

## ABSTRACT

Evaporation of liquid film is of great importance, especially to the automotive industry, owing to its prevalence in automotive wet components. Thin liquid films usually deposit/spread in the inlet ports of engines using port fuel injection (PFI), at the nozzle tip of gasoline direct injection (GDI) engines, on the piston head of GDI and diesel engines, etc. It is important to predict the evaporation rate of these liquid films which have the thickness of the order of micrometers and may potentially lead to carbon deposits and consequent emissions. In this work, results of extensive experimental and numerical investigations of the evaporation of single and multi-component hydrocarbon film are presented. Liquid films are created by spraying the fuel on a smooth aluminum plate, and its evaporation pattern is studied at various temperatures of the plate. The film thickness reduction was monitored over time using a confocal point probe until the liquid film is completely evaporated. A one-dimensional numerical model is developed to predict the reduction of film thickness due to evaporation for single and multi-component fuels. The numerical results compared well with the measurements.

© 2019 Elsevier Ltd. All rights reserved.

## 1. Introduction

Fuel injection technology is used extensively in both diesel and gasoline engines. In such engines, during the injection phase, the fuel spray tends to hit solid surfaces like the piston bowl in case of diesel and GDI engines, intake ports in case of PFI engines [44]. This results in the formation of liquid films that could lead to pollutant emissions, as they often form carbon deposits and lead to formation of particulate matters. In GDI injectors, inner wall and tip of the nozzle get wet by gasoline, thereby forming a thin film at the end of injection [26]. This, over a period of time, results in tip sooting and coking of the injector nozzle [40,32]. So, it is essential for the designers to understand the timescale of evaporation of the liquid film of gasoline or diesel which is composed of multiple components with different volatility. There are many experimental studies conducted on the evaporation of sessile droplets of single

and multi-component fuels at different conditions [21,10]. In the case of liquid film evaporation from a hot surface, conjugate heat transfer and multi-component dynamics coupled with variation in surface topology makes it more difficult to study the process. In most of the experimental studies, the liquid film on the surface is formed by spreading of a droplet of either single component or multi-component fuels. Itaru and Kunihide [22] investigated evaporation of a water droplet on smooth, hot surfaces (80–450 °C) of copper, brass, carbon steel and stainless steel. They characterized the vaporization of water on these surfaces from nucleate boiling to film boiling conditions. Evaporation of hydrocarbon fuels including gasoline and diesel were investigated by Fardad and Ladomatatos [12] by heating liquid droplet on a metal plate at various temperatures. The approximate height of the droplet was obtained from the contact angle and the radius of the wetted area after complete spreading. They observed that the maximum vaporization takes place near the saturation temperature of the fuel. Further increase in the surface temperature far beyond the saturation temperature leads to reduction in the vaporization rate as a cushion of vapor forms below the liquid film which reduces the heat transfer from the metal surface to the liquid film. Stanglmaier et al. [34] studied the vaporization of fuel drops on a heated surface to understand the fuel wall interactions within the gasoline direct injection

\* Corresponding author.

E-mail addresses: [sandeep.mouvanal@continental-corporation.com](mailto:sandeep.mouvanal@continental-corporation.com) (S. Mouvanal), [quentin.lamiel@continental-corporation.com](mailto:quentin.lamiel@continental-corporation.com) (Q. Lamiel), [nicolas.lamarque@continental-corporation.com](mailto:nicolas.lamarque@continental-corporation.com) (N. Lamarque), [jerome.helie@continental-corporation.com](mailto:jerome.helie@continental-corporation.com) (J. Helie), [axel.burkhardt@continental-corporation.com](mailto:axel.burkhardt@continental-corporation.com) (A. Burkhardt), [shamit@iitm.ac.in](mailto:shamit@iitm.ac.in) (S. Bakshi), [dhiman@iitm.ac.in](mailto:dhiman@iitm.ac.in) (D. Chatterjee).

engine. They observed a strong influence of the engine pressure during different strokes of engine operation on evaporation. Vaporization of gasoline drops on the piston gets reduced due to the Leidenfrost effect when the pressure in the cylinder is low whereas the evaporation rate quickly increases as pressure rises in the compression stroke.

In all the above studies, it was difficult to measure the film thickness accurately because the surface of the film is curved due to surface tension and wall adhesion. Hence, an average thickness was calculated based on the geometry (droplet spread radius and the contact angle). Refractive index matching method (RIM) has been used to study the film thickness of the film formed by the liquid spray. This methodology was introduced by Drake et al. [7] and used by Maligne and Bruneaux [27], Habchi et al. [19] and Ding et al. [6] to measure wall film thickness in an optical direct injection engine. Using this method, thickness of thin films on a rough surface can be measured. A liquid with refractive index close to the quartz window is deposited on the rough surface of the window. The liquid and solid refractive indices match, so, when light travels through the solid-liquid interface, the intensity of scattered light from the roughness elements present on the solid surface is less. As the roughness elements slowly gets exposed with evaporation of the film, the scattered light intensity from the rough surface increases [6]. Thus the light intensity can be calibrated with the film thickness. But, this method will work only for very thin films and depend on the depth of the roughness elements on the surface.

Recently, a more accurate method to measure the film thickness of liquid film spread over a larger area was developed with the use of a confocal optical device. Using this method, the dynamic thickness of film during evaporation and boiling was studied by Gong et al. [14]. The working liquid used to make the thin film was pure water with the thickness ranging in between 500 and 1000  $\mu\text{m}$ . They also analyzed the dynamics/evolution of liquid film evaporating on a heated surface and estimated its critical thickness at rupture which was compared with lubrication theory [15]. Further, they measured and analyzed instantaneous film thickness with heating from low heat flux to critical heat flux [16,17]. The dynamics of film indicates influence of scales induced by the nucleation, growth, and collapse of bubble(s).

The evaporation process is also numerically modeled to predict the rate of evaporation and composition of the liquid film. For simplicity, fuels are modeled as a single component in most multi-dimensional models [5]. In order to capture the real behaviour of complex fuels containing a mixture of multiple components, multi-component evaporation models are developed which can be classified as continuous multi-component (CMC) models and discrete multi-component (DMC) models. The CMC model is based on the continuous thermodynamics approach [37,41]. DMC models track individual components and its composition during evaporation. However, most of the studies in literature deals with the evaporation of droplets [43,35,9] and a very few on evaporation of thin films. Ra and Reitz [29] presented a vaporization model for discrete multi-component fuel sprays. Their vaporization model for single and multi-component droplets considered both normal and flash-boiling conditions. A discrete multi-component fuel evaporation model with liquid turbulence effects was developed by Abianeh and Chen [1] which was validated against direct numerical simulation. Another similar model for the droplet evaporation was developed by Su and Chen [36]. Due to the lack of experimental results, validation was done using an exact solution for evaporation on a semi-infinite plate.

A lumped multi-component evaporation model was developed by Wang et al. [42] to study the evaporation of a wall film of multi-component diesel surrogate inside the injector nozzle. The model gave the time-dependent concentration of each species in the mixture and was used for the calculation of combustion chem-

istry. However, the model lacked experimental validation of the evaporation rate. Evaporation model for hydrocarbon fuel based on the measurement of single droplet evaporation from a heated surface and based on refractive index matching method for the liquid film formed by spray was also reported by Habchi [18] and Habchi et al. [19].

Though there are many models available in the literature as listed above, a simple phenomenological model to predict multi-component evaporation of liquid film is not available for quick calculations in industrial applications with reasonable accuracy. Available models either lack experimental validation or are based on the measurements of single droplet evaporation gently deposited on the heated surface. In a recent study by Bhat et al. [3], single droplet impact and spreading of various hydrocarbon fuels on a heated steel plate in the film evaporation regime was presented. However, this study do not look at the temporal variation of film thickness. To the best of the knowledge of the authors, there is no work available in the literature which measures the liquid film thickness variation over time for thin films of hydrocarbon fuels, which is an essential parameter to understand the rate of evaporation.

With this background, the following contributions are made in this paper:

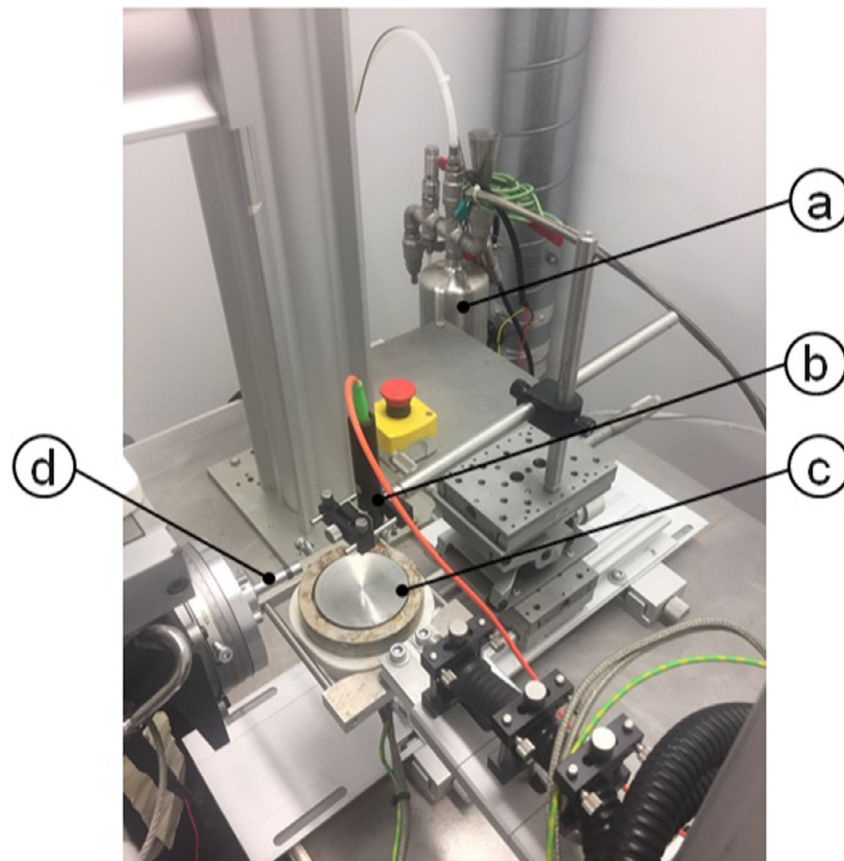
- The dynamic film thickness of hydrocarbon fuels are measured at various surface temperatures using a confocal optical device which has an accuracy to measure the film thickness close to 1  $\mu\text{m}$ . Also, the film thickness reported here is below 50  $\mu\text{m}$ , and hence represents the typical thickness observed in practical cases of film wetting on GDI injector nozzle tip.
- A simple lumped evaporation model is developed and validated with the above-mentioned experimental results. This model can be used for quick calculation of the total evaporation time, temporal variation of film thickness and fuel composition of a thin multi-component fuel film.

## 2. Experimental setup and methodology

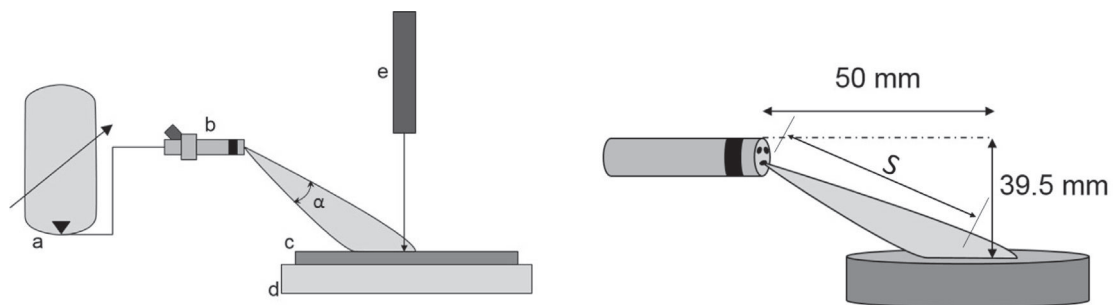
The experimental setup is shown in Fig. 1. It consists of a smooth aluminum plate onto which the spray from the injector is targeted. This three-hole injector is pressurized by dry air at 10 bar from a pressure vessel. The aluminum plate is attached with a heating system (heating collar) controlled by a PID regulator.

The temperature is measured using thermocouples attached to the aluminum plate. The temperature can be varied from ambient temperature to 130 °C. As shown in Fig. 2(a), the injector is placed in such a way that fuel from one of the injector hole impinges on the aluminum plate, the other two holes are sealed. The fuel is injected for a duration of 3 ms on the hot plate. Fig. 2, also shows the typical distance at which the injector is placed from the heated aluminum plate.

The thickness measurement is performed by an interferometric confocal device manufactured by STIL (Stilsa-sensors), which is placed above the aluminum plate. The specification of the confocal system is as follows: working distance = 4.2 cm, spot size = 32  $\mu\text{m}$ , measuring range = 1–90  $\mu\text{m}$  and selected sampling rate = 1 kHz. It is used to obtain the temporal variation of the film thickness at a point and thus the total evaporation time (lifetime), the vaporization rate of the liquid film which is formed by the spray impingement. The working principle of the optical device is described by Gong et al. [14]. Basically, in this device, a beam of white light is dispersed using an optical system of multiple lenses. Thus the white light is focussed at different adjacent points along the optical axis through the objective lenses. The solid substrate placed in this region mostly reflects the monochromatic light focussed on its surface. The reflected monochromatic light is received by the spec-



**Fig. 1.** Experimental setup. (a) pressure vessel, (b) confocal device, (c) aluminum plate, (d) injector.



(a) Experimental setup. a: pressure vessel, b: injector, c: aluminum plate, d: heating system, e: confocal device.

(b) Injector position with respect to the impacted wall (two of the nozzle holes are blocked during the experiment.)

**Fig. 2.** Schematic representation of the experimental setup.

trometer. When a liquid film is present on the substrate, reflections from both the liquid and the liquid-solid interface will be received in the spectrometer showing two peak signals. The difference between the two peaks can be related to the thickness of the film on the substrate.

For accurate measurement, the axis of the measurement device and the liquid film have to be orthogonal to each other as shown in Fig. 2(a). To get the lifetime of the film, the measurement spot is placed over the area where the film stays for the longest period. The confocal device can reliably measure thickness up to 3  $\mu\text{m}$ . Below this value, uncertainties increase. Hence, the lifetime is obtained by extrapolating the curve from the point at which the thickness reaches a value of 3  $\mu\text{m}$ , assuming that the evaporation rate remains constant beyond this time.

The liquid film is created by impinging a spray from a high-pressure injector on a smooth, heated aluminum plate, as shown in Fig. 1. The film thickness is monitored over time by the confocal device. For each fuel, the measurement is repeated ten times for each wall temperature, and the average values of the film thickness is plotted with time along with the standard deviation in the measured value. The Measurement is carried out for 5–6 temperatures varying between ambient and the saturation temperatures of each hydrocarbon fuel.

### 3. Numerical model

The schematic of the 1-D evaporation process is shown in Fig. 3. Here  $\delta$  is the thickness of the film which varies over time. The wall

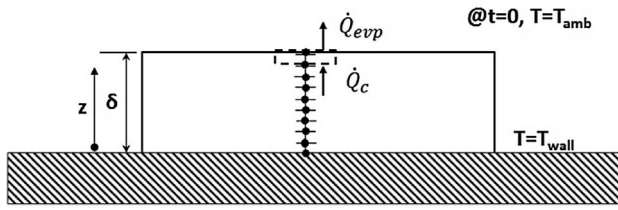


Fig. 3. Schematic showing the grids and boundary conditions in the numerical model.

is treated as isothermal with the wall temperature fixed at  $T_{wall}$ . At steady state, on the surface of the film the conduction heat flux ( $\dot{Q}_c$ ), is equal to the evaporation heat flux ( $\dot{Q}_{evp}$ ). The evaporation heat flux  $\dot{Q}_{evp}$  is the sum of the product of the evaporated mass of each fuel component with its corresponding latent heat of vaporization.

The assumptions made for the model are as follows:

1. The liquid film formed by the spray is assumed to have a uniform thickness.
2. The cooling of the plate by the spray is ignored.
3. The multi-component fuel is assumed to be homogeneous in composition.
4. The dynamics of the liquid film during the initial phase of spray impingement as reported by Chaves et al. [4], where large fluctuations in the film thickness occur are ignored in this study. This phase is trimmed out of the measurement results, and pure evaporation phase is considered for analysis.
5. The heat loss to the ambient (through diffusion or natural convection) is ignored as it is negligible compared to the heat required by the phase change process (evaporation) [8].
6. The species concentration in the film is assumed to remain homogeneous during evaporation of the film owing to the small value of the film thickness (rapid mixing model).

In order to numerically solve this problem, the 1-D heat equation is discretized by the finite difference method using the semi-implicit scheme. It is solved with the relevant initial and boundary conditions.

The initial and boundary conditions to solve the discretized equation is given as:

- at  $t = 0$ ,  $T = T_{amb}$
- at  $z = 0$ ,  $T = T_{wall}$
- at  $z = \delta$ ,  $\dot{Q}_c = \dot{Q}_{evp}$

Here,  $\dot{Q}_c$  is the conduction heat flux and  $\dot{Q}_{evp}$  is the heat flux due to evaporation at the free surface. The condition on the free surface is thus given as is shown by Eq. (1),

$$K \frac{dT}{dz} = \sum_{i=1}^n \dot{m}_i \Delta H_i, \quad (1)$$

where  $K$  is the thermal conductivity of the liquid mixture,  $n$  is the total number of components,  $\dot{m}_i$  is the evaporation mass flux of the  $i^{th}$  component,  $\Delta H_i$  is latent heat of the  $i^{th}$  component. The film thickness can be obtained from the mass conservation equation on the free surface as below.

$$\rho_f \frac{d\delta}{dt} = \sum_{i=1}^n \dot{m}_i, \quad (2)$$

where  $\rho_f$  is the density of the liquid mixture. Both the thermal conductivity and the density of the mixture are obtained from the mole fraction weighted averages of the components. Considering a film model [39,2] it can be said that the molecular diffusion of mass through the film is same as the convective mass transfer between the film and the ambient. Thus the evaporation rate for the  $i^{th}$  component,  $\dot{m}_i$ , can be expressed as in Eq. (3).

$$\dot{m}_i = D_{v,i} \frac{\rho_{v,i}}{L}, \quad (3)$$

where  $D_{v,i}$  is the diffusion coefficient and  $\rho_{v,i}$  is the density of the  $i^{th}$  component in the vapor at equilibrium and  $L$  is length scale representing the vapor film thickness above the film and expressed as the product of a constant  $C$  and the concentration boundary layer thickness ( $\delta_{c,i}$ ). The concentration boundary layer thickness can be expressed according to Eq. (4)[13].

$$\delta_{c,i} = \frac{3}{\sqrt{Sc}} \sqrt{\frac{v\eta}{U_0}}, \quad (4)$$

where  $Sc$  is the Schmidt number,  $v$  is the kinematic viscosity,  $\eta$  is a length scale representing the length along the plate for a boundary layer over a flat plate. For all the simulations presented here  $\eta$  is taken as 1 cm which is the average radius of the wetted area on the aluminum plate on which the spray impinges.  $U_0$  is the convective velocity. The convective velocity ( $U_0$ ) is calculated as the mean of the entrainment velocity of air during the injection of the fuel drops by the spray at a distance  $s$  from the nozzle based on Eq. (5) [33].

$$U(s) = \frac{U_f}{8\tilde{s}^2} (\sqrt{1 + 16\tilde{s}^2} - 1). \quad (5)$$

Here,  $U_f$  is the injection velocity at the exit of nozzle calculated based on the pressure difference between nozzle inlet and ambient as,  $U_f = \sqrt{2\Delta P/\rho_f}$ . The other parameter,  $\tilde{s} = s/s^+$  and  $s^+$  is given by Eq. (6).

$$s^+ = \sqrt{\frac{\rho_f}{\rho_a} \frac{d_f}{\tan(\alpha/2)}}. \quad (6)$$

where  $\rho_f$  is the liquid density,  $\rho_a$  is the air density,  $d_f = \sqrt{C_a}d$ , is the effective nozzle hole diameter with  $C_a = 0.9$ ,  $d$  is the hole diameter, and  $\alpha$  is the spray cone angle. The parameters used to calculate  $U(s)$  are listed in Table 1. As the vapor is assumed as an ideal gas, then the vapor density at equilibrium of the  $i^{th}$  component can be expressed in terms of the vapor pressure and temperature as shown in Eq. (7):

$$\rho_{v,i} = \frac{P_{v,i}}{R_i T}. \quad (7)$$

$P_{v,i}$  is the partial pressure of vapour of the  $i^{th}$  species in the mixture and  $R_i$  is the specific gas constant for the  $i^{th}$  gas. Using Raoult's law [30],  $P_{v,i}$  is given as,

$$P_{v,i} = x_i P_{total} = y_i P_{sat,i}(T). \quad (8)$$

$P_{total}$  is the total pressure and  $x_i$  is the mole fraction of the  $i^{th}$  component in the gas mixture. Using Raoult's law [30] and assuming the liquid mixture as an ideal solution, the mole fraction of the  $i^{th}$  component in the vapour phase can be obtained from the mole fraction of this component in the liquid phase ( $y_i$ ) using Eq. (8).  $P_{sat,i}(T)$  is the saturation pressure of the  $i^{th}$  component at the liquid temperature  $T$ . By combining Eqs. (3)–(8), mass flux of evaporation can be expressed as shown in Eq. (9).



**Table 1**  
Parameters for calculating entrainment velocity.

$\Delta P$ [bar]	$\alpha$ [°]	$\rho_a$ [kg/m <sup>3</sup> ]	s [mm]	d [μm]
9	30	1.25	63.7	165

$$\dot{m}_i = D_{v,i} \left( \frac{y_i P_{sat,i}(T)}{C \delta_{c,i} RT} \right). \quad (9)$$

In the multi-component mixture, the diffusion coefficient of one component is dependent on the presence of other components and the interaction between them in the molecular level. Diffusion coefficient for multi-component mixture is defined in Eq. (10), based on the work of Fairbanks and Wilke [11].

$$D_{v,i} = \frac{1 - y_i}{\sum_{j=1}^n \frac{y_j}{D_{ij}}}, \quad i \neq j. \quad (10)$$

In Eq. (10),  $D_{ij}$  is the binary diffusion coefficient ([39]) and is given as in Eq. (11).

$$D_{ij} = \frac{0.0266T^{1.5}}{M^{0.5} P \sigma^2 \Omega}. \quad (11)$$

where  $M$  is the mixture molecular weight,  $P$  is the pressure in Pa,  $\sigma$  is the Lennard-Jones parameter and  $\Omega$  is the collision integral. The collision integral  $\Omega$ , for the components in the range of temperature selected here are found to be very close to 1 [20]. Thus, to simplify the calculations, we take the value as 1.

The saturation pressure,  $P_{sat,i}$  for each component is calculated with the Antoine equation ([38]) as shown in Eq. (12).

$$\log_{10}(P_{sat,i}) = A - \frac{B}{T + D}. \quad (12)$$

where  $A$ ,  $B$ ,  $D$  are constants listed in Table 2 and  $T$  is the fuel temperature. All the fuel properties for the different fuels are shown in Table 3.

The heat equation within the film along with the energy and mass conservation equations (Eqs. (1) and (2)) discussed above are solved in order to get the evaporation characteristics of the liquid film. An iterative method is adopted to solve these non-linear equations for each time step. Time step ( $\Delta t$ ) used for the calculation is 1 μs and the initial grid size ( $\Delta z$ ) was taken as 1 μm. The grid size keeps reducing over time when the thickness reduces since the number of nodes is kept constant. In all the calculations, instability was not observed if the time step size is maintained as 1 μs. Using a higher value of time step resulted in instability at the last phase

**Table 2**  
Antoine's constant for calculating saturation pressure ([28]).

Fuel	$A$	$B$	$D$
n-hexane	4.003	1171.53	-48.78
n-heptane	4.028	1268.63	-56.199
iso-octane	3.94	1257.84	-52.42
n-decane	4.079	1501.27	-78.67

**Table 3**  
Fluid properties of single component fuels (adapted from NIST [28]).

Fuel	$T_{sat,i}$ [°C]	$M_i$ [g/mol]	$\rho_{f,i}$ [kg/m <sup>3</sup> ]	$K_i$ [W/m K]	$C_{p,i}$ [J/K]	$\Delta H_i$ [kJ/mol]
n-hexane	67.8	86.17	654.8	0.124	2268.6	31.1
n-heptane	98.2	100.21	670.4	0.140	2400	36.3
iso-octane	98.8	114.22	692.1	0.135	2223.6	35.1
n-decane	173.9	142.28	730.2	0.147	2209.5	51.3

of the calculation (below 5 μm film thickness) when the grid size is very small.

## 4. Results and discussion

### 4.1. Single component evaporation

The temporal variation of film thickness is measured as discussed in Section 2. Film thickness variation and total evaporation time (lifetime) are measured independently for three different hydrocarbons in order to fix the model constant  $C$  for Eq. (9) of the numerical model. For the present study, n-hexane, iso-octane, and n-decane are selected as single component fuels since they can be used to represent a three-component gasoline surrogate as reported by Köpple et al. [24].

The spray injection on the aluminum plate is followed by the film formation and is a very dynamic phase with dominance of the inertia, viscous and surface tension forces [25]. Also, during this period the temperature on the plate could drop due to the spray impact [23]. In order to avoid these uncertainties, the initial part of the thickness variation curve is trimmed, and only the linear evaporation dominated film thickness variation is considered for analysis.

The film thickness varies across the surface of the liquid film and is not uniform [31]. The film thickness is measured at a single point by the interferometric confocal device. Hence, for each experiment, the initial thickness can vary. But, the slope of thickness variation over time for a given temperature, which represents the rate of evaporation, does not vary much as shown in Fig. 4. Here, four different experimental cases are plotted at a wall temperature of 30 °C. As mentioned, it can be seen that the initial thickness varies for different experiments (18–35 μm) but the slope remains the same. This helps to average all the experiments to a single curve for a particular temperature and derive the average evaporation time for the complete evaporation of a liquid film with a certain initial thickness. Figure 5 shows the typical average thickness variation over time for n-decane at wall temperatures of 70 °C and 90 °C. It can be seen that the uncertainty in predicting thickness increases considerably towards the end when the film thickness reduces below 3 μm. Hence, a linear extrapolation is used to get the total evaporation time. It can be seen from Fig. 5 that the initial average thickness varies for different temperature conditions. In order to compare the total evaporation time for each hydrocarbon fuel at different temperatures, an initial film thickness of 20 μm is considered. Figure 6 shows the total evaporation time for a 20 μm thick liquid film of n-hexane, iso-octane and n-decane at various wall temperatures. Since n-hexane is the lightest component among the three, it can be observed that it evaporates at a faster rate compared to the other two fuels, and n-decane, the heaviest fuel evaporates at a much lower rate compared to the others. At lower temperatures, the rate of evaporation is slower and it increases with a rise in wall temperature. At temperatures near to the saturation temperature of each fuel, the evaporation rate does not increase substantially with a further increase in temperature. The film evaporation at temperatures higher than saturation temperature is not considered in the present study.



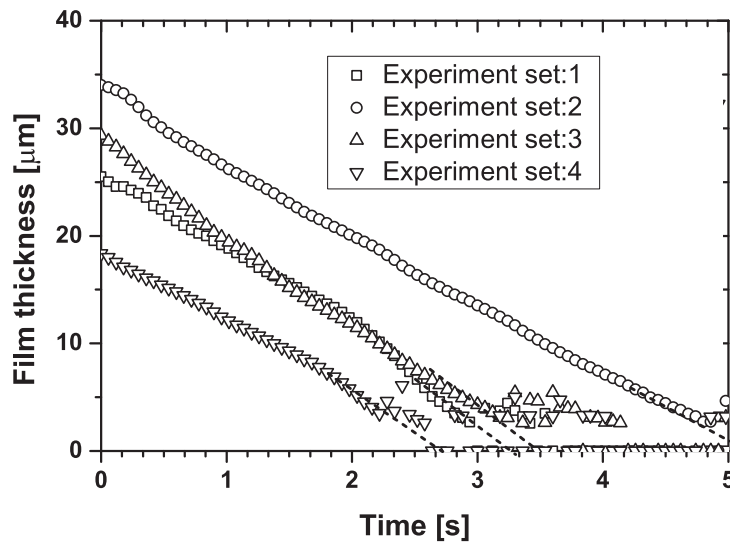


Fig. 4. Variation of film thickness of iso-octane with time at 30 °C for different injections.

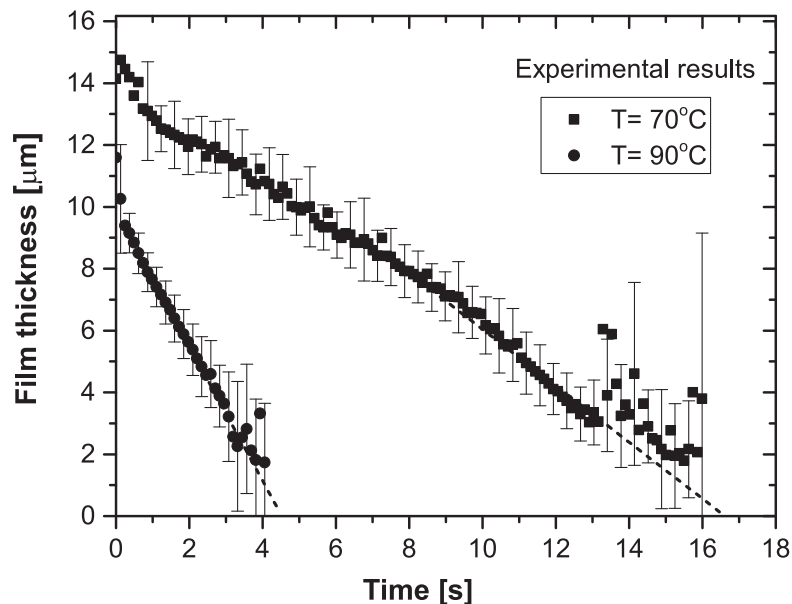


Fig. 5. Typical thickness evolution with respect to time for n-decane.

#### 4.1.1. Correlation for the numerical model constant

Based on the measurement data, a generalized model constant  $C$  for the numerical model as shown in Eq. (9) needs to be derived for all fuels and all surface temperatures. To achieve this, numerical simulations are performed and the value of  $C$  giving closest comparison with the measurement was obtained for each condition. These values of  $C$  are plotted against the non dimensional temperature,  $T^* = \frac{(T_{sat} - T_w)}{T_{sat}}$  as shown in Fig. 7. It was observed that the points follow a trend, so a regression analysis is performed to obtain a generalized correlation for the model constant, which can be used for numerical simulation for different hydrocarbon fuels at varying wall temperature conditions. Based on this, the model constant can be expressed in terms of  $T^*$  as per Eq. (13). It should be noted that the value of  $C$  is influenced by the saturation temperature of the fuel and the wall temperature.

$$C = -0.55 + 0.542e^{(7.39T^*)}. \quad (13)$$

This generalized correlation for  $C$  is used in Eq. (9) to perform 1-D numerical simulations for single and multiple-component fuels as discussed below.

#### 4.1.2. Comparison of numerical results with measurement

n-heptane, a fuel not used for deriving the correlation of the model constant given by Eq. (13), is selected to test the general applicability of the numerical model for similar hydrocarbon fuels. It can be seen from Fig. 8 that the numerical simulation closely matches with the experimental results for both the total evaporation time and the temporal variation of film thickness.

Further simulations are performed for n-hexane, iso-octane, and n-decane, as single component fuels. Fig. 9(a) shows the total evaporation time for a 20  $\mu\text{m}$  thick n-hexane fuel film, at various temperatures starting from the ambient temperature of 23–50 °C. It can be seen that the simulations match closely with the measurements. The total evaporation time for the liquid film reduces

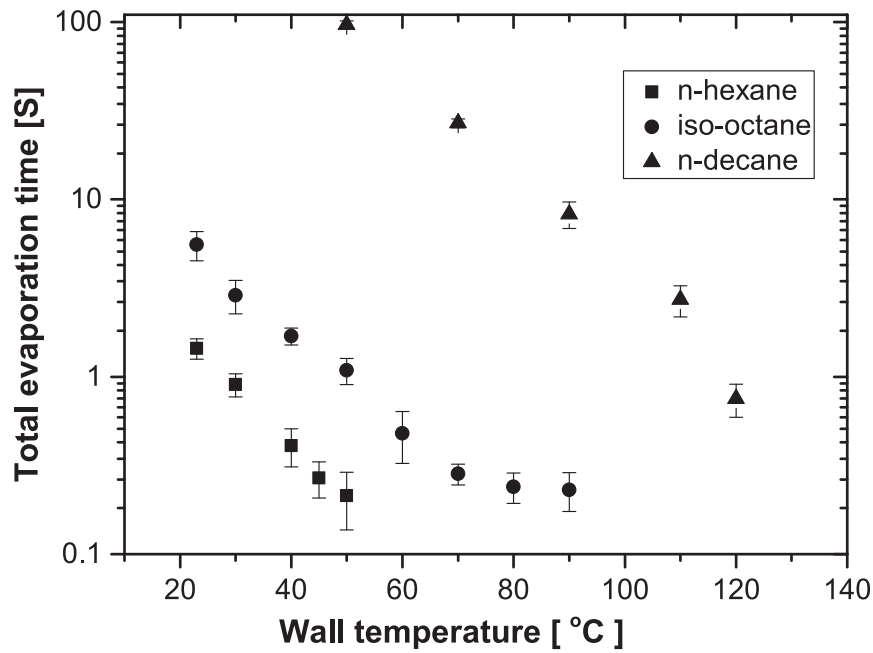


Fig. 6. Total evaporation time of 20 μm film of n-hexane, iso-octane and n-decane at various temperatures.

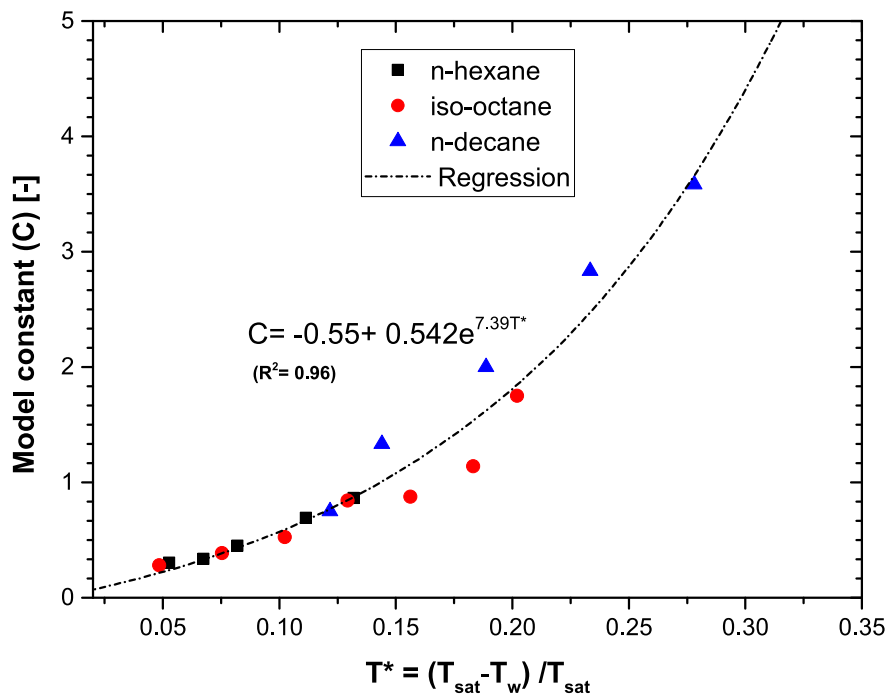


Fig. 7. Regression fit for the model constant C. The square of correlation coefficient ( $R^2$ ) of the curve fit is 0.96.

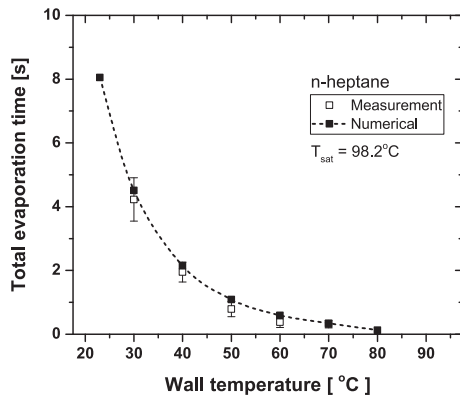
considerably when the wall temperature reaches the saturation temperature. The second fuel used here, iso-octane(2,2,4-Trime thylpentane), is a heavier component. Fig. 10 shows these results. The temperature is varied between 23 °C and 90 °C. Again, the agreement is good between the simulation and experiment.

The evaporation pattern of n-decane, the heaviest of the three fuels is shown in Fig. 11. As shown in Fig. 11(a) the time taken for total evaporation of 20 μm thick liquid film from the heated aluminum plate is much higher compared to the other fuels discussed above. Even at 50 °C, the liquid film takes more than 100

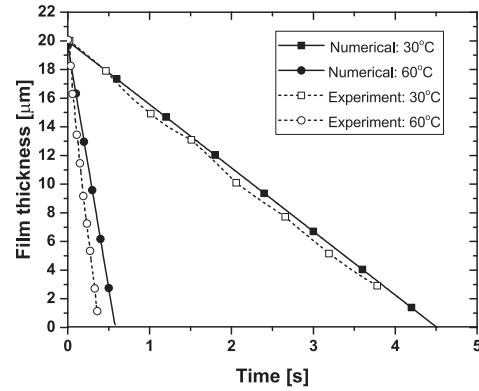
s for complete evaporation of a 20 μm film. It can be observed that at higher temperatures, the curve becomes asymptotic. The temporal variation of thickness over time is shown in Fig. 11(b). Good agreement between simulation and experimental results is again observed.

#### 4.2. Multi-component evaporation

In this section, the evaporation of multi-component liquid film is presented in detail with one two-component and another three-

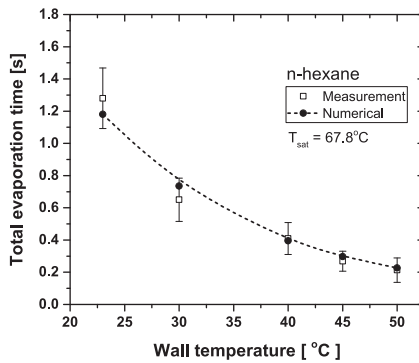


(a) Total evaporation time at different wall temperatures for a 20  $\mu\text{m}$  thick film of n-heptane.

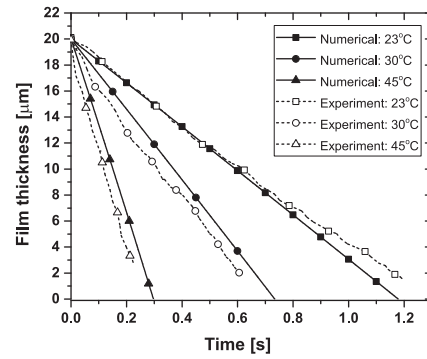


(b) Temporal variation of film thickness for a 20  $\mu\text{m}$  film of n-heptane at different temperatures.

Fig. 8. Evaporation of n-heptane liquid film.

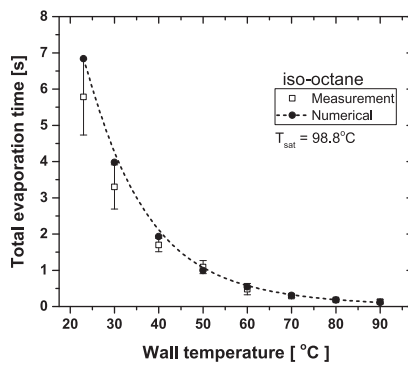


(a) Total evaporation time at different wall temperatures for a 20  $\mu\text{m}$  thick film of n-hexane.

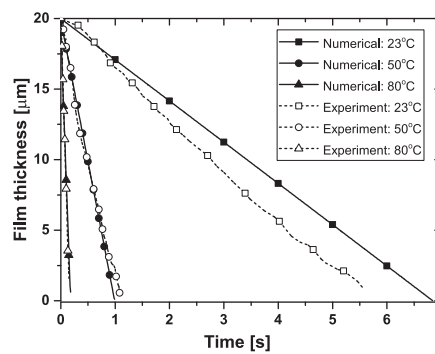


(b) Temporal variation of film thickness for a 20  $\mu\text{m}$  film of n-hexane at different temperatures.

Fig. 9. Evaporation of n-hexane liquid film.



(a) Total evaporation time at different wall temperatures for a 20  $\mu\text{m}$  thick film of iso-octane.



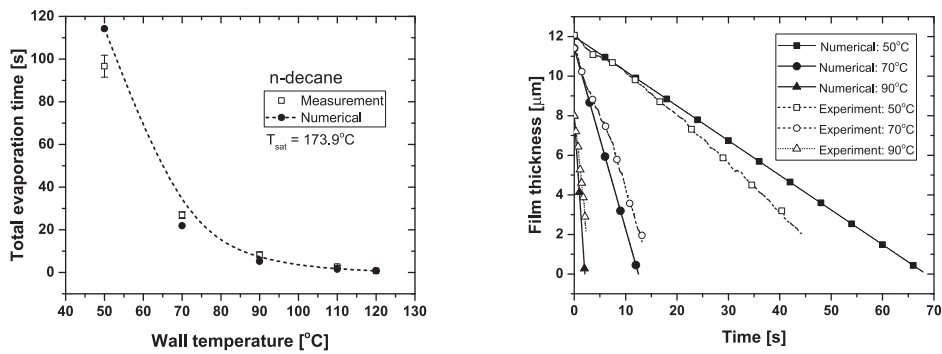
(b) Temporal variation of film thickness for a 20  $\mu\text{m}$  film of iso-octane at different temperatures.

Fig. 10. Evaporation of iso-octane liquid film.

component fuel. Two-component fuel is prepared from n-hexane and iso-octane with an equal mass-fraction of 0.5 each. The three-component fuel, which represents a gasoline surrogate, is prepared from n-hexane, iso-octane and n-decane with the mass-fractions as 0.35, 0.45 and 0.2 respectively as reported by Köpple et al. [24].

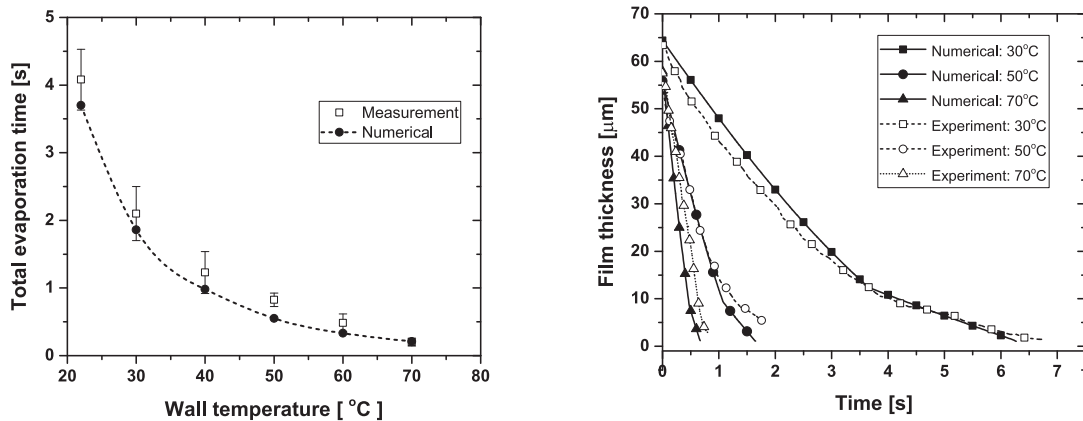
#### 4.2.1. Two-component evaporation: n-hexane and iso-octane

A mixture of n-hexane and iso-octane with 50:50 composition by mass is injected on the hot plate at various temperatures. The evaporation time and thickness variation are monitored using the optical device. The variation of total evaporation time with temperature is shown in Fig. 12(a) and the variation of film thickness



(a) Total evaporation time at different wall temperatures for a 20 μm thick film of n-decane. (b) Temporal variation of film thickness for film of n-decane at different temperatures.

Fig. 11. Evaporation of n-decane liquid film.



(a) Total evaporation time at different wall temperatures for a 20 μm thick film. (b) Temporal variation of film thickness.

Fig. 12. Evaporation of two component fuel (n-hexane and iso-octane in 50:50 by weight).

Table 4  
Comparison of the slopes of single and multicomponent evaporation.

Temperature (°C)	Slope of first part in n-hexane-iso-octane mixture (μm/s)	Slope of n-hexane (single component) (μm/s)	Slope of second part in n-hexane-iso-octane mixture (μm/s)	Slope of iso-octane (single component) (μm/s)
30	-13.3	-29.4	-2.95	-6.06
50	-40.5	-93.8	-8.16	-18.42

with time is shown in Fig. 12(b). At each temperature point, the measurement is repeated ten times, and the average curve is plotted and compared with the 1-D numerical calculations in Fig. 12.

Fig. 12(b) shows the total evaporation time of a 20 μm thick two-component liquid film from the hot aluminum plate at various temperatures. From the temporal variation of thickness, as in Fig. 12(b), it is clear that there exists two slopes. The initial steep slope is due to the faster evaporation of the lighter component, n-hexane, and the later, less steep slope is based on the slower evaporation rate of the heavier component, iso-octane in the mixture. However, it can be seen from Table 4 that the slope of the first part is different from the slope of the single-component evaporation of the lighter component (n-hexane). Same is true for the heavier component, iso-octane (Table 4). It may be noted that during the multi-component evaporation all the components are present in different proportions on the liquid surface. In the numerical model, the model constant C is selected in such a way that its value is based on the lightest component in the mixture until the mass-fraction of this component reaches a value of 0.1. This captures the

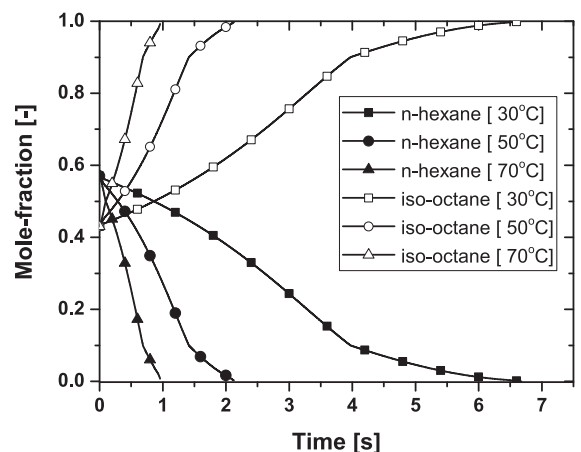


Fig. 13. Concentration variation of two component fuel corresponding to Fig. 12a (n-hexane and iso-octane in 50:50 by weight).

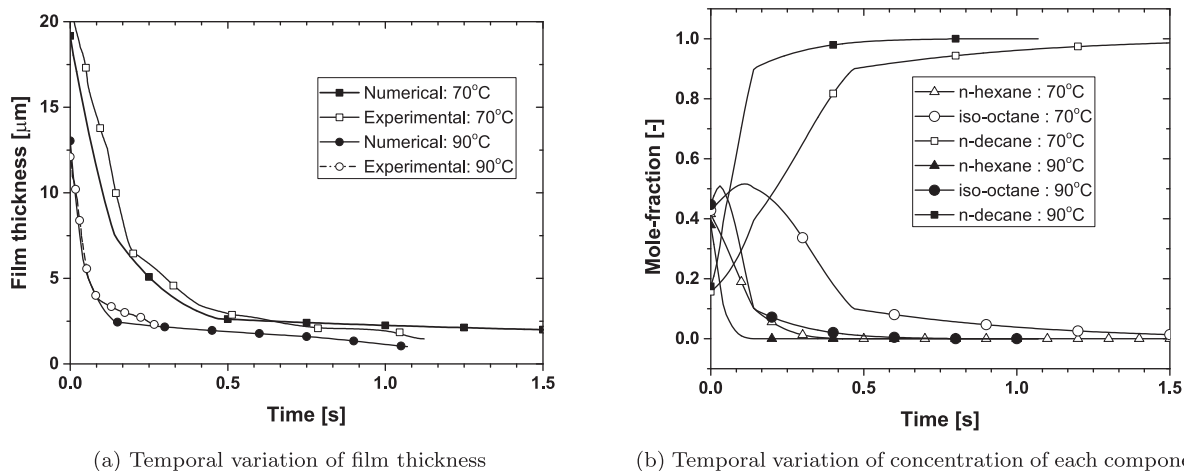


Fig. 14. Evaporation of three-component fuel (n-hexane, iso-octane and n-decane in 35:45:20 by mass).

sharpest slope in the initial stage of the evaporation process. After that, the model constant is switched to that of the second lighter component in the mixture until its mass-fraction also reaches a value of 0.1. This switching of the model constant is continued until all the components are completely evaporated. This methodology represents that the rate of reduction of the film thickness is primarily dependent on the evaporation of the most volatile component present adequately in the mixture at that instant. Fig. 13 shows the variation of the concentration of each component over time. The mole-fraction of the lighter component reduces over time, and the heavier component will be predominant in the mixture. When the heavier component dominates the presence in the mixture, the evaporation rate reduces as observed in Fig. 12(a).

#### 4.2.2. Three-component evaporation: n-hexane, iso-octane and n-decane

Fig. 14(a) shows the temporal variation of film thickness at 70 °C and 90 °C of the three-component gasoline surrogate. It can be observed that there exist three slopes during the evaporation process of the three-component thin liquid film. The initial slope is very steep and represents the rapid evaporation rate of the lightest component among the three, followed by a lesser slope representing the rate dominated by the evaporation of iso-octane and finally very low slope corresponding to slow evaporating n-decane in the mixture. This is achieved numerically by switching the value of the model constant  $C$  as described in Section 4.2.1.

It can be observed that for the 20 μm thick film of the mixture at 70 °C, the first slope exists until the film thickness reaches around 7–8 μm. After that, up to 3–4 μm film thickness, the slope shifts to a lower level. Beyond this, the film comprises mainly of the heaviest component, n-decane and hence the slope is very small prolonging the complete evaporation of the film to longer duration. Here the values beyond 2–3 μm is not shown in the plot because of the limitations of the measurement.

Fig. 14(b) shows the variation of concentration of each component in the mixture at various temperatures. It can be observed that the lightest component, n-hexane evaporates much earlier leaving iso-octane and n-decane in the liquid film. Moreover, after some time n-decane dominates the mixture and the evaporation rate is very slow. The close agreement of the numerical result and the experimental result shows that this method can be reliably used for quick estimation of the evaporation time of thin films in gasoline engine components which will be a valuable information for the engine designers.

## 5. Conclusion

In this study, the evaporation of a thin fuel film (10–50 μm) on a heated wall is investigated. Several single component hydrocarbons (n-hexane, n-heptane, iso-octane, n-decane) are used. A two-component and a three-component mixture representing gasoline are also used. The film thickness is measured using a very accurate confocal device which can measure thickness down to 2–3 μm. Thus the measurements could be made with very realistic film thickness as observed in wet-components of gasoline injection systems. The variation of film thickness with time was found to be linear for single component fuel and representing fractional distillation for the multi-component fuel. A model was developed to estimate the temporal variation of film thickness and evaporation time of the film for both single and multi-component fuels. A model constant depending on the saturation temperature of the fuel and the wall temperature was obtained. It was shown that the model can predict accurately the time of evaporation of thin films. Thus it will be a useful tool for designers of engines and fuel injection systems.

## Declaration of Competing Interest

None.

## Appendix A. Supplementary material

Supplementary data associated with this article can be found, in the online version, at <https://doi.org/10.1016/j.ijheatmasstransfer.2019.06.066>.

## References

- [1] O.S. Abianeh, C. Chen, A discrete multicomponent fuel evaporation model with liquid turbulence effects, *Int. J. Heat Mass Transf.* 55 (2012) 6897–6907.
- [2] B. Abramzon, W. Sirignano, Droplet vaporization model for spray combustion calculations, *Int. J. Heat Mass Transf.* 32 (1989) 1605–1618.
- [3] M. Bhat, R. Sakthikumar, D. Sivakumar, Fuel drop impact on heated solid surface in film evaporation regime, *Chem. Eng. Sci.* 202 (2019) 95–104.
- [4] H. Chaves, A.M. Kubitzek, F. Obermeier, Dynamic processes occurring during the spreading of thin liquid films produced by drop impact on hot walls, *Int. J. Heat Fluid Flow* 20 (1999) 470–476.
- [5] G. Desoutter, C. Habchi, B. Cuenot, T. Poinot, Single-component liquid film evaporation model development and validation using direct numerical simulations, 2006.
- [6] C.P. Ding, M. Sjöberg, D. Vuilleumier, David L. Reuss, X. He, B. Böhm, Fuel film thickness measurements using refractive index matching in a stratified-charge si engine operated on e30 and alkylate fuels, *Exp. Fluids* 59 (2018) 59.

- [7] M.C. Drake, T.D. Fansler, A.S. Solomon, G. Szekeley, Piston fuel films as a source of smoke and hydrocarbon emissions from a wall-controlled spark-ignited direct-injection engine. Technical Report. SAE Technical Paper, 2003.
- [8] V. Ebrahimian, Development of Multi-Component Evaporation Models and 3D Modeling of NOx-SCR Reduction System. Ph.D. thesis. Ph. D. Thesis, Institut National Polytechnique de Toulouse (INP Toulouse), Toulouse, France, 2011.
- [9] A. Elwardany, S.S. Sazhin, A. Farooq, Modelling of heating and evaporation of gasoline fuel droplets: a comparative analysis of approximations, *Fuel* 111 (2013) 643–647.
- [10] H.Y. Erbil, Evaporation of pure liquid sessile and spherical suspended drops: a review, *Adv. Colloid Interface Sci.* 170 (2012) 67–86.
- [11] D. Fairbanks, C. Wilke, Diffusion coefficients in multicomponent gas mixtures, *Industr. Eng. Chem.* 42 (1950) 471–475.
- [12] D. Fardad, N. Ladommatos, Evaporation of hydrocarbon compounds, including gasoline and diesel fuel, on heated metal surfaces, *Proc. Inst. Mech. Eng., Part D: J. Autom. Eng.* 213 (1999) 625–645.
- [13] S.M. Ghiaasiaan, *Convective Heat and Mass Transfer*, CRC Press, 2018, pp. 52–53.
- [14] S. Gong, W. Ma, T.N. Dinh, Diagnostic techniques for the dynamics of a thin liquid film under forced flow and evaporating conditions, *Microfluid. Nanofluid.* 9 (2010) 1077–1089.
- [15] S. Gong, W. Ma, T.N. Dinh, Simulation and validation of the dynamics of liquid films evaporating on horizontal heater surfaces, *Appl. Therm. Eng.* 48 (2012) 486–494.
- [16] S. Gong, W. Ma, H. Gu, An experimental investigation on bubble dynamics and boiling crisis in liquid films, *Int. J. Heat Mass Transf.* 79 (2014) 694–703.
- [17] S. Gong, W. Ma, C. Wang, Y. Mei, H. Gu, An investigation on dynamic thickness of a boiling liquid film, *Int. J. Heat Mass Transf.* 90 (2015) 636–644.
- [18] C. Habchi, A comprehensive model for liquid film boiling in internal combustion engines, *Oil Gas Sci. Technol.-Revue de l'Institut Français du Pétrole* 65 (2010) 331–343.
- [19] C. Habchi, N. Lamarque, J. Helie, S. Jay, Experimental and numerical investigation of dispersed and continuous liquid film under boiling conditions, in: *Class Europe. 28th european conference on Liquid Atomization and Spray Systems*, Editorial Universitat Politècnica de València, 2017, pp. 921–928.
- [20] J.O. Hirschfelder, C.F. Curtiss, B.R. Bird, *Molecular Theory of Gases and Liquid*, Chapman & Hall, London, 1964.
- [21] H. Hu, R.G. Larson, Evaporation of a sessile droplet on a substrate, *J. Phys. Chem. B* 106 (2002) 1334–1344.
- [22] M. Itaru, M. Kunihide, Heat transfer characteristics of evaporation of a liquid droplet on heated surfaces, *Int. J. Heat Mass Transf.* 21 (1978) 605–613.
- [23] J. Kim, Spray cooling heat transfer: the state of the art, *Int. J. Heat Fluid Flow* 28 (2007) 753–767.
- [24] F. Köpple, P. Jochmann, A. Kufferath, M. Bargende, Investigation of the parameters influencing the spray-wall interaction in a gdi engine-prerequisite for the prediction of particulate emissions by numerical simulation, *SAE Int. J. Engines* 6 (2013) 911–925.
- [25] Q. Lamiel, N. Lamarque, J. Hélie, D. Legendre, Spreading model for wall films generated by high-pressure sprays, in: *Class Europe. 28th european conference on Liquid Atomization and Spray Systems*, Editorial Universitat Politècnica de València, 2017, pp. 138–145.
- [26] P. Leick, B. Bork, J.N. Geiler, Experimental characterization of tip wetting in gasoline di injectors, in: *ICLASS. 14thTriennial International Conference on Liquid Atomization and Spray Systems*, Chicago, IL, USA, July 22–26, 2018.
- [27] D. Maligne, G. Bruneaux, Time-resolved fuel film thickness measurement for direct injection si engines using refractive index matching, 2011.
- [28] NIST, National institute of standards and technology, chemistry webbook, srd 69, 2018. <<https://webbook.nist.gov/chemistry/>>.
- [29] Y. Ra, R.D. Reitz, A vaporization model for discrete multi-component fuel sprays, *Int. J. Multiph. Flow* 35 (2009) 101–117.
- [30] F. Raoult, General law of the vapor pressure of solvents, *Comp. Rend.* 104 (1887) 1430–1433.
- [31] F. Schulz, F. Beyrau, Comparison of the spray and the spray/wall interaction of two gasoline injectors, *Int. J. Autom. Technol.* 19 (2018) 615–622.
- [32] F. Schulz, W. Samenfink, J. Schmidt, F. Beyrau, Systematic lif fuel wall film investigation, *Fuel* 172 (2016) 284–292.
- [33] D.L. Siebers, Scaling liquid-phase fuel penetration in diesel sprays based on mixing-limited vaporization. Technical Report. SAE technical paper, 1999.
- [34] R.H. Stanglmaier, C.E. Roberts, C.A. Moses, Vaporization of individual fuel drops on a heated surface: a study of fuel-wall interactions within direct-injected gasoline (DIG) engines. Technical Report. SAE Technical Paper, 2002.
- [35] G. Strotos, M. Gavaises, A. Theodorakakos, G. Bergeles, Numerical investigation of the evaporation of two-component droplets, *Fuel* 90 (2011) 1492–1507.
- [36] M. Su, C. Chen, Heating and evaporation of a new gasoline surrogate fuel: a discrete multicomponent modeling study, *Fuel* 161 (2015) 215–221.
- [37] J. Tamim, W.L. Hallett, A continuous thermodynamics model for multicomponent droplet vaporization, *Chem. Eng. Sci.* 50 (1995) 2933–2942.
- [38] G.W. Thomson, The antoine equation for vapor-pressure data, *Chem. Rev.* 38 (1946) 1–39.
- [39] S.R. Turns, *An Introduction to Combustion Concepts and Applications*, McGraw-hill, New York, 1996, pp. 707–709.
- [40] C. Wang, H. Xu, J.M. Herreros, J. Wang, R. Cracknell, Impact of fuel and injection system on particle emissions from a gdi engine, *Appl. Energy* 132 (2014) 178–191.
- [41] D. Wang, F.L. Chia-fon, Continuous multicomponent fuel film vaporization model for multidimensional engine modeling, Technical Report. SAE Technical Paper, 2005.
- [42] Y. Wang et al., Study of Deposit Formation Inside Diesel Injectors Nozzles. Ph. D. thesis, Institute of Technology, Massachusetts, 2012.
- [43] J.S. Wu, K.H. Hsu, P.M. Kuo, H.J. Sheen, Evaporation model of a single hydrocarbon fuel droplet due to ambient turbulence at intermediate reynolds numbers, *Int. J. Heat Mass Transf.* 46 (2003) 4741–4745.
- [44] F. Zhao, M.C. Lai, D.L. Harrington, Automotive spark-ignited direct-injection gasoline engines, *Progr. Energy Combust. Sci.* 25 (1999) 437–562.

## **8.4 Spreading model for wall films generated by high-pressure sprays**

This proceedings paper has been presented at the ILASS Valencia in 2017. It is the first step in the derivation of the fuel spreading model derived in this PhD thesis. The spreading was performed with n-heptane onto a rough plate.

# Spreading Model for Wall Films Generated by High-Pressure Sprays

Q. Lamiel, N. Lamarque, J. Hélie, D. Legendre\*

## Abstract

This paper presents a new model developed to predict the area of wall films that may develop in gasoline direct injection engines (GDI). In a always more restrictive legislation on gas emissions the injection process in internal combustion (IC) engines has been highlighted as a domain of great concern in order to satisfy these requirements. Many spray wall interactions models exist in literature and are included in different CFD tools. Most often they are based on the sum of single drop-wall impacts. The specificity of the present model lies in its simplicity and the way the film is treated globally. Here its propagation is predicted using a balance between the momentum given by the spray and the viscous shear stress. Jointly with the theoretical model, an experimental set-up has been built up, an optical measurement technique called Refractive Index Matching method is used to follow the development of the wall film.

It has been found that the area of the wall film is proportional to the duration of injection, while the distance between the injector and the wall has not shown significant influence on the evolution of area. The influence of the injection pressure has also been identified, when the pressure is doubled the radius of the film is multiplied by  $\sqrt[3]{2}$ . Eventually the model predicts that film thickness decreases as fuel pressure rises.

## Keywords

automotive sprays, spray-wall impingement, refractive index matching method

## Introduction

Fuel impingement in an internal combustion (IC) engine is a critical phenomenon. Despite progresses in gasoline direct injection (GDI) sytem design, fuel spray-wall impingement still happens for certain engine conditions and leads to liquid deposits. These wall films on the piston or the cylinder liner strongly affect mixture formation and entail bad local mixture homogeneity. This has been identified as a major source of pollutant emissions, especially particulate matter [1, 2]. As a consequence, it is essential to have a good understanding of these spray-wall interactions and identify the key factors to keep them under control.

Drop-wall impingement is a topic widely studied in literature, because many applications (automotive, aeronautics, cooling, fire safety, printing, painting, agrochemicals, phamaceutical to name some) strongly depend on the performances of atomisers and spray systems [3]. Many models have been derived with success to describe the different impact regimes (on cold or hot surfaces) and the spreading characteristics of single droplets [4, 5, 6]. Some of them are commonly used in CFD tools and coupled with a Lagrangian description of the spray [7, 8, 9].

Nevertheless, it has been shown that spray-wall impingement implies many phenomena, which cannot be completely described by single droplet-wall impact models [5, 10]. Moreover, while available computational power has strongly increased and despite some success, CFD tools sometimes remain expensive to simulate all the different engine conditions, for a first screening or even while optimising injector targeting and injection timings. In the present paper, a simple model based on basic conservation laws is proposed to describe wall film spreading in non- or low-volatile conditions. It is compared and validated with experimental measurements using the refractive index matching method and high-speed video imaging.

## Spray-wall interactions and experimental setup

When a GDI spray impinges upon the wall, the very numerous liquid droplets ( $10^9$  to  $10^{10}$ ) are either deposited or splashed and pushed away because of the high momentum, as depicted on Figure 1. In non-vaporising conditions, the deposited liquid mass quickly generates a continuous wall film. It then propagates under the effect of mass deposition and the spray dynamic pressure. While both the spray and the film can be observed on classical shadowgraph pictures like Figure 1, the film spreading can be better tracked with the refractive index matching (RIM) method.

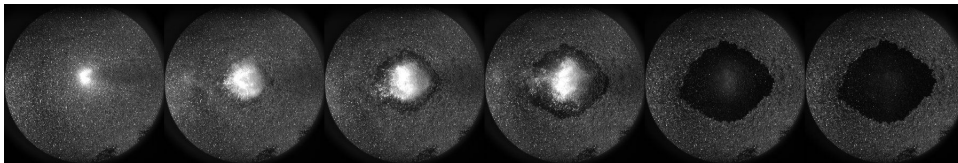
The experimental setup is presented in Figure 3. It is here composed of a GDI injector (b), fed by a high-pressure pump (a), which generates a spray (c) that impinges upon a transparent roughened quartz plate (e); the impingement and the spreading of the liquid are recorded with a high speed video camera (g). The camera is directed towards a mirror (f) placed under the impingement plate in order to observe the phenomena from below. The light source (d) is an optical fiber which illuminates the quartz plate at grazing angle. This method of visualisation is called Refractive Index Matching method (RIM) and it has originally been introduced by Drake [1] to study a DI engine then used by Yang and Gandhi in a Diesel engine [11]. Finally Maligne and Bruneaux [12] used it in a pressure chamber to compare wall films created by different types of GDI injectors. As the liquid fills in the surface

\*Q. Lamiel's PhD director, professor at INPT



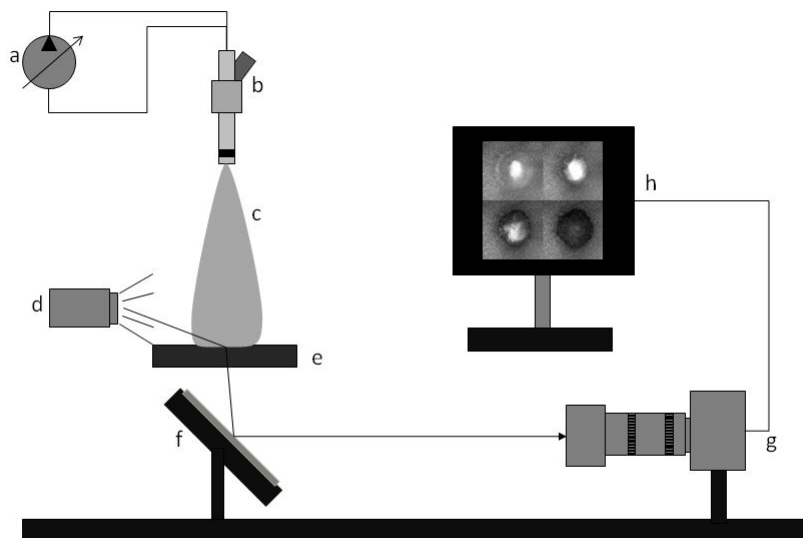


**Figure 1.** GDI spray impinging upon a smooth plate. Fuel pressure is 100bar.



**Figure 2.** Images of injection as visualised on the RIM setup for  $P_i = 200\text{bar}$ ,  $T_i = 5\text{ms}$  and  $d_W = 50\text{mm}$  images are displayed every 1.5ms

troughs, the illuminated plate scatters less light towards the camera. This enables to clearly identify the wall film footprint and its surface can be evaluated (see Figure 2). After a fine calibration, the wall film thickness is quantified [1, 11, 12]. The injector used for this study has three holes. In this particular case, it is tilted by  $30^\circ$ , hence one of the plumes impacts upon the plate vertically and the spreading is homogeneous in the radial direction. Using a specially developed image post-processing, the edge of the liquid film can be tracked through time.

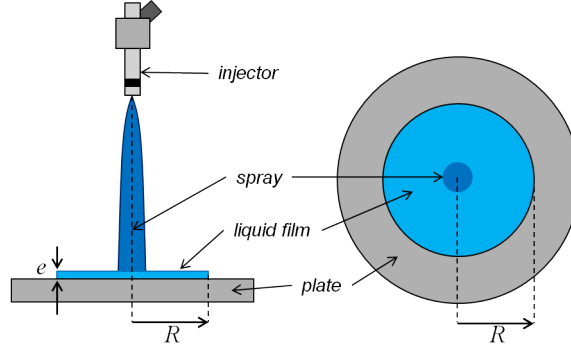


**Figure 3.** Sketch of the Refractive Index Matching experimental setup

### Wall-film spreading modelling

As very well underlined in [10], spray-wall impingement is a very complex phenomenon with many interactions between the incoming droplets and the perturbed film surface. Taking into account all the details (especially because the film is strongly perturbed by many simultaneous impacts) would be a tremendous effort. The purpose

here is not to develop yet another very fine drop-wall interaction model to be implemented in a CFD tool. In this section is derived a simple global model, which describes the wall film propagation. The first hypothesis is the wall film has a puddle or a pizza shape, with a homogeneous thickness  $e$  (see Figure 4). Surface tension effects, which are strong at the wall film edge and create a rim, are here neglected. Only a steady-state balance between a driving (spray pressure / momentum transfer) and a counteracting force in the radial propagation direction is considered.



**Figure 4.** Sketch of the modelled problem. The film thickness is supposed to be homogeneous.

The wall film spreading model relies on the use of the mass and momentum conservation equations, outside the impact zone. Considering the characteristic lengths and times (thickness  $e \simeq 10\mu\text{m}$ , radius  $R \simeq 10\text{mm}$ , injection time  $T_i \simeq 1\text{ms}$ ), the thin wall film is supposed to be in the lubrication regime. Considering that the mass is totally ( $K_m = 1$ ) or partially ( $K_m \leq 1$ ) transferred in the film, the mass balance writes:

$$\frac{d\pi R^2 e}{dt} = K_m Q, \quad (1)$$

where  $Q$  stands for the injection discharge of the injector, then assuming a constant film thickness and that  $Q$  is constant during the injection process:

$$R = \sqrt{\frac{K_m Q t}{\pi e}}. \quad (2)$$

This shows that the radius of the film is proportional to the square root of time, the thickness of the film needs to be derivated to exactly know the evolution of the film.

Now looking at the momentum balance and keeping in mind that the film is in the lubrication regime (i.e. the flow is then parallel and pressure only depends on  $r$ ):

$$\frac{\partial p}{\partial r} = \eta \frac{\partial^2 v_r}{\partial z^2}, \quad (3)$$

On the one hand a simple approximation on the pressure gradient gives:

$$\frac{\partial p}{\partial r} \approx \frac{\Delta P}{R}. \quad (4)$$

Defining  $\Delta P = P_s - P_a$  and  $P_s = P_a + P_d$  then  $\Delta P = P_d$ , which is the dynamic pressure given by the spray or, introducing  $K_p$  to take into account the fact that the film pressure in the impingement zone may not be equal to the spray total pressure  $\Delta P = K_p P_d$ .

On the other hand stress can be approximated as:

$$\eta \frac{\partial^2 v_r}{\partial z^2} \approx \frac{\eta V}{e^2}. \quad (5)$$

where  $V$  is the depth-averaged radial velocity. It can be used to express the wall film spreading velocity, by writing  $V = \dot{R}$ . Expressing  $e$  with the help of Eq 3 - 5 we get:

$$e = \sqrt{\frac{\eta V R}{2\pi K_p P_d}}, \quad (6)$$

and with  $VR \propto Q/e$  we get an expression for the thickness:

$$e \propto \sqrt[3]{\frac{\eta Q}{P_d}}. \quad (7)$$

As the discharge coefficient  $Q$  is varying like  $P_i^{1/2}$ , a trend for the evolution of  $e$  and  $R$  is found:

$$e \propto P_i^{-1/6} \quad \text{and} \quad R \propto P_i^{1/3}. \quad (8)$$

For convenience Eq 2 & 7 can be rewritten using  $K_P$ ,  $K_m$ ,  $\eta$ ,  $P_d$  and  $Q$  and it comes:

$$e = \sqrt[3]{\frac{\eta K_m Q}{2\pi K_P P_d}}, \quad (9)$$

and,

$$R^6 - R_0^6 = K \frac{P_d Q^2}{\pi^2 \eta} t^3, \quad (10)$$

where  $R_0$  stands for the impinging zone of the spray, inside this zone the flow is more complex and the accuracy of the model is not guaranteed. And the prefactor  $K$  is defined as :

$$K = 2K_P K_m^2, \quad (11)$$

and takes into account that the spray mass and momentum may only be partially transferred to the liquid film. In what follows, we set  $K_P = 1$  for simplicity, which means that the pressure at the film centre is the spray dynamic pressure. The value of  $K_m$  will be discussed in the next section.

## Results and discussion

This present paragraph shows the results obtained applying the RIM method and the comparison with the proposed model. Table 1 summarises the different operating points. Fuel pressure  $P_i$ , injection time  $T_i$  and injector-wall distance  $d_W$  have been varied within realistic ranges with respect to automotive applications.

**Table 1.** Operating points tested in the present study

Factor	Unit	Values
Fuel pressure $P_i$	<i>bar</i>	50, 100, 200
Injection time $T_i$	<i>ms</i>	1 to 5
Injector-wall distance $d_W$	<i>mm</i>	30, 40, 50, 60, 70

Figure 5 shows how the wall film area evolves in time. Whatever the injection time, the area growths collapse and, in the steady-state range are proportional to time. Here, only  $d_W = 50\text{mm}$  is displayed, as the injector wall-distance has very little influence on the phenomenon. Hence, it confirms the radius evolution as the square root of time, as shown by Eq 2. It can also be observed that, once the injection is finished, the wall film still has some inertia and continues spreading at a much slower rate; the assumption of a constant thickness is then questionable.

Figure 6 shows the film thickness obtained with the calibration of the RIM method. The gray level is roughly homogeneous on the whole puddle and variations are mainly due to the surface irregularities that can scatter light differently, the profile is made 2s after the start of injection. A steady state is reached and it is assumed that, no droplets that could disturb the measure, are present above the film surface. Hence a measurement of the mean film thickness is realised knowing the film surface. A value of  $3.7\mu\text{m}$  is found, with the assumption of constant thickness we can calculate the deposited mass of heptane. It is compared to the injected mass, and it provides the mass ratio  $K_m = 15.11\%$

A reasonable assumption is to say that a part of the mass deposited at the end of injection has already vaporised after 2s. After a quick evaluation (based on experiments about vaporisation rates of heptane droplets gently deposited on a plate), we can say that almost twice the mass was present at the end of injection. This gives a new value for  $K_m = 29\%$ , then the thickness at the end of injection is obtained using Eq 12:

$$e_{(t=T_i)} = \frac{e_{(t=2s)} A_{(t=2s)}}{A_{(t=T_i)}}. \quad (12)$$

The thickness of the film at the end of injection is  $14.8\mu\text{m}$ .

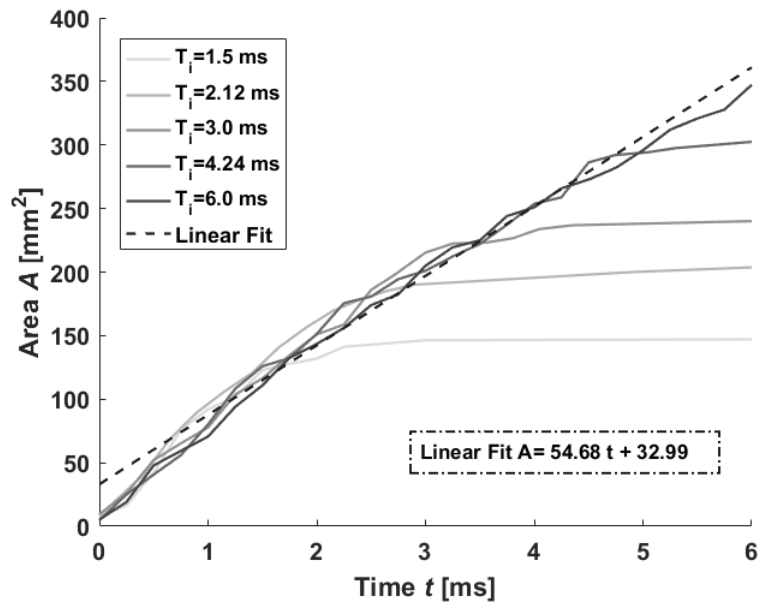


Figure 5. Wall film area time evolution for the operating point  $P_i = 100\text{bar}$ ,  $d_W = 50\text{mm}$  and different injection times.

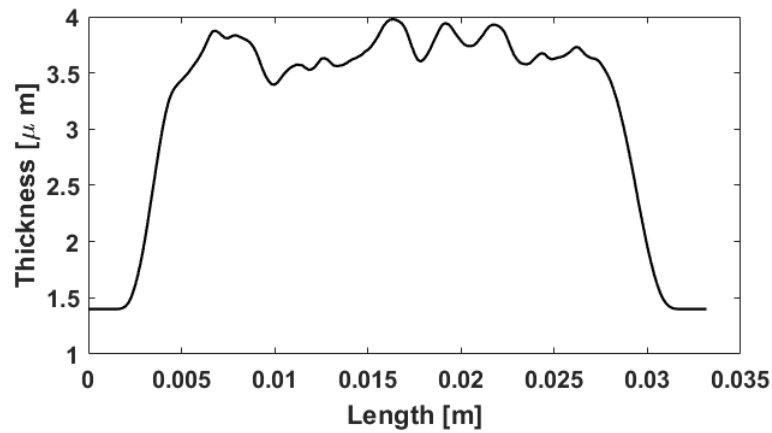


Figure 6. Thickness profile for a film of heptane obtained 2s after the end of injection;  $P_i = 100\text{bar}$ ,  $d_W = 60\text{mm}$ ,  $T_i = 5.0\text{ms}$

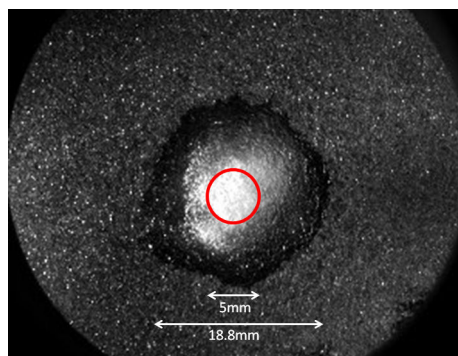


Figure 7. Normal impingement of spray on rough plate;  $P_i = 100\text{bar}$ ,  $d_W = 60\text{mm}$ ,  $T_i = 5.0\text{ms}$ . Red zone highlights the area where momentum is transferred to the film

On the other hand the model gives with Eq 9 and the slope of Figure 5 a thickness of  $16.8\mu\text{m}$  that is to say a relative error of 12% of the measured thickness.

It has been shown in previous studies that there is less deposited mass when fuel pressure increases [13]. Never-

theless, from 50 to 200bar, changes of  $K$  are not expected to be very high. Then, for simplicity,  $K_m$  is set to 0.29 in what follows which gives a value of 0.58 for  $K$ . According to Figure 5 and to Eq 10 a value of  $12.5 \times 10^3$  Pa for  $P_d$  is obtained. To understand the meaning of this value a simple calculation is performed, taking a value of  $K_P = 1$  (which is what we assume in the model) means that the momentum is conserved from the injector hole to the impact plate. In other words the pressure force is constant, which can be expressed by:

$$P_d A_s = P_i A_o, \quad (13)$$

where  $A_s$  is the area where the spray momentum is transferred to the liquid film and  $A_o$  is the area of the injector hole, then  $A_s = 18.2\text{mm}^2$  which correspond to a radius of 2.4mm which is really close to what we can observe on Figure 7.

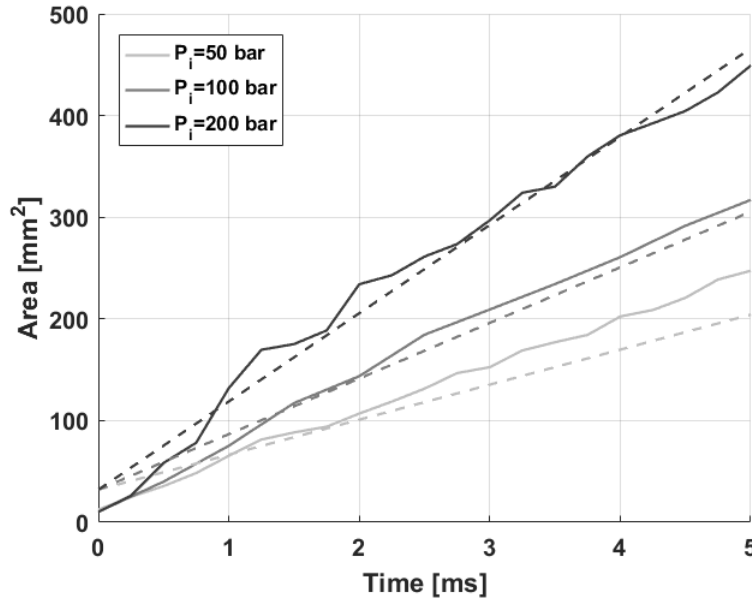


Figure 8. Wall film area time evolution for different fuel pressures  $T_i = 5\text{ms}$ ,  $d_W = 50\text{mm}$ .

Figure 8 shows the film area time evolution for different fuel pressures. As expected, area is growing linearly with time. From one fuel pressure to another, the slope of the fitting curve is changing. It is admitted that  $P_d$  varies linearly with  $P_i$ , while  $Q$  varies as  $\sqrt{P_i}$ .

Based on the value of  $K$  calculated above with  $P_i = 100\text{bar}$ , one gets for the coefficient in Eq 10, for a fuel pressure  $P_1$ :

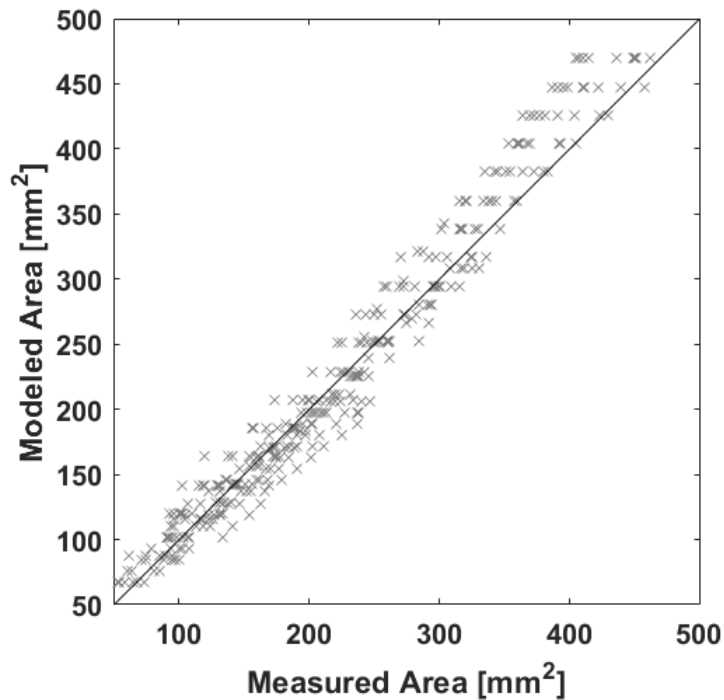
$$\left( \frac{P_d Q^2}{\pi^2 \eta} \right)_{P_1} = \left( \frac{P_1}{100 \cdot 10^5} \right)^{2/3} \left( \frac{P_d Q^2}{\pi^2 \eta} \right)_{100\text{bar}}. \quad (14)$$

Eq 14 then enables to determine the slope of the fitting lines and gives 34.4 and 86.8 for  $P_i = 50\text{bar}$  and  $P_i = 200\text{bar}$ , respectively they are represented on Figure 8. It is clear that the dependency  $R \propto P_i^{1/3}$  is correctly grasped by the model, however the prediction for the tests at 50bar is a bit below the experimental data. It could come from the value of  $K_m$ . Indeed it has been shown [13] that an increase in pressure causes a decrease in the deposited mass.

Eventually, the comparison between the model, and the experiment can be visualised on Figure 9. Here all the data collected at various pressure, injection duration and wall distance are displayed. The first bisector is represented in plain line to help visualise the quality of the model. Thus, Figure 9 shows the model fits well with the experimental measurements.

### Conclusions and perspectives

The model presented in this paper is based on mass conservation and a steady-state balance between the spray pressure and viscous stresses. The model predictions are compared with experimental results obtained using the refractive index matching method and high-speed video imaging. Despite its simplicity, it clearly shows its ability to fairly predict the time evolution of the film radius ( $R \propto t^{1/2}$ ), as well as the influence of the fuel injection pressure ( $R \propto P_i^{1/3}$ ). It is also able to predict the wall film thickness with reasonable accuracy ( $e \propto (\eta Q / P_D)^{1/3}$ ).



**Figure 9.** Comparison between measured and modeled area realised at 50, 100 and 200bar with injection time of 5.0ms and variable distance of injection

The model is currently extended to take into account oblique spray-wall impingement, so as to be more representative of typical impact angles in GDI engines. Heat transfers and phase changes will be then added to include the effects of the strong vaporisation when the wall temperature reaches boiling conditions. Variation of fuels and greater pressure range will be done, in order to validate the evolution of  $e$  as  $P^{-1/6}$ .

### Acknowledgements

ANR and ANRT are acknowledged for their financial support.

### Nomenclature

$V$	Depth averaged radial velocity [ $\text{m}\cdot\text{s}^{-1}$ ]
$v_r$	Velocity in the fuel [ $\text{m}\cdot\text{s}^{-1}$ ]
$e$	Thickness of the liquid film [m]
$P_d$	Pressure transmitted by the spray [Pa]
$Q$	Discharge of the injector [ $\text{m}^3\cdot\text{s}^{-1}$ ]
$K_P$	Pressure transmission coefficient
$K_m$	Deposited mass ration
$K$	Prefactor
$\eta$	Dynamic viscosity [Pa.s]
$R$	Radius of the wall film [m]
$A$	Area of the wall film [ $\text{m}^2$ ]
$A_s$	Area of spray impingement [ $\text{m}^2$ ]
$A_o$	Area of the injector hole [ $\text{m}^2$ ]
$P_i$	Pressure of injection [Pa]
$T_i$	Duration of injection [s]
$d_W$	Injector-wall distance [m]

### References

- [1] Michael C Drake, Todd D Fansler, Arun S Solomon, and GA Szekely. Piston fuel films as a source of smoke and hydrocarbon emissions from a wall-controlled spark-ignited direct-injection engine. Technical report, SAE Technical Paper, 2003.
- [2] Florian Steimle, Andre Kulzer, Herwig Richter, Dietmar Schwarzenthal, and Claudia Romberg. Systematic analysis and particle emission reduction of homogeneous direct injection si engines. Technical report, SAE

- Technical Paper, 2013.
- [3] Nasser Ashgriz. *Handbook of atomization and sprays: theory and applications*. Springer Science & Business Media, 2011.
  - [4] AL Yarin. Drop impact dynamics: splashing, spreading, receding, bouncing... *Annu. Rev. Fluid Mech.*, 38:159–192, 2006.
  - [5] ALN Moreira, AS Moita, and MR Panao. Advances and challenges in explaining fuel spray impingement: How much of single droplet impact research is useful? *Progress in energy and combustion science*, 36(5):554–580, 2010.
  - [6] Sander Wildeman, Claas Willem Visser, Chao Sun, and Detlef Lohse. On the spreading of impacting drops. *Journal of Fluid Mechanics*, 805:636–655, 2016.
  - [7] Donald W Stanton and Christopher J Rutland. Modeling fuel film formation and wall interaction in diesel engines. Technical report, SAE Technical Paper, 1996.
  - [8] P.J. O'Rourke and A.A. Amsden. A spray/wall interaction submodel for the kiva-3 wall film model. Technical report, SAE Technical Paper, 2000.
  - [9] CX Bai, H Rusche, and AD Gosman. Modeling of gasoline spray impingement. *Atomization and Sprays*, 12(1-3), 2002.
  - [10] Davood Kalantari and Cameron Tropea. Spray impact onto flat and rigid walls: Empirical characterization and modelling. *International Journal of Multiphase Flow*, 33(5):525–544, 2007.
  - [11] Bo Yang and Jaal Ghandhi. Measurement of diesel spray impingement and fuel film characteristics using refractive index matching method. Technical report, SAE Technical Paper, 2007.
  - [12] David Maligne and Gilles Bruneaux. Time-resolved fuel film thickness measurement for direct injection si engines using refractive index matching. Technical report, SAE Technical Paper, 2011.
  - [13] F Schulz, W Samenfink, J Schmidt, and F Beyrau. Systematic lif fuel wall film investigation. *Fuel*, 172:284–292, 2016.

## 8. APPENDIX

---



# Bibliography

- [1] Task 3.1: Study of the secondary spray and the liquid wall film generated by a gdi injector. Technical report, ANR ASTRIDE technical report, 2014. 7
- [2] C. Arcoumanis and J.-C. Chang. Heat transfer between a heated plate and an impinging transient diesel spray. *Experiments in Fluids*, 16(2):105–119, 1993. xxi, 122, 137, 138, 139, 140
- [3] N. Ashgriz. *Handbook of atomization and sprays: theory and applications*. Springer Science & Business Media, 2011. 16
- [4] C. Bai and A. Gosman. Development of methodology for spray impingement simulation. *SAE transactions*, pages 550–568, 1995. xxi, 149, 150
- [5] C. Bai, H. Rusche, and A. Gosman. Modeling of gasoline spray impingement. *Atomization and Sprays*, 12(1-3), 2002. xii, 16, 18, 81
- [6] T. Benzler, S. Faust, T. Dreier, and C. Schulz. Low-pressure effective fluorescence lifetimes and photo-physical rate constants of one-and two-ring aromatics. *Applied Physics B*, 121(4):549–558, 2015. 155
- [7] J. Breitenbach, I. V. Roisman, and C. Tropea. From drop impact physics to spray cooling models: a critical review. *Experiments in Fluids*, 59(3):55, 2018. xxi, 146, 151, 165
- [8] F. Briscoe and P. Shaw. Spread and evaporation of liquid. *Progress in Energy and Combustion Science*, 6(2):127–140, 1980. 166
- [9] T. J. Bruno. Improvements in the measurement of distillation curves. 1. a composition-explicit approach. *Industrial & engineering chemistry research*, 45(12):4371–4380, 2006. xxii, 152, 153, 154

## BIBLIOGRAPHY

---

- [10] H. S. Carslaw and J. C. Jaeger. Conduction of heat in solids. *Oxford: Clarendon Press, 1959, 2nd ed.*, 1959. 138
- [11] G. Castanet, O. Caballina, and F. Lemoine. Drop spreading at the impact in the leidenfrost boiling. *Physics of Fluids*, 27(6):063302, 2015. 150
- [12] G. Castanet, T. Liénart, and F. Lemoine. Dynamics and temperature of droplets impacting onto a heated wall. *International Journal of Heat and Mass Transfer*, 52(3-4):670–679, 2009. 146, 149
- [13] C. Chiang, M. Raju, and W. Sirignano. Numerical analysis of convecting, vaporizing fuel droplet with variable properties. *International journal of heat and mass transfer*, 35(5):1307–1324, 1992. xxi, 148
- [14] N. A. Chigier. *Energy, combustion, and environment*. McGraw-Hill New York, 1981. 147
- [15] R. Clift, J. Grace, and M. Weber. Bubbles, drops, and particles—academic press. *New York*, 510, 1978. 147
- [16] H. Dageförde, A. Kiefer, W. Samenfink, W. Wiese, and A. Kufferath. Requirements for spray and tip design of a multi-hole injector for disi engines. *Proceedings of ICLASS, Tainan*, 2015. 3
- [17] J. Dernote, C. Mounaïm-Rousselle, F. Halter, and P. Seers. Evaluation of butanol–gasoline blends in a port fuel-injection, spark-ignition engine. *Oil & Gas Science and Technology—Revue de l’Institut Français du Pétrole*, 65(2):345–351, 2010. 4
- [18] M. C. Drake, T. D. Fansler, A. S. Solomon, and G. Szekely. Piston fuel films as a source of smoke and hydrocarbon emissions from a wall-controlled spark-ignited direct-injection engine. , SAE Technical Paper, 2003. 57, 59, 65
- [19] M. Duff and J. Towey. Two ways to measure temperature using thermocouples feature simplicity, accuracy, and flexibility. *Analog dialogue*, 44(10):1–6, 2010. xv, 70

- 
- [20] P. Eastwood. *Particulate emissions from vehicles*, volume 20. John Wiley & Sons, 2008. 4
- [21] T. D. Fansler and S. E. Parrish. Spray measurement technology: a review. *Measurement Science and Technology*, 26(1):012002, 2014. 84
- [22] H. Foucart, C. Habchi, J. Le Coz, and T. Baritaud. Development of a three dimensional model of wall fuel liquid film for internal combustion engines. , SAE Technical Paper, 1998. 81
- [23] M. Frenklach and J. Warnatz. Detailed modeling of pah profiles in a sooting low-pressure acetylene flame. *Combustion science and technology*, 51(4-6):265–283, 1987. 4
- [24] C. Habchi. A comprehensive model for liquid film boiling in internal combustion engines. *Oil & Gas Science and Technology—Revue de l Institut Français du Pétrole*, 65(2):331–343, 2010. xxv, 37, 38, 164, 166
- [25] Z. Han, Z. Xu, and N. Trigui. Spray/wall interaction models for multidimensional engine simulation. *International Journal of Engine Research*, 1(1):127–146, 2000. 17, 81
- [26] M. Hartmann, I. Gushterova, M. Fikri, C. Schulz, R. Schießl, and U. Maas. Auto-ignition of toluene-doped n-heptane and iso-octane/air mixtures: High-pressure shock-tube experiments and kinetics modeling. *Combustion and Flame*, 158(1):172–178, 2011. 155
- [27] J. Heinlein and U. Fritsching. Droplet clustering in sprays. *Experiments in fluids*, 40(3):464–472, 2006. 84
- [28] J. Hélie, N. Lamarque, J.-L. Fremaux, P. Serrecchia, M. Khosravi, and O. Berke-meier. The process of tip wetting at the spray injection end. *International Journal of Engine Research*, page 1468087419840842, 2019. xi, 3, 151
- [29] J. Hélie, N. Lamarque, I. Krotow, T. Mimori, M. Albert, and K. Dobashi. GDI spray targeting - a contribution to design rules and tools for low particle emissions. , Japan SAE Technical Paper, 2018. xiii, 40, 41

## BIBLIOGRAPHY

---

- [30] S. Henkel, Y. Hardalupas, A. Taylor, C. Conifer, R. Cracknell, T. K. Goh, P.-B. Reinicke, M. Sens, and M. Rieß. Injector fouling and its impact on engine emissions and spray characteristics in gasoline direct injection engines. *SAE International Journal of Fuels and Lubricants*, 10(2):287–295, 2017. xi, xxi, 3, 4, 66, 152
- [31] J. B. Heywood. Internal combustion engine fundamentals. 1988. 8
- [32] K. Horvat. *Computational modelling of spray impingement accounting for the wall film formation*. Shaker, 2007. 15
- [33] H. E. Huppert. Flow and instability of a viscous current down a slope. *Nature*, 300(5891):427, 1982. 84, 106
- [34] F. P. Incropera, A. S. Lavine, T. L. Bergman, and D. P. DeWitt. *Fundamentals of heat and mass transfer*. Wiley, 2007. 166
- [35] L. M. Itani, G. Bruneaux, A. Di Lella, and C. Schulz. Two-tracer lif imaging of preferential evaporation of multi-component gasoline fuel sprays under engine conditions. *Proceedings of the Combustion Institute*, 35(3):2915–2922, 2015. 155
- [36] C. Jiang, H. Xu, D. Srivastava, X. Ma, K. Dearn, R. Cracknell, and J. Krueger-Venus. Effect of fuel injector deposit on spray characteristics, gaseous emissions and particulate matter in a gasoline direct injection engine. *Applied energy*, 203:390–402, 2017. xxi, 152
- [37] D. Kalantari. *Characterization of liquid spray impact onto walls and films*. PhD thesis, Technische Universität, 2007. 15
- [38] D. Kalantari and C. Tropea. Spray impact onto flat and rigid walls: Empirical characterization and modelling. *International Journal of Multiphase Flow*, 33(5):525–544, 2007. 15, 88, 151
- [39] A. Kanury. Introduction to combustion phenomena, gordon and breach, new york. 1975, 1975. 147
- [40] J. E. Ketterer and W. K. Cheng. On the nature of particulate emissions from disl engines at cold-fast-idle. *SAE International Journal of Engines*, 7(2):986–994, 2014. xi, 4, 5, 48

- [41] K. Ko and M. Arai. Diesel spray impinging on a flat wall, part i: Characteristics of adhered fuel film in an impingement diesel spray. *Atomization and Sprays*, 12(5&6), 2002. 91, 92, 117
- [42] F. Köpple, P. Jochmann, A. Kufferath, and M. Bargende. Investigation of the parameters influencing the spray-wall interaction in a gdi engine-prerequisite for the prediction of particulate emissions by numerical simulation. *SAE International Journal of Engines*, 6(2):911–925, 2013. xiii, 2, 35, 36, 40, 46, 153
- [43] D. Kuhnke. *Spray/wall interaction modelling by dimensionless data analysis*. Shaker, 2004. 81
- [44] N. Lamarque, C. Schmit, and J. Hélie. Refractive index matching method to study gasoline spray-wall impingement. *9th ICMF, Firenze, Italy*, 2016. xi, 3, 115
- [45] Q. Lamiel, N. Lamarque, J. Hélie, and D. Legendre. Spreading model for wall films generated by high-pressure sprays. In *ILASS-Europe 2017*, 2017. 57, 97, 99, 117
- [46] Q. Lamiel, N. Lamarque, J. Helie, and D. Legendre. On the spreading of high-pressure spray-generated liquid wall films. *Physical Review Fluids*, Under revision, 2019. 166
- [47] F. Leach, T. Knorscg, C. Laidig, and W. Wiese. A review of the requirements for injection systems and the effects of fuel quality on particulate emissions from gdi engines. 2018. 2, 4
- [48] S. Y. Lee and S. U. Ryu. Recent progress of spray-wall interaction research. *Journal of mechanical science and technology*, 20(8):1101, 2006. xxi, 149, 150
- [49] J. G. Leidenfrost. On the fixation of water in diverse fire. *International Journal of Heat and Mass Transfer*, 9(11):1153–1166, 1966. 37, 148
- [50] X. Li, H. Pan, X. Dong, D. Hung, and M. Xu. Spray impingement wall film breakup by wave entrainment. *Proceedings of the Combustion Institute*, 37(3):3287–3294, 2019. 106

## BIBLIOGRAPHY

---

- [51] J. H. Lienhard. *A heat transfer textbook*. Courier Corporation, 2011. 166
- [52] H. Luo, K. Nishida, S. Uchitomi, Y. Ogata, W. Zhang, and T. Fujikawa. Effect of temperature on fuel adhesion under spray-wall impingement condition. *Fuel*, 234:56–65, 2018. 65, 115
- [53] S. Makhoulf. *Contribution à l'étude de l'impact de la cavitation sur les processus physiques de l'atomisation primaire des jets d'injecteurs essence*. PhD thesis, 2015. xii, 12, 14, 51, 101
- [54] D. Maligne and G. Bruneaux. Time-resolved fuel film thickness measurement for direct injection si engines using refractive index matching. , SAE Technical Paper, 2011. 57, 59, 61
- [55] Manner sensortelemetrie. *Operating manual telemetry system*. xii, 30
- [56] U. Meingast, L. Reichelt, and U. Renz. Measuring transient wall heat flux under diesel engine conditions. *International Journal of Engine Research*, 5(5):443–452, 2004. xxi, 136, 138, 139, 140
- [57] Y. Miura, K. Miyahara, S. Sasaki, T. Kashio, and K. Yoshida. Development of a gasoline direct injector fouling test and its application to study of keep-clean performance at different additive treat rates. Technical report, SAE Technical Paper, 2016. 4
- [58] M. J. Moran, H. N. Shapiro, D. D. Boettner, and M. B. Bailey. *Fundamentals of engineering thermodynamics*. John Wiley & Sons, 2010. xii, 27, 28
- [59] A. Moreira, A. Moita, and M. Panao. Advances and challenges in explaining fuel spray impingement: How much of single droplet impact research is useful? *Progress in energy and combustion science*, 36(5):554–580, 2010. xxi, 14, 16, 17, 18, 148, 149, 150
- [60] A. Moreira and M. O. Panao. Spray-wall impact. In *Handbook of Atomization and Sprays*, pages 441–455. Springer, 2011. 81
- [61] S. Mouvanal. *Hydrothermal phenomenon in GDI injector nozzle associated with carbon deposit formation*. PhD thesis, Indian institute of technology Madras, Chennai, 2019. 20

- [62] S. Mouvanal, Q. Lamiel, N. Lamarque, J. Helie, A. Burkhardt, S. Bakshi, and D. Chatterjee. Evaporation of thin liquid film of single and multi-component hydrocarbon fuel from a hot plate. *International Journal of Heat and Mass Transfer*, 141:379–389, 2019. 157
- [63] C. Mundo, M. Sommerfeld, and C. Tropea. Droplet-wall collisions: experimental studies of the deformation and breakup process. *International journal of multiphase flow*, 21(2):151–173, 1995. 16, 17
- [64] J. Naber and R. D. Reitz. Modeling engine spray/wall impingement. , SAE Technical Paper, 1988. 81
- [65] J. D. Naber and D. L. Siebers. Effects of gas density and vaporization on penetration and dispersion of diesel sprays. *SAE transactions*, pages 82–111, 1996. 11
- [66] J. Neumeister, J. Taylor, and D. Gurney. Virtual air path calibration of a multi cylinder high performance gdi engine using 1d cycle simulation. Technical report, SAE Technical Paper, 2007. 24
- [67] S. Nukiyama. The maximum and minimum values of the heat  $q$  transmitted from metal to boiling water under atmospheric pressure. *International Journal of Heat and Mass Transfer*, 9(12):1419–1433, 1966. 37, 147
- [68] C. Oh and W. K. Cheng. Assessment of gasoline direct injection engine cold start particulate emission sources. *SAE International Journal of Engines*, 10(4):1556–1565, 2017. 4
- [69] P. O'Rourke and A. Amsden. A spray/wall interaction submodel for the kiva-3 wall film model. , SAE Technical Paper, 2000. 81
- [70] T. Pauer, H. Yilmaz, J. Zumbrägel, and E. Schünemann. New generation bosch gasoline direct-injection systems. *MTZ worldwide*, 78(7-8):16–23, 2017. 3
- [71] R. Payri, F. Salvador, J. Gimeno, and A. Garcia. Flow regime effects over non-cavitating diesel injection nozzles. *Proceedings of the Institution of Mechanical Engineers, Part D: Journal of Automobile Engineering*, 226(1):133–144, 2012. 12, 131

## BIBLIOGRAPHY

---

- [72] R. Payri, F. Salvador, J. Gimeno, and R. Novella. Flow regime effects on non-cavitating injection nozzles over spray behavior. *International Journal of Heat and Fluid Flow*, 32(1):273–284, 2011. xi, 11, 12, 13
- [73] W. F. Piock, B. Befrui, A. Berndorfer, and G. Hoffmann. Fuel pressure and charge motion effects on gdi engine particulate emissions. *SAE International Journal of Engines*, 8(2):464–473, 2015. 3
- [74] T. Poinso and D. Veynante. *Theoretical and numerical combustion*. RT Edwards, Inc., 2005. 4, 35
- [75] L. Reichelt, U. Meingast, and U. Renz. Calculating transient wall heat flux from measurements of surface temperature. *International Journal of Heat and Mass Transfer*, 45(3):579–584, 2002. 122, 136, 137, 138, 141
- [76] M. Rein. Interactions between drops and hot surfaces. In *Drop-Surface Interactions*, pages 185–217. Springer, 2002. xxi, 148, 149, 150
- [77] I. Roisman, L. Araneo, and C. Tropea. Effect of ambient pressure on penetration of a diesel spray. *International journal of multiphase flow*, 33(8):904–920, 2007. xi, 12, 13
- [78] I. V. Roisman, R. Rioboo, and C. Tropea. Normal impact of a liquid drop on a dry surface: model for spreading and receding. *Proceedings of the Royal Society of London. Series A: Mathematical, Physical and Engineering Sciences*, 458(2022):1411–1430, 2002. 16
- [79] A. Roque. *Experimental study of spray-wall-flame interaction on the formation of soot and solid deposit. Application to gasoline direct injection (GDI) engines*. PhD thesis, Université d’Orleans, 2020. 19
- [80] A. Roque, F. Foucher, W. Imoehl, and J. Helie. Generation and oxidation of soot due to fuel films utilizing high speed visualization techniques. Technical report, SAE Technical Paper, 2019. 155
- [81] D. Sabathil, A. Koenigstein, P. Schaffner, J. Fritzsche, and A. Doehler. The influence of disi engine operating parameters on particle number emissions. Technical report, SAE Technical Paper, 2011. 3



- [82] P. Sandoz, G. Tribillon, and H. Perrin. High-resolution profilometry by using phase calculation algorithms for spectroscopic analysis of white-light interferograms. *Journal of Modern Optics*, 43(4):701–708, 1996. 74
- [83] S. Sazhin, G. Feng, and M. Heikal. A model for fuel spray penetration. *Fuel*, 80(15):2171–2180, 2001. 11
- [84] J. Schindelin, I. Arganda-Carreras, E. Frise, V. Kaynig, M. Longair, T. Pietzsch, S. Preibisch, C. Rueden, S. Saalfeld, B. Schmid, et al. Fiji: an open-source platform for biological-image analysis. *Nature methods*, 9(7):676, 2012. 82, 107
- [85] F. Schulz and F. Beyrau. Systematic investigation of fuel film evaporation. Technical report, SAE Technical Paper, 2018. 92
- [86] F. Schulz, W. Samenfink, J. Schmidt, and F. Beyrau. Systematic lif fuel wall film investigation. *Fuel*, 172:284–292, 2016. 91, 92, 117
- [87] T. J. Seebeck. *Magnetische polarisation der metalle und erze durch temperatur-differenz*. Number 70. W. Engelmann, 1895. 69
- [88] J. Sevik, M. Pamminger, T. Wallner, R. Scarcelli, S. Wooldridge, B. Boyer, S. Miers, and C. Hall. Influence of charge motion and compression ratio on the performance of a combustion concept employing in-cylinder gasoline and natural gas blending. *Journal of Engineering for Gas Turbines and Power*, 140(12):121501, 2018. 40
- [89] K. Sienski, R. Eden, and D. Schaefer. 3-d electronic interconnect packaging. In *1996 IEEE Aerospace Applications Conference. Proceedings*, volume 1, pages 363–373. IEEE, 1998. xxi, 138, 139
- [90] N. Silvi and E. Dussan V. The rewetting of an inclined solid surface by a liquid. *The Physics of fluids*, 28(1):5–7, 1985. 84, 106
- [91] W. A. Sirignano. *Fluid dynamics and transport of droplets and sprays*. Cambridge University Press, 1999. MB. 146, 147
- [92] K. D. Squires and J. K. Eaton. Preferential concentration of particles by turbulence. *Physics of Fluids A: Fluid Dynamics*, 3(5):1169–1178, 1991. 84

## BIBLIOGRAPHY

---

- [93] D. W. Stanton and C. J. Rutland. Modeling fuel film formation and wall interaction in diesel engines. *SAE transactions*, pages 808–824, 1996. 17
- [94] D. W. Stanton and C. J. Rutland. Multi-dimensional modeling of thin liquid films and spray-wall interactions resulting from impinging sprays. *International Journal of Heat and Mass Transfer*, 41(20):3037–3054, 1998. 17, 81
- [95] C. Stow and M. Hadfield. An experimental investigation of fluid flow resulting from the impact of a water drop with an unyielding dry surface. *Proceedings of the Royal Society of London. A. Mathematical and Physical Sciences*, 373(1755):419–441, 1981. 17
- [96] D. Tanaka, R. Uchida, T. Noda, A. Kolbeck, S. Henkel, Y. Hardalupas, A. Taylor, and A. Aradi. Effects of fuel properties associated with in-cylinder behavior on particulate number from a direct injection gasoline engine. Technical report, SAE Technical Paper, 2017. 66, 166
- [97] M. Trujillo, W. Mathews, C. Lee, and J. Peters. Modelling and experiment of impingement and atomization of a liquid spray on a wall. *International Journal of Engine Research*, 1(1):87–105, 2000. 16, 81
- [98] D. Wang and A. Watkins. Numerical modeling of diesel spray wall impaction phenomena. *International Journal of Heat and Fluid Flow*, 14(3):301–312, 1993. 81
- [99] F. Williams. Some aspects of metal particle combustion. *Physical and Chemical Aspects of Combustion: A Tribute to Irv Glassman*, 1, 1997. 147
- [100] B. Yang and J. Ghandhi. Measurement of diesel spray impingement and fuel film characteristics using refractive index matching method. , SAE Technical Paper, 2007. 57, 59, 61
- [101] A. Yarin and D. Weiss. Impact of drops on solid surfaces: self-similar capillary waves, and splashing as a new type of kinematic discontinuity. *Journal of fluid mechanics*, 283:141–173, 1995. 16
- [102] A. L. Yarin, I. V. Roisman, and C. Tropea. *Collision phenomena in liquids and solids*. Cambridge University Press, 2017. 149

## BIBLIOGRAPHY

---

- [103] Y. Zhang, M. Jia, H. Liu, and M. Xie. Development of an improved liquid film model for spray/wall interaction under engine-relevant conditions. *International Journal of Multiphase Flow*, 79:74–87, 2016. 81